Dissertation zur Erlangung des Doktorgrades
der Fakultät für Chemie und Pharmazie
der Ludwig-Maximilians-Universität München

Computational Study on the Electronic, Magnetic and Spectroscopic Properties of the $BaFe_2As_2$ Family

Gerald Norman Rudolf Derondeau

aus

Gräfelfing, Deutschland

2016

Erklärung

Diese Dissertation wurde im Sinne von § 7 der Promotionsordnung vom 28. November 2011 von Herrn Prof. Dr. Hubert Ebert betreut.

Eidesstattliche Versicherung

Diese Dissertation wurde eigenständig und ohne unerlaubte Hilfe erarbeitet.

München, 27.10.2016

(Gerald Derondeau)

Dissertation eingereicht am	03.11.2016
1. Gutachter:	Prof. Dr. Hubert Ebert
2. Gutachter:	Prof. Dr. Dirk Johrendt
Mündliche Prüfung am	23.01.2017

Acknowledgements

First, I would like to thank Prof. Dr. Hubert Ebert for supervising my PhD Thesis. I was glad to have the opportunity to follow my own ideas, combined with his support and help for me in order to finish this work.

Special thanks go to PD Dr. Ján Minár who had a huge part in supervising me. He helped me with the topic of iron pnictides and was always interested in our results. I also deeply appreciate his trust in me and my ideas.

I would like to thank Prof. Dr. Dirk Johrendt for his time to review this thesis as an expert on the field of iron pnictides. Additionally, I like to thank Prof. Dr. Achim Hartschuh, Prof. Dr. Bettina Lotsch and Prof. Dr. Christian Ochsenfeld for being additional members of my thesis committee.

I am grateful to Dr. Alexander Yaresko for his help in the beginning of my PhD and his invitation for me to the MPI Stuttgart. Furthermore, I appreciate the great scientific cooperation with Dr. Federico Bisti and Dr. Vladimir Strocov from the Swiss Light Source of the Paul Scherrer Institute.

Special thanks go to Prof. Dr. Peter Krüger of the Chiba University for his kind hospitality during my time in Japan. In this context I would also like to thank Dr. Keisuke Hatada and Dr. Didier Sébilleau.

I like to thank all my colleagues, namely Dr. Stephan Borek, Dr. Sven Bornemann, Dr. Jürgen Braun, Kristina Chadova, Dr. Diemo Ködderitzsch, Michael Maaß, Dr. Sergiy Mankovsky, Laurent Nicolaï, Martin Offenberger, Dr. Masako Ogura, Svitlana Polesya, Rita Römling, Sebastian Wimmer and Henrieta Volfová. It was always a pleasure working with every of you.

I would like to thank all the friends of our group I was able to work with during many conferences and meetings, in particular Dr. Stanislav Chadov, Dr. Martin Lüders and Dr. Ondřej Šipr.

My final appreciation is for Dr. Tobias Stürzer, who was the first who started my passion for the iron pnictides.

Contents

1 Introduction **1**

2 Theoretical framework **5**

2.1 The Korringa-Kohn-Rostoker Green function method 6
  2.1.1 General properties of the single-particle Green function 7
  2.1.2 The free electron Green function 9
  2.1.3 Solving the single site scattering problem 12
  2.1.4 Solving the multiple scattering problem 15
  2.1.5 Substitutionally disordered alloys 18
  2.1.6 Calculation of observables 20
  2.1.7 Hyperfine interactions 21
  2.1.8 Dynamical mean field theory within SPR-KKR 22
2.2 Angle-resolved photoemission spectroscopy 24
  2.2.1 Experimental setup 24
  2.2.2 General theory 25
  2.2.3 One-step model of photoemission 27
  2.2.4 Surface related states as observed in ARPES 30
2.3 Transport properties 31
  2.3.1 General introduction 31
  2.3.2 Kubo equation 32
  2.3.3 Kubo-Greenwood equation 34

3 High-temperature iron pnictide superconductors **37**

3.1 Classification of iron pnictides 38
3.2 The subgroup of the 122-compounds 43
  3.2.1 The $BaFe_2As_2$ mother compound 43
  3.2.2 Substituted $BaFe_2As_2$ superconductors 44

4 The antiferromagnetic ground state 47
4.1 Motivation 47
4.2 Publication: Physical Review B 90, 184509 49
4.3 Discussion 59

5 Anisotropic properties seen in photoemission 61
5.1 Motivation 61
5.2 Publication: Physical Review B 93, 144513 63
5.3 Discussion 74

6 Impact of the photoemission response 75
6.1 Motivation 75
6.2 Publication: arXiv 1606.08977 78
6.3 Additional calculations 93
6.4 Discussion 97

7 Anisotropic magnetoresistance 99
7.1 Motivation 99
7.2 Publication: arXiv 1608.08077 101
7.3 Discussion 114

8 Relativistic hyperfine interactions 115
8.1 Motivation 115
8.2 Publication: Physical Review B 94, 214508 117
8.3 Discussion 126

9 Summary 127

A Computational details 131

B Structural details 135

Bibliography 141

Curriculum Vitae 161

List of Publications 163

Chapter 1

Introduction

The phenomenon of superconductivity (SC) gives the opportunity to transport an electrical current in a material without any resistance below a given critical temperature T_c. High-tech applications for superconductors are numerous, however, a broad application is hindered by the low temperatures which are necessary for the superconducting state to persist. Thus, it is not surprising that the ongoing search for new high-temperature superconductors, in a hope of finding maybe the long anticipated room temperature superconductor, shapes several fields of modern science.

Recently, in 2015, the field of high-temperature superconductivity (HT-SC) has experienced groundbreaking news with the realization of superconductivity up to a critical temperature of 203 K in H_3S, which is the hydrogen-rich, high-pressure phase of the well known compound H_2S.[1] Notably, the fundamental idea of hydrogen-rich superconductors goes back to the theoretical work of Ashcroft[2] in 1968 who proposed metallic hydrogen to be a superconductor with a very high critical temperature. The hydrogen-rich H_3S system is the first time in history that a previously unknown compound was first predicted from theory to be a high-temperature superconductor[3,4], which was later experimentally confirmed.[1,5] This emphasizes the crucial role theory plays nowadays for new advances in the field of HT-SC.

Considering this actual relevance of SC in research, with more than fifty thousand publications in the last ten years[A], one would not expect that the phenomenon is known for more than 100 years. It was first discovered by Onnes[6,7] in 1911 for mercury below its critical temperature T_c of 4.2 K. For a long period of time nobody believed that superconductivity could ever exist at temperatures above approximately 20 K. This was supported by the BCS theory[8] of Bardeen, Cooper and Schrieffer

---

[A] According to a search in the Web of Science v.5.22.3 performed in August 2016 for the terms superconductor or superconductivity and for the years from 2005 to 2015 who presented in 1957 a reasonable concept for the occurrence of superconductivity. However, within this theory the formation of the necessary Cooper pairs is bound to a phonon mediated interaction which was believed to restrict the critical temperature to around 30 K.[B] In 1986 Bednorz and Müller discovered superconductivity in the cuprate $La_{1.85}Ba_{0.15}CuO_4$[9] with a surprising T_c of 35 K. Nowadays this extraordinary discovery is known as the beginning of high-temperature superconductivity. Shortly after, a huge amount of new cuprate superconductors with intriguing high T_c values was found. Although the cuprates have high critical temperatures, their material properties are rather poor due to their ceramic nature.

It was only in 2008 when the iron arsenides or more general the transition metal pnictides were discovered as second family of high-temperature superconductors. Great international interest followed as Kamihara *et al.*[10,11] reported a critical temperature of 26 K in fluorine doped LaOFeAs. Previously, superconductivity was already discovered in LaOFeP[12] and LaONiP[13,14], however, the relatively low T_c values of about 7 K let these discoveries pass without further notification. The highest reported critical temperature of an iron pnictide so far is 55 K in $SmO_{1-x}F_xFeAs$[15], which has been at this point the highest T_c since the days of the cuprate superconductors. Because of these relatively high T_c values already under normal pressure and because the iron pnictides are metals instead of ceramics, leading to more desired material properties, this group is still very promising for the field of superconductivity. As it was already stressed, not only the experimental advances have brought valuable new insights, but also theoretical investigations of the iron pnictides have been performed very extensively and are an important field of nowadays condensed matter science.

However, most iron pnictides are quite difficult to characterize computationally by density functional theory (DFT).[16–18] This is at least partly due to the complex phase diagrams the iron superconductors exhibit, meaning most compounds show a structural and magnetic phase transition at low temperatures. In particular, it is typically necessary to dope the respective mother compounds e.g. by substitution of elements in order to suppress the antiferromagnetic order and to induce superconductivity. Furthermore, it is commonly believed that the emergence of unconventional superconductivity in the iron pnictides is mediated by antiferromagnetic spin fluctuations and thus connected to their complex magnetic properties.[19–21]

This work concentrates on a first-principles theoretical description of primarily the antiferromagnetic phase of the iron pnictides and their related anisotropic properties.

[B] That conventional superconductivity cannot exceed around 40 K was commonly believed until the latter mentioned H_3S was discovered, which is considered to be a conventional superconductor[1]

For this goal it is most reasonable to focus on the so-called 122-family of iron pnictides based on the mother compound $BaFe_2As_2$ as a prototype system, originally discovered as a superconductor by Rotter *et al.*[22,23]. The superconductors of this family were most extensively studied concerning their magnetic properties[18,24–26], different elements for substitution[22,27–30], angle-resolved photoemission spectroscopy (ARPES)[31–37], transport properties[38–44] and hyperfine interactions[45–48]. Consequently, the $BaFe_2As_2$ family provides a huge range of experimental data concerning all physical properties of interest, making it the ideal candidate for an extensive theoretical study.

A theoretical approach which can comprehensively deal with the iron pnictides should be able to account for several key issues. First of all, the chemical disorder which is introduced through the substitution of elements has to be dealt with, as it was stressed to be of significant importance.[49–52] Very recently, also the impact of spin-orbit coupling for the iron superconductors was emphasized[53], meaning the treatment of relativistic effects must not be neglected. Ideally, one should be able to handle strong correlations if necessary, which are commonly discussed for the iron pnictides.[54–59] Last but not least, spectroscopic properties like e.g. ARPES[31–37] or electrical transport[38–44] are two main fields of interest for the iron superconductors, which are typically difficult to describe by theory. One possible approach to deal simultaneously with the mentioned issues is the Munich SPR-KKR program package of Ebert *et al.*[60,61] which is based on the multiple scattering Korringa-Kohn-Rostoker-Green function (KKR-GF) method. The present work is the first that applies the Munich SPR-KKR package in great detail to the field of iron pnictides, providing an additional and useful approach to the established community. This gives in particular the opportunity to discover new roads and possibilities in order to understand unconventional superconductivity in this important family of high-temperature superconductors.

Therefore, Chapter 2 will mainly introduce the physical and mathematical background of the applied KKR-GF method. Furthermore, the theoretical basics behind ARPES and electrical transport are briefly introduced. In Chapter 3 the chemical aspects of the iron pnictides are presented in general and also the 122-family of $BaFe_2As_2$, as compound of interest, is discussed in detail. After this general background the thesis is split into five Chapters, each one build around a respective publication of the author. Chapter 4 introduces first work on the antiferromagnetic, orthorhombic phase of $BaFe_2As_2$ and $Ba(Fe_{1-x}Co_x)_2As_2$ which focuses on the magnetic properties and the resulting anisotropy in the electronic structure. Chapter 5 continues with the previous publication but now investigates directly the detwinned ARPES spectra of $BaFe_2As_2$ and $Ba(Fe_{1-x}Co_x)_2As_2$. Based on this work one can understand the anisotropy observed in ARPES spectra as a direct consequence of the antiferromagnetic order. Furthermore, surface effects are discussed helping to identify the surface termination. Chapter 6 is related to ARPES experiments performed at the Swiss Light Source (SLS) of the Paul Scherrer Institute in Switzerland on optimally doped $(\mathrm{Ba}_{1-x}\mathrm{K}_x)\mathrm{Fe}_2\mathrm{As}_2$. The applied ARPES calculations in combination with dynamical mean field theory (DMFT) approaches for strong correlations will reveal important consequences for the effective mass enhancements based on effects which are related to the ARPES spectra rather than to correlations. Chapter 7 investigates the extensively discussed resistivity anisotropy of $\mathrm{BaFe}_2\mathrm{As}_2$ and its substituted compounds based on the Kubo-Greenwood formalism. Apart from common theories which explain this phenomenon in terms of spin fluctuations or extended impurity states one can understand this observation in terms of an anisotropic magnetoresistance based on the anisotropic electronic structure. Chapter 8 finally compares a huge variety of different types of substitution in $\mathrm{BaFe}_2\mathrm{As}_2$ and calculates the corresponding hyperfine fields including spin-orbit coupling. This gives important insights for the experimentally used $^{57}\mathrm{Fe}$ Mössbauer spectroscopy. Finally, Chapter 9 summarizes all results and concludes about the gained new insights.

Chapter 2

Theoretical framework

The basis of quantum mechanics was already derived in the 1920s by the work of e.g. de Broglie[62], Heisenberg[63], Born and Jordan[64], Schrödinger[65], and Dirac[66–68]. Even today the relativistic, time-dependent Dirac equation[66] (2.1) is the most sophisticated basis in order to describe electronic properties. In a short notation it can be expressed by

$$i\gamma^{\mu}\partial_{\mu}\psi \quad = \quad m\psi \, , \tag{2.1}$$

as written on the commemorative marker stone in Westminster Abbey using natural units ($\hbar = c = 1$), the gamma matrices γ^{μ} for $\mu = 0, 1, 2, 3$, the 4-gradient ∂_{μ}, the particle mass m and the wave function ψ.

Of course more feasible approaches are used to solve the electronic many particle problem, most of them based on the much simpler Schrödinger equation. In quantum chemistry Hartree-Fock[69,70] (HF), second order Møller-Plesset perturbation theory[71] (MP2), configuration interaction (CI) or the more sophisticated coupled cluster (CC) approach[72,73] are commonly used. However, these methods are rather impracticable to describe solids, thus density functional theory (DFT) is nowadays the most often used approach in the field of solid state theory. The history of DFT goes back to the late 1920s to the work of Thomas and Fermi[74–76], however, the validity of a mapping to the density was first only postulated and could not be proved until 1964 by the Hohenberg-Kohn theorems[77].

Apart from these common knowledge approaches this chapter will focus on the Korringa-Kohn-Rostoker-Green function (KKR-GF) method to derive electronic properties as used in the Munich spin polarized relativistic Korringa-Kohn-Rostoker (SPR-KKR) code package[61] applied for the presented work. In addition the physical properties behind the phenomena of interest should be briefly reviewed.

2.1 The Korringa-Kohn-Rostoker Green function method

Most approaches to calculate the electronic properties of a given system are based on the Schrödinger equation[65] using wave functions. These wave functions are usually expanded in terms of a defined basis set and the eigenvalue principle is applied to solve the corresponding problem. Common examples are the pseudopotential methods where plane waves are used as a basis or linear band structure methods[78] like e.g. the linear augmented plane wave (LAPW) method which uses a separation of space in interstitial space described by plane waves and a linear combination of atomic like orbitals near the nuclei.[79] However, variational methods suffer from the problem that a high number of basis functions is needed for very accurate results.

A different approach is used in the KKR method which is based on multiple scattering theory (MST). The basic idea of the present version of the KKR ansatz goes back to the work of Korringa[80] in 1947 and Kohn and Rostoker[81] in 1954. The central feature of the KKR method is an integral formulation of the Schrödinger equation with an implied minimal basis set provided by energy and angular momentum dependent partial waves. It is further possible to provide the Green function (GF) of a system, as shown by Beeby[82] in 1964. The modern development of non-relativistic KKR was influenced by the work of Faulkner[83,84], Faulkner and Stocks[85] and Gyorffy and Stocks[86]. A relativistic formulation of the KKR formalism was established by the work of Onodera and Okazaki[87], Strange *et al.*[88], Weinberger[89] and Ebert[90].

Using a KKR-GF approach has several advantages. First, one should emphasize the direct access to the Green function for a given system, which is enough to calculate all single-particle expectation values and furthermore it does not implicitly require spatial periodicity concerning the arrangement of atoms. In addition, the Green function of a perturbed system is rather easy to access by means of the Dyson equation. The approach is split into two separate parts: the first potential-step considers only the solution of a single-site problem, whereas the multiple scattering scenario can be accounted for by the second geometry-step involving an array of finite or infinite scattering centers. Altogether, these properties make the KKR-GF method extremely powerful when talking about vacancies or impurities in a crystal[91], when considering surfaces and interfaces[92] and also for disordered alloys[93]. Additionally, this approach is in particular useful to describe unoccupied states which can have arbitrarily large energies as is needed for spectroscopic applications.

The decomposition of space is generally done into an atomic region seen as an isolated system which is embedded into an electron gas. For example, the muffin-tin approach implies touching spheres for the atomic regions and an interstitial space with a constant potential . Also very common in the KKR-GF formalism is the so-called atomic sphere approximation (ASA), which uses overlapping spheres for the atomic centers until a filling of space is reached. In a more sophisticated way a full potential (FP) approach can be used, which describes the space in terms of Wigner-Seitz cells leading to a non-spherical description.

The time-independent formalism of the modern KKR-GF method will be briefly summarized in the following, based on the work of Ebert[61,94–96] and others[97–99].

2.1.1 General properties of the single-particle Green function

The time-independent Schrödinger equation[65], associated with the Hamiltonian $\hat{\mathcal{H}}$ and energy E, can be expressed by avoiding the eigenstates $|\psi\rangle$ in favor of the integral operator $\hat{G}$:

$$(E-\hat{\mathcal{H}})\hat{G} \;=\; \hat{1} \qquad \text{or} \qquad \hat{G} \;=\; (E-\hat{\mathcal{H}})^{-1}\;. \tag{2.2}$$

Here, $\hat{G}$ is called the resolvent operator, or equivalently the Green operator of the Hamiltonian $\hat{\mathcal{H}}$. For known eigenvalues E_i and eigenstates $|\psi_i\rangle$ one can define $\hat{G}$ in its spectral representation

$$\hat{G} \;=\sum_i \frac{|\psi_i\rangle\langle\psi_i|}{E-E_i}\;, \tag{2.3}$$

as a solution to the inhomogeneous Schrödinger equation for a complete set of orthonormal wave functions $|\psi_i\rangle$. However, for a continuous eigenvalues spectrum the summation of equation (2.3) has to be replaced by an integral. To be more specific, this summation is not defined for a Hermitian operator and has to be evaluated as a contour integral because of singularities at the real energies E_i. This leads to a discontinuity of the Green function. Thus, the limits while approaching the real axis from the upper and lower complex half-plane have to be investigated separately.[100] Consequently, two kinds of Green functions are defined, depending whether the complex energy argument approaches the real axis from above ($\hat{G}^+$, retarded Green function) or from below ($\hat{G}^-$, advanced Green function). They are formally given by the corresponding spectral representation,

$$\hat{G}^{\pm} \;=\; \lim_{\delta\to 0^+}(E-\hat{\mathcal{H}}\pm i\delta)^{-1}\;, \tag{2.4}$$

$$\hat{G}^{\pm} \;=\; \lim_{\delta\to 0^+}\sum_i \frac{|\psi_i\rangle\langle\psi_i|}{E-E_i\pm i\delta}\;. \tag{2.5}$$

The relation between the retarded and advanced Green functions is given by the expression $(\hat{G}^+)^\dagger = \hat{G}^-$, while the so-called homogeneous Green function $\widetilde{G}$ is defined as the difference between $\hat{G}^+$ and $\hat{G}^-$:

$$\widetilde{G} = \hat{G}^+ - \hat{G}^- = 2i \operatorname{Im} \hat{G}^+ . \tag{2.6}$$

If necessary, the Green operator $\hat{G}$ can be always recovered from

$$\hat{G}(E) = \frac{i}{2\pi} \int_{-\infty}^{+\infty} \frac{\widetilde{G}(E')}{E - E'} \, \mathrm{d}E' . \tag{2.7}$$

For a perturbed system the full Hamiltonian $\hat{\mathcal{H}} = \hat{\mathcal{H}}_0 + \hat{V}$ splits into that of an unperturbed reference system $\hat{\mathcal{H}}_0$ and the perturbation $\hat{V}$. With respect to equation (2.2) the Green function of the full perturbed system $\hat{G} = (E - \hat{\mathcal{H}}_0 - \hat{V})^{-1}$ can lead to the Dyson equation (2.8) as implicit representation. This can be iteratively reformulated with the transition- or T-operator $\hat{T}$:

$$\begin{aligned}
\hat{G} &= \hat{G}_0 + \hat{G}_0 \hat{V} \hat{G} , && (2.8)\\
&= \hat{G}_0 + \hat{G}_0 \hat{V} \hat{G}_0 + \hat{G}_0 \hat{V} \hat{G}_0 \hat{V} \hat{G}_0 + \ldots , \\
&= \hat{G}_0 + \hat{G}_0 \left(\hat{V} + \hat{V} \hat{G}_0 \hat{V} + \ldots \right) \hat{G}_0 , \\
&= \hat{G}_0 + \hat{G}_0 \hat{T} \hat{G}_0 , && (2.9)\\
\hat{T} &= \hat{V} + \hat{V} \hat{G}_0 \hat{V} + \ldots , && (2.10)\\
&= \hat{V} + \hat{V} \hat{G}_0 \hat{T} = \hat{V} (1 - \hat{G}_0 \hat{V})^{-1} . && (2.11)
\end{aligned}$$

Hence, the full perturbed $\hat{G}$ can be determined from the unperturbed reference system $\hat{G}_0$ and the transition-operator $\hat{T}$. The Dyson equation can also be written in terms of the real space representation

$$G(\boldsymbol{r}, \boldsymbol{r}', E) = G_0(\boldsymbol{r}, \boldsymbol{r}', E) + \int \mathrm{d}^3 r'' \, G_0(\boldsymbol{r}, \boldsymbol{r}'', E) V(\boldsymbol{r}'') G(\boldsymbol{r}'', \boldsymbol{r}', E) , \tag{2.12}$$

equivalent to equation (2.8). Analogously, the Schrödinger equation of a perturbed system is given by

$$(E - \hat{\mathcal{H}}_0) |\psi\rangle = \hat{V} |\psi\rangle = |\chi\rangle . \tag{2.13}$$

By expanding $|\psi\rangle = \sum_i a_i |\phi_i\rangle$ and $|\chi\rangle = \sum_i b_i |\phi_i\rangle$ in the orthonormal basis of the eigenfunctions of $\hat{\mathcal{H}}_0$ one can derive

$$|\psi\rangle \quad = \quad \sum_i \frac{|\phi_i\rangle\langle\phi_i|}{E - E_i}\,\hat{V}|\psi\rangle \quad = \quad \hat{G}_0\hat{V}|\psi\rangle \ . \tag{2.14}$$

However, equation (2.14) is not the full solution to the inhomogeneous Schrödinger equation, because one neglects all solutions $|\phi^0\rangle$, which satisfy the homogeneous problem $(E - \hat{\mathcal{H}}_0)|\phi^0\rangle = 0$, with $\hat{V}$ being zero. These solutions can be added to $|\psi\rangle$, leading to the Lippmann-Schwinger equation,

$$\begin{aligned} |\psi\rangle \ &= \ |\phi^0\rangle + \hat{G}_0\hat{V}|\psi\rangle \ , & (2.15) \\ &= \ |\phi^0\rangle + \hat{G}_0\hat{V}|\phi^0\rangle + \hat{G}_0\hat{V}\hat{G}_0\hat{V}|\phi^0\rangle + ... \ , & (2.16) \end{aligned}$$

which is an implicit representation of $|\psi\rangle$. Thus it is a transformation of the Schrödinger differential equation into an integral equation, in which the boundary conditions are already implicitly contained in $|\phi^0\rangle$. Using the Born expansion in equation (2.16) together with the definition of the T-operator from equation (2.10) on can derive an expression of $|\psi\rangle$ in terms of $|\phi^0\rangle$:

$$|\psi\rangle \ = \ |\phi^0\rangle + \hat{G}_0\hat{T}|\phi^0\rangle = \ (1 + \hat{G}_0\hat{T})|\phi^0\rangle \ . \tag{2.17}$$

2.1.2 The free electron Green function

To derive solutions to the multiple scattering problem one starts from the non-relativistic description of a free electron having momentum $\boldsymbol{p}$ and energy $E = \frac{p^2}{2m}$ which is scattered at a localized potential V. The corresponding scattered state $\psi(\boldsymbol{r}, E)$ is described in terms of the Lippmann-Schwinger equation

$$\psi(\boldsymbol{r}, E) = e^{i\boldsymbol{pr}} + \int \mathrm{d}^3r' \ G^0(\boldsymbol{r}, \boldsymbol{r}', E)V(\boldsymbol{r}')\psi(\boldsymbol{r}', E) \ , \tag{2.18}$$

with an incoming free electron represented by a plane wave $e^{i\boldsymbol{pr}}$ and the retarded free electron Green function $G^0(\boldsymbol{r}, \boldsymbol{r}', E)$ describing an outgoing spherical wave. Using the spectral representation of the Green function (2.5) one can express $G^0(\boldsymbol{r}, \boldsymbol{r}', E)$ in terms of a plane wave basis, leading after a summation over all states to[101,102]

$$G^0(\boldsymbol{r}, \boldsymbol{r}', E) = -\frac{1}{4\pi}\frac{e^{ip|\boldsymbol{r}-\boldsymbol{r}'|}}{|\boldsymbol{r} - \boldsymbol{r}'|} \ . \tag{2.19}$$

This Green function does not violate explicitly the translational symmetry of a crystal as it depends only on the difference $|\boldsymbol{r}-\boldsymbol{r}'|$ and not on the separated positions $\boldsymbol{r}$ and $\boldsymbol{r}'$. One can rewrite $G^0(\boldsymbol{r},\boldsymbol{r}',E)$ in its angular momentum representation

$$G^0(\boldsymbol{r},\boldsymbol{r}',E) = -ip \begin{cases} \sum_L j_\ell(pr)h_\ell^+(pr')Y_L(\hat{r})Y_L^*(\hat{r}') & \text{for} \quad r < r' \\ \sum_L h_\ell^+(pr)j_\ell(pr')Y_L(\hat{r})Y_L^*(\hat{r}') & \text{for} \quad r > r' \end{cases} , \tag{2.20}$$

expressing the plane waves in terms of complex spherical harmonics

$$e^{i\boldsymbol{pr}} = 4\pi \sum_L i^\ell j_\ell(pr) Y_L^*(\hat{p}) Y_L(\hat{r}) \; , \tag{2.21}$$

and using a combined angular index $L=(\ell,m)$ and the spherical Bessel functions $j_\ell(pr)$ and first kind Hankel functions $h_\ell^+(pr)$[C].[103]

For a relativistic formulation one can start from the free electron Dirac equation

$$\left(E - \left[c\boldsymbol{\alpha}\cdot\hat{\boldsymbol{p}} + \beta\,\frac{c^2}{2}\right]\right) G^0(\boldsymbol{r},\boldsymbol{r}',E) = \delta(\boldsymbol{r}-\boldsymbol{r}')\,\mathbb{1}_4 \; , \tag{2.22}$$

using atomic Rydberg units[D], the momentum operator $\hat{\boldsymbol{p}}$, the vector $\boldsymbol{\alpha}$ of the 4×4 Dirac matrices and the 4×4 matrix β:

$$\boldsymbol{\alpha} = \begin{bmatrix} 0 & \boldsymbol{\sigma} \\ \boldsymbol{\sigma} & 0 \end{bmatrix} \qquad \text{and} \qquad \beta = \begin{bmatrix} \mathbb{1}_2 & 0 \\ 0 & -\mathbb{1}_2 \end{bmatrix} , \tag{2.23}$$

with the standard Pauli matrices $\boldsymbol{\sigma}$, given by

$$\sigma_x = \begin{bmatrix} 0 & 1 \\ 1 & 0 \end{bmatrix} , \; \sigma_y = \begin{bmatrix} 0 & -i \\ i & 0 \end{bmatrix} , \; \sigma_z = \begin{bmatrix} 1 & 0 \\ 0 & -1 \end{bmatrix} . \tag{2.24}$$

Thus, $G^0(\boldsymbol{r},\boldsymbol{r}',E)$ is a 4×4 matrix which is constructed from the four-component solutions of the free electron Dirac equation in analogy to equation (2.20):

$$G^0(\boldsymbol{r},\boldsymbol{r}',E) = -ip \begin{cases} \sum_\Lambda j_\Lambda(\boldsymbol{r},E)h_\Lambda^{+\times}(\boldsymbol{r}',E) & \text{for} \quad r < r' \\ \sum_\Lambda h_\Lambda^+(\boldsymbol{r},E)j_\Lambda^\times(\boldsymbol{r}',E) & \text{for} \quad r > r' \end{cases} . \tag{2.25}$$

Here, the combined spin-angular index $\Lambda=(\kappa,\mu)$ is used, respectively $-\Lambda=(-\kappa,\mu)$,

---

[C] The Hankel functions of first h_α^+ and second h_α^- kind are defined as combination of Bessel functions j_α and von Neumann functions n_α, meaning $h_\alpha^\pm = j_\alpha \pm i n_\alpha$

[D] In particular: $\hbar = 2m_e = \frac{e^2}{2} = 1$

having the magnetic quantum numbers μ and the quantum numbers κ which include the orbital and angular momentum quantum numbers ℓ and j. This leads in particular to the following relations:

$$\kappa = \begin{cases} -\ell-1 & \text{for} \quad j=\ell+\frac{1}{2} \\ \ell & \text{for} \quad j=\ell-\frac{1}{2} \end{cases}, \tag{2.26}$$

$$j = |\kappa| - \frac{1}{2}, \tag{2.27}$$

$$-j \leq \mu \leq +j, \tag{2.28}$$

$$\ell = \begin{cases} -\kappa-1 & \text{for} \quad \kappa<0 \\ \kappa & \text{for} \quad \kappa\geq 0 \end{cases}, \tag{2.29}$$

$$\bar{\ell} = \ell - S_\kappa \qquad \text{with} \quad S_\kappa = \frac{\kappa}{|\kappa|}. \tag{2.30}$$

Furthermore, we use in equation (2.25) the relativistic momentum $p=\sqrt{E^2/c^2-m^2c^2}$ in addition to the corresponding four-component wave functions $j_\Lambda(\boldsymbol{r},E)$ and $h_\Lambda^+(\boldsymbol{r},E)$, which are the relativistic versions of the Bessel and Hankel functions in the form of bispinors

$$j_\Lambda(\boldsymbol{r},E) = \sqrt{\frac{E+mc^2}{c^2}} \begin{pmatrix} j_\ell(pr)\chi_\Lambda(\hat{r}) \\ \frac{icpS_\kappa}{E+mc^2} j_{\bar{\ell}}(pr)\chi_{-\Lambda}(\hat{r}) \end{pmatrix}, \tag{2.31}$$

$$h_\Lambda^+(\boldsymbol{r},E) = \sqrt{\frac{E+mc^2}{c^2}} \begin{pmatrix} h_\ell^+(pr)\chi_\Lambda(\hat{r}) \\ \frac{icpS_\kappa}{E+mc^2} h_{\bar{\ell}}^+(pr)\chi_{-\Lambda}(\hat{r}) \end{pmatrix}, \tag{2.32}$$

and the left-hand side solutions of the Dirac equation as row spinors

$$j_\Lambda^\times(\boldsymbol{r},E) = \sqrt{\frac{E+mc^2}{c^2}} \begin{pmatrix} j_\ell(pr)\chi_\Lambda^\dagger(\hat{r}) \\ \frac{-icpS_\kappa}{E+mc^2} j_{\bar{\ell}}(pr)\chi_{-\Lambda}^\dagger(\hat{r}) \end{pmatrix}^T, \tag{2.33}$$

$$h_\Lambda^{+\times}(\boldsymbol{r},E) = \sqrt{\frac{E+mc^2}{c^2}} \begin{pmatrix} h_\ell^+(pr)\chi_\Lambda^\dagger(\hat{r}) \\ \frac{-icpS_\kappa}{E+mc^2} h_{\bar{\ell}}^+(pr)\chi_{-\Lambda}^\dagger(\hat{r}) \end{pmatrix}^T. \tag{2.34}$$

Finally, the spin-angular functions χ_Λ are expressed using Clebsch-Gordan coefficients $C(\ell\frac{1}{2}j;\mu-m_s,m_s)$, complex spherical harmonics $Y_\ell^{m_\ell}(\hat{r})$ and the Pauli spinor χ_{m_s}:

$$\chi_\Lambda(\hat{r}) = \sum_{m_s=\pm\frac{1}{2}} C(\ell\frac{1}{2}j;\mu-m_s,m_s)\, Y_\ell^{\mu-m_s}(\hat{r})\, \chi_{m_s}. \tag{2.35}$$

2.1.3 Solving the single site scattering problem

As equation (2.25) gives the relativistic solution for the Green function of a free electron, the next step is to evaluate the changes while the electron moves under the influence of a spherically symmetric scattering potential $V(\boldsymbol{r})$ of radius r_{crit}. For a muffin-tin construction this $V(\boldsymbol{r})$ follows

$$V(\boldsymbol{r}) \quad = \quad \begin{cases} V(r) & \text{for} \quad r \leq r_{\text{crit}} \\ 0 & \text{for} \quad r > r_{\text{crit}} \end{cases} \quad . \tag{2.36}$$

Thus, one rewrites the Dirac equation in spherical coordinates, with $V(\boldsymbol{r})$ represented by an effective potential V_{eff} and an effective magnetic field B_{eff}, according to relativistic spin-polarized DFT:

$$\left(E - \left[i\gamma_5\sigma_r c\left(\frac{\partial}{\partial r} + \frac{1}{r}(1-\beta\hat{K})\right) + V(\boldsymbol{r}) + (\beta-1)\frac{c^2}{2}\right]\right)\Psi_\nu(\boldsymbol{r},E) = 0 \ , \tag{2.37}$$

$$V(\boldsymbol{r}) = V_{\text{eff}}(r) + \beta\sigma_z B_{\text{eff}}(r) \ . \tag{2.38}$$

Herein, the spin-orbit operator $\hat{K}$, described by the orbital angular momentum operator $\hat{\boldsymbol{L}}$, and the matrices γ_5 and σ_r are defined with respect to

$$\hat{K} = \boldsymbol{\sigma}\cdot\hat{\boldsymbol{L}} + 1 \qquad \text{with} \quad \hat{\boldsymbol{L}} = \hat{\boldsymbol{r}}\times\hat{\boldsymbol{p}} \ , \tag{2.39}$$

$$\gamma_5 = \begin{bmatrix} 0 & -\mathbb{1}_2 \\ -\mathbb{1}_2 & 0 \end{bmatrix} \qquad \text{and} \qquad \sigma_r = \frac{1}{r}\,\boldsymbol{r}\cdot\boldsymbol{\sigma} \ . \tag{2.40}$$

To solve equation (2.37) for ν linearly independent solutions one follows the ansatz

$$\Psi_\nu(\boldsymbol{r},E) = \sum_\Lambda \Phi_{\Lambda\nu}(\boldsymbol{r},E) = \sum_\Lambda \begin{pmatrix} g_{\Lambda\nu}(r,E)\chi_\Lambda(\hat{r}) \\ if_{\Lambda\nu}(r,E)\chi_{-\Lambda}(\hat{r}) \end{pmatrix} \ , \tag{2.41}$$

with the four-component wave function $\Psi_\nu(\boldsymbol{r},E)$ having a large $g_\kappa(r,E)$ and a small $f_\kappa(r,E)$ radial component and corresponding spin-angular functions $\chi_\Lambda(\hat{r})$.

Inserting $\Psi_\nu(\boldsymbol{r},E)$ from equation (2.41) into the Dirac equation (2.37) using spherical coordinates and projecting onto the basis $|\chi_\Lambda\rangle$ leads to the following set of coupled radial differential equations:

$$\begin{aligned}\frac{\partial}{\partial r} P_{\Lambda\nu}(r,E) &= -\ \frac{\kappa}{r} P_{\Lambda\nu}\ +\ \left[\frac{E - V_{\text{eff}}(r)}{c^2} + 1\right] Q_{\Lambda\nu}(r,E) \\ &\quad +\ \frac{B_{\text{eff}}(r)}{c^2} \sum_{\Lambda'} \langle\, \chi_\Lambda \mid \sigma_z \mid \chi_{\Lambda'}\, \rangle\; Q_{\Lambda'\nu}(r,E)\ ,\end{aligned} \tag{2.42}$$

$$\begin{aligned}\frac{\partial}{\partial r} Q_{\Lambda\nu}(r,E) &= +\ \frac{\kappa}{r} Q_{\Lambda\nu}\ -\ [E - V_{\text{eff}}(r)]\, P_{\Lambda\nu}(r,E) \\ &\quad +\ B_{\text{eff}}(r) \sum_{\Lambda'} \langle\, \chi_\Lambda \mid \sigma_z \mid \chi_{\Lambda'}\, \rangle\; P_{\Lambda'\nu}(r,E)\ ,\end{aligned} \tag{2.43}$$

using $P_{\Lambda\nu}(r,E) = rg_{\Lambda\nu}(r,E)$ and $Q_{\Lambda\nu}(r,E) = crf_{\Lambda\nu}(r,E)$. The corresponding spin-angular matrix elements of σ_z are defined by

$$\langle\, \chi_\Lambda \mid \sigma_z \mid \chi_{\Lambda'}\, \rangle \ = \delta_{\mu\mu'} \begin{cases} -\frac{\mu}{(\kappa+1/2)} & \text{for} \quad \kappa = \kappa' \\ -\sqrt{1 - (\frac{\mu}{\kappa+1/2})^2} & \text{for} \quad \kappa = -\kappa' - 1 \\ \ \ 0 & \text{otherwise}\ . \end{cases} \tag{2.44}$$

With respect to the selection rules (2.44) only coupling between partial waves of the same magnetic quantum number ($\Delta\mu = 0$) is allowed, however, coupling for $\Delta\ell = 0, \pm 2, \pm 4, \ldots$ leads to an infinite set of coupled equations in (2.42) and (2.43). However, higher terms for $\Delta\ell \neq 0$ are in the order of $\frac{1}{c^2}$ and thus small enough to be reasonably neglected.[104] Thus, $\Delta\ell = 0$ can be applied, restricting the number of coupling terms to at most two: $\Lambda_1 = (\kappa, \mu)$ and $\Lambda_2 = (-\kappa - 1, \mu)$. Still, truncating the angular momentum expansion in equation (2.41) at $\ell_{\max}$ leads to a set of $2(\ell_{\max} + 1)^2$ linearly independent solutions which can be obtained by numerically solving equations (2.42) and (2.43). The integration for the regular solutions is started at the innermost radial mesh point ($r \to 0$), demanding a boundary condition according to

$$\Psi_\nu(\boldsymbol{r}, E) \to \Psi_\Lambda(\boldsymbol{r}, E) \quad \text{for} \quad r \to 0\,, \tag{2.45}$$

meaning pure spin-angular character in the vicinity of the origin. The following functions $\Psi_\nu(\boldsymbol{r}, E)$ are constructed by expanding $\Psi_\Lambda(\boldsymbol{r}, E)$ at $r = 0$ and outward integration according to the coupled radial differential equations (2.42) and (2.43), mixing continuously other spin-angular contributions in.

The single-site scattering Green function $G(\boldsymbol{r}, \boldsymbol{r}', E)$ can be now written using the

Dyson equation (2.12), leading to:

$$G(\boldsymbol{r},\boldsymbol{r}',E) = G^0(\boldsymbol{r},\boldsymbol{r}',E) + \int \mathrm{d}^3r'' \int \mathrm{d}^3r'''\ G^0(\boldsymbol{r},\boldsymbol{r}'',E)t(\boldsymbol{r}'',\boldsymbol{r}''',E)G^0(\boldsymbol{r}''',\boldsymbol{r}',E)\ . \tag{2.46}$$

By inserting $G^0(\boldsymbol{r},\boldsymbol{r}',E)$ from equation (2.25) (for $r,r' > r_{\text{crit}}$) into (2.46) one arrives at the following equations, with the definition of $t_{\Lambda\Lambda'}$ given by equation (2.50):

$$\begin{aligned} G(\boldsymbol{r},\boldsymbol{r}',E) &= -ip\sum_{\Lambda} j_\Lambda(\boldsymbol{r},E)h_\Lambda^{+\times}(\boldsymbol{r}',E) + \Bigg((-ip)^2 \int \mathrm{d}^3r'' \int \mathrm{d}^3r''' \\ &\qquad \sum_{\Lambda} h_\Lambda^{+}(\boldsymbol{r},E)j_\Lambda^{\times}(\boldsymbol{r}'',E)t(\boldsymbol{r}'',\boldsymbol{r}''',E)\sum_{\Lambda'} j_{\Lambda'}(\boldsymbol{r}''',E)h_{\Lambda'}^{+\times}(\boldsymbol{r}',E)\Bigg)\ , \end{aligned} \tag{2.47}$$

$$= -ip\sum_{\Lambda} j_\Lambda(\boldsymbol{r},E)h_\Lambda^{+\times}(\boldsymbol{r}',E) + (-ip)^2\sum_{\Lambda\Lambda'} h_\Lambda^{+}(\boldsymbol{r},E)t_{\Lambda\Lambda'}(E)h_{\Lambda'}^{+\times}(\boldsymbol{r}',E)\ , \tag{2.48}$$

$$= -ip\sum_{\Lambda\Lambda'} \big[j_\Lambda(\boldsymbol{r},E) - iph_\Lambda^{+}(\boldsymbol{r},E)t_{\Lambda\Lambda'}(E)\big]h_{\Lambda'}^{+\times}(\boldsymbol{r}',E)\ , \tag{2.49}$$

$$t_{\Lambda\Lambda'}(E) = \int \mathrm{d}^3r'' \int \mathrm{d}^3r'''\ j_\Lambda^{\times}(\boldsymbol{r}'',E)t(\boldsymbol{r}'',\boldsymbol{r}''',E)j_{\Lambda'}(\boldsymbol{r}''',E)\ . \tag{2.50}$$

To ensure a proper and smooth boundary behavior not only for $r > r_{\text{crit}}$ but also over whole space $r < r_{\text{crit}}$ one extends the free electron solutions to

$$j_\Lambda(\boldsymbol{r},E) \to J_\Lambda(\boldsymbol{r},E) \quad \text{and} \quad h_\Lambda^{+}(\boldsymbol{r},E) \to H_\Lambda(\boldsymbol{r},E)\ , \tag{2.51}$$

and defines $R_\Lambda(\boldsymbol{r},E)$ and $R_\Lambda^{\times}(\boldsymbol{r},E)$ according to:

$$R_\Lambda(\boldsymbol{r},E) = J_\Lambda(\boldsymbol{r},E) - ip\sum_{\Lambda'} H_{\Lambda'}(\boldsymbol{r},E)t_{\Lambda'\Lambda}(E)\ , \tag{2.52}$$

$$R_\Lambda^{\times}(\boldsymbol{r},E) = J_\Lambda^{\times}(\boldsymbol{r},E) - ip\sum_{\Lambda'} t_{\Lambda\Lambda'}(E)H_{\Lambda'}^{\times}(\boldsymbol{r},E)\ . \tag{2.53}$$

Thus, the complete single-site scattering Green function $G(\boldsymbol{r},\boldsymbol{r}',E)$ is given by

$$G(\boldsymbol{r},\boldsymbol{r}',E) = -ip\begin{cases} \sum_\Lambda R_\Lambda(\boldsymbol{r},E)H_\Lambda^{\times}(\boldsymbol{r}',E) & \text{for} \quad r < r' \\ \sum_\Lambda H_\Lambda(\boldsymbol{r},E)R_\Lambda^{\times}(\boldsymbol{r}',E) & \text{for} \quad r > r' \end{cases}\ . \tag{2.54}$$

The same result can be alternatively formulated using the functions Z_Λ,

$$Z_\Lambda(\boldsymbol{r},E) = \sum_{\Lambda'} R_{\Lambda'}(\boldsymbol{r},E)t^{-1}_{\Lambda'\Lambda}(E) = \sum_{\Lambda'} J_{\Lambda'}(\boldsymbol{r},E)t^{-1}_{\Lambda'\Lambda}(E) - ipH_\Lambda(\boldsymbol{r},E)\ , \tag{2.55}$$

giving for $G(\boldsymbol{r},\boldsymbol{r}',E)$:

$$G(\boldsymbol{r},\boldsymbol{r}',E) = -ip\begin{cases} \sum_{\Lambda\Lambda'} Z_\Lambda(\boldsymbol{r},E)t_{\Lambda'\Lambda}H^\times_{\Lambda'}(\boldsymbol{r}',E) & \text{for} \quad r<r' \\ \sum_{\Lambda\Lambda'} H_\Lambda(\boldsymbol{r},E)t_{\Lambda\Lambda'}Z^\times_{\Lambda'}(\boldsymbol{r}',E) & \text{for} \quad r>r' \end{cases}, \tag{2.56}$$

which results finally for the single-site scattering Green function $G(\boldsymbol{r},\boldsymbol{r}',E)$ in

$$G(\boldsymbol{r},\boldsymbol{r}',E) = \sum_{\Lambda\Lambda'} Z_\Lambda(\boldsymbol{r},E)t_{\Lambda\Lambda'}Z^\times_{\Lambda'}(\boldsymbol{r}',E) - \begin{cases} \sum_\Lambda Z_\Lambda(\boldsymbol{r},E)J^\times_\Lambda(\boldsymbol{r}',E) & \text{for} \quad r<r' \\ \sum_\Lambda J_\Lambda(\boldsymbol{r},E)Z^\times_\Lambda(\boldsymbol{r}',E) & \text{for} \quad r>r' \end{cases}. \tag{2.57}$$

The only thing left now is an efficient procedure to evaluate the corresponding elements of the t-matrix $t_{\Lambda\Lambda'}(E)$, which was derived by Ebert and Gyorffy[105], giving:

$$t_{\Lambda\Lambda'}(E) = \frac{i}{2p}\left([a(E)-b(E)]b^{-1}(E)\right)_{\Lambda\Lambda'}\ , \tag{2.58}$$

with the auxiliary matrices $a_{\Lambda\Lambda'}(E)$ and $b_{\Lambda\Lambda'}(E)$ according to

$$a_{\Lambda\Lambda'}(E) \quad = \quad -ipr^2[h^-_\Lambda(\boldsymbol{r},E)\Phi_{\Lambda\nu}(\boldsymbol{r},E)]_r\ , \tag{2.59}$$

$$b_{\Lambda\Lambda'}(E) \quad = \quad ipr^2[h^+_\Lambda(\boldsymbol{r},E)\Phi_{\Lambda\nu}(\boldsymbol{r},E)]_r\ . \tag{2.60}$$

The term in square brackets of (2.59) and (2.60) corresponds to the relativistic form of the Wronskian expression:[105]

$$[h^+_\Lambda(\boldsymbol{r},E)\Phi_{\Lambda\nu}(\boldsymbol{r},E)]_r = h^+_\ell(pr)cf_{\Lambda\nu}(r,E) - \frac{p}{1+E/c^2}S_\kappa h^+_{\bar\ell}(pr)g_{\Lambda\nu}(r,E)\ . \tag{2.61}$$

2.1.4 Solving the multiple scattering problem

The multiple scattering process assumes that the electrons can propagate freely between the different atomic sites acting as scattering centers with every scattering process finished before the next one starts. Thus, the propagation in the presence of the perturbation potential $\hat{V}$ splits up into a sum of non-overlapping single-site scattering events. Using the single-site scattering operator t^i with the non-overlapping single-site potentials v^i, given by $t^i = v^i + v^i\hat{G}_0t^i$ with respect to equation (2.11), one can define the scattering operator $\hat{T}$,

$$\hat{T} \quad = \quad \sum_i t^i + \sum_{i\neq j} t^i \hat{G}_0 t^j + \sum_{\substack{i\neq k\\ k\neq j}} t^i \hat{G}_0 t^k \hat{G}_0 t^j + \ldots \quad = \quad \sum_{ij} \hat{\tau}^{ij} \; , \tag{2.62}$$

with the scattering path operator $\hat{\tau}^{ij}$, introduced by Gyorffy and Stott[106]. This $\hat{\tau}^{ij}$ acts on an incident electron wave at side j and creates an outgoing wave at site i including all possible scattering events in between:

$$\hat{\tau}^{ij} \quad = \quad t^i \delta_{ij} + t^i \hat{G}_0 t^j + \sum_{\substack{i\neq k\\ k\neq j}} t^i \hat{G}_0 t^k \hat{G}_0 t^j + \ldots \quad = \quad t^i \delta_{ij} + \sum_{i\neq k} t^i \hat{G}_0 \hat{\tau}^{kj} \; . \tag{2.63}$$

For the single-site Green function G^n and the operator T^{nn} describing the whole scattering of the system without scattering site n, one arrives at the corresponding real space representation

$$G(\boldsymbol{r},\boldsymbol{r}',E) = G^n(\boldsymbol{r},\boldsymbol{r}',E) + \int \mathrm{d}^3 r'' \int \mathrm{d}^3 r'''\; G^n(\boldsymbol{r},\boldsymbol{r}'',E) T^{nn}(\boldsymbol{r}'',\boldsymbol{r}''',E) G^n(\boldsymbol{r}''',\boldsymbol{r}',E) \; , \tag{2.64}$$

with in reference to equation (2.62) the term T^{nn} is given by

$$T^{nn}(\boldsymbol{r},\boldsymbol{r}',E) = \sum_{i\neq n}\sum_{j\neq n} \tau^{ij}(\boldsymbol{r},\boldsymbol{r}',E) \; , \tag{2.65}$$

including the real space representation of τ^{ij}:

$$\begin{aligned}\tau^{ij}(\boldsymbol{r},\boldsymbol{r}',E) &= \delta_{ij} t^i(\boldsymbol{r},\boldsymbol{r}',E) \\ &\quad + \int \mathrm{d}^3 r'' \int \mathrm{d}^3 r'''\; t^i(\boldsymbol{r},\boldsymbol{r}''',E) \sum_{k\neq i} G_0(\boldsymbol{r}'',\boldsymbol{r}''',E) \tau^{kj}(\boldsymbol{r}''',\boldsymbol{r}',E) \; . \end{aligned} \tag{2.66}$$

Using spherical functions to describe the Green function in a real space representation implies the use of site-centered coordinates $\boldsymbol{r}_i = \boldsymbol{r} - \boldsymbol{R}_i$. Thus, the Green function is expanded around different sites leading to the rewritten $G_0^{ij}(\boldsymbol{r}_i,\boldsymbol{r}_j',E)$:

$$G_0(\boldsymbol{r},\boldsymbol{r}',E) = G_0(\boldsymbol{r}_i + \boldsymbol{R}_i, \boldsymbol{r}_j' + \boldsymbol{R}_j, E) = G_0^{ij}(\boldsymbol{r}_i,\boldsymbol{r}_j',E) = G_0(\boldsymbol{r}_i - \boldsymbol{r}_j', \boldsymbol{R}_j - \boldsymbol{R}_i, E) \; . \tag{2.67}$$

Because of non-overlapping sites one has always $|\boldsymbol{R}_j - \boldsymbol{R}_i| > |\boldsymbol{r}_i - \boldsymbol{r}_j'|$. Now one can avoid irregular Hankel functions $h_\Lambda(\boldsymbol{r},E)$ by using regular Bessel functions $j_\Lambda(\boldsymbol{r},E)$

around two different sites leading to a new equation for $G_0^{ij}(\boldsymbol{r}_i, \boldsymbol{r}'_j, E)$:

$$G_0^{ij}(\boldsymbol{r}_i, \boldsymbol{r}'_j, E) = \sum_{\Lambda\Lambda'} j_\Lambda(\boldsymbol{r}_i, E) G^{ij}_{0,\Lambda\Lambda'} j^{\times}_{\Lambda'}(\boldsymbol{r}'_j, E) \ . \tag{2.68}$$

The term $G^{ij}_{0,\Lambda\Lambda'}$ depends not on the single-sites potentials but only on the relative position between the two scattering sites i and j. Thus, these functions are commonly called structure constants or structural Green functions. They are defined by

$$G^{ij}_{0,\Lambda\Lambda'} = -4\pi i p \sum_{\Lambda''} i^{\ell-\ell'-\ell''} h^{+}_{\Lambda''}(\boldsymbol{R}_j - \boldsymbol{R}_i, E) C_{\Lambda\Lambda'\Lambda''} \ , \tag{2.69}$$

using the Gaunt coefficients $C_{\Lambda\Lambda'\Lambda''}$ according to

$$C_{\Lambda\Lambda'\Lambda''} = \int d\Omega \, Y_{\ell}^{\mu-m_s *}(\hat{r}) Y_{\ell'}^{\mu'-m_s}(\hat{r}) Y_{\ell''}^{\mu''-m_s}(\hat{r}) \ . \tag{2.70}$$

Inserting equation (2.69) into (2.66) one can formulate the following matrix equation

$$\tau^{ij}_{\Lambda\Lambda'}(E) = \delta_{ij} t^{i}_{\Lambda\Lambda'}(E) + \sum_{k\neq i} \sum_{\Lambda''\Lambda'''} t^{i}_{\Lambda\Lambda''}(E) G^{ik}_{0,\Lambda''\Lambda''''}(E) \tau^{kj}_{\Lambda'''\Lambda''}(E) \ , \tag{2.71}$$

with the matrix elements of the scattering path operator given by

$$\tau^{ij}_{\Lambda\Lambda'}(E) = \int \mathrm{d}^3 r \int \mathrm{d}^3 r' \, j^{\times}_{\Lambda}(\boldsymbol{r}_i, E) \tau^{ij}(\boldsymbol{r}_i, \boldsymbol{r}'_j, E) j_{\Lambda'}(\boldsymbol{r}'_j, E) \ . \tag{2.72}$$

One can set up the Green function of the whole system now in analogy to the single-site scattering by going from the single-site t-matrix to the multiple scattering operator τ^{ij}. Thus the Green function $G(\boldsymbol{r}_i, \boldsymbol{r}'_j, E)$ can be written in analogy to the single-site expression (2.57) by the following equation using the functions $Z_\Lambda(\boldsymbol{r}_i, E)$ and $J_\Lambda(\boldsymbol{r}_i, E)$:

$$\begin{aligned} G(\boldsymbol{r}_i, \boldsymbol{r}'_j, E) \ &= \sum_{\Lambda\Lambda'} Z_\Lambda(\boldsymbol{r}_i, E) \tau^{ij}_{\Lambda\Lambda'}(E) Z^{\times}_{\Lambda'}(\boldsymbol{r}'_j, E) \\ &- \delta_{ij} \begin{cases} \sum_\Lambda Z_\Lambda(\boldsymbol{r}_i, E) J^{\times}_\Lambda(\boldsymbol{r}'_i, E) & \text{for} \quad r < r' \\ \sum_\Lambda J_\Lambda(\boldsymbol{r}_i, E) Z^{\times}_\Lambda(\boldsymbol{r}'_i, E) & \text{for} \quad r > r' \end{cases} \ . \end{aligned} \tag{2.73}$$

Alternatively one can express $G(\boldsymbol{r}_i, \boldsymbol{r}'_j, E)$ in terms of the functions $R_\Lambda(\boldsymbol{r}_i, E)$ and

$H_\Lambda(\boldsymbol{r}_i, E)$, using the structural Green function $G^{ij}_{\Lambda'\Lambda}(E)$:

$$\begin{aligned} G(\boldsymbol{r}_i, \boldsymbol{r}'_j, E) \; &= \sum_{\Lambda\Lambda'} R_\Lambda(\boldsymbol{r}_i, E) G^{ij}_{\Lambda\Lambda'}(E) R^\times_{\Lambda'}(\boldsymbol{r}'_j, E) \\ &\quad - \delta_{ij}\; ip \begin{cases} \sum_\Lambda R_\Lambda(\boldsymbol{r}_i, E) H^\times_\Lambda(\boldsymbol{r}'_i, E) & \text{for} \quad r < r' \\ \sum_\Lambda H_\Lambda(\boldsymbol{r}_i, E) R^\times_\Lambda(\boldsymbol{r}'_i, E) & \text{for} \quad r > r' \end{cases} . \end{aligned} \tag{2.74}$$

With the relativistic multiple scattering Green function $G(\boldsymbol{r}_i, \boldsymbol{r}'_j, E)$ given by equations (2.73) and (2.74) one remains with the problem of determining the scattering path operator τ^{ij} or the structural Green function G^{ij}, respectively. For an ordered infinite system of scatterers the corresponding τ^{ij} can be obtained by means of a lattice Fourier transformation. The term $\tau^{ij}_{\Lambda\Lambda'}(E)$ is given by an integral over the first Brillouin zone (BZ) according to

$$\tau^{ij}_{\Lambda\Lambda'}(E) = \frac{1}{\Omega_{\mathrm{BZ}}} \int_{\Omega_{\mathrm{BZ}}} \mathrm{d}^3k \;\; \left[t^{-1}(E) - G_0(\boldsymbol{k}, E)\right]^{-1}_{\Lambda\Lambda'} \; e^{i\boldsymbol{k}(\boldsymbol{R}_i - \boldsymbol{R}_j)} \; , \tag{2.75}$$

with $G_0(\boldsymbol{k}, E)$ as the Fourier transform of the free electron Green function $G_0(\boldsymbol{r}, \boldsymbol{r}', E)$. Herein, the matrix $[t^{-1}(E) - G_0(\boldsymbol{k}, E)]$ corresponds to the so-called KKR-matrix, which has to be inverted in order to obtain the scattering super matrix $\tau^{ij}_{\Lambda\Lambda'}(E)$.

2.1.5 Substitutionally disordered alloys

Assuming a chemically disordered substitutional alloy $A_{x_\mathrm{A}}B_{x_\mathrm{B}}$ (with $x_\mathrm{A} + x_\mathrm{B} = 1$) destroys the underlying Bloch symmetry of the crystal and is thus difficult to describe within DFT. One simple approach is the virtual crystal approximation (VCA), which substitutes the atoms in a disordered compound by a dummy atom Z with the averaged atomic mass $Z = x_\mathrm{A} Z_\mathrm{A} + x_\mathrm{B} Z_\mathrm{B}$. By doing so one restores the Bloch symmetry but looses all individual information about the involved components. Another possibility is to use supercells, which can account for disorder effects. However, such an approach suffers under the computational effort as it is necessary to use preferably very large supercells and to average over several different supercell compositions.[49]

Within the KKR-GF method the coherent potential approximation (CPA) can be applied, which is the best possible single-site approach to describe random substitutional alloys.[107] The idea is based on seeking the configuration-averaged electronic Green function $\langle G \rangle$, which is a valid procedure in contrary to using a configuration-averaged wave function. To implement this idea Korringa[108] and Beeby[109] represented the t-matrix within the average t-matrix approximation (ATA) as t_{ATA}:

$$\langle t\rangle \;=\; t_{\mathrm{ATA}} \;=\; x_{\mathrm{A}}t_{\mathrm{A}} + x_{\mathrm{B}}t_{\mathrm{B}} \;. \tag{2.76}$$

However, this will lead to a Green function that does not stringently give a positive definite density of states (DOS) for real energies. This issue was removed by Soven[93] by introducing an auxiliary CPA medium which is meant to represent the configurational average and thus acts like a mean field. This medium is defined in a way that embedding the components into it will reproduce the CPA medium itself if the respective concentration-weighted averages are taken. The consequence of this assumption is that the proper averages should cause no additional scattering compared with the CPA medium, resulting in the following equations with the component projected scattering path operators τ^{ii}_{A} and τ^{ii}_{B}:

$$x_{\mathrm{A}}\tau^{ii}_{\mathrm{A}} + x_{\mathrm{B}}\tau^{ii}_{\mathrm{B}} \;=\; \tau^{ii}_{\mathrm{CPA}} \;, \tag{2.77}$$

$$\tau^{ii}_{\alpha} \;=\; \left[t^{-1}_{\alpha} - t^{-1}_{\mathrm{CPA}} + (\tau^{ii}_{\mathrm{CPA}})^{-1}\right]^{-1} \qquad \text{for:} \qquad \alpha = \mathrm{A,B} \;. \tag{2.78}$$

In addition, equation (2.79) has to be satisfied:

$$\underline{\underline{\tau}}_{\mathrm{CPA}} \;=\; \left(\underline{\underline{t}}^{-1}_{\mathrm{CPA}} - \underline{\underline{G}}_{0}\right)^{-1} \;. \tag{2.79}$$

The procedure starts in practice with a guess $t_{\mathrm{CPA}} \approx t_{\mathrm{ATA}}$ and evaluates t_{CPA} and τ^{ii}_{CPA} using an iterative algorithm.[110] The Green function of the disordered system can be expressed in terms of the component weighted average, according to

$$G^{\mathrm{CPA}}(\boldsymbol{r},\boldsymbol{r}',E) = \sum_{\alpha=A,B,\ldots} x_{\alpha}G^{\alpha}(\boldsymbol{r},\boldsymbol{r}',E) \;. \tag{2.80}$$

In contrast to the VCA the CPA provides a coherent potential V_{CPA} which implies that the electronic states described by the CPA have a finite lifetime, due to their complex energy eigenvalues. Still, it should be noted that the CPA is a single-site theory and consequently short-range order is not included. However, this issue can be handled with respect to recent developments in the field of non-local CPA.[111,112]

2.1.6 Calculation of observables

As already mentioned the Green function can provide a straightforward access to all physical observables. This is in particular true for the electron density $n(\boldsymbol{r})$, the density of states $n(E)$, and the spin- and orbital magnetic moments μ_{spin} and μ_{orb}:

$$\begin{aligned}
n(\boldsymbol{r}) &= -\frac{1}{\pi}\ \mathrm{Im}\ \mathrm{Tr} \int^{E_{\mathrm{F}}} \mathrm{d}E\ G(\boldsymbol{r},\boldsymbol{r},E)\ , && (2.81)\\
n(E) &= -\frac{1}{\pi}\ \mathrm{Im}\ \mathrm{Tr} \int_{\Omega} \mathrm{d}^3r\ G(\boldsymbol{r},\boldsymbol{r},E)\ , && (2.82)\\
\mu_{\mathrm{spin}} &= -\frac{1}{\pi}\ \mathrm{Im}\ \mathrm{Tr} \int^{E_{\mathrm{F}}} \mathrm{d}E \int_{\Omega} \mathrm{d}^3r\ \beta\sigma_z G(\boldsymbol{r},\boldsymbol{r},E)\ , && (2.83)\\
\mu_{\mathrm{orb}} &= -\frac{1}{\pi}\ \mathrm{Im}\ \mathrm{Tr} \int^{E_{\mathrm{F}}} \mathrm{d}E \int_{\Omega} \mathrm{d}^3r\ l_z G(\boldsymbol{r},\boldsymbol{r},E)\ . && (2.84)
\end{aligned}$$

For these quantities only the diagonal parts of $G(\boldsymbol{r}_i,\boldsymbol{r}'_j,E)$ are needed because of the trace in these equations. Thus, it is sufficient to calculate only the scattering path operators τ^{ii}. The analytical properties of $G(\boldsymbol{r}_i,\boldsymbol{r}'_j,E)$ further lead to the advantage that the energy integration can be carried out on a contour in the complex energy plane, requiring in practice only about 32 energy mesh points for sufficient numerical accuracy.

Another important quantity for detailed informations on the electronic structure is the Bloch spectral function (BSF) $A_{\mathrm{B}}(\boldsymbol{k},E)$. The BSF is defined as the imaginary part of the Fourier transform of $G(\boldsymbol{r}_i,\boldsymbol{r}'_j,E)$ and provides a $\boldsymbol{k}$-resolved density of states:

$$A_{\mathrm{B}}(\boldsymbol{k},E) = -\frac{1}{\pi}\ \mathrm{Im}\ \mathrm{Tr}\ \frac{1}{N}\sum_{ij}^{N} e^{i\boldsymbol{k}(\boldsymbol{R}_i-\boldsymbol{R}_j)} \int_{\Omega} \mathrm{d}^3r\ G(\boldsymbol{r}+\boldsymbol{R}_i,\boldsymbol{r}'+\boldsymbol{R}_j,E)\ , \qquad (2.85)$$

with the property,

$$n(E) = \frac{1}{\Omega_{\mathrm{BZ}}} \int_{\Omega_{\mathrm{BZ}}} \mathrm{d}^3k\ A_{\mathrm{B}}(\boldsymbol{k},E)\ . \qquad (2.86)$$

For an ordered periodic system $A_{\mathrm{B}}(\boldsymbol{k},E)$ corresponds to the dispersion relation $E(\boldsymbol{k})$. However, the advantage of the Bloch spectral function is that it is still well-defined for a disordered system, while the dispersion relation $E(\boldsymbol{k})$ breaks down for a broken Bloch symmetry. This allows for the investigation of the impact of disorder on the band structure of substitutionally disordered alloys.

2.1.7 Hyperfine interactions

The magnetic hyperfine interaction of an atom derives in the most general description from the interaction of the electronic current density $\boldsymbol{j}$ with the vector potential $\boldsymbol{A}_n(\boldsymbol{r})$ associated with the nuclear magnetic moment. This means in particular that the total angular momentum of an electron stemming from spin-orbit coupling can interact with the magnetic field of the nucleus, leading to contributions to the hyperfine field B_{hf} that are not accounted by a non-relativistic approach.

Within SPR-KKR[113] the relativistic operator $\hat{H}_{\mathrm{hf}}$ is formulated based on the electronic current density operator $\hat{\boldsymbol{j}} = ec\boldsymbol{\alpha}$ coupling to the vector potential $\boldsymbol{A}_n$ as given by

$$\hat{H}_{\mathrm{hf}} = e\boldsymbol{\alpha} \cdot \boldsymbol{A}_n(\boldsymbol{r}) = e\boldsymbol{\alpha} \cdot (\boldsymbol{\mu}_n \times \boldsymbol{r}) A_n(r) , \tag{2.87}$$

where $\boldsymbol{A}_n$ stems from the nuclear magnetic dipole $\boldsymbol{\mu}_n$ with $A_n(r)$ being the radial part of the nuclear vector potential. Contributions of tightly bound core electrons E_{hf}^{core} and valence bands electrons E_{hf}^{val} to the hyperfine interaction energy E_{hf} are separated by this conventional splitting of the electronic system. Thus, E_{hf}^{core} is obtained by

$$E_{\mathrm{hf}}^{core} = \sum_{n\Lambda} \langle \Phi_{n\Lambda} | \hat{H}_{\mathrm{hf}} | \Phi_{n\Lambda} \rangle , \tag{2.88}$$

while E_{hf}^{val} is given in terms of the electronic Green function with an energy integration extending over the range of occupied states of the valence band up to the Fermi energy E_F:

$$E_{\mathrm{hf}}^{val} = -\frac{1}{\pi} \, \mathrm{Tr} \, \mathrm{Im} \int^{E_F} \mathrm{d}E \int \mathrm{d}^3 r \; \hat{H}_{\mathrm{hf}} \, G(\boldsymbol{r}, \boldsymbol{r}, E) . \tag{2.89}$$

The hyperfine field B_{hf} represents the nuclear Zeeman splitting and is an interaction parameter related to E_{hf} by

$$B_{\mathrm{hf}} = \frac{E_{\mathrm{hf}}}{\mu_n} , \tag{2.90}$$

with the magnetic moment of the nucleus μ_n.

Typically, the finite size of the atomic core is ignored, which means B_{hf} splits into five different contributions within the fully relativistic approach. Two contributions are due to s-electrons and they are conventionally ascribed to the Fermi contact interaction. The larger of both parts is the core polarization contribution B_s^c which is proportional to the local spin magnetic moment μ_{spin}.[114–116] In addition, there is a s-electron contribution from the valence band B_s^v that is due to the polarization and the population mechanism.[117] All states apart from the $p_{1/2}$-states with higher angular momentum, i.e. first of all p- and d-states, have a zero probability density at the nucleus and thus do not contribute to B_{hf} via the Fermi contact term. If spin-orbit coupling is fully accounted for, there is an additional contribution due to the spin-orbit induced orbital magnetization.[113,118] Furthermore, for systems with low symmetry a spin-dipolar contribution for the non-s electrons can contribute.[113,118] However, because the orbital contribution is in general dominating compared to the spin-dipolar one, the term orbital is used for the total field connected with non-s electrons in the following. Thus, for a transition metal the remaining three contributions are the orbital field B^c_{ns} of the non-s core states and the orbital fields B^v_p and B^v_d of the valence electrons with p- and d-character, respectively. More details on the decomposition of B_{hf} can be found in Ref.[113] by Battocletti and Ebert.

2.1.8 Dynamical mean field theory within SPR-KKR

Within DFT a respective exchange-correlation potential V_{xc} has to be chosen in order to calculate the effective potential V_{eff}. The most commonly used scheme is the local density approximation (LDA), which is justified for systems with only slightly varying density, treating the single points in space locally as a homogeneous free electron gas. When dealing with strongly correlated matter, having e.g. more localized d and f electrons with strong Coulomb interactions the LDA is no longer applicable. One sophisticated approach to deal with strongly correlated matter within DFT is the dynamical mean-field theory (DMFT), leading to so-called LDA+DMFT approaches which can be also implemented within the KKR-GF method.[119,120] The basic idea of DMFT is that in the limit of infinite dimensions the self energy Σ becomes local.[121,122] Thus, it was assumed that in finite but not too low dimension, the infinite lattice can be mapped approximately onto an impurity problem, which can be solved self-consistently.[122] The physics behind DMFT is non-trivial and a detailed explanation goes beyond the scope of this work, thus, more details can be found in Ref.[119]. In general, the electronic properties of a system are given by

$$\left[E - \hat{\mathcal{H}} - \hat{\Sigma}(E)\right] \hat{G} \;=\; \hat{1}\;, \tag{2.91}$$

with the complex energy E and the effective self-energy operator $\hat{\Sigma}(E)$ which is assumed to be a single-site quantity for site n according to

$$\hat{\Sigma}(E) \;=\; \sum_{ij} |\phi_{ni}\rangle\, \Sigma_{ij}(E)\, \langle\phi_{nj}|\;. \tag{2.92}$$

The self-energy matrix $\Sigma_{ij}(E)$ is a solution to the many-body problem of an impurity placed into an effective medium which is described by the so-called bath Green function matrix $\mathcal{G}$ given by

$$\mathcal{G}_{ij}^{-1}(E) \;=\; G_{ij}^{-1}(E) + \Sigma_{ij}(E) \; . \tag{2.93}$$

Here, the one-electron Green function matrix $G_{ij}(E)$ is a projection of $\hat{G}(E)$ onto the impurity site calculated via

$$G_{ij}(E) \;=\; \langle \phi_{ni} | \hat{G}(E) | \phi_{nj} \rangle \; . \tag{2.94}$$

Consequently, the self-energy $\Sigma_{ij}(E)$ and the bath Green function $\mathcal{G}_{ij}(E)$ depend on each other, which means the problem has to be solved self-consistently. Thus, apart from solving equation (2.91) one has to find the self-energy $\Sigma_{ij}(E)$ by solving the effective many-body problem. This can be done by available DMFT-solvers[119], e.g. for the presented work a perturbative SPTF (spin-polarized T-matrix + FLEX) solver was applied.

For systems like the iron pnictides, the strength of correlation effects is under discussion[32,54–56,59,123,124] and thus one cannot straightforwardly know to what extent strong correlations have to be accounted for. An example of strong correlations within the iron pnictides, dealt with by means of LDA+DMFT, is discussed in Chapter 6.

2.2 Angle-resolved photoemission spectroscopy

2.2.1 Experimental setup

All kinds of photoemission spectroscopy are based on the photoeffect, which was initially observed by Hertz[125] in 1887 and first explained by Einstein[126] in 1905. The variety of applications is significant, however, for the scope of this work the focus will be specifically angle-resolved photoemission spectroscopy (ARPES).[127–129]

ARPES is one of the most important tools to study the electronic structure of solids as it provides experimentally direct access to k-resolved information. The corresponding setup (see Fig. 2.1) is realized via a ray of monochromatic light, typically synchrotron radiation, with energy $h\nu$ that hits the sample surface under fixed conditions, defined by the spherical coordinates Θ_{ph} and Φ_{ph}. This leads to the emission of photoelectrons which can be detected and characterized angle-resolved by the polar (Θ_{el}) and the azimuth (Φ_{el}) emission angles. To analyze a whole area in $\boldsymbol{k}$-space for a constant Φ_{el} it is also possible to tilt the surface of the sample under the incoming light along a fixed rotation axis.

Obviously the escape of an electron from the material is only possible if the energy of the absorbed photon is large enough. It is not only necessary to overcome the binding energy E_{B} which is required to liberate the electron, but also the work function ϕ_0 which is required to remove the excited electron from the sample surface. The final kinetic energy of the emitted electron E_{kin} is then given by

$$E_{\mathrm{kin}} = h\nu - |E_{\mathrm{B}}| - \phi_0 \; . \tag{2.95}$$

The momentum $\boldsymbol{K}$ of the photoelectron in the vacuum depends only on the emission angles Θ_{el} and Φ_{el} and the kinetic energy E_{kin} of the electrons, all measurable during the experiment. Because the momentum of the probe surface $\boldsymbol{k}$ is related to $\boldsymbol{K}$, ARPES can derive k-resolved information. However, it is necessary to distinguish between the in-plane $\boldsymbol{k}_{\parallel}$ component (parallel to sample surface) and the z-component $\boldsymbol{k}_{\perp}$ (perpendicular to sample surface) of the wave vector $\boldsymbol{k}$. The translational symmetry of the crystal in the xy-plane preserves $\boldsymbol{k}_{\parallel}$, hence, for a negligible incoming photon momentum compared to the emitted electron momentum one can directly calculate

$$|\boldsymbol{k}_{\parallel}| = \frac{1}{\hbar}\sqrt{2m_{\mathrm{e}}E_{\mathrm{kin}}}\sin\Theta_{\mathrm{el}} \; . \tag{2.96}$$

However, the perpendicular component $\boldsymbol{k}_{\perp}$ is not conserved across the sample surface

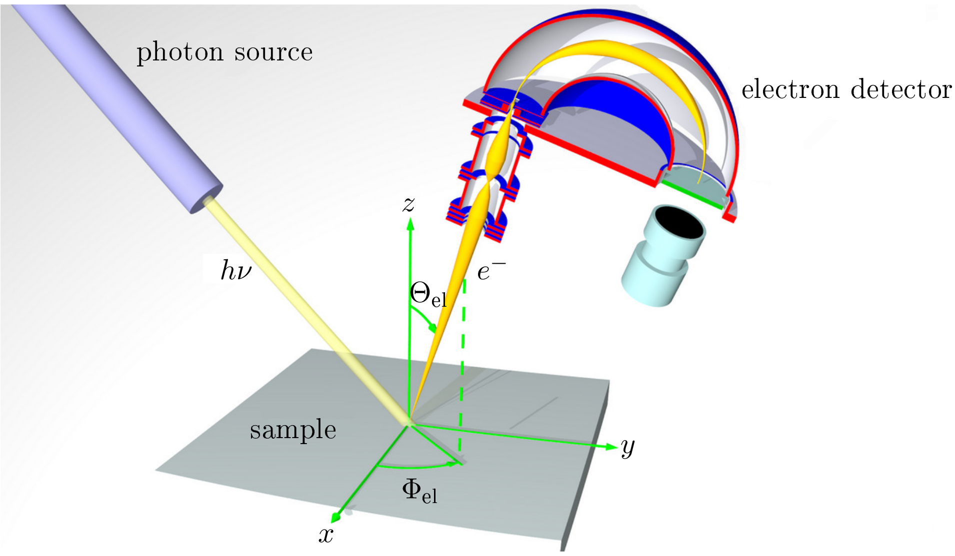

Figure 2.1. Schematic geometry of an ARPES experiment, where the emission direction of the electron is specified by the emission angles Θ_{el} and Φ_{el}.

due to the lack of translational symmetry along the surface normal. This uncertainty is of minor relevance for strongly two-dimensional systems with a negligible dispersion along z as e.g. many cuprate superconductors have.[127] Nevertheless, such an assumption is invalid for the iron pnictides, which have a pronounced 3D electronic structure. For a free-electron final state inside the solid one can obtain $\boldsymbol{k}_\perp$ from

$$\boldsymbol{k}_\perp = \frac{1}{\hbar}\sqrt{2m_{\mathrm{e}}\left(E_{\mathrm{kin}}\cos^2\Theta_{\mathrm{el}} + V_0\right)}\,, \tag{2.97}$$

with the inner potential $V_0 = |E_0| + \phi_0$, representing the energy of the bottom of the valence band with respect to the vacuum level E_{vac}. For photon energies between 10 eV and 100 eV the mean free path of the electrons is in the order of 10 Å at maximum. Thus, ARPES in this energy range is sensitive for the surface of the material. To have a stronger focus on bulk properties one uses higher photon energies in the regime of soft X-rays, ranging from approximately 300 eV up to 1 keV. For energies above 1 keV one enters the regime of hard X-rays.

In the following the general theory of ARPES including the one-step model and the theory of surface related phenomena will be briefly reviewed based on the work of Braun[128] and the work of Braun and Donath[129,130], respectively.

2.2.2 General theory

The quantity of most interest to describe the photoemission process is the corresponding photocurrent. To derive an expression for it one starts from first-order time-dependent perturbation theory, assuming a small perturbation Δ. Here, the transition probability per unit time w between the N-electron final state $|\Psi_f\rangle$ and initial state $|\Psi_i\rangle$ is defined according to Fermi's golden rule:

$$w = \frac{2\pi}{\hbar} |\langle\Psi_f|\Delta|\Psi_i\rangle|^2 \, \delta(E_f - E_i - h\nu) \, , \tag{2.98}$$

with the corresponding energies of final and initial state E_f and E_i and the excitation energy $h\nu$, respectively. This transition probability w can be used to derive the photoemission intensity $I(h\nu)$ which is related to the one-electron spectral density $A_{i,i'}$ of the initial state:[131,132]

$$I(h\nu) = \frac{1}{\hbar} \sum_{f,i,j} \Delta^*_{f,i} A_{i,i'}(E_i) \Delta_{i',f} \, , \tag{2.99}$$

$$A_{i,i'}(E_i) = \sum_s \langle\Psi_i|a^\dagger_{i'}|\Psi^s_f\rangle \, \delta(E_f - E_i - h\nu) \, \langle\Psi^s_f|a_i|\Psi_i\rangle \, , \tag{2.100}$$

using the one-electron matrix element $\Delta_{f,i} = \langle\phi_f|\Delta|\phi_i\rangle$ and corresponding creation $a^\dagger_i$ and annihilation a_i operators for an electron i. Herein, one defines $|\Psi_i\rangle = |\Psi^0_N\rangle$ and $|\Psi^s_f\rangle = a^\dagger_i|\Psi^s_{N-1}\rangle$ with the excited $(N-1)$-particle state $|\Psi^s_{N-1}\rangle$ and the ground state $|\Psi^0_N\rangle$. At this point only the sudden approximation for the final state has been applied, meaning the excitation of an electron happens so fast that there is no interaction between the corresponding one-particle photoelectron state and the remaining $(N-1)$-electron $|\Psi^s_{N-1}\rangle$ excited state, implying $a_i|\Psi^0_N\rangle = 0$.

The one-electron spectral density $A_{i,i'}$ can be connected to a retarded one-electron Green function $G_{i,i'}(E_i)$ of the interacting system, which means the photoemission intensity of equation (2.99) can be written as

$$I(h\nu) = -\frac{1}{\hbar\pi} \mathrm{Im} \sum_{f,i,i'} \langle\phi_f|\Delta|\phi_i\rangle \, G_{i,i'}(E_i) \, \langle\phi_{i'}|\Delta^*|\phi_f\rangle \, , \tag{2.101}$$

and by using the representation $G(E_i) = \sum_{i,i'} |\phi_i\rangle G_{i,i'}(E_i)\langle\phi_{i'}|$ on arrives at

$$I(h\nu) = -\frac{1}{\hbar\pi} \mathrm{Im} \sum_f \langle\phi_f|\Delta G(E_i)\Delta^*|\phi_f\rangle \, . \tag{2.102}$$

The remaining final state $|\phi_f\rangle$ corresponds a time-reversed spin-polarized low energy electron diffraction (SPLEED) state $|\boldsymbol{k}_{||}, \epsilon_f\rangle$, depending on the wave vector component parallel to the surface $\boldsymbol{k}_{||}$ and the single particle energy ϵ_f of the final state.[133] Note, that from now on the one-particle energies $\epsilon(\boldsymbol{k})$ are used, which result from band structure calculations based on DFT[128]. By introducing the Green function G_2 for the final state one can express these states by means of

$$|\phi_f\rangle \;=\; G_2^-|\boldsymbol{k}_{||},\epsilon_f\rangle \qquad \text{and} \qquad \langle\phi_f| \;=\; \langle\epsilon_f,\boldsymbol{k}_{||}|G_2^+ \;, \tag{2.103}$$

with the propagators $G_2^\pm$ derived from the KKR multiple scattering approach.[133–135] The operator Δ accounts for the coupling to the electromagnetic field. Within the dipole approximation it reduces to $\Delta \approx \frac{e}{mc}\boldsymbol{A}_0 \cdot \hat{\boldsymbol{p}}$, for the momentum operator $\hat{\boldsymbol{p}}$ and the spatially constant amplitude of the electromagnetic vector potential $\boldsymbol{A}_0$. So far $G(E_i)$ contains all many-body effects within its complex self-energy $\Sigma(E_i)$. In the non-interacting limit, meaning for a zero self-energy $\Sigma(E_i) = 0$ the term $G(E_i)$ can be expressed as retarded Green function of the initial state G_1^+. Combining equations (2.102) and (2.103) and for zero temperature $T = 0$ K the photoemission intensity can be finally written according to

$$I(\epsilon_f,\boldsymbol{k}_{||}) \;=\; -\frac{1}{\hbar\pi}\text{Im}\;\langle\epsilon_f,\boldsymbol{k}_{||}|G_2^+\Delta G_1^+\Delta^* G_2^-|\boldsymbol{k}_{||},\epsilon_f\rangle \;. \tag{2.104}$$

At this point it is important to note, that occupied and unoccupied states can be investigated within the same theoretical framework due to a simple geometrical relation between the photoemission intensity $I(\epsilon_f,\boldsymbol{k}_{||})$ and the inverse photoemission intensity $I^{\text{invers}}(\epsilon_f,\boldsymbol{k}_{||})$, given by[136]

$$I(\epsilon_f,\boldsymbol{k}_{||}) \;=\; \frac{2(\epsilon_f - h\nu)c^2\cos\Theta_{\text{el}}}{\omega^2\cos\Theta_{\text{ph}}} I^{\text{invers}}(\epsilon_f,\boldsymbol{k}_{||}) \;. \tag{2.105}$$

2.2.3 One-step model of photoemission

Equation (2.104) is the basis of the so-called one-step model of photoemission, which was first developed by Pendry *et al.*[133] and which is used in the SPR-KKR code package to calculate ARPES spectra. The following will describe the relativistic one-step theory for a semi-infinite stack of layers. For this reason equation (2.104) will be rewritten in terms of a real space representation, describing the corresponding photocurrent $I(\epsilon_f,\boldsymbol{k}_{||})$:

$$I(\epsilon_f,\boldsymbol{k}_{||}) \;=\; -\frac{1}{\pi}\text{Im}\int \mathrm{d}^3r \int \mathrm{d}^3r' \;\Psi_f^\dagger(\boldsymbol{r})\Delta G_1^+(\boldsymbol{r},\boldsymbol{r}')\Delta^\dagger\Psi_f(\boldsymbol{r}') \;, \tag{2.106}$$

with the time-reversed SPLEED state $\Psi_f^\dagger(\boldsymbol{r}) = \langle \boldsymbol{r}|G_2^+|\epsilon_f, \boldsymbol{k}_{||}\rangle$. Herein, the propagators $G_2^\pm$ and G_1^+ are expressed by 4×4 matrices and $\Psi_f^\dagger(\boldsymbol{r})$ is a four-component Dirac spinor. The relativistic interaction operator is defined by $\Delta = -\boldsymbol{\alpha} \cdot \boldsymbol{A}_0$.

The corresponding wave field of the final state $\Psi_f(\boldsymbol{r})$ can be obtained everywhere within the crystal, knowing the scattering properties of each layer. It is also sufficient to account only for a finite number of layers because the amplitude of the wave field continuously diminishes further inside the crystal. Thus, one remains with the so far unknown initial state propagator G_1^+. One can split the photocurrent into four different contributions:

$$I(\epsilon_f, \boldsymbol{k}_{||}) \; = \; I^{\text{atom}}(\epsilon_f, \boldsymbol{k}_{||}) + I^{\text{intra}}(\epsilon_f, \boldsymbol{k}_{||}) + I^{\text{inter}}(\epsilon_f, \boldsymbol{k}_{||}) + I^{\text{surf}}(\epsilon_f, \boldsymbol{k}_{||}) \; . \tag{2.107}$$

The first three contributions can be easily denoted starting from (2.106) and replacing G_1^+ by the corresponding Green functions:

$$\begin{aligned} I^{\text{atom}}(\epsilon_f, \boldsymbol{k}_{||}) &= -\frac{1}{\pi}\text{Im} \int \mathrm{d}^3 r \int \mathrm{d}^3 r' \; \Psi_f^\dagger(\boldsymbol{r}) \Delta G_{1\text{atom}}^+(\boldsymbol{r}, \boldsymbol{r}') \Delta^\dagger \Psi_f(\boldsymbol{r}') \; , & (2.108) \\ I^{\text{intra}}(\epsilon_f, \boldsymbol{k}_{||}) &= -\frac{1}{\pi}\text{Im} \int \mathrm{d}^3 r \int \mathrm{d}^3 r' \; \Psi_f^\dagger(\boldsymbol{r}) \Delta G_{1\text{intra}}^+(\boldsymbol{r}, \boldsymbol{r}') \Delta^\dagger \Psi_f(\boldsymbol{r}') \; , & (2.109) \\ I^{\text{inter}}(\epsilon_f, \boldsymbol{k}_{||}) &= -\frac{1}{\pi}\text{Im} \int \mathrm{d}^3 r \int \mathrm{d}^3 r' \; \Psi_f^\dagger(\boldsymbol{r}) \Delta G_{1\text{inter}}^+(\boldsymbol{r}, \boldsymbol{r}') \Delta^\dagger \Psi_f(\boldsymbol{r}') \; . & (2.110) \end{aligned}$$

Here, $G_{1\text{atom}}^+$ accounts for single site atomic contribution of the photocurrent, $G_{1\text{intra}}^+$ considers for multiple scattering of the initial state inside the jth layer and $G_{1\text{inter}}^+$ involves multiple scattering between the initial state and all other layers of the semi-infinite crystal. These contributions can be written explicitly as follows:

$$\begin{aligned} I^{\text{atom}}(\epsilon_f, \boldsymbol{k}_{||}) &= -\frac{1}{\pi}\text{Im}\left(ik_1 \sum_j \sum_{\kappa\kappa'\kappa''} \sum_{\mu\mu'\mu''} A_{j\kappa}^{\mu} D_{\kappa\mu\kappa'\mu'} M_{\kappa\kappa'\kappa''} D_{\kappa'\mu'\kappa''\mu''}^{*} A_{j\kappa''}^{\mu''*} \right) , & (2.111) \\ I^{\text{intra}}(\epsilon_f, \boldsymbol{k}_{||}) &= -\frac{1}{\pi}\text{Im}\left(ik_1 \sum_j \sum_{\kappa\kappa'} \sum_{\mu\mu'} A_{j\kappa}^{\mu} \tilde{M}_{\kappa\kappa'} D_{\kappa\mu\kappa'\mu'} B_{j\kappa'}^{\mu'} \right) , & (2.112) \\ I^{\text{inter}}(\epsilon_f, \boldsymbol{k}_{||}) &= -\frac{1}{\pi}\text{Im}\left(ik_1 \sum_j \sum_{\kappa\kappa'} \sum_{\mu\mu'} A_{j\kappa}^{\mu} \tilde{M}_{\kappa\kappa'} D_{\kappa\mu\kappa'\mu'} G_{j\kappa'}^{\mu'} \right) . & (2.113) \end{aligned}$$

This implies the spherical coefficients of the final state $A_{j\kappa}^{\mu}$ as well as the radial and angular matrix elements $M_{\kappa\kappa'\kappa''}$, $\tilde{M}_{\kappa\kappa'}$ and $D_{\kappa\mu\kappa'\mu'}$, plus the spherical coefficients for the intralayer part $B_{j\kappa'}^{\mu'}$ and interlayer part $G_{j\kappa'}^{\mu'}$ of the initial state wave field at the jth layer, respectively.

The last contribution based on the photocurrent I^{surf} accounts for the surface of the semi-infinite crystal. This contribution is treated non-relativistically because relativistic effects were shown to be negligible in the surface barrier region.[137] Thus, I^{surf} is defined according to

$$I^{\mathrm{surf}}(\epsilon_f, \boldsymbol{k}_{||}) \;=\; -\frac{1}{\pi}\mathrm{Im}\int \mathrm{d}^3r\ \Psi_f^{*\mathrm{surf}}(\boldsymbol{r})\Delta\Psi_i^{\mathrm{surf}}(\boldsymbol{r}')\ , \tag{2.114}$$

$$\Psi_i^{\mathrm{surf}}(\boldsymbol{r}) \;=\; \int \mathrm{d}^3r'\ G^{+}_{1\mathrm{surf}}(\boldsymbol{r},\boldsymbol{r}')\Delta^*\Psi_f^{\mathrm{surf}}(\boldsymbol{r}')\ . \tag{2.115}$$

Because surface corrugations have only a small impact it is sufficient to treat the barrier potential depending only on z. For such a z-dependent surface barrier potential $V_B(z)$, the z-axis was defined pointing into the crystal, the initial and final state wave fields have to be calculated numerically in the surface region.[138] These wave fields $\Psi_i^{\mathrm{surf}}(\boldsymbol{r})$ and $\Psi_f^{\mathrm{surf}}(\boldsymbol{r})$ can be split into a z-dependent and a corresponding parallel component as shown in the following:

$$\Psi_i^{\mathrm{surf}}(\boldsymbol{r}) = \sum_{\boldsymbol{g}s}\phi_{\boldsymbol{g}s}(z)e^{i\boldsymbol{k}_{i\boldsymbol{g}_{||}}(\boldsymbol{r}-\boldsymbol{c})_{||}} \qquad \text{and} \qquad \Psi_f^{\mathrm{surf}}(\boldsymbol{r}) = \sum_{\boldsymbol{g}s}\lambda_{\boldsymbol{g}s}(z)e^{i\boldsymbol{k}_{f\boldsymbol{g}_{||}}(\boldsymbol{r}-\boldsymbol{c})_{||}}\ . \tag{2.116}$$

This implies the regular solutions of the Schrödinger equation $\phi_{\boldsymbol{g}s}$ and $\lambda_{\boldsymbol{g}s}$ to the reciprocal lattice vector $\boldsymbol{g}$ for $V_B(z)$ in the range $-\infty < z < c_z$ and for the spin index s. Here, c_z corresponds to the point where the surface potential matches smoothly with the inner potential of the bulk. Finally, the surface contribution can be evaluated as

$$I^{\mathrm{surf}}(\epsilon_f, \boldsymbol{k}_{||}) \;=\; -\frac{1}{\pi}\frac{A_z}{2\omega c}\,\mathrm{Im}\left(e^{i\boldsymbol{q}_{||}\cdot\boldsymbol{c}_{||}}\sum_{\boldsymbol{g}s}\int_{-\infty}^{c_z} dz\ \phi_{\boldsymbol{g}s}(z)\ \frac{dV_B}{dz}\ \lambda_{\boldsymbol{g}s}(z)\ e^{iq_z z}\right)\ , \tag{2.117}$$

for A_z being the z component of $\boldsymbol{A}_0$ and $\boldsymbol{q}$ as wave vector of the photon field.

Lifetime effects in the final and initial states can be accounted for on the basis of a parametrized complex inner potential $V_{\mathrm{o}}(E) = V_{\mathrm{or}}(E) + iV_{\mathrm{oi}}(E)$, while the real part corresponds to the reference energy inside the crystal with respect to the vacuum level. The surface barrier potential connects this inner potential of the bulk crystal with the vacuum level. A realistic description for the surface potential is given by the spin-dependent Rundgren-Malmström barrier $V^{\uparrow\downarrow}(z)$, which connects the asymptotic region $\sim \frac{1}{z}$ to the bulk muffin-tin zero V_{or} by a third-order polynomial in z.[139]

2.2.4 Surface related states as observed in ARPES

The origin of various spectral features can be ascribed to different electronic states which can be observed in an ARPES measurement. Clearly, it is highly desirable to be able to distinguish between different states in a theoretical approach, especially concerning their surface character.[129,130]

First of all, one can define bulk states (BS) which have almost no surface character at all. The wave function of these states extends deeply into the bulk crystal and shows marginal decay only. Such states are characterized by a distinguished k_z dispersion which can be seen by measurements with varying photon energies. On the other hand, the one-step model of photoemission can be used to identify surface related states, as the origin of surface states has long been developed in multiple scattering theory.[140,141] A surface state (SS) is characterized by a wave function that only exists at the vicinity of the surface, between the asymptotic limit and the inner bulk potential. Such a state has almost no penetration depth into the bulk crystal. Consequently, it shows no k_z dispersion and can be observed for small photon energies which guarantee a surface sensitive spectrum. The condition for the occurrence of such a surface state is given by the so called determinant condition $D(E, \boldsymbol{k})$ given by

$$D(E, \boldsymbol{k}) = \det\left(\mathbb{1} - \boldsymbol{R}_{\mathrm{b}}(E, \boldsymbol{k})\boldsymbol{R}_{\mathrm{v}}(E, \boldsymbol{k})\right) = 0 \; , \tag{2.118}$$

using the reflection matrices of the bulk crystal $\boldsymbol{R}_{\mathrm{b}}$ and of the surface barrier potential $\boldsymbol{R}_{\mathrm{v}}$. In addition, one can define a third type of state, a so-called surface resonance (SR). These surface resonances are wave functions which have their origin at the vicinity of the surface but they can penetrate through several layers into the bulk crystal. The wave function shows an exponential decay inside the bulk, however, as a combination between bulk state and surface state a surface resonance can also be observed for comparably high photon energies in the soft X-ray regime. Correspondingly, a surface resonance is indicated by a minimum of $D(E, \boldsymbol{k})$. Note, that sometimes the term surface resonance is also used for a state with bulk Bloch asymptotic behavior and a strong resonance at the vicinity of the surface.

For better visualization one typically plots $1/|D(E, \boldsymbol{k})|$ to identify the origin of a state. If this expression is bigger than approximately 10^3 one can speak about a surface state. For values between 10^0 and 10^3 the state is defined as a surface resonance. Smaller values indicate a bulk state.

2.3 Transport properties

Describing the transport properties of metals is a well-established and important field of condensed matter physics, yet also an exceptional complex one. Concerning the scope of this thesis, especially longitudinal transport described by linear response theory will prove useful to study the iron pnictide superconductors. Consequently, the following will give a brief overview mainly based on the work of Banhart[142] and Lowitzer[98] concerning the different approaches to study transport properties with focus on the relevant equations applied.

2.3.1 General introduction

When talking about electron transport in a material the first important aspect to note is that an ideal crystal with translational symmetry at a temperature of $T = 0$ K shows no resistivity at all. This can be easily understood assuming an electron wave which gets scattered at the crystal lattice but which can be reconstructed from constructive interference without energy loss after the scattering process. A perturbation of the translational symmetry, however, will lead to partly deconstructive interference, preventing a loss-free electron transport. This breaking of translational symmetry can be induced by either static perturbations like defects or alloying or it can emerge from dynamic perturbations like thermal lattice fluctuations with respect to electron-phonon interactions. Considering the temperature $T = 0$ K, the interest of this work is solely focused on static perturbations induced by alloying the concerning the material of interest.

Obviously, the description of electron transport in solids requires a statistic approach as it is not possible to treat every particle individually. In this context one can distinguish between two different methods, namely the kinetic theories and the linear response theories. Kinetic theories are based on a statistic distribution function like for example the Boltzmann equation in its semi-classical or quantum mechanical form. These kinetic theories are typically useful for very strong external fields, however, they fail for strong scattering in concentrated alloys. The second approach is based on the assumption of a fast equilibrium state, meaning one describes the response of the system to a small perturbation. Because it is typically sufficient to consider only the first order of the response these approaches are called linear response theories. A linear response approach is in particular useful for strong scattering, meaning for concentrated alloys, however, the external field cannot be arbitrarily strong.

Thus, when dealing with an alloy A_xB_{1-x} within the framework of KKR the most reasonable approach will be based on linear response theory. The expected behavior of the resistivity for varying x can be described by the so-called Nordheim curves. This implies a minima in resistivity for the weakest scattering at $x = 0$ or 1 and a maximum for the strongest scattering at $x = 0.5$. Solving this issue quantitatively is based on an approach first proposed by Kubo and others.[143–145] Thus, the following will introduce the corresponding Kubo equation and the Kubo-Greenwood equation.

2.3.2 Kubo equation

The Kubo formalism can be understood as a whole set of equations which describe linear response by means of correlation functions of the perturbation and the response in a full quantum mechanical picture. First proposed by Green[146] in order to investigate transport in liquids it was Kubo[145] who formulated the corresponding equations to study electrical conductivity in solids. Starting from a system in equilibrium described by a Hamiltonian $\hat{H}_0$ one assumes a small time-dependent perturbation $\hat{W}(t)$. The expectation value of an arbitrary operator $\hat{D}$ can be expressed using the density matrix ρ_0,

$$\langle \hat{D} \rangle \;=\; \mathrm{Tr}(\rho_0 \hat{D}) \qquad \text{with} \qquad \rho_0 \;=\; \frac{e^{-\beta \hat{H}_0}}{\mathrm{Tr}(e^{-\beta \hat{H}_0})} \,, \tag{2.119}$$

using $\beta = (k_\mathrm{B} T)^{-1}$ with the Boltzmann constant k_B and the temperature T. In order to calculate the expectation value of a time-dependent operator $\langle \hat{D} \rangle_t$ one also needs to account for a time-dependent density matrix $\rho(t)$. Access to $\rho(t)$ is given by the von-Neumann-equation using a commutator between the total Hamiltonian $\hat{H} = \hat{H}_0 + \hat{W}(t)$ and $\rho(t)$:

$$i\hbar \frac{\partial}{\partial t} \rho(t) = \Big[(\hat{H}_0 + \hat{W}(t)), \rho(t) \Big] \;. \tag{2.120}$$

It is useful to transform equation (2.120) to the interacting picture

$$i\hbar \frac{\partial}{\partial t} \rho(t) = \Big[\hat{W}_I(t)), \rho_I(t) \Big] \;, \tag{2.121}$$

while avoiding $\hat{H}_0$ using the interaction terms $W_I(t)$ and $\rho_I(t)$:

$$W_I(t) = e^{i\hat{H}_0 t/\hbar}\, W(t)\, e^{-i\hat{H}_0 t/\hbar} \qquad \text{and} \qquad \rho_I(t) = e^{i\hat{H}_0 t/\hbar}\, \rho(t)\, e^{-i\hat{H}_0 t/\hbar} \;. \tag{2.122}$$

Integrating over time will lead to an expression for $\rho(t)$ which has to be solved iteratively. For small perturbations it is reasonable to account only for the first order term and neglect higher terms, leading to a linear response approach. Thus, $\rho(t) \approx \rho^{(1)}(t)$

which leads to

$$\rho^{(1)}(t) = \rho_0 - \frac{i}{\hbar}\int_{-\infty}^{t} \mathrm{d}t' \; e^{-i\hat{H}_0 t/\hbar} \; \left[\hat{W}_I(t'), \rho_0\right] \; e^{i\hat{H}_0 t/\hbar} \, . \tag{2.123}$$

This can be used to describe $\langle\hat{D}\rangle_t$, giving the following equations:

$$\begin{aligned} \langle\hat{D}\rangle_t &= \mathrm{Tr}(\rho_0\hat{D}) - \frac{i}{\hbar}\,\mathrm{Tr}\int_{-\infty}^{t} \mathrm{d}t' \; e^{-i\hat{H}_0 t/\hbar} \; \left[\hat{W}_I(t'), \rho_0\right] \; e^{i\hat{H}_0 t/\hbar} \, \hat{D} \, , & (2.124) \\ &= \langle\hat{D}\rangle - \frac{i}{\hbar}\int_{-\infty}^{\infty} \mathrm{d}t' \; \Theta(t-t') \; \langle\left[\hat{D}_I(t), \hat{W}_I(t')\right]\rangle \, . & (2.125) \end{aligned}$$

Here, the step function $\Theta(t-t')$ assures that only perturbations for $t < t'$ are accounted for the system at time t. With (2.125) the central equation of linear response theory was derived, as it allows for calculation of the expectation value of an arbitrary time-dependent operator $\langle\hat{D}\rangle_t$ of the perturbated system using only the commutator of the unperturbated density matrix ρ_0 and the operator for the perturbation $\hat{D}$.

In order to calculate now the response of a solid to an external electric field $\boldsymbol{E}_t$ one has to specify the operators of interest. Consequently, one has $\hat{D} = \hat{\boldsymbol{j}}$ with $\hat{\boldsymbol{j}}$ being the electric current operator as response of the system. The interaction operator $\hat{W}_t$ is defined by the frequency ω dependent electric field $\boldsymbol{E}_t = \boldsymbol{E}_0 e^{-i(\omega+i\delta)t}$ (with $\delta \to 0^+$, meaning for $t \to -\infty$ the system is unperturbed) and the electric dipole moment operator $\hat{\boldsymbol{P}} = \sum_{i=1}^{N} q_i \hat{\boldsymbol{r}}_i$ (with the charge q_i and the position operator $\hat{\boldsymbol{r}}_i$), leading finally to $\hat{W}_t = -\hat{\boldsymbol{P}} \cdot \boldsymbol{E}_t$. Insertion into equation (2.125) leads to

$$\langle\hat{j}_\mu\rangle_t = \frac{i}{\hbar}\sum_\nu \int_{-\infty}^{\infty} \mathrm{d}t' \; \Theta(t-t') \; \langle\left[\hat{j}_{\mu,I}(t), \hat{P}_{\nu,I}(t')\right]\rangle \; E_{0,\nu} e^{-i(\omega+i\delta)t'}, \tag{2.126}$$

while the term $\langle\hat{D}\rangle$ drops out because no current appears in the unperturbated system. Equation (2.126) can be reformulated in terms of

$$\langle\hat{j}_\mu\rangle_t = \frac{i}{\hbar}\sum_\nu \int_{-\infty}^{\infty} \mathrm{d}t'' \; \Theta(-t'') \; \langle\left[\hat{j}_\mu, \hat{P}_{\nu,I}(t'')\right]\rangle \; E_{t,\nu} e^{-i(\omega+i\delta)t''}, \tag{2.127}$$

where now only one operator from the commutator is still time dependent. Combined with the relation $j_\mu = \sigma_{\mu\nu}E_\nu$ one obtains the conductivity tensor:

$$\sigma_{\mu\nu} = \frac{i}{\hbar}\int_{-\infty}^{\infty} \mathrm{d}t \; \Theta(-t) \; \langle\left[\hat{j}_\mu, \hat{P}_{\nu,I}(t)\right]\rangle \; e^{-i(\omega+i\delta)t}. \tag{2.128}$$

Using the Kubo identity for any operator $\hat{A}$ given by

$$\left[\hat{A}(t), \rho\right] = -i\hbar\rho \int_0^{(k_{\mathrm{B}}T)^{-1}} \mathrm{d}\lambda \, \dot{\hat{A}}(t - i\hbar\lambda) \,, \tag{2.129}$$

together with the expression $\dot{\hat{\boldsymbol{P}}} = V\hat{\boldsymbol{j}}$, one can rewrite equation (2.128) to its final form leading to the Kubo equation:

$$\sigma_{\mu\nu} = V \int_0^{(k_{\mathrm{B}}T)^{-1}} \mathrm{d}\lambda \int_0^{\infty} \mathrm{d}t \, \langle \hat{j}_\mu \hat{j}_{I,\mu}(t + i\hbar\lambda) \rangle \, e^{i(\omega + i\delta)t}. \tag{2.130}$$

The Kubo equation demands only the restriction to small perturbations, otherwise it is an exact equation within a full many-body framework. Thus, solving the Kubo equation proves too difficult to be a feasible approach for the moment. Assuming the independent electron approximation and neglecting the dependence on ω the so-called Bastin equation can be derived.[147] Going additionally to the athermal limit of $T = 0$ K one obtains the so-called Kubo-Strěda equation.[148,149] Using the Kubo-Strěda approach the full conductivity tensor $\boldsymbol{\sigma}$ is available with all off-diagonal parts. Considering only the diagonal, symmetric part of $\boldsymbol{\sigma}$ one gets the Kubo-Greenwood equation.[150] For the scope of this thesis, the more complex Bastin and Kubo-Strěda formalism are not treated in detail. Transport properties for the iron pnictides are evaluated for the collinear antiferromagnetic phases only, meaning only the symmetric part of the transport tensor is relevant. Thus, the following will focus directly on the Kubo-Greenwood approach.

2.3.3 Kubo-Greenwood equation

To derive the Kubo-Greenwood equation one can start from the Kubo-Strěda equation for the full conductivity tensor as given by

$$\begin{aligned} \sigma_{\mu\nu} = & \frac{\hbar}{4\pi V} \mathrm{Tr} \langle \hat{j}_\mu (G^+ - G^-) \hat{j}_\nu G^- - \hat{j}_\mu G^+ \hat{j}_\nu (G^+ - G^-) \rangle_c \\ & + \frac{e}{4\pi i V} \mathrm{Tr} \langle (G^+ - G^-)(\hat{r}_\mu \hat{j}_\nu - \hat{r}_\nu \hat{j}_\mu) \rangle_c \,. \end{aligned} \tag{2.131}$$

Here, $\langle \; \rangle_c$ indicates a configurational average with respect to an alloy, with G^+ and G^- are the retarded and advanced Green function with respect to equation (2.4). All energy dependent Green functions are evaluated at the Fermi energy E_F. Using the relations $(G^+ - G^-) = 2i\mathrm{Im}\, G^+$, $G^+ = \mathrm{Re}\, G^+ + i\mathrm{Im}\, G^+$ and $G^- = \mathrm{Re}\, G^+ - i\mathrm{Im}\, G^+$

the Kubo-Středa equation (2.131) is reformulated to the following expressions:

$$\begin{aligned}
\sigma_{\mu\nu} &= \frac{i\hbar}{2\pi V}\,\mathrm{Tr}\langle \hat{j}_\mu \mathrm{Im}\,G^+ \hat{j}_\nu (\mathrm{Re}\,G^+ - i\mathrm{Im}\,G^+) - \hat{j}_\mu(\mathrm{Re}\,G^+ + i\mathrm{Im}\,G^+)\hat{j}_\nu \mathrm{Im}\,G^+\rangle_c \\
&\quad + \frac{e}{2\pi V}\,\mathrm{Tr}\langle \mathrm{Im}\,G^+(\hat{r}_\mu \hat{j}_\nu - \hat{r}_\nu \hat{j}_\mu)\rangle_c\,, \qquad (2.132)\\
&= \underbrace{\frac{i\hbar}{2\pi V}\,\mathrm{Tr}\langle [\hat{j}_\mu \mathrm{Im}\,G^+ \hat{j}_\nu - \hat{j}_\nu \mathrm{Im}\,G^+ \hat{j}_\mu]\mathrm{Re}\,G^+\rangle_c}_{\sigma^A_{\mu\nu}} \\
&\quad + \underbrace{\frac{\hbar}{\pi V}\,\mathrm{Tr}\langle \hat{j}_\mu \mathrm{Im}\,G^+ \hat{j}_\nu \mathrm{Im}\,G^+\rangle_c}_{\sigma^B_{\mu\nu}} \\
&\quad + \underbrace{\frac{e}{2\pi V}\,\mathrm{Tr}\langle \mathrm{Im}\,G^+(\hat{r}_\mu \hat{j}_\nu - \hat{r}_\nu \hat{j}_\mu)\rangle_c}_{\sigma^C_{\mu\nu}}\,, \qquad (2.133)\\
&= \sigma^A_{\mu\nu} + \sigma^B_{\mu\nu} + \sigma^C_{\mu\nu}\,. \qquad (2.134)
\end{aligned}$$

These three terms of the Kubo-Středa equation fulfill equation (2.135):

$$\sigma^A_{\mu\nu} = -\sigma^A_{\nu\mu} \quad \text{and} \quad \sigma^B_{\mu\nu} = \sigma^B_{\nu\mu} \quad \text{and} \quad \sigma^C_{\mu\nu} = -\sigma^C_{\nu\mu}\,. \qquad (2.135)$$

Thus, it is obvious that only $\sigma^B_{\mu\nu}$ contributes to the diagonal part of the conductivity tensor $\boldsymbol{\sigma}$. Consequently, the final Kubo-Greenwood equation[150] for the symmetric part of the conductivity tensor is given by

$$\sigma_{\mu\mu} = \frac{\hbar}{\pi V}\,\mathrm{Tr}\langle \hat{j}_\mu \mathrm{Im}\,G^+ \hat{j}_\mu \mathrm{Im}\,G^+\rangle_c\,. \qquad (2.136)$$

Chapter 3

High-temperature iron pnictide superconductors

It started in 2008 with the discovery of unconventional high-temperature superconductivity up to 26 K in fluorine doped LaOFeAs as discovered by Kamihara *et al.*[10,11]. In the following years a large variety of different superconducting iron based compounds were found which all share common structural motifs. Today, the iron pnictides and the iron chalcogenides are separated into several subgroups although the underlying physics seem similar in most cases.[151,152]

Antiferromagnetic order and spin fluctuations play a significant role for the emergence of superconductivity which is nowadays discussed in terms of a $s^{\pm}$ pairing state.[19,153] The Fermi surface as seen in ARPES measurements is quite complex and shows clear indications for good nesting between hole and electron pockets.[31,33] Most compounds undergo a phase transition from a tetragonal to a low temperature orthorhombic phase, typically accompanied by the formation of long-range antiferromagnetic order. In this context strong in-plane anisotropy is reported, often discussed in relation to a nematic order.[39,154,155] Concerning electronic properties, strong many-body correlations seem of importance for some systems.[54,55]

Overall, the iron pnictides are a highly complex family of materials which are still today far from fully understood. Thus, this chapter will give a brief overview concerning the iron-based superconductors. It will deal with the different subgroups and common physical and chemical properties that all iron pnictides share. Additionally, the so-called 122-compounds which are relevant for this work will be discussed in more detail.

3.1 Classification of iron pnictides

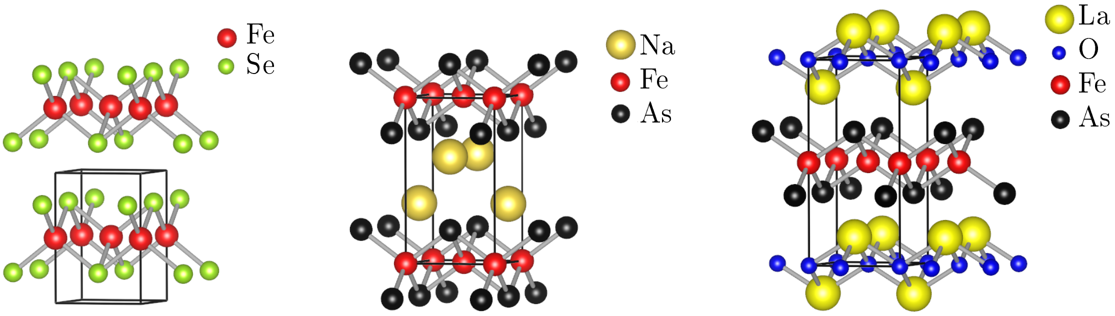

FeSe
11-compound

NaFeAs
111-compound

LaOFeAs
1111-compound

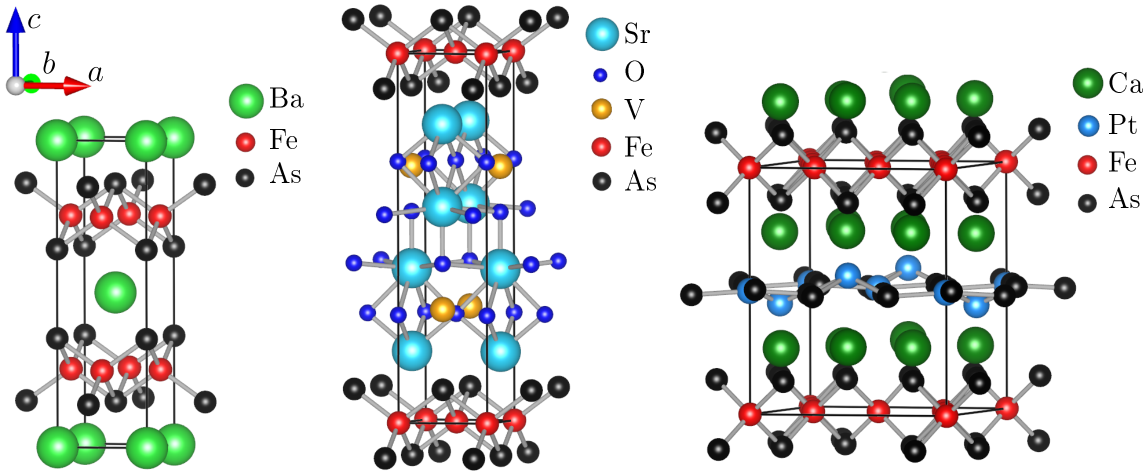

$BaFe_2As_2$
122-compound

Sr_2VO_3FeAs
21311-compound

$(CaFeAs)_{10}Pt_4As_8$
α-1048-compound

Figure 3.1. Crystal structures of the most important iron pnictide/chalcogenide based compounds. The FeAs/FeSe-tetrahedron layer represents the common structural motif.

Structural motif

The large family of iron based superconductors known so far is separated into several subgroups according to the stoichiometry of the respective mother-compound. An overview of the different crystal structures for the most relevant iron based compounds is given in Fig. 3.1. The structure types can be formally deduced from the *anti*-PbO[156], *anti*-PbFCl[157], $ThCr_2Si_2$[158] and ZrCuSiAs[159] structures. The simplest of these subgroups are the 11-compounds which are strictly spoken not based on an iron pnictide but an iron chalcogenide, namely FeSe.[160] There are also the 111-compounds AFeAs[161] (A = Li, Na) and the 1111-compounds LOFeAs[10,11,162–167] (L = La, Ce, Pr, Nd, Sm, Gd, Dy) which were discovered first. The focus of this thesis is on

$BaFe_2As_2$ which is the prototype of the 122-compounds $(A/E)Fe_2As_2$[23,168,169] (A = Na, K, Rb, Cs; E = Ca, Sr, Ba). Notable are also the complex 21311-compounds E_2MO_3FeAs[170–172] (E = Sr, Ba; M = Sc, V, Cr). Since 2011 the new 1038 and 1048 iron pnictides are known, namely $(CaFeAs)_{10}Pt_3As_8$ and $(CaFeAs)_{10}Pt_4As_8$.[173–175] They posses quite complex structures with several different phases and can have critical temperatures up to a maximum of 35 K.[176,177] In 2014 the $[(Li_{1-x}Fe_x)OH](Fe_{1-y}Li_y)Se$ system was discovered, which notably shows the coexistence of superconductivity and $3d$-ferromagnetism.[178]

All different iron based compounds have one structural motif in common, namely the very characteristic assembly of the iron pnictide/chalcogenide layer. This layer consists of e.g. edge-sharing $FeAs_{4/4}$ tetrahedrons and has formally a negative charge. It is generally believed that these highly functional FeAs layers, which are separated by arbitrary cations or cationic layers, are mainly responsible for the occurrence of superconductivity. Furthermore, it should be mentioned that the respective mother compounds, with very little exceptions, normally show no superconductivity. Only after a reasonable substitution of elements or after a geometrical distortion, for example induced by pressure, superconductivity can occur. One distinguishes indirect doping[179,180], meaning the substitution on an arbitrary site outside the FeAs layer and direct doping[181], meaning substitution within the FeAs layer itself. For both types of substitution charge doping in terms of hole- or electron-doping is possible and normally both can lead to superconductivity.[23,27] There are also cases in which isovalent doping can lead to the occurrence of superconductivity.[28,30,182,183]

Phase transitions

The phase diagrams of all iron pnictide superconductors show similar behavior and properties with increasing dopant concentration x. In Fig. 3.2 the phase diagrams for (A) $CeO_{1-x}F_xFeAs$ and (B) $Ba(Fe_{1-x}Co_x)_2As_2$ are shown as generic examples. Generally, the undoped mother compounds at room-temperature are Pauli-paramagnets. Thus, the white regions of the phase diagram can be fairly well approximated as a paramagnetic state, although the phase diagrams here shown are simplified, not accounting for spin-fluctuations and possible anomalies.[185] By cooling the undoped compound, one arrives at a structural phase transition at T_{s}, typically from a tetragonal to an orthorhombic symmetry. This is connected to the occurrence of long-range antiferromagnetic (AFM) order at T_{N}, which can be described in terms of a commensurate spin-density wave (SDW) state. These two features are found always separated from

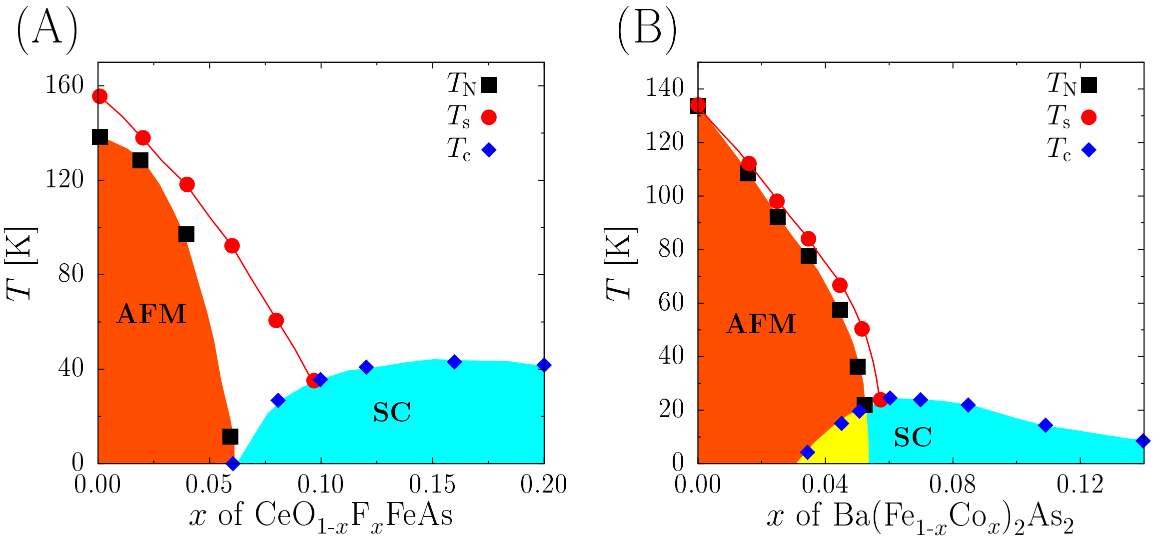

Figure 3.2. Schematic phase diagram of (A) $CeO_{1-x}F_xFeAs$ and (B) $Ba(Fe_{1-x}Co_x)_2As_2$. The phase region of long-range antiferromagnetic order is marked in orange, while the superconducting region is marked on cyan. In (B) one has also a coexistence region marked in yellow. The data is reproduced from the work of Zhao *et al.*[162] and Lester *et al.*[184].

each other.[186] However, for the 1111-compounds (Fig. 3.2 (A)) there is a clear separation with a $P4/nmm$ to $Cmma$ phase transition at $T_s \approx 155$ K and a magnetic ordering at lower temperature of $T_N \approx 140$ K, while for the undoped 122-compound (Fig. 3.2 (B)) the structural phase transition from $I4/mmm$ to $Fmmm$ and the commensurate SDW ordering appear close together at a temperature $T_s \approx T_N \approx 135$ K.[22,187]

When the dopant concentration x increases, the structural phase transition and the antiferromagnetic ordering do progressively take place at lower temperatures until they are completely suppressed when a critical concentration x_{crit} is reached. At the vicinity of the magnetic long-range order breakdown, a commensurate to incommensurate transition for the SDW state is principally possible, but typically only for a very narrow region of the phase diagram.[26] This suppression of both, the ordered SDW state and the structural phase transition at low temperatures, does obviously correlate with the occurrence of superconductivity. In this context one should note a coexistence region between superconductivity and antiferromagnetic order in the phase diagram of Fig. 3.2 (B) marked in yellow, that is controversially discussed in the literature. This coexistence is known for several iron pnictides leading to the suggestion that the full suppression of long-range magnetic order is not a mandatory requirement for the occurrence of superconductivity. On the other hand, a phase separation in the nanometer range into a non-magnetic superconducting and an antiferromagnetic non-superconducting phase was proposed.[188] However this was proven wrong for the

K-doped 122-compound.[189] Thus, nowadays the common opinion favors rather the assumption of a coexistence between superconductivity and magnetism.[187,189,190]

In-plane anisotropy

The phase transitions common for all iron pnictides described in the latter subsection have some important physical consequences as they result in a symmetry breaking of the C_4 rotational symmetry leading to a C_2 symmetry. Thus, one can expect an in-plane anisotropy for the electronic structure and all related physical properties. In experiment this in-plane anisotropy was not properly observed for a long time due to the fact that the structural phase transition in the iron pnictides is typically accompanied by a significant twinning of the single crystals which leads to an averaging of anisotropic effects.[191] However, it was possible to cancel out the effects of twinning by using a device to apply uniaxial stress during the measurement, leading to detwinned data showing strong in-plane anisotropy in e.g. electrical transport and ARPES spectra.[36,38,39,192,193] In fact, this anisotropy is considerably stronger than what could be expected only from the structural anisotropy between the a and b axes, which is rather small. Consequently, the magnetic anisotropy of the antiferromagnetic state should be of most relevance concerning the question of in-plane anisotropy in the iron pnictides.

Furthermore, there is a region for $T_\mathrm{N} < T < T_\mathrm{s}$ called nematic phase, showing also strong electronic anisotropy specified as nemanticity.[194] This anisotropy is discussed in terms of spin fluctuations and nematic symmetry breaking, possibly induced by anisotropic impurity states as seen in scanning tunneling microscopy.[40,41,43,154,155,195,196]

Spin-density waves

The magnetic order in the iron pnictides can be described by a so-called spin-density wave (SDW), which was first proposed by Overhauser and Arrott in 1959.[197] It is described as an instability in the non-interacting electron gas, which can lead to the formation of a broken-symmetry ground state. In order to evaluate the properties of a SDW state, consider the enhanced magnetic susceptibility $\chi(\boldsymbol{q})$:[198]

$$\chi(\boldsymbol{q}) = \frac{\chi_0(\boldsymbol{q})}{1 - I\chi_0(\boldsymbol{q}))}\ , \tag{3.1}$$

with χ_0 as so-called unenhanced susceptibility which is calculated in the absence of any enhancing exchange-correlation effects and a corresponding exchange-correlation integral I. For a paramagnetic ground state $\chi(\boldsymbol{q})$ is positive and finite for any $\boldsymbol{Q}$.

Obviously, $\chi(\boldsymbol{q})$ diverges for $I\chi_0(\boldsymbol{q}) = 1$. Such a singular behavior indicates an instability of the paramagnetic state towards the spontaneous formation of a state with spin order. Thus, a sufficiently strong exchange-correlation interaction I together with a large $\chi_0(\boldsymbol{q})$ are the requirements for a SDW to emerge. These preconditions are easily fulfilled for a one-dimensional system, in which the susceptibility diverges for $\boldsymbol{Q} = 2k_\mathrm{F}$ with k_F as Fermi wave vector. It should be noted that this corresponds to the perfect nesting condition $\epsilon_{\boldsymbol{k}+\boldsymbol{Q}_i} = \epsilon_{\boldsymbol{k}}$.

For $\boldsymbol{Q} = \boldsymbol{0}$ the enhanced susceptibility from equation (3.1) recovers the Stoner criterion for ferromagnetism.[199] Thus, for such $\boldsymbol{q}$-vectors an instability towards a ferromagnetic ground state is expected. If $\boldsymbol{Q}$ is commensurate with any reciprocal lattice vector an antiferromagnetic ground state will be realized, while different high symmetric points of the Brillouin zone represent different antiferromagnetic configurations. Divergence of $\chi(\boldsymbol{q})$ for a $\boldsymbol{Q}$ incommensurate with the reciprocal lattice would imply a transition to a state of non-commensurate magnetization. Such a ground state has a spatial spin density modulation, meaning there is a difference between the density for electrons with spins polarized upwards ($\rho_\uparrow(x) \equiv \rho_+(x)$) and the density for electrons with spins polarized downwards ($\rho_\downarrow(x) \equiv \rho_-(x)$). This difference is finite and modulated in space as a function of the position, thus, the SDW has electron densities for both spin-channels $\rho_\pm(x)$ which are out of phase by π:[198]

$$\rho_\pm(x) = \frac{1}{2}\rho_0 \left[1 \pm \rho_1 \cos \boldsymbol{Q}x\right] \ . \tag{3.2}$$

The total charge ρ_0 of a SDW is always constant and independent of the position x. Consequently, the SDW ground state for an incommensurate $\boldsymbol{Q}$ with a long period in the order of several lattice parameters can be accompanied with a spiral-like rotation of neighboring spins, also incommensurate with the lattice. An important example is the antiferromagnetism in chromium, which was identified to be a static kind of SDW resulting from Fermi surface nesting mechanism.[200,201]

Analogously, the long-range antiferromagnetic order of the iron pnictides has its origin in a commensurate SDW state with e.g. for $\mathrm{BaFe_2As_2}$ a vector $\boldsymbol{Q}_\mathrm{AFM} = (1, 0, 1)$, corresponding to antiferromagnetic coupling along the a and c axes. For Co doping also incommensurate SDW states can be realized with the propagation vector $\boldsymbol{\tau} = \boldsymbol{Q}_\mathrm{AFM} + (0, \epsilon, 0) = (1, \epsilon, 1)$ for a small incommensurability $\epsilon \approx 0.02 - 0.03$.[26]

3.2 The subgroup of the 122-compounds

3.2.1 The $BaFe_2As_2$ mother compound

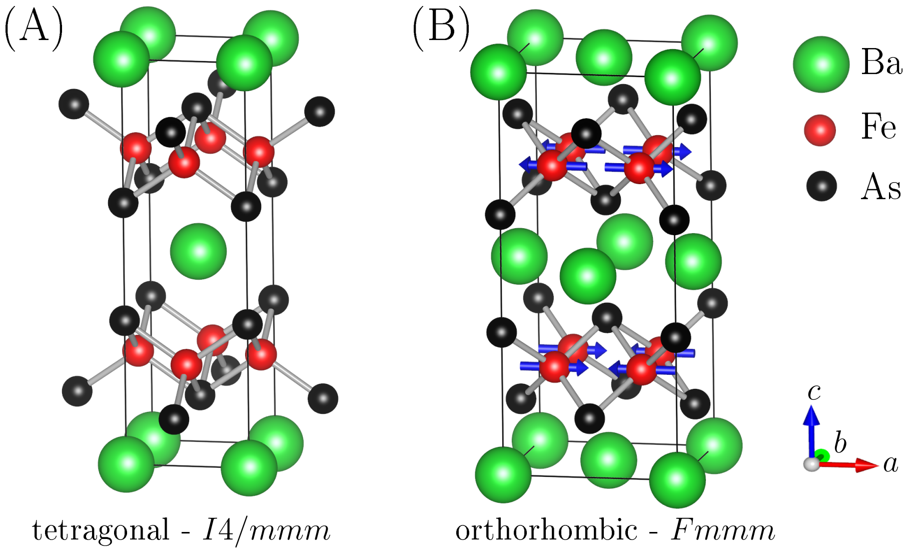

Figure 3.3. Crystal structures of the Ba-122 mother compound $BaFe_2As_2$ in (A) its room-temperature tetragonal phase and in (B) its low-temperature, antiferromagnetic orthorhombic phase. The blue arrows represent ordered magnetic moments.

For the Ba-122 mother compound $BaFe_2As_2$ two crystal structures are of importance. Fig. 3.3 (A) shows the paramagnetic tetragonal phase at room-temperature, while Fig. 3.3 (B) gives the orthorhombic low-temperature antiferromagnetic phase. The transition between both is actually split into two processes (see also the phase diagram already shown in Fig. 3.2 (B)). First, a from tetragonal $I4/mmm$ to orthorhombic $Fmmm$ second-order phase transition occurs at $T_s = 134.5$ K.[186] This can be structurally described by a 45° rotation of the unit cell in the ab plane. Compared with the tetragonal phase, the a axis is marginally stretched in the orthorhombic structure, whereas the now shorter b axis is clinched. The structural transition is followed by a first-order antiferromagnetic transition at $T_N = 133.75$ K.[186] These two phase transitions evolve for increasing substitution (e.g. with Co or Rh) into two clearly split second-order transitions.[186]

Consequently, only the orthorhombic phase can exhibit a commensurate SDW state, corresponding to an antiferromagnetic order with all spins rotated in-plane and aligned parallel to the a axis. The orientation of spins is well examined by several groups using neutron diffraction, ^{57}Fe Mössbauer spectroscopy or Muon spin relaxation (μSR) experiments.[22,24,25,45,202,203] The coupling is antiferromagnetic along the longer a axis and the c axis and ferromagnetic along the b axis. Although there is no question about the spin orientation, the magnetic moments for Fe were reported differently depending on the used analytical method. For neutron diffraction so far 0.99 μ_B[25] are reported for $BaFe_2As_2$ single crystals grown in Sn flux and 0.87 μ_B[24] were measured with powder probes. However, one should note that crystals grown in a Sn flux are known to incorporate Sn into the crystal.[204,205] Using ^{57}Fe Mössbauer spectroscopy the hyperfine field was determined to have a saturation value of 5.47 T at 4.2 K, which was used to estimate the magnetic moment to be between 0.4 μ_B and 0.5 μ_B.[22,45] Muon spin relaxation spectroscopy shows in principle results similar to the Mössbauer spectroscopy with estimated moments around 0.5 μ_B.[202,203] The issue of magnetic moments derived from Mössbauer spectroscopy will be also discussed in Chapter 8 of this thesis.

In addition to the $BaFe_2As_2$ prototype also the other 122-compounds $SrFe_2As_2$ and $CaFe_2As_2$ are known. However, the Sr-122 and Ca-122 compounds are quite similar in their physical and chemical behavior to the Ba-122 compound which was most extensively studied among the 122-compounds.[23,206–210] One should mention the existence of a high pressure collapsed tetragonal phase for $CaFe_2As_2$[211–213], although for the scope of this work this phenomenon is of minor interest.

3.2.2 Substituted $BaFe_2As_2$ superconductors

$Ba_{1-x}K_xFe_2As_2$

Superconductivity within the 122-compounds was first discovered in potassium doped $Ba_{1-x}K_xFe_2As_2$[22,23,214] which up to now has still the highest critical temperature with $T_c = 38$ K. In this hole doped compound superconductivity first occurs for $x \approx 0.1$ and persists over the whole doping regime up to KFe_2As_2. The long-range antiferromagnetic order finally breaks down for $x_{crit} \approx 0.25$, thus a real coexistence between superconductivity and antiferromagnetism has been observed.[189]

This compound is also known for its especially complex ARPES spectra which were extensively studied in literature and which cannot be explained using DFT-based electronic band structure calculations.[33,215–221] The in-plane resistivity anisotropy reported of this compound is rather small and may even show sign changes.[43,222]

$\mathbf{Ba(Fe_{1-x}Co_x)_2As_2}$

Soon after the discovery of superconductivity in hole doped $BaFe_2As_2$ the first electron doped Ba-122 superconductor using Co doping was reported with a T_c up to 22 K.[27] Nowadays, $Ba(Fe_{1-x}Co_x)_2As_2$ is still the prototype for electron doping induced superconductivity in the 122 subgroup and it was also extensively studied.[184,223–225] The respective phase diagram was shown in Fig. 3.2 (B). Superconductivity emerges first for $x \approx 0.04$, while the antiferromagnetic order persists up to $x_{\mathrm{crit}} \approx 0.07$. Superconductivity again vanishes in the over doped regime corresponding to $x > 0.2$.

Strong in-plane anisotropy in electric transport was first discovered for the Co doped $BaFe_2As_2$ compound after detwinning of the crystals.[39] Thus, the system is also one of the most famous prototypes with respect to unusual strong in-plane anisotropy, not only seen in transport measurements[42,222,226,227] but also seen in ARPES spectra.[36]

$\mathbf{Ba(Fe_{1-x}\boldsymbol{TM}_x)_2As_2}$ with $\boldsymbol{TM}$ = Ni, Rh, Pd

Similar to the Co doped compound superconductivity is also found in Ni substituted $Ba(Fe_{1-x}Ni_x)_2As_2$ with a maximum $T_c \approx 20$ K.[29,228] Assuming TM^{2+} ions Co will formally donate one electron to the FeAs layer, while Ni gives two electrons. Thus, the occurrence of superconductivity and the suppression of long-range antiferromagnetic order happens in $Ba(Fe_{1-x}Ni_x)_2As_2$ for lower doping ratios x compared to the Co compound. However, the critical temperature in $Ba(Fe_{1-x}Ni_x)_2As_2$ and the size of the superconducting dome are reduced. $Ba(Fe_{1-x}Ni_x)_2As_2$ has its maximum in T_c for $x \approx 0.04$ but the superconducting behavior vanishes already for $x > 0.08$.[228]

Apart from the 3*d* elements Co and Ni the corresponding 4*d* elements Rh and Pd are known to induce superconductivity in $Ba(Fe_{1-x}Rh_x)_2As_2$ and $Ba(Fe_{1-x}Pd_x)_2As_2$.[229] The phase diagrams of the Rh and Pd compounds are in principle completely analogous to those of the 3*d* Co and Ni systems with maximal critical temperatures of $T_c \approx 24$ K and $T_c \approx 19$ K for the Rh and Pd superconductors respectively.

Non-superconducting $\mathbf{Ba(Fe_{1-x}\boldsymbol{TM}_x)_2As_2}$ with $\boldsymbol{TM}$ = Cu, Mn

Continuing the electron doping 3*d* row from Co to Ni one advances further to Cu. Yet, the trend of smaller superconducting domes and lower critical temperatures also continues as it is very difficult to prove superconductivity in $Ba(Fe_{1-x}Cu_x)_2As_2$. There are reports of only one superconducting sample around $x \approx 0.04$ with a $T_c \approx 2$ K.[230] As it was not reproduced one counts $Ba(Fe_{1-x}Cu_x)_2As_2$ today rather as a non-superconducting example where the excessive electron doping suppresses the superconductivity before it can really emerge.[228,230–232]

Trying to directly hole dope $BaFe_2As_2$ leads to $Ba(Fe_{1-x}Mn_x)_2As_2$ which is also non-superconducting. This compound is however unique among the iron pnictides as the antiferromagnetic order persists after the orthorhombic to tetragonal phase transition. It seems that a complicated competition between different antiferromagnetic states allows for the persisting magnetic order and thus for a suppression of superconductivity.[232–234]

$BaFe_2(As_{1-x}P_x)_2$

It was rather unexpected to find evidence for suppressed magnetic order and superconductivity in isovalent doped iron pnictides, thus the P doped $BaFe_2(As_{1-x}P_x)_2$ was one of the first ones.[30,182] Superconductivity emerges from $x > 0.2$ on until it vanishes again for $x > 0.7$. The maximal critical temperature of $T_c \approx 30$ K is rather high, however, the mechanism for superconductivity seems to be not fundamentally different from charge doped iron pnictides.

$Ba(Fe_{1-x}Ru_x)_2As_2$

Another example of superconductivity induced by isovalent doping is $Ba(Fe_{1-x}Ru_x)_2As_2$ with a maximum in the critical temperature of $T_c \approx 17$ K for $x \approx 0.3$.[28,183] The phase diagram is similar to that of the other iron pnictides, the antiferromagnetic order is suppressed at $x_{crit} \approx 0.3$ and superconductivity emerges from $x \approx 0.2$ on until it vanishes for $x \approx 0.6$. From the theoretical point of view it has an advantage over the P doped $BaFe_2(As_{1-x}P_x)_2$ compound, because the substitution takes place on the Fe sites. This makes $Ba(Fe_{1-x}Ru_x)_2As_2$ more closely related to the $Ba(Fe_{1-x}Co_x)_2As_2$ system and thus comparisons between both more promising.[51]

There exist also several detailed ARPES studies on this system which support the assumption of a more or less isoelectronic character of the electronic structure and the Fermi surface.[37,235]

Chapter 4

The antiferromagnetic ground state

4.1 Motivation

The motivation for this thesis was based on own preliminary work on the iron pnictides, first experimental one on 1038 systems[176,177] and subsequent theoretical investigations starting with a lab report followed by a Master's thesis[236] on $Ba(Fe_{1-x}Co_x)_2As_2$.

At the beginning, the focus was on the question whether the substitution of Co into $BaFe_2As_2$ in terms of $Ba(Fe_{1-x}Co_x)_2As_2$ really leads to electron doping. At this time, there was work stating that the injected electron of Co is rather localized at the Co atoms due to charge localization and thus cannot lead to real electron doping of the whole system.[237–239] This was in contradiction with DOS calculations showing the expected broadening of states at the Fermi level, for the Fe d-states as well as for the Co d-states. The question was soon sufficiently answered e.g. by Berlijn *et al.*[49] who argued that none of the above pictures is individually sufficient to answer the issue of localization. They used a sophisticated supercell approach with an average over 10 randomly-shaped supercells containing 400 atoms each in order to treat nonmagnetic $Ba(Fe_{0.875}Co_{0.125})_2As_2$. Their results clearly showed that there is no support for a localization of the injected Co d-electron, thus, one can speak of electron doping. In order to understand the results, they emphasized the substantial importance of disorder effects which have been treated by their elaborate supercell approach.

However, the CPA was at this time practically not known to the community working on iron pnictides. At that time Khan *et al.*[52,240] were the first to present CPA calculations on the iron pnictides, however, the important advantages of this approach were not sufficiently clarified. In particular, the CPA allows for an investigation of almost arbitrary dopant concentrations x, which is from practical reasons not possible for a supercell approach. Even more important, the computational effort of a credible supercell calculations is by orders of magnitude higher compared to the CPA. In particular, an average over 4000 atoms was used by Berlijn *et al.*[49] to calculate nonmagnetic $\mathrm{Ba(Fe_{0.875}Co_{0.125})_2As_2}$, while a similar result can be obtained from the CPA using only 1 cell with no more than 5 atoms. Note, that the disorder effects discussed by Berlijn *et al.*[49] can be fully reproduced by the CPA.

The idea was to target a more complex situation with the CPA, which implies a higher computational effort and thus limits the applicability of the supercell approach. Most theoretical investigations at this time were performed on the nonmagnetic, tetragonal phase, however, only little work considered the full antiferromagnetic, orthorhombic phase. There are two apparent reasons which make the antiferromagnetic case more complicated. First going from a 2-Fe unit cell to a 4-Fe cell in order to correctly account for the magnetic order doubles the size of the unit cell and significantly increases the computational effort. Secondly, DFT seemed to have problems in describing the magnetic properties of the iron pnictides correctly.[16,18,19] In this context one has to mention that the magnitude of the magnetic moment was typically overestimated by DFT.[16,124,241–243] To describe the magnetic properties of the iron pnictides was thus a challenging issue and it seemed even more beneficial if one was able to equally account for the disorder introduced through substitution in doped compounds.

Thus, the antiferromagnetic, orthorhombic phase of $\mathrm{Ba(Fe_{1-x}Co_x)_2As_2}$ was studied by means of the KKR-CPA in order to prove its applicability to this complex iron pnictide prototype compound as a prove of principle for all subsequent work. In particular, not only the magnetic moments and the electronic band structure can be investigated, but also the magnetic exchange coupling constants J_{ij} can be calculated and applied for subsequent Monte Carlo simulations.

4.2 Publication: Physical Review B 90, 184509

Theoretical investigation of the electronic and magnetic properties of the orthorhombic phase of $Ba(Fe_{1-x}Co_x)_2As_2$

Gerald Derondeau,[1] Svitlana Polesya,[1] Sergiy Mankovsky,[1] Hubert Ebert,[1] and Ján Minár[1,2]

[1]*Department Chemie, Physikalische Chemie, Universität München, München, Germany*
[2]*NewTechnologies-Research Center, University of West Bohemia, Pilsen, Czech Republic*

published in: Physical Review B **90**, 184509 (2014).

PHYSICAL REVIEW B **90**, 184509 (2014)

Theoretical investigation of the electronic and magnetic properties of the orthorhombic phase of Ba(Fe$_{1-x}$Co$_x$)$_2$As$_2$

Gerald Derondeau,[1,*] Svitlana Polesya,[1] Sergiy Mankovsky,[1] Hubert Ebert,[1] and Ján Minár[1,2]
[1]*Department Chemie, Physikalische Chemie, Universität München, Butenandtstr. 5-13, 81377 München, Germany*
[2]*NewTechnologies-Research Center, University of West Bohemia, Pilsen, Czech Republic*

(Received 12 September 2014; revised manuscript received 27 October 2014; published 12 November 2014)

We present a comprehensive study on the low-temperature orthorhombic phase of Ba(Fe$_{1-x}$Co$_x$)$_2$As$_2$ based on the Korringa-Kohn-Rostoker-Green function approach. Using this band-structure method in combination with the coherent potential approximation alloy theory we are able to investigate the evolution of the magnetic and electronic properties of this prototype iron pnictide for arbitrary concentrations x, while dealing with the chemical disorder without uncontrolled simplifications by using solely a rigid-band shift or the virtual crystal approximation. We discuss the development of the site-resolved magnetic moments for the experimentally observed stripe antiferromagnetic order together with the strong electronic anisotropy of the Fermi surface and compare it with angle-resolved photoemission spectroscopy measurements of detwinned crystals. We furthermore calculate magnetic exchange coupling parameters J_{ij} and use them for Monte Carlo simulations on the basis of the classical Heisenberg model to get an insight on the temperature dependence of the magnetic ordering on the cobalt concentration.

DOI: 10.1103/PhysRevB.90.184509 PACS number(s): 74.20.Pq, 74.62.En, 74.70.Xa

I. INTRODUCTION

Over the last few years, the iron pnictides received tremendous interest, following the discovery of high-temperature superconductivity in La(O$_{1-x}$F$_x$)FeAs [1,2]. Its mechanism of superconductivity is generally considered to be unconventional and it is most likely connected to magnetic fluctuations [3–5]. This makes the magnetic behavior of the iron pnictides crucial to understand their underlying physics and superconductivity. However, this question turned out to be far from trivial [6,7]. The complex magnetism of these compounds allows no straightforward description concerning several aspects which results in the fact that even today the iron pnictides are far from fully understood.

To name a few examples, there was considerable discussion whether the magnetic moments are better described by an itinerant [4,6,8–10] or a localized [11–13] model, there is still no consensus over the strength of correlation effects [14,15] and finally the magnitude of the magnetic moments is highly sensible on the system and computational parameters, which leads to several seemingly quite different reports in literature [7,16–19]. Experimental neutron diffraction data predict for the low-temperature phase of BaFe$_2$As$_2$ magnetic moments around 0.9μ_B per Fe atom (0.99μ_B in Sn flux [16], 0.87μ_B for powder probes [20]), while from ^{57}Fe Mössbauer spectroscopy [17,21] and μSR spectroscopy [22,23] consistently a value of around 0.5μ_B is estimated. However, in density functional theory (DFT) calculations, the magnitude of the magnetic moments is considerably overestimated, ranging from approximately 1.2μ_B up to 2.6μ_B [7,8,24–26]. Furthermore, it is well known that the magnetic moment depends surprisingly strong on the free structural parameter z of the As position, introducing another degree of freedom which makes reliable predictions even more difficult [7,11,27].

It is believed that the commensurate magnetic spin-density-wave (SDW) state and the superconducting state compete with each other, implying that the suppression of the long-range magnetic order is coupled to the emergence of superconductivity [3,21,28]. Consequently, the understanding of the magnetic state is crucial to understand the superconducting behavior of these compounds.

In this paper, we address the magnetic state of the undoped mother compound BaFe$_2$As$_2$ and focus on the impact of chemical disorder effects induced by substitution of Fe by Co. Most theoretical studies on the doping dependence of iron pnictides are based on a virtual crystal approximation (VCA) which introduces an averaged atomic charge Z for atomic sites with chemical disorder [3,24,29]. Using the VCA one should keep in mind that site-resolved information is lost and disorder is not properly described. Recent publications stressed that it is not sufficient for the iron pnictides to neglect these more complex disorder effects and proved the necessity of more sophisticated approaches [30,31]. As an example, impurity scattering is discussed to be the crucial aspect for the newly discovered in-plane resistivity anomaly in Ba(Fe$_{1-x}$Co$_x$)$_2$As$_2$ which shows the pressing need to account for disorder effects in an appropriate way within a theoretical description [32–34].

It is very difficult for wave-function-based methods to achieve a reasonable inclusion of disorder effects, the most common way is to use supercells [30,35]. The major disadvantage of such an approach is the high computational effort which limits its possible applications. Using a Korringa-Kohn-Rostoker-Green function (KKR-GF) based method the coherent potential approximation (CPA) is a more straightforward way to account for disorder compared to a supercell calculation but with considerably less computational effort needed. Up to now, investigations of the iron pnictides using the CPA are extremely rare and recent in literature but nevertheless very promising [36,37]. In this paper, we will exploit the significant advantages of the CPA method to deal with the substitution induced disorder in iron pnictides to achieve an improved

---

[*] gerald.derondeau@cup.uni-muenchen.de

theoretical description for the doping-dependent evolution of these compounds.

II. COMPUTATIONAL APPROACH

All calculations have been performed self-consistently and fully relativistically within the four component Dirac formalism, using the MUNICH SPR-KKR program package [38]. We used always the local density approximation (LDA) exchange-correlation potential with the parametrization given by Vosko, Wilk, and Nusair [39]. The structural setup was based on an orthorhombic unit cell of $BaFe_2As_2$ with four Fe atoms per cell (4-Fe unit cell) in order to account for the experimentally observed stripe antiferromagnetic spin state with antiferromagnetic coupling along a and c and ferromagnetic chains along b [see Fig. 1(a)]. With spin-orbit coupling included by the four-component Dirac formalism, the self-consistent field (SCF) calculations considered an orientation of the magnetic moments along the a axis, consistently with experiment [16]. We used a dense $\boldsymbol{k}$ mesh of $20 \times 18 \times 20$ points and considered for s, p, and d orbitals as basis. As spherical approximation we used a so-called full-charge ansatz which uses Voronoi polyeder as within the full-potential scheme. Although all aspherical parts of the charge density are fully accounted for, the aspherical parts of the potential are neglected in a full-charge ansatz. We confirmed that the electronic structure in a full-charge calculation is comparable to the results from a real full-potential calculation but is achievable with strongly reduced computational effort. The exchange coupling constants J_{ij} were calculated using the Lichtenstein formula [40–42]. The definition of the various J_{ij} Fe-Fe coupling parameters between Fe atoms is shown in Fig. 1(b). The treatment of disorder introduced through Co substitution is fully dealt with on a CPA level.

Within this work, we used the experimental lattice parameters and the experimental As position z of $BaFe_2As_2$ [17]. However, in case of a large concentration regime ($0 \leqslant x_{\mathrm{Co}} \leqslant 0.25$) it is reasonable to consider structural relaxation as well. Because there is no complete experimental data set for the whole substitutional range, we used a linear interpolation based on available experimental data and Vegard's law which is commonly used for alloys [43]. Thus, we used the experimentally observed lattice constants from Sefat *et al.* [44] for $BaFe_2As_2$ and $Ba(Fe_{0.9}Co_{0.1})_2As_2$ and extrapolated linearly on this basis the change in the crystallographic c parameter under Co substitution in the orthorhombic phase. The lattice constants a and b were not changed for the calculations because their deviation in experiment is reported small enough to be assumed as unchanged within experimental uncertainty [44]. The validity of such an extrapolation is further supported by other work which shows similar trends in the lattice parameters [24,45]. The linear change of the As position was accounted for on the basis of single-crystal x-ray diffraction data from a publication by Merz *et al.* [46]. All used structure parameters are summarized in Table I of the Appendix.

The phase transition from orthorhombic to tetragonal was intentionally not considered because we wanted to focus on the magnetic state and have the results comparable over the whole doping regime.

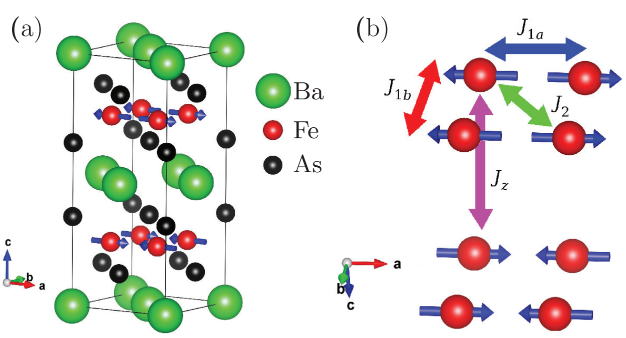

FIG. 1. (Color online) Crystal and magnetic structure of orthorhombic $BaFe_2As_2$. The blue arrows on Fe indicate the spin magnetic moments. (a) Conventional orthorhombic $Fmmm$ low-temperature unit cell. (b) Magnetic structure of the Fe atoms with the nearest- and next-nearest-neighbor exchange interactions. The color code of the J_{ij} values corresponds to Fig. 8.

III. RESULTS AND DISCUSSION

A. Magnetic moments

For the undoped orthorhombic mother-compound $BaFe_2As_2$ we found a total magnetic moment of $1.19\mu_{\mathrm{B}}$, having a spin magnetic moment of $1.14\mu_{\mathrm{B}}$ and an orbital magnetic moment of $0.05\mu_{\mathrm{B}}$. It should be noted that this is in quite reasonable agreement with experimental neutron diffraction data [16,20] compared to other literature, considering that we used a LDA exchange-correlation potential and the experimental As position without structural optimization [6,7,25,26].

In Fig. 2, we show the evolution of the different contributions to the total magnetic moment depending on the increasing substitution of Co on the Fe sites. For each doping ratio x the system was calculated fully self-consistently with the

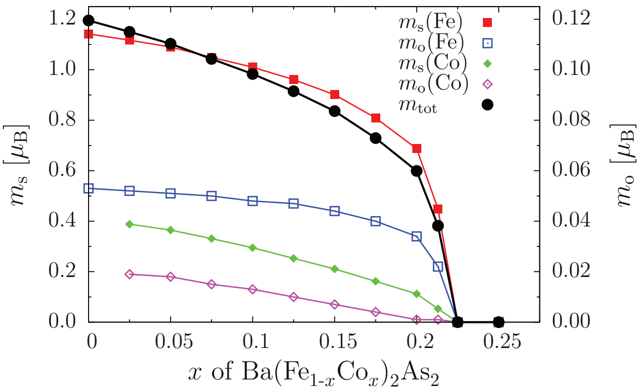

FIG. 2. (Color online) Magnetic spin moments (m_s) and orbital moments (m_o) of Fe and Co for increasing Co ratio x. The black line corresponds to the total magnetic moment which is the substitution-dependent sum over all other plotted contributions. To show spin and orbital moments in one graph the black, red, and green curves correspond to the left y axis while the blue and magenta plots belong to the right y axis which is reduced by one order of magnitude.

CPA. The use of VCA calculations is insufficient for such an investigation, not only because of the intrinsic deficiencies of the made assumptions, but also because the VCA loses every site-resolved information. Here, we can distinguish the magnetic spin and orbital moments of Fe and Co, respectively. Considering the lowest investigated Co concentration of 2.5% per Fe in $Ba(Fe_{0.975}Co_{0.025})_2As_2$ one has a total magnetic moment of $1.15\mu_B$ with already a noteworthy reduction compared to the undoped case ($1.19\mu_B$). On the one hand side, this reduction is approximately due to the individual decrease of the Fe magnetic moments and on the other hand due to the smaller contribution of Co. In fact, the magnetic moments of Co are almost by a factor of 3 smaller compared to the Fe magnetic moments. This is a strong difference compared to the bulk metals bcc-Fe and hcp-Co where the difference in the magnetic moments is small and only about 36%. On the other hand, $BaFe_2As_2$ has a clear magnetic transition with finite moments while $BaCo_2As_2$ is a solely paramagnetic metal without any signs for a magnetic transition [47].

For increasing doping ratio x obviously the influence of Co on the decrease in the magnetic moments gets more and more pronounced. Considering only the Co magnetic spin and orbital moments it is obvious that they decrease more or less linearly until they vanish completely. The decrease in the Fe magnetic moments is less pronounced for low-doping concentrations but gets significantly higher for x values above 0.1. In the x range between 0.2 and 0.225, the Co moments finally vanish, which is accompanied by a drastic collapse of the Fe magnetic moments and the system becomes paramagnetic. This collapse of antiferromagnetic order differs from the experimental phase diagram [48] of $Ba(Fe_{1-x}Co_x)_2As_2$ because the experimentally observed disappearance of long-range magnetic order is coupled to an incommensurate SDW state or fluctuating magnetic moments and not to a nonmagnetic state.

Nevertheless, it gives a very interesting insight on the influence of Co doping on the magnetic order in $BaFe_2As_2$ and shows a clear nonlinear behavior. It further quantifies how increasing substitution of Co on Fe sites weakens the fixed commensurate SDW state until the influence becomes strong enough to totally suppress magnetic long-range order. Although this gives no direct information about the possible existence of another spin state with fluctuating magnetic moments, Co substitution proves to be quite efficient in suppressing the commensurate SDW state in $BaFe_2As_2$ which is obviously its crucial influence.

Finally, the influence of the As z position on the magnetic moments should be briefly discussed. As we stressed before, we used a linear extrapolation of $z(x)$ depending on the Co ratio x, based on experimental data to have our results as close to experiment as possible. Because this means for the case of Co doping a decrease in $z(x)$ it is obvious that this implies also a reduction of the magnetic moments, as discussed before by several authors [6,7,11,27]. For the case of $Ba(Fe_{0.9}Co_{0.1})_2As_2$ we calculated in addition the case where the As position was not changed and has the experimental value for $x = 0$, i.e., $z(0.0) = 0.3538$ instead of $z(0.1) = 0.3529$. Comparing the corresponding moments one can approximately compare the influence on the magnetic moments induced either by Co doping or the chance in the As position. For $z(0.1)$ (see results from Fig. 2) one has for $Ba(Fe_{0.9}Co_{0.1})_2As_2$ a total magnetic moment of $0.98\mu_B$ (Fe_{spin}: $1.01\mu_B$, Co_{spin}: $0.29\mu_B$) while the same system with an unchanged $z(0.0)$ value gave a total magnetic moment of $1.07\mu_B$ (Fe_{spin}: $1.10\mu_B$, Co_{spin}: $0.34\mu_B$). Compared with the undoped $BaFe_2As_2$ with a total moment of $1.19\mu_B$ it is obvious that the experimental adjustment of $z(x)$ further reduces the magnetic moment as one would expect. Nevertheless, it is also clear that the most crucial influence on the moment is due to the substitution of Co and not the reduction in z. Consequently, one would expect the total collapse of magnetic moments for constant z values for slightly higher doping ratios x.

It should be noted that our extrapolation of $z(x)$ for increasing Co substitution is based on experimental data and cannot be compared to the much stronger and unreliable deviation in z obtained by structure optimizations with nonmagnetic general gradient approximation (GGA) calculations which are reported in literature to give already for the undoped $BaFe_2As_2$ compound an As position of $z(\text{GGA nonmagnetic}) = 0.3448$ [for comparison: $z(\text{GGA magnetic}) = 0.3520$, $z(\text{expt}) = 0.3545$ [6]].

B. Bloch spectral functions

First, we demonstrate that the CPA is able to reproduce all disorder effects necessary for a complete description of the electronic structure. Berlijn *et al.* [30] calculated the band structure of nonmagnetic, tetragonal $Ba(Fe_{0.875}Co_{0.125})_2As_2$ for 10 randomly configured supercells containing 400 atoms each in order to gain a description of disorder effects. In Fig. 3, we show the Bloch spectral function for the same system calculated with the CPA but using only one cell having five atoms. As we do not have the band-structure data of Berlijn *et al.* [30] available in a numerical form, a quantitative comparison is not possible. Nevertheless, an inspection of these data demonstrates full accordance between the two calculation schemes. First of all, the supercell calculation shows clearly a moderate scatter of the individual energy bands implying for a given energy E a well-defined average value $\bar{\boldsymbol{k}}$ with a width $\Delta\boldsymbol{k}$ that is much smaller than the dimension of the Brillouin zone. This means disorder gives rise to a finite lifetime reflected by $\Delta\boldsymbol{k}$ but does not destroy a well-defined dispersion relation $E(\bar{\boldsymbol{k}})$ for the configurational average. This

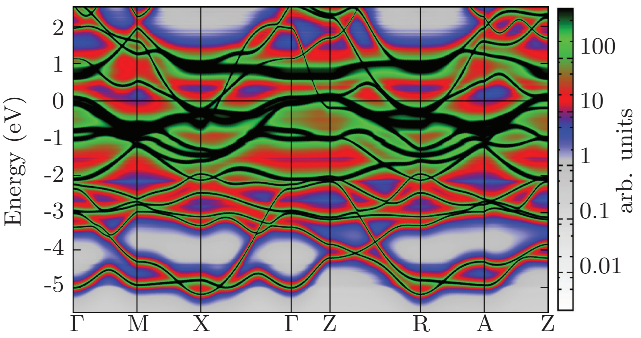

FIG. 3. (Color online) Bloch spectral function of nonmagnetic, tetragonal $Ba(Fe_{0.875}Co_{0.125})_2As_2$ calculated with the CPA, using one cell with five atoms. The corresponding Brillouin zone can be found in Fig. 10 in the Appendix.

important result is obviously fully in line with the Bloch spectral function $A_{\mathbf{k}}(E)$ calculated by means of the KKR-CPA. In a qualitative comparison one can also see that the disorder-induced band broadening given by the CPA is in line with Berlijn's results [30] concerning intensity as well as position in reciprocal space. For example, the broadening is strong in the energy window from approximately -2 to 1 eV but weak for energies below -2 eV. This is exactly the same information that could be deduced from the supercell calculation. Thus, we have further confidence concerning the applicability of the CPA to treat the disorder in doped iron pnictides.

To further investigate the anisotropic effects of the stripe antiferromagnetic order depending on the Co concentration we compare the shapes of the different Fermi surfaces (FS) with each other. To evaluate the electronic structure, we used the converged potentials to calculate corresponding Bloch spectral functions at the Fermi level which should reveal the strong in-plane anisotropy. To see these important anisotropic effects in angle-resolved photoemission spectroscopy (ARPES) experiments it is necessary to efficiently detwin the single crystal after the structural and magnetic phase transitions at low temperatures, for example, by applying in-plane uniaxial stress. Corresponding precise ARPES measurements of detwinned crystals of $BaFe_2As_2$ which show the strong in-plane anisotropy of the electronic structure are indeed available in literature [49,50].

Concerning calculations, one should keep in mind that the FS depends strongly on the magnetic moment which is not easy to capture adequately. Furthermore, one must understand the increasing backfolding of bands with simultaneously increasing number Fe atoms per unit cell. Still, to describe the experimentally observed stripe antiferromagnetic state with antiferromagnetic coupling along c one needs to consider at least a unit cell with four different Fe atoms (4-Fe). The effects of backfolding are schematically explained in Fig. 4 where we show the corresponding Brillouin zone (BZ) [Fig. 4(a)] and compare the Fermi surfaces of orthorhombic undoped $BaFe_2As_2$ derived from strict nonmagnetic calculations of a 2-Fe [Fig. 4(b)], a 4-Fe [Fig. 4(c)], and a 8-Fe [Fig. 4(d)] unit cell. In the primitive 2-Fe unit cell [Fig. 4(b)] all points Γ, X, Y, and Z are distinct. Note that the directions of X and Y correspond directly to the real-space a and b directions. In the 4-Fe unit cell [Fig. 4(c)], the backfolding results in two points we will call Y′ and X′ where Y′ is a superposition of Γ and Y while X′ is the corresponding superposition of X and Z. Further backfolding results in Fig. 4(d) for the case of an 8-Fe unit cell where only one point Γ″ is the superposition of Γ, X, Y, and Z. Because the calculations of the stripe magnetic state require at least the 4-Fe unit cell, the Fermi surfaces will correspond to an equivalent backfolding with only X′ and Y′ being distinct.

In Fig. 5(a), we show the Fermi surface of undoped $BaFe_2As_2$ in its stripe antiferromangetic state. Even considering the expected 4-Fe unit-cell backfolding, the strong in-plane anisotropy of the electronic structure is obvious. The red points correspond to the reconstructed Brillouin zone of Yin *et al.* [49] which was derived from ARPES measurements on detwinned crystals. This reconstructed BZ is a combination of all measured ARPES data and would hence correspond to an overlay of X′ and Y′ in the definition of Fig. 4(c). The good

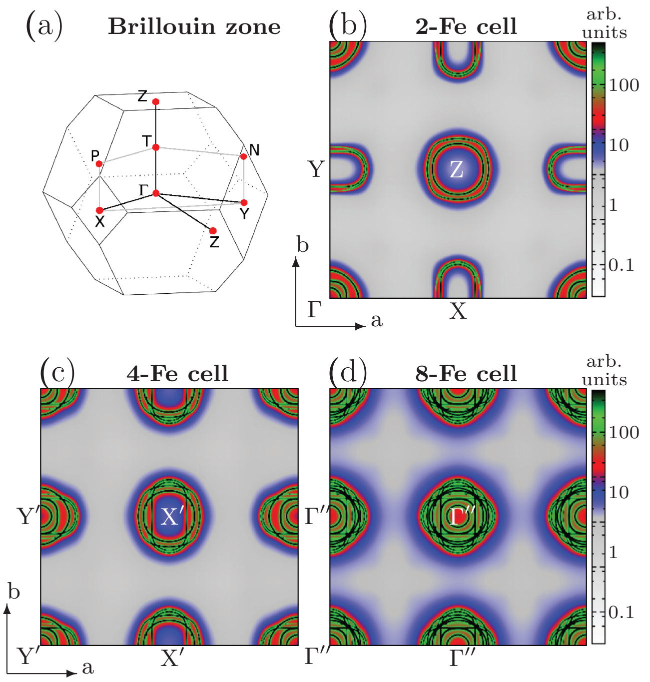

FIG. 4. (Color online) (a) Brillouin zone of orthorhombic $BaFe_2As_2$. Corresponding Fermi surfaces are derived from nonmagnetic calculations in the ΓXY plane for increasing size of the unit cell, (b) two Fe per cell, (c) four Fe per cell, (d) eight Fe per cell, showing increasing backfolding of the bands.

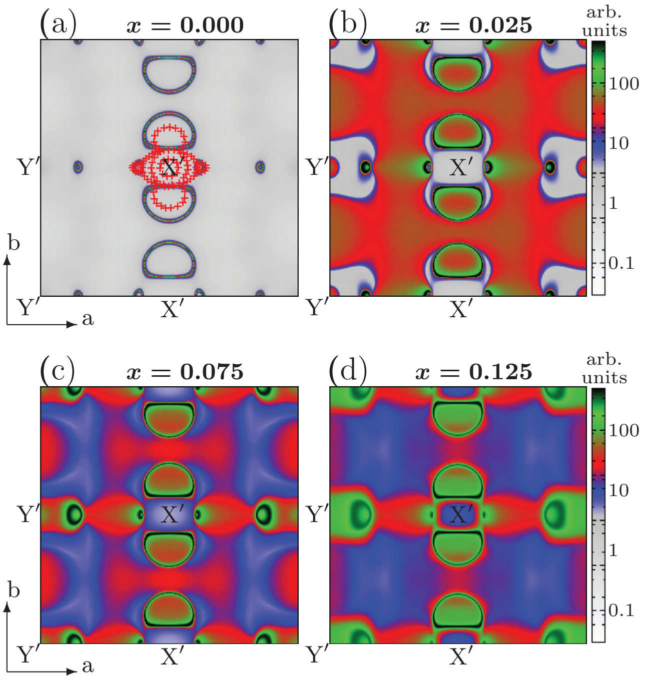

FIG. 5. (Color online) Fermi surfaces of the experimental stripe antiferromagnetic state of orthorhombic $Ba(Fe_{1-x}Co_x)_2As_2$ calculated with a 4-Fe unit cell for different Co concentrations x. (a) Undoped $BaFe_2As_2$ with an overlay of the reconstructed Brillouin zone of Yin *et al.* [49] from ARPES measurements, (b) $Ba(Fe_{0.975}Co_{0.025})_2As_2$, (c) $Ba(Fe_{0.925}Co_{0.075})_2As_2$, (d) $Ba(Fe_{0.875}Co_{0.125})_2As_2$.

agreement with the experimental ARPES data is obvious. We lose in the calculations the inner circles of the reconstructed BZ which would arise from bands around Γ but the most important bands, namely, the anisotropic ones are strikingly well preserved. They are described in literature as small bright spots along X (corresponding to the antiferromagnetic real-space *a* direction) and larger petals along Y (corresponding to ferromagnetic real-space *b* direction) [49]. The bright spots along X are perfectly reproduced. The petals along Y are a bit bigger than in experiment, but their characteristics are clearly identifiable. More or less comparable Fermi surfaces for the stripe antiferromagnetic iron pnictides were predicted, for example, by Andersen and Boeri [51].

In addition to the undoped Ba-122 compound, we performed the calculation of Bloch spectral functions for the whole Co doping regime considered in this work. The CPA allows a very precise investigation of the influence of Co on the electronic structure considering the induced chemical disorder. Furthermore, it is interesting to see the change in the Fermi surface for decreasing strength of the long-range antiferromagnetic order. In Fig. 5(b), the shape of the FS has not drastically changed, however, a blur in the intensity is already quite visible. These blurs or band broadening effects are due to the disorder induced by Co. For the higher concentrations in Figs. 5(c) and 5(d), the shape of the bright spots along *a* starts to change. While the spots around X′ shrink the ones around Y′ increase in size and start to blur out. This trend continues as can be seen in Fig. 6(a), which shows for $x = 0.175$ still a comparable FS before the antiferromagnetic order collapses for higher Co concentrations. The initially bright spots around Y′ have developed to petal-like structure like the ones around X′ along the *b* direction. However, they are still clearly distinguishable through the different strength of band blurring. The crucial change of the FS happens in Fig. 6(b) where the anisotropic features finally start to vanish and become symmetric propellerlike structures. Note, however, that the electronic structure along the *b* direction, with ferromagnetic coupling, is perfectly sharp with no signs of disorder effects, while the band blur along the *a* direction, with antiferromagnetic coupling, is strongest in this picture. For $x = 0.213$ in Fig. 6(c) the matching of the propeller structures is already nearly perfect although there is still a finite magnetic moment on Fe. Additionally, a squarelike feature forms around X′ which originates most likely through the backfolding from the original Z point in the 2-Fe unit cell. The collapse of long-range magnetic order is complete in Fig. 6(d) where now the propeller structures are perfectly symmetric. There are clearly no in-plane anisotropic features of the electronic structure left. Note that the absence of a perfect fourfold rotational symmetry of the FS is only due to the effects of backfolding in the ΓXY plane (compare Fig. 4).

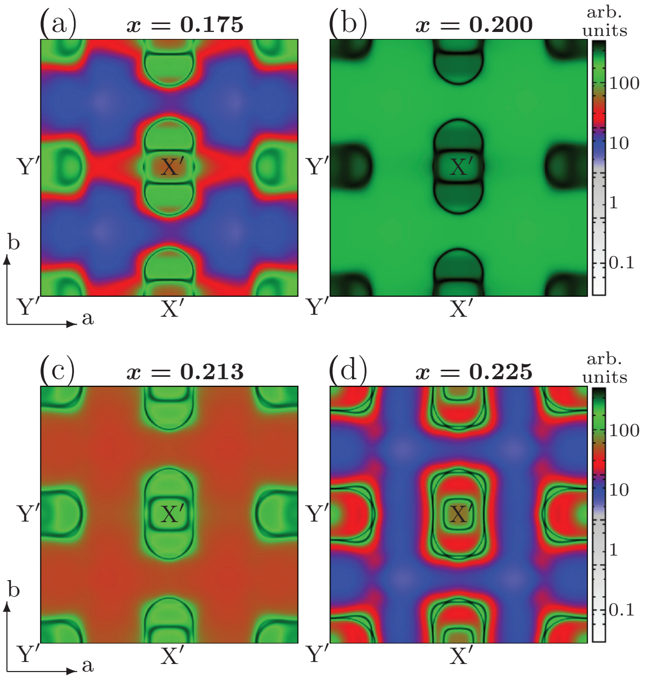

FIG. 6. (Color online) Fermi surfaces of the experimental stripe antiferromagnetic state of orthorhombic Ba(Fe$_{1-x}$Co$_x$)$_2$As$_2$ calculated with a 4-Fe unit cell for different Co concentrations x. These Fermi surfaces are close to the collapse of long-range antiferromagnetic order (a) Ba(Fe$_{0.825}$Co$_{0.175}$)$_2$As$_2$, (b) Ba(Fe$_{0.8}$Co$_{0.2}$)$_2$As$_2$, (c) Ba(Fe$_{0.787}$Co$_{0.213}$)$_2$As$_2$, (d) Ba(Fe$_{0.775}$Co$_{0.225}$)$_2$As$_2$.

The same effect is more clearly visible if one shifts the Bloch spectral function from the ΓXY plane with $\boldsymbol{k}_z = 0.5$ towards the Z point. The corresponding TPN plane [see Fig. 4(a)] has the property to show the restoration of the fourfold rotational symmetry after the collapse of long-range magnetic order despite the backfolding of bands in a 4-Fe unit cell. While Fig. 7(a) for the magnetic state with $x = 0.0$ has an obvious twofold rotational symmetry, the fourfold rotational symmetry is clearly restored after the collapse of the long-range antiferromagnetic order in Fig. 7(b) for $x = 0.225$. Note further that this disappearance of the in-plane anisotropy occurs for an orthorhombic lattice. Consequently, one can state that the origin of the strong anisotropy in ARPES measurements is practically only due to the stripe antiferromagnetic order while the effect of the lattice distortion is practically neglectable.

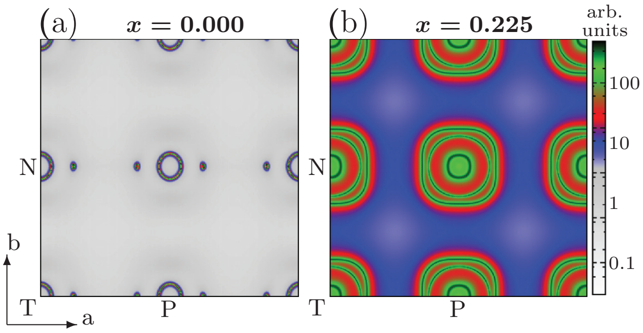

FIG. 7. (Color online) Fermi surfaces of Ba(Fe$_{1-x}$Co$_x$)$_2$As$_2$ calculated with a 4-Fe unit cell in the TPN plane, which is shifted by $\boldsymbol{k}_z = 0.5$ in Z direction. (a) For $x = 0.0$ the fourfold rotational symmetry in the magnetic state is clearly broken. (b) For $x = 0.225$ in the paramagnetic state the fourfold rotational symmetry is in principle perfectly restored, despite the 4-Fe unit cell and despite the orthorhombic distortion.

It is also striking that the band blurring effects for $x = 0.225$ [see Fig. 6(d)] are significantly reduced compared to, for example, $x = 0.2$ [see Fig. 6(b)]. This is surprising as one would expect a continuous increase of the band blurring effects to the maximum of substitutional disorder at 50% Co substitution. The deviation from the expected behavior is obviously connected to the antiferromagnetic order and its collapse for $x = 0.225$. Additionally, the in-plane anisotropy of the disorder in Fig. 6(b) may be an interesting first indication for anisotropic effects in the transport properties at the proximity of the magnetic phase. It has recently been discussed that these effects are possibly due to anisotropic scattering properties [33]. Still, an investigation of only the Fermi surface is insufficient for even qualitative statements and specific calculations of the linear-response properties [52] of these systems are necessary and planned for the future.

C. Exchange-coupling constants

To further investigate the magnetic structure of orthorhombic $\mathrm{Ba(Fe_{1-x}Co_x)_2As_2}$, we investigated the exchange-coupling constants J_{ij} between sites i and j. Calculations are based on the magnetic force theorem and implemented in the multiple scattering formalism by the formula of Lichtenstein *et al.* [40–42].

We focus our discussion on the most important coupling constants J_{1a}, J_{1b}, J_2, and J_z between neighboring Fe atoms, defined according to Fig. 1(b). Experimentally, it is often not possible to directly determine these values independently but one fits the experimental data based on a chosen model, e.g., a Heisenberg model [53,54]. Sometimes, the relative strength of the different coupling constants is further fixed in their ratio based on theoretical calculations while fitting [53]. Although there are numerous calculations in literature on the relative and absolute strength of the coupling constants, there is no clear consensus and the published values differ in magnitude and ratio [11,27,53–56]. Thus, it is difficult to compare the results due to different definitions of the exchange-coupling constants, the different approximations to calculate them and because the calculated magnetic moments may differ significantly. For the iron pnictides, it is known that the exchange energies are quite sensitive with respect to the magnitude of the magnetic moment, which consequently may result in different absolute values [11,27,55].

The exchange-coupling constants discussed here refer to a Fe atom in center coupling with the neighboring Fe atoms or substituted Co atoms on Fe sites. The corresponding classical Heisenberg Hamiltonian has the form $\mathcal{H} = -\sum_{ij} J_{ij}\mathbf{e}_i\mathbf{e}_j$, where we use unit vectors $\mathbf{e}_{i(j)}$ instead of spin vectors $\mathbf{S}_{i(j)}$ [41,57]. Here, a negative sign corresponds to antiferromagnetic coupling, while a positive sign favors a ferromagnetic interaction. The coupling constants between Fe and Co behave in principle similarly, only the absolute values of Co are reduced by a factor of approximately 3, which could be expected as it is a similar ratio compared to the relative strength of the magnetic moments.

We plotted the isotropic exchange-coupling constants for Fe coupling with Fe as a function of the Co doping ratio x in Fig. 8. Here, J_Δ is defined as $J_{1a} - J_{1b}$ and corresponds to the real-space in-plane anisotropy between a and b. As can be seen in the plot, J_Δ decreases nearly linearly for increasing Co substitution. J_{1a} and J_{1b} are the dominating interaction parameters with significant dependence on the Co doping, while J_2 and J_z are smaller and their change due to Co substitution is only weak. Interestingly, J_{1a} shows a strong and continuous decrease while J_{1b} even shows a small increase in the coupling strength for low Co ratios and reaches a maximum at 7.5% of Co substitution. The derived coupling constants are in reasonable agreement with experimental neutron diffraction data on $\mathrm{BaFe_2As_2}$ [53,58,59]. The values seem a bit smaller, but this is primarily due to the definition of the Heisenberg Hamiltonian (see above) with the spin moment incorporated into the J_{ij}'s [41,57].

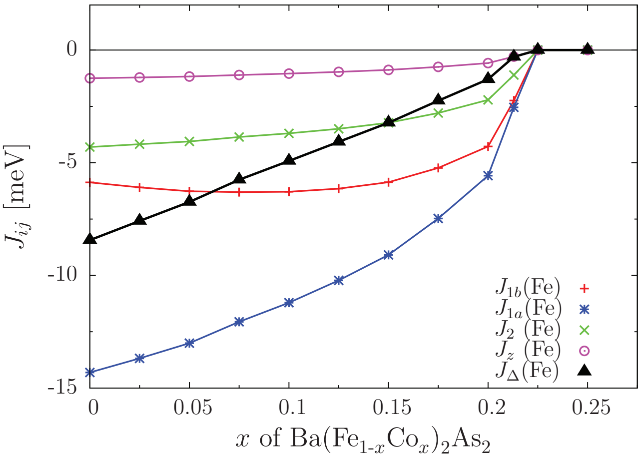

FIG. 8. (Color online) Isotropic exchange-coupling constants J_{ij} of Fe coupling with neighboring Fe atoms. J_Δ is defined as $J_{1a} - J_{1b}$.

It should be noted that the signs for all calculated nearest-neighbor interactions are negative and would hence prefer an antiferromagnetic order. As the system obviously cannot fulfill all of these conditions at the same time, there is a competition of magnetic states, in accordance with other reports in literature [55,60].

D. Monte Carlo simulations

To solve the problem of competing magnetic states on an accurate level we performed Monte Carlo simulations based on the classical Heisenberg model. It should be noted that although the iron pnictides have clearly itinerant aspects in their magnetic structure, it is still too rash to completely dismiss the Heisenberg model for predictions of the magnetic ordering. On a simple level, the Heisenberg model was successfully used in several publications giving useful results as long as one keeps the underlying approximations in mind [53–55].

For the Monte Carlo simulations we used 2744 atoms and solved the competition of magnetic states in an accurate way as we reproduced correctly the experimental stripe antiferromagnetic structure as magnetic ground state for $T = 0$ K as seen in Fig. 9(a). These calculations allowed us further to include temperature-dependent effects to evaluate, for example, the Néel temperature T_N of the ground state. For the undoped $\mathrm{BaFe_2As_2}$, the estimated Néel temperature of $T_\mathrm{N} \approx 142$ K is in perfect agreement with the experimental $T_{\mathrm{N,\,expt}} \approx 140$ K.

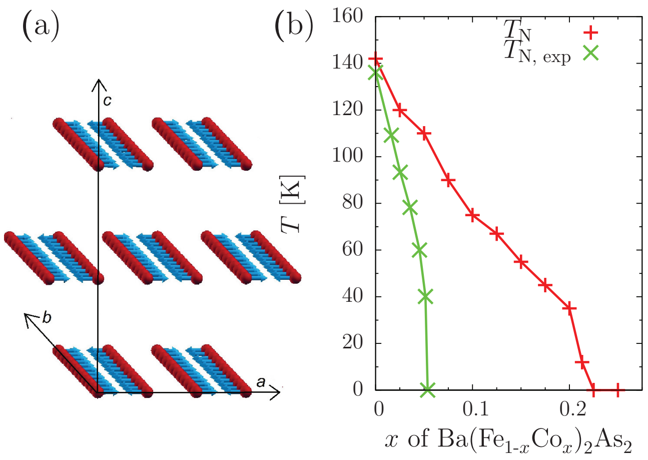

FIG. 9. (Color online) (a) Magnetic ground state of $BaFe_2As_2$ according to Monte Carlo simulations. (b) Evolution of the Néel temperatures T_N depending on the Co concentration x in $Ba(Fe_{1-x}Co_x)_2As_2$. The experimental data $T_{N,\,expt}$ were reproduced from the work of Lester *et al.* [48].

These results make us confident that the exchange-coupling constants are in the right order of magnitude and the Heisenberg model can be successfully used as a satisfying basis for Monte Carlo simulations.

We further evaluated the change of the Néel temperature for increasing Co substitution and show this behavior in Fig. 9(b) together with experimental data taken from the work of Lester *et al.* [48]. One should still keep in mind that the calculated collapse of antiferromagnetic order happens for relatively high Co ratios, meaning it cannot be directly compared to the experimental phase diagram concerning the Co concentration as we did not consider for incommensurate spin states.

Still, accounting for this stretching of the calculated phase diagram, the overall trends in the behavior of the Néel temperature in Fig. 9(b) are rather well reproduced. Also, in the experimental data from Lester *et al.* [48] one can see a split of the Co dependence of the Néel temperature in two approximately linear regions with different slope. Experimentally, in the first region T_N decreases from 140 K down to approximately 40 K until the proximity of the magnetic collapse is reached. For higher Co ratios, the decrease of T_N from 40 K down to 0 K (collapse of long-range magnetic order) goes faster, leading to an almost perpendicular drop of the Néel temperature. In the calculated Néel temperatures, one can see also these two regions with the same behavior, even for the same values of T_N.

IV. SUMMARY

In this work, we evaluated the magnetic and electronic properties of $Ba(Fe_{1-x}Co_x)_2As_2$ in its orthorhombic, stripe antiferromagnetic ordered state. The substitution of Co on Fe sites was dealt within the CPA which allows in a quite sophisticated way to deal with the disorder of the system on a level beyond a VCA or a rigid-band-shift calculation. We further showed that the CPA results are fully in line with expensive supercell calculations of Berlijn *et al.* [30].

We calculated the site-resolved magnetic spin and orbital moments fully relativistically over a wide doping regime from $x = 0.0$ to 0.25 in steps of 2.5%. For the undoped $BaFe_2As_2$, we got a total magnetic moment of $1.19\mu_B$ per Fe which is smaller and closer to experimental neutron data compared to other publications which used LDA and the experimental, not optimized As position z [6,7,25,26]. We found decreasing magnetic moments on Fe and Co in $Ba(Fe_{1-x}Co_x)_2As_2$ for increasing Co concentration as expected until the system becomes paramagnetic at $x = 0.225$. Although this collapse of long-range magnetic order cannot be directly compared to the disappearance of antiferromagnetic order in the phase diagram, it is still important concerning the decreasing stability of a commensurate SDW state under Co substitution.

The change of the electronic structure at the Fermi level was also evaluated with special focus on the strong in-plane anisotropy observed in ARPES measurements. We were able to reproduce the anisotropic feature of the Fermi surface in an adequate way and observed that this anisotropy decreases together with the magnetic moments until it completely vanishes where the system becomes paramagnetic. As this was obtained in an orthorhombic lattice, it is quite clear that the origin of this exceptional strong electronic anisotropy is only due to the stripe magnetic order while the lattice distortion effects between a and b can be neglected.

Furthermore, we calculated the isotropic exchange-coupling constants J_{ij} for Fe and Co. We observed strong in-plane anisotropy between J_{1a} and J_{1b} which again consequently decreases for increasing Co concentration. The coupling constants had the same sign for all nearest-neighbor interactions, indicating competition of magnetic states and showed reasonable agreement with experimental values [53,58,59]. The dilemma of competing magnetic states could be successfully solved by Monte Carlo simulations based on a classical Heisenberg model, which reproduced almost perfect Néel temperatures and the stripe antiferromagnetic spin state as magnetic ground state.

Overall, we showed successfully the decrease of the strong in-plane anisotropy $Ba(Fe_{1-x}Co_x)_2As_2$ for increasing Co concentration within the CPA. Thus, the CPA has proven to be a highly valuable and precise tool to investigate the influence of chemical disorder introduced by substitution of elements which is crucial for understanding the iron pnictides.

ACKNOWLEDGMENTS

We thank A. Yaresko for his extraordinary help and valuable discussions. Further thanks go to D. Johrendt for his help. We acknowledge the financial support from the Deutsche Forschungsgemeinschaft DFG (Projects No. EB 154/24-2 within FOR 1346 and No. EB 154/26-1) and from the Bundesministerium für Bildung und Forschung BMBF (Project No. 05K13WMA). We further thank for the support from CENTEM (Project No. CZ.1.05/2.1.00/03.0088).

APPENDIX

In Fig. 10, the tetragonal Brillouin zone of $BaFe_2As_2$ is shown with its definition of high-symmetric points corresponding to Fig. 3.

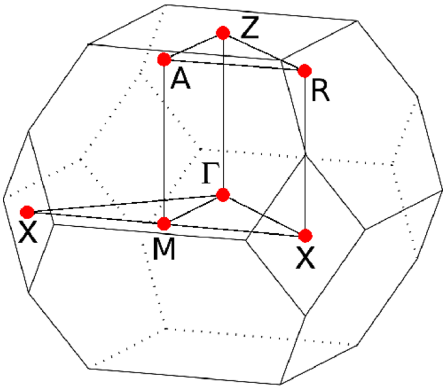

FIG. 10. (Color online) Brillouin zone of tetragonal $BaFe_2As_2$, corresponding to Fig. 3.

TABLE I. Summary of all used structure parameters of orthorhombic $Ba(Fe_{1-x}Co_x)_2As_2$ (space group 69, *Fmmm*).

Co ratio x	Lattice constants (Å)	As position
$x = 0.000$	$a = 5.6146$ $b = 5.5742$ $c = 12.9453$	$z = 0.3538$
$x = 0.025$	$c = 12.9349$	$z = 0.3536$
$x = 0.050$	$c = 12.9244$	$z = 0.3534$
$x = 0.075$	$c = 12.9140$	$z = 0.3531$
$x = 0.100$	$c = 12.9035$	$z = 0.3529$
$x = 0.125$	$c = 12.8931$	$z = 0.3527$
$x = 0.150$	$c = 12.8827$	$z = 0.3525$
$x = 0.175$	$c = 12.8722$	$z = 0.3522$
$x = 0.200$	$c = 12.8618$	$z = 0.3520$
$x = 0.213$	$c = 12.8564$	$z = 0.3519$
$x = 0.225$	$c = 12.8514$	$z = 0.3518$
$x = 0.250$	$c = 12.8409$	$z = 0.3516$

In Table I, all structure parameters used for the calculations are summarized for the sake of completeness. For the undoped compound only the experimental lattice values from Rotter *et al.* [17] were used. For increasing Co concentration, the change of the lattice parameters was linearly extrapolated on basis of experimental data and Vegard's law. For the c axis, we used results from Sefat *et al.* [44], while the change of the As position was linearly extrapolated based on single-crystal x-ray diffraction data of Merz *et al.* [46]. Similar trends of the lattice parameters are also found elsewhere in literature [24,45]. Note that a and b were held constant over the whole doping regime.

---

[1] Y. Kamihara, T. Watanabe, M. Hirano, and H. Hosono, J. Am. Chem. Soc. **130**, 3296 (2008).

[2] H. Takahashi, K. Igawa, K. Arii, Y. Kamihara, M. Hirano, and H. Hosono, Nature (London) **453**, 376 (2008).

[3] D. J. Singh, Phys. Rev. B **78**, 094511 (2008).

[4] I. I. Mazin, D. J. Singh, M. D. Johannes, and M. H. Du, Phys. Rev. Lett. **101**, 057003 (2008).

[5] R. M. Fernandes, D. K. Pratt, W. Tian, J. Zarestky, A. Kreyssig, S. Nandi, M. G. Kim, A. Thaler, N. Ni, P. C. Canfield, R. J. McQueeney, J. Schmalian, and A. I. Goldman, Phys. Rev. B **81**, 140501 (2010).

[6] I. I. Mazin and M. D. Johannes, Nat. Phys. **5**, 141 (2009).

[7] I. I. Mazin, M. D. Johannes, L. Boeri, K. Koepernik, and D. J. Singh, Phys. Rev. B **78**, 085104 (2008).

[8] A. N. Yaresko, G.-Q. Liu, V. N. Antonov, and O. K. Andersen, Phys. Rev. B **79**, 144421 (2009).

[9] I. Opahle, H. C. Kandpal, Y. Zhang, C. Gros, and R. Valentí, Phys. Rev. B **79**, 024509 (2009).

[10] J. Fink, S. Thirupathaiah, R. Ovsyannikov, H. A. Dürr, R. Follath, Y. Huang, S. de Jong, M. S. Golden, Y.-Z. Zhang, H. O. Jeschke, R. Valentí, C. Felser, S. Dastjani Farahani, M. Rotter, and D. Johrendt, Phys. Rev. B **79**, 155118 (2009).

[11] M. J. Han, Q. Yin, W. E. Pickett, and S. Y. Savrasov, Phys. Rev. Lett. **102**, 107003 (2009).

[12] L. X. Yang *et al.*, Phys. Rev. Lett. **102**, 107002 (2009).

[13] L. Craco, M. S. Laad, S. Leoni, and H. Rosner, Phys. Rev. B **78**, 134511 (2008).

[14] P. Werner, M. Casula, T. Miyake, F. Aryasetiawan, A. J. Millis, and S. Biermann, Nat. Phys. **8**, 331 (2012).

[15] D. H. Lu, M. Yi, S.-K. Mo, A. S. Erickson, J. Analytis, J.-H. Chu, D. J. Singh, Z. Hussain, T. H. Geballe, I. R. Fisher, and Z.-X. Shen, Nature (London) **455**, 81 (2008).

[16] Y. Su, P. Link, A. Schneidewind, T. Wolf, P. Adelmann, Y. Xiao, M. Meven, R. Mittal, M. Rotter, D. Johrendt, T. Brueckel, and M. Loewenhaupt, Phys. Rev. B **79**, 064504 (2009).

[17] M. Rotter, M. Tegel, D. Johrendt, I. Schellenberg, W. Hermes, and R. Pöttgen, Phys. Rev. B **78**, 020503 (2008).

[18] H. Gretarsson *et al.*, Phys. Rev. B **84**, 100509 (2011).

[19] P. Vilmercati, A. Fedorov, F. Bondino, F. Offi, G. Panaccione, P. Lacovig, L. Simonelli, M. A. McGuire, A. S. M. Sefat, D. Mandrus, B. C. Sales, T. Egami, W. Ku, and N. Mannella, Phys. Rev. B **85**, 220503 (2012).

[20] Q. Huang, Y. Qiu, W. Bao, M. A. Green, J. W. Lynn, Y. C. Gasparovic, T. Wu, G. Wu, and X. H. Chen, Phys. Rev. Lett. **101**, 257003 (2008).

[21] M. Rotter, M. Tegel, I. Schellenberg, F. M. Schappacher, R. Pöttgen, J. Deisenhofer, A. Günther, F. Schrettle, A. Loidl, and D. Johrendt, New J. Phys. **11**, 025014 (2009).

[22] A. A. Aczel *et al.*, Phys. Rev. B **78**, 214503 (2008).

[23] T. Goko *et al.*, Phys. Rev. B **80**, 024508 (2009).

[24] D. Kasinathan, A. Ormeci, K. Koch, U. Burkhardt, W. Schnelle, A. Leithe-Jasper, and H. Rosner, New J. Phys. **11**, 025023 (2009).

[25] A. Sanna, F. Bernardini, G. Profeta, S. Sharma, J. K. Dewhurst, A. Lucarelli, L. Degiorgi, E. K. U. Gross, and S. Massidda, Phys. Rev. B **83**, 054502 (2011).

[26] E. Aktürk and S. Ciraci, Phys. Rev. B **79**, 184523 (2009).

[27] Z. P. Yin, S. Lebègue, M. J. Han, B. P. Neal, S. Y. Savrasov, and W. E. Pickett, Phys. Rev. Lett. **101**, 047001 (2008).

[28] D. K. Pratt, M. G. Kim, A. Kreyssig, Y. B. Lee, G. S. Tucker, A. Thaler, W. Tian, J. L. Zarestky, S. L. Bud'ko, P. C. Canfield, B. N. Harmon, A. I. Goldman, and R. J. McQueeney, Phys. Rev. Lett. **106**, 257001 (2011).

[29] J. T. Park *et al.*, Phys. Rev. B **82**, 134503 (2010).

[30] T. Berlijn, C.-H. Lin, W. Garber, and W. Ku, Phys. Rev. Lett. **108**, 207003 (2012).

[31] L. Wang, T. Berlijn, Y. Wang, C.-H. Lin, P. J. Hirschfeld, and W. Ku, Phys. Rev. Lett. **110**, 037001 (2013).

[32] J.-H. Chu, J. G. Analytis, K. De Greve, P. L. McMahon, Z. Islam, Y. Yamamoto, and I. R. Fisher, Science **329**, 824 (2010).

[33] S. Ishida, M. Nakajima, T. Liang, K. Kihou, C. H. Lee, A. Iyo, H. Eisaki, T. Kakeshita, Y. Tomioka, T. Ito, and S. Uchida, Phys. Rev. Lett. **110**, 207001 (2013).

[34] M. N. Gastiasoro, P. J. Hirschfeld, and B. M. Andersen, Phys. Rev. B **89**, 100502 (2014).

[35] G. Levy, R. Sutarto, D. Chevrier, T. Regier, R. Blyth, J. Geck, S. Wurmehl, L. Harnagea, H. Wadati, T. Mizokawa, I. S. Elfimov, A. Damascelli, and G. A. Sawatzky, Phys. Rev. Lett. **109**, 077001 (2012).

[36] S. N. Khan and D. D. Johnson, Phys. Rev. Lett. **112**, 156401 (2014).

[37] S. N. Khan, A. Alam, and D. D. Johnson, Phys. Rev. B **89**, 205121 (2014).

[38] H. Ebert, D. Ködderitzsch, and J. Minár, Rep. Prog. Phys. **74**, 096501 (2011).

[39] S. H. Vosko, L. Wilk, and M. Nusair, Can. J. Phys. **58**, 1200 (1980).

[40] A. I. Liechtenstein, M. I. Katsnelson, V. P. Antropov, and V. A. Gubanov, J. Magn. Magn. Mater. **67**, 65 (1987).

[41] S. Mankovsky, S. Bornemann, J. Minár, S. Polesya, H. Ebert, J. B. Staunton, and A. I. Lichtenstein, Phys. Rev. B **80**, 014422 (2009).

[42] H. Ebert and S. Mankovsky, Phys. Rev. B **79**, 045209 (2009).

[43] L. Vegard, Z. Phys. **5**, 17 (1921).

[44] A. S. Sefat, R. Jin, M. A. McGuire, B. C. Sales, D. J. Singh, and D. Mandrus, Phys. Rev. Lett. **101**, 117004 (2008).

[45] N. Ni, M. E. Tillman, J.-Q. Yan, A. Kracher, S. T. Hannahs, S. L. Bud'ko, and P. C. Canfield, Phys. Rev. B **78**, 214515 (2008).

[46] M. Merz, P. Schweiss, P. Nagel, T. Wolf, H. v. Loehneysen, and S. Schuppler, arXiv:1306.4222.

[47] A. S. Sefat, D. J. Singh, R. Jin, M. A. McGuire, B. C. Sales, and D. Mandrus, Phys. Rev. B **79**, 024512 (2009).

[48] C. Lester, J.-H. Chu, J. G. Analytis, S. C. Capelli, A. S. Erickson, C. L. Condron, M. F. Toney, I. R. Fisher, and S. M. Hayden, Phys. Rev. B **79**, 144523 (2009).

[49] M. Yi, D. Lu, J.-H. Chu, J. G. Analytis, A. P. Sorini, A. F. Kemper, B. Moritz, S.-K. Mo, R. G. Moore, M. Hashimoto, W.-S. Lee, Z. Hussain, T. P. Devereaux, I. R. Fisher, and Z.-X. Shen, Proc. Natl. Acad. Sci. USA **108**, 6878 (2011).

[50] Y. Kim, H. Oh, C. Kim, D. Song, W. Jung, B. Kim, H. J. Choi, C. Kim, B. Lee, S. Khim, H. Kim, K. Kim, J. Hong, and Y. Kwon, Phys. Rev. B **83**, 064509 (2011).

[51] O. Andersen and L. Boeri, Ann. Phys. **523**, 8 (2011).

[52] D. Ködderitzsch, S. Lowitzer, J. B. Staunton, and H. Ebert, Phys. Status Solidi B **248**, 2248 (2011).

[53] R. A. Ewings, T. G. Perring, R. I. Bewley, T. Guidi, M. J. Pitcher, D. R. Parker, S. J. Clarke, and A. T. Boothroyd, Phys. Rev. B **78**, 220501 (2008).

[54] J. Zhao, D.-X. Yao, S. Li, T. Hong, Y. Chen, S. Chang, W. Ratcliff, J. W. Lynn, H. A. Mook, G. F. Chen, J. L. Luo, N. L. Wang, E. W. Carlson, J. Hu, and P. Dai, Phys. Rev. Lett. **101**, 167203 (2008).

[55] T. Yildirim, Phys. Rev. Lett. **101**, 057010 (2008).

[56] F. Ma, Z.-Y. Lu, and T. Xiang, Phys. Rev. B **78**, 224517 (2008).

[57] S. Polesya, G. Kuhn, S. Mankovsky, H. Ebert, M. Regus, and W. Bensch, J. Phys.: Condens. Matter **24**, 036004 (2012).

[58] N. Qureshi, P. Steffens, S. Wurmehl, S. Aswartham, B. Büchner, and M. Braden, Phys. Rev. B **86**, 060410 (2012).

[59] L. W. Harriger, H. Q. Luo, M. S. Liu, C. Frost, J. P. Hu, M. R. Norman, and P. Dai, Phys. Rev. B **84**, 054544 (2011).

[60] Q. Si and E. Abrahams, Phys. Rev. Lett. **101**, 076401 (2008).

4.3 Discussion

The publication presented in this chapter was successful concerning its original motivation. The antiferromagnetic phase of $Ba(Fe_{1-x}Co_x)_2As_2$ could be well described and the CPA proved to be a powerful and valid tool to study the disorder of iron pnictides fully comparable to the extensive supercell approach.

In particular, a strong anisotropy was found in the electronic structure as seen in the Fermi surface cuts, which is in qualitative agreement with experimental ARPES spectra of detwinned crystals.[36] However, from experiment alone it was not definitely clear whether this anisotropy arises from the orthorhombic lattice distortion or from the anisotropic magnetic behavior or from a combination of both. Theory could verify that the lattice distortion, which is indeed very small ($a/b \approx 1.007$), has no apparent influence on the anisotropy of the electronic structure. Thus, the magnetic ordering alone, meaning antiferromagnetically ordered chains along a and ferromagnetically ordered chains along b is the relevant origin of the anisotropic behavior. This anisotropy will be discussed in more detail in the subsequent publications, as it is an important intrinsic property of the iron pnictides in their antiferromagnetic phase and has consequences for e.g. ARPES (see Chapter 5) and for electrical transport (see Chapter 7). The already here mentioned anisotropy in disorder will be especially relevant for transport considerations.

It was also a valuable finding to theoretically describe the magnetic phase diagram of $Ba(Fe_{1-x}Co_x)_2As_2$ depending on the dopant concentration x in a type-resolved way including spin-orbit coupling. Especially the reproduced breakdown of antiferromagnetic order at x_{crit} was an important success because the disappearance of long range antiferromagnetic order is obviously coupled to the occurrence of superconductivity.[21,26] Understanding this magnetic breakdown is thus a crucial key in order to search for new types of substitution which might also induce superconductivity. However, at this point the agreement with experiment is reasonably good but not quite perfect. The reproduced $x_{\mathrm{crit}} = 0.225$ is significantly higher than the experimentally observed $x_{\mathrm{crit,ex}} \approx 0.07$[184] for $Ba(Fe_{1-x}Co_x)_2As_2$. Also the magnitude of the magnetic moment in the calculations of undoped $BaFe_2As_2$ with 1.19 μ_{B} is still higher than the 0.87 μ_{B}[24] predicted from neutron diffraction.[E] During the time of this thesis some possible improvements to these results became apparent. It was already mentioned, that the magnetic properties of the iron pnictides are highly sensible on computational param-

---

[E] The apparent difference in the estimated magnetic moment between neutron diffraction[24] and ^{57}Fe Mössbauer spectroscopy[22,45] will be discussed in more detail in Chapter 8.

eters, which means that a careful study is necessary. It was found that an increase of the angular momentum expansion ℓ_{max} has a huge impact on the results within KKR. Better results could be obtained by going from $\ell_{\mathrm{max}} = 2$ within the present publication to $\ell_{\mathrm{max}} = 3$ or 4 as will be used in the subsequent work. More details on the computational subtleties can be found in Appendix A. Consequently, the magnitude of the magnetic moment and the concentration x_{crit} will deviate in the further studies from the results presented in the previous due to subtle improvements. However, the trends and the physical implications stay the same during the whole thesis and for all of the presented work.

Noteworthy is also the consistent description of the antiferromagnetic order within DFT and the Monte Carlo simulations. The experimentally observed spin structure was applied for the DFT calculations in order to make close comparisons with experiment possible. However, this proves not automatically that the proper ground state orientation within theory was considered. In particular, the presented exchange coupling constants J_{ij} showed the same sign for J_{1a}, J_{1b} and J_2 indicating that an antiferromagnetic coupling for all of them would be preferred. Obviously, this leads to magnetic frustration because at least one of these couplings must be ferromagnetic for geometrical reasons. Yet, how the system solves this frustration cannot be derived from the J_{ij} values only, indicating the need for Monte Carlo simulation. Here, the experimental spin structure with ferromagnetic coupling along the b axis was not predefined, but nevertheless exactly this spin structure was obtained. In particular, also the Néel temperature T_{N} for the mother compound $\mathrm{BaFe_2As_2}$ was reproduced in very good agreement with experiment. This ensures that the applied KKR-GF approach gives a trustworthy and consistent theoretical description of the antiferromagnetic phase of the iron pnictides, providing a basis for further studies.

Chapter 5

Anisotropic properties seen in photoemission

5.1 Motivation

Based on the latter publication, preliminary work on $BaFe_2As_2$ and $Ba(Fe_{1-x}Co_x)_2As_2$ in their antiferromagnetic phase was available and could be applied for further and more comprehensive studies. One important advantage of the KKR-GF method is the comparably easy access to spectroscopic quantities via the Green function. Therefore, the one-step model of photoemission (see section 2.2) can be applied in order to calculate the ARPES spectra of the iron pnictide superconductors. Such an approach accounts in detail for the experimental geometry and is thus directly comparable to ARPES experiments. Consequently, all effects stemming from the photoemission experiment are by construction included in these calculations. These effects due to the photoemission response can be e.g. matrix element effects, surface effects, polarization effects as well as initial and final state effects. The possible impact of these ARPES related effects will be more extensively discussed in Chapter 6.

For now, the main motivation was to investigate the anisotropy of the electronic structure as already seen in the latter publication in direct comparison to ARPES experiments. In this context it is important to understand that the anisotropic properties of the low-temperature phases of the iron pnictides were not correctly observed for quite a long time. One of the first ARPES publications on $BaFe_2As_2$ from Fink *et al.*[31] in April 2009 could not resolve a difference in the electronic structure for 300 K and 20 K, respectively. Subsequently, the ARPES spectra of the low-temperature antiferromagnetic phase in $BaFe_2As_2$ and $Ba(Fe_{1-x}Co_x)_2As_2$ were resolved and they showed considerable differences from the room-temperature data.[34,35,244,245] However, the formation of twinned single crystals during the phase transition from tetragonal to orthorhombic resulted in mixed magnetic domains which are orthogonal to each other.[191,246] Thus, macroscopic tools like ARPES could only see the averaged information, while information on the anisotropy was lost. Only in 2011 first ARPES measurements on detwinned single crystals were performed[36,193], using a device to apply uniaxial stress during the measurement, effectively detwinning the sample this way. Thus, one has to distinguish three types of ARPES measurements for the $BaFe_2As_2$ family resulting in three different types of spectra. First, the spectra of the room-temperature paramagnetic phase having a distinct C_4 rotational symmetry and secondly the spectra of twinned crystals in the low-temperature antiferromagnetic phase which are typically close to C_4 symmetry due to the twinning. Additionally, there are the spectra of detwinned crystals in the antiferromagnetic phase showing the real anisotropy and having a distinct C_2 rotational symmetry. Only the last ones are interesting concerning the anisotropic properties and these were of most interest for the present work.[36,193]

Thus, the ARPES spectra of antiferromagnetic $BaFe_2As_2$ and $Ba(Fe_{1-x}Co_x)_2As_2$ were calculated by means of the one-step model of photoemission and compared to recent data of detwinned single crystals by Yin *et al.*[36]. Applying the CPA allows for a distinct study of the evolution of the anisotropic bands depending on the concentration x until x_{crit} is reached. Furthermore, the inclusion of surface effects can be used in order to discuss different surface terminations. It should be noted, that there is no real consensus about the surface termination in $BaFe_2As_2$ from experimental scanning tunneling microscopy (STM) and low-energy electron-diffraction (LEED) measurements.[247–250]

Note further, that from now on the parameters for the calculations marginally changed, leading to results closer to experiment for the magnetic moments and the critical concentration x_{crit}. For more details see Appendix A.

5.2 Publication: Physical Review B 93, 144513

Theoretical study on the anisotropic electronic structure of antiferromagnetic $BaFe_2As_2$ and Co-doped $Ba(Fe_{1-x}Co_x)_2As_2$ as seen by angle-resolved photoemission

Gerald Derondeau,[1] Jürgen Braun,[1] Hubert Ebert,[1] and Ján Minár[1,2]

[1] *Department Chemie, Physikalische Chemie, Universität München, München, Germany*
[2] *NewTechnologies-Research Center, University of West Bohemia, Pilsen, Czech Republic*

published in: Physical Review B **93**, 144513 (2016).

This publication is part of the Physical Review B Kaleidoscope from April 2016.

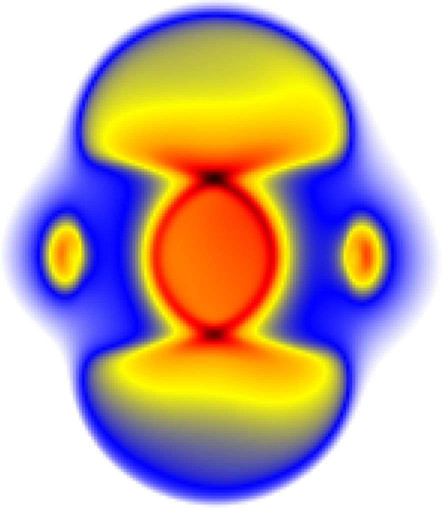

PHYSICAL REVIEW B **93**, 144513 (2016)

Theoretical study on the anisotropic electronic structure of antiferromagnetic $BaFe_2As_2$ and Co-doped $Ba(Fe_{1-x}Co_x)_2As_2$ as seen by angle-resolved photoemission

Gerald Derondeau,[1,*] Jürgen Braun,[1] Hubert Ebert,[1] and Ján Minár[1,2]
[1]*Department Chemie, Physikalische Chemie, Universität München, Butenandtstrasse 5-13, 81377 München, Germany*
[2]*New Technologies Research Center, University of West Bohemia, Pilsen, Czech Republic*

(Received 17 February 2016; revised manuscript received 14 April 2016; published 25 April 2016)

By means of one-step model calculations the strong in-plane anisotropy seen in angle-resolved photoemission of the well-known iron pnictide prototype compounds $BaFe_2As_2$ and $Ba(Fe_{1-x}Co_x)_2As_2$ in their low-temperature antiferromagnetic phases is investigated. The fully relativistic calculations are based on the Korringa-Kohn-Rostoker–Green function approach combined with the coherent potential approximation alloy theory to account for the disorder induced by Co substitution on Fe sites in a reliable way. The results of the calculations can be compared directly to experimental spectra of detwinned single crystals. One finds very good agreement with experiment and can reveal all features of the electronic structure contributing to the in-plane anisotropy. In particular the local density approximation can capture most of the correlation effects for the investigated system without the need for more advanced techniques. In addition, the evolution of the anisotropy for increasing Co concentration x in $Ba(Fe_{1-x}Co_x)_2As_2$ can be tracked almost continuously. The results are also used to discuss surface effects and it is possible to identify clear signatures to make conclusions about different types of surface termination.

DOI: 10.1103/PhysRevB.93.144513

I. INTRODUCTION

Nowadays the family of iron pnictides is a well-established and important prototype system for unconventional high-temperature superconductivity. Starting with the first famous compound $La(O_{1-x}F_x)FeAs$ [1,2] in 2008, today several different subfamilies with a wide structural variety are known.

All different groups of iron pnictides share some common physical properties, such as their interesting and sometimes puzzling magnetic behavior. Most compounds show a phase transition at low temperatures from a tetragonal to an orthorhombic crystal symmetry which is typically accompanied by the formation of long-range antiferromagnetic order [3,4]. It is common belief that the suppression of these phase transitions for example by chemical substitution is crucial for the emergence of unconventional superconductivity [5,6]. Although it is obvious that an understanding of the magnetic fluctuations in the iron pnictides is mandatory to unveil the physics underlying the superconductivity, this task has proven to be more complex than anticipated [6–8].

For example, there was discussion in the literature about whether the magnetic moments are better described by an itinerant [6,7,9–11] or a localized [12–14] model and there is up to now no consensus concerning the role of correlation effects [15–18]. Furthermore, the magnitude of the magnetic moments is difficult to reproduce within density functional theory (DFT) and it is known to be quite sensitive to computational parameters [3,8,19–21].

One of the most important experimental tools to get insight into the electronic structure of the iron pnictides is angle-resolved photoemission spectroscopy (ARPES). There are numerous publications on this topic, although it was shown that DFT calculations have typically problems in reproducing all features of the ARPES spectra correctly [17,22–25]. This is often ascribed to strong correlation effects, although this question is still under discussion [17,26,27].

Another important difficulty which so far is often ignored is the connection between the magnetic phase of the iron pnictides and the resulting consequences for ARPES. This is due to the formation of twinned crystals during the phase transition from tetragonal to orthorhombic and it results in mixed magnetic domains which are orthogonal to each other. Macroscopic tools such as ARPES or transport measurements can so only see the averaged information, while information on the anisotropy is lost [28,29]. This is a huge drawback considering a comprehensive study of the electronic structure in the iron pnictides, as it is known that the in-plane anisotropy plays a significant role [30–32]. In experiment it is possible to effectively detwin the crystals by applying uniaxial stress during the measurement. This was already done successfully for the 122-prototype $BaFe_2As_2$ in the undoped and in the Co-doped case. However, such measurements are connected with several technical difficulties and consequently they are rarely done [28,29]. Yet, to fully understand the electronic properties of the iron pnictide superconductors in a comprehensive way and to get a deeper insight concerning the influence of the in-plane anisotropy in the magnetic phase such studies are absolutely mandatory. Although there are nowadays experimental data on detwinned crystals showing clearly the anisotropy in the Fermi surface there is hardly any theoretical work focusing on this problem of magnetic anisotropy in ARPES data.

In this work this issue is addressed by a comprehensive DFT study on the magnetic phase of $Ba(Fe_{1-x}Co_x)_2As_2$ and on the corresponding ARPES spectra. The computational results can be directly compared to the available experimental ARPES data on detwinned crystals [28,29].

In order to deal with this complex situation the Korringa-Kohn-Rostoker–Green function (KKR-GF) approach is used,

---

[*] gerald.derondeau@cup.uni-muenchen.de

2469-9950/2016/93(14)/144513(10)

which was already shown to be indeed a very useful and accurate tool to deal with the iron pnictides [33]. The impact of disorder due to substitution is dealt with by means of the coherent potential approximation (CPA), giving results fully compatible with supercell calculations and more reliable than those based on the virtual crystal approximation (VCA) [33].

II. COMPUTATIONAL DETAILS

All calculations have been performed self-consistently and fully relativistically within the four component Dirac formalism, using the Munich SPR-KKR program package [34,35]. The orthorhombic, antiferromagnetic phase of $BaFe_2As_2$ is investigated in its experimentally observed stripe spin state using a full 4-Fe unit cell. This implies antiferromagnetic chains along the a and c axes and ferromagnetic chains along the b axis. The lattice parameters where chosen according to experimental x-ray data and the experimental As position z [19]. To account for the influence of substitution in $Ba(Fe_{1-x}Co_x)_2As_2$ a linear interpolation for the lattice parameters with respect to the concentration x is used based on available experimental data [19,36] and Vegard's law [37]. More details on the procedure can be found in a previous publication [33]. The treatment of disorder introduced by substitution is dealt with by means of the CPA. The basis set considered for a $l_{\max} = 4$ includes s, p, d, f, and g orbitals. For the electronic structure calculations the local density approximation (LDA) exchange-correlation potential with the parametrization given by Vosko, Wilk, and Nusair was applied [38].

The spectroscopical analysis is based on the fully relativistic one-step model of photoemission in its spin density matrix formulation. For more technical details on these calculations see Refs. [39,40]. The geometry of the spectroscopy setup was taken from experiment including a tilt of the sample around either the a or b axis. The incident light hit the sample under a constant polar angle $\theta_{\text{light}} = -45^\circ$ and an azimuthal angle ϕ_{light} of either 180° or 270°. These geometries are referred to as $\boldsymbol{q}_{||\text{AFM}}$ and $\boldsymbol{q}_{||\text{FM}}$, meaning the direction of the incident light is either parallel to the antiferromagnetic or the ferromagnetic in-plane directions. The corresponding electrons were collected with an angle ϕ_{electron} of 0° or 90° and a varying angle θ_{electron} between -15° and 15°. This geometry is in line with the experimental setup. If not indicated otherwise, an As-terminated surface was chosen. However, the question of surface termination will be discussed in more detail in the following.

Compared with previous work [33] on this compound, we increased the $l_{\max}$ expansion for better numerical results. The important difference is however the application of the one-step model of photoemission, which allows for a comprehensive spectroscopical study which is significantly more credible when discussing ARPES spectra.

III. RESULTS AND DISCUSSION

A. Magnetic moments

To describe the anisotropy of the iron pnictides in ARPES calculations reasonably well one needs first to ensure that the spin-dependent potentials from the self-consistent field (SCF) calculations are accurate enough. Obviously, the magnetic ordering plays a significant role concerning the anisotropy of the electronic structure and hence the quality of the theoretical description of the ARPES spectra is determined by the quality of the spin-dependent potentials.

The most meaningful indication for a proper description of the magnetic state is good agreement with experimental data on the magnetic order. For the iron pnictides this is known to be a nontrivial task as the magnetic moments are often overestimated by DFT [7,8,16]. For the undoped mother compound $BaFe_2As_2$ a total magnetic moment of $0.73\mu_B$ was obtained. Experiment reports a total magnetic moment of approximately $0.9\mu_B$ from neutron diffraction [3,41] while ^{57}Fe Mössbauer spectroscopy [19,42] and μSR spectroscopy [43,44] coherently give a value of around $0.5\mu_B$. Hence, the calculated total magnetic moment is found in good agreement with experiment and captures the proper order of magnitude accurately [7–9,16,45,46].

More importantly, the CPA allows us to evaluate the substitution-dependent self-consistent evolution of the magnetic moments with increasing Co concentration in $Ba(Fe_{1-x}Co_x)_2As_2$. The corresponding results are shown in Fig. 1, where the results for spin and orbital magnetic moments are given in an atom-resolved way. The total magnetic moment is calculated as a substitutionally averaged sum over all contributions.

In agreement with experiment the total magnetic moment shows a nearly linear decay until the long-range magnetic order disappears [47]. In the calculations the critical Co substitution for the disappearance of antiferromagnetic order occurs for $x_{\text{crit}} = 0.15$, which is in reasonably good agreement with the experimental value $x_{\text{crit,exp}} \approx 0.07$ [45,48]. It should be mentioned that the results in Fig. 1 are slightly improved with respect to experiment in comparison with our previous work [33] due to the higher $l_{\max}$ expansion used here.

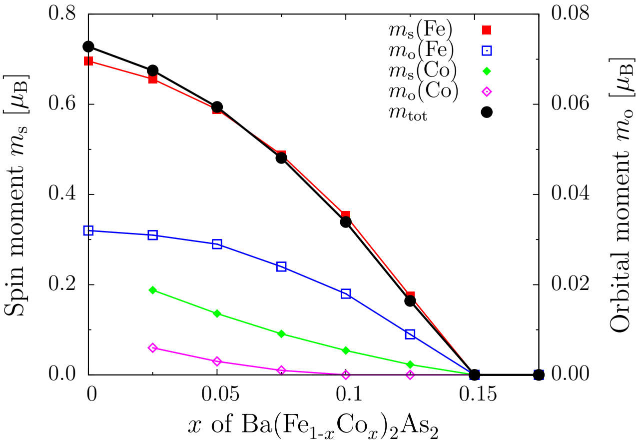

FIG. 1. Magnetic spin moments (m_s) and orbital moments (m_o) of Fe and Co for increasing Co substitution x. The black line corresponds to the total (spin and orbital) magnetic moment which is the substitutionally averaged sum over all other contributions. The left axis corresponds to the spin magnetic moments m_s, while the right axis shows the orbital magnetic moments m_o.

However, the trends in the magnetic moments and the resulting conclusions are the same.

B. Anisotropy of the undoped compound

As the one-step model of photoemission fully accounts for matrix elements as well as for surface effects the resulting spectra can be directly compared to experimental ARPES data.

As stressed before, it is extremely difficult to see the magnetic anisotropy correctly in experimental spectra because of the twinning of crystals. Here reference is made especially to the work of Yi *et al.* [28], who did remarkable measurements on detwinned single crystals of $BaFe_2As_2$ and $Ba(Fe_{1-x}Co_x)_2As_2$ by applying uniaxial stress to the crystals. Similar results were obtained for example by Kim *et al.* [29]. In this context it is important to note that the Brillouin zone (BZ) of the magnetic 4-Fe spin-density-wave (SDW) state is only half the size compared to the BZ in the nonmagnetic 2-Fe state. For that reason it is most appropriate to use in the following notation for the 4-Fe SDW BZ where the information of $\bar{\Gamma}$ and $\bar{X}$ from the nonmagnetic BZ is down-folded to one $\bar{\Gamma}$ point [28,49].

In Fig. 2 the Fermi surface around the $\bar{\Gamma}$ point is shown in the SDW BZ as calculated from the spin-dependent potentials for a photon energy of $h\nu = 22$ eV. The overlay of black points corresponds to the experimentally measured BZ, reproduced from the work of Yi *et al.* [28]. As can be seen, the agreement of the calculated Fermi surface and the experimental data is remarkably good. Characteristic are the bright intensity spots along the $\boldsymbol{k}_x$ direction (i.e., along a), corresponding directly to the antiferromagnetic order along the a axis and the bigger pedal-like structures along the $\boldsymbol{k}_y$ direction (i.e., along b) which corresponds to the ferromagnetic order along the b axis.

It should be noted that in Fig. 2 the intensity over two different light polarizations was averaged, namely for the direction of the incident light either parallel to the antiferromagnetic a axis $\boldsymbol{q}_{||\mathrm{AFM}}$ or parallel to the ferromagnetic b axis $\boldsymbol{q}_{||\mathrm{FM}}$. All features of the electronic structure are visible for both polarizations of light. However, the intensity patterns vary notably with the polarization due to matrix element effects, indicating strong multiorbital character, just as seen in experiment [28]. If not indicated otherwise this averaging will be applied in the following. For comparison the two contributions to the total Fermi surface for $h\nu = 22$ eV are shown polarization-resolved in Fig. 3, for the incident light direction being either parallel to the b-axis $\boldsymbol{q}_{||\mathrm{FM}}$ [Fig. 3(a)] or parallel to the a-axis $\boldsymbol{q}_{||\mathrm{AFM}}$ [Fig. 3(b)].

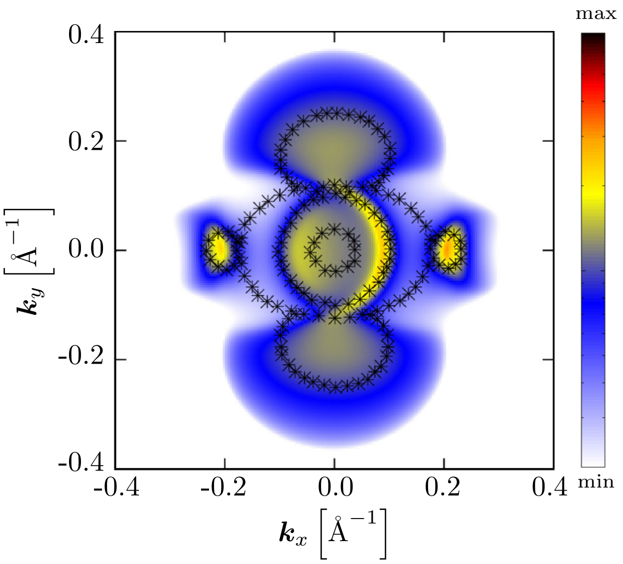

FIG. 2. Calculated ARPES spectrum mapping the Fermi surface of $BaFe_2As_2$ at $\bar{\Gamma}$ in the 4-Fe SDW BZ for a photon energy of $h\nu = 22$ eV. The overlay of black points is a reconstruction of the SDW BZ from experimental ARPES data, reproduced from the work of Yi *et al.* [28].

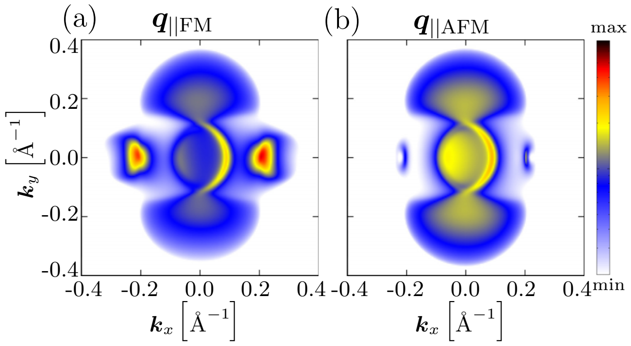

FIG. 3. Calculated ARPES spectra mapping the Fermi surface of $BaFe_2As_2$ for the polarization of light being either parallel to the ferromagnetic b axis (a) or parallel to the antiferromagnetic a axis (b).

It can be seen that for $\boldsymbol{q}_{||\mathrm{FM}}$ the intensity of the bright spots along the a axis is significantly enhanced while for $\boldsymbol{q}_{||\mathrm{AFM}}$ the intensity around the inner circle of $\bar{\Gamma}$ is enhanced. This polarization dependence is again in full agreement with the experimental findings [28].

At this point it was shown that the detwinned, antiferromagnetic Fermi surface obtained by the calculations agrees very well with experiment. One may also ask how the Fermi surface of a twinned, antiferromagnetic crystal should look and how does it differ from the nonmagnetic case. Therefore, the calculated Fermi surfaces for both cases are shown in Fig. 4 and compared with experimental ARPES data [49] of twinned $BaFe_2As_2$ crystals at $T = 150$ K (a) and $T = 10$ K (b). Please note that the transition from a paramagnetic to an antiferromagnetic state occurs at around $T = 140$ K; accordingly the experimental data shown as overlay of black points corresponds to the nonmagnetic and the twinned antiferromagnetic state, respectively. The representation of the twinned Fermi surface is based on a superposition of spectra obtained independently for antiferromagnetic states rotated by 90° against each other which is supposed to be a good approximation for twinned crystals; see for example the work of Tanatar *et al.* [50].

Comparing the nonmagnetic and the twinned antiferromagnetic state with each other it is obvious that there is a significant difference in the shape of the Fermi surface which is due to the underlying change of the electronic structure during the magnetic phase transition. However, the twinned Fermi surface is in principle isotropic along $\boldsymbol{k}_x$ and $\boldsymbol{k}_y$ due to the fact that the in-plane anisotropy cancels

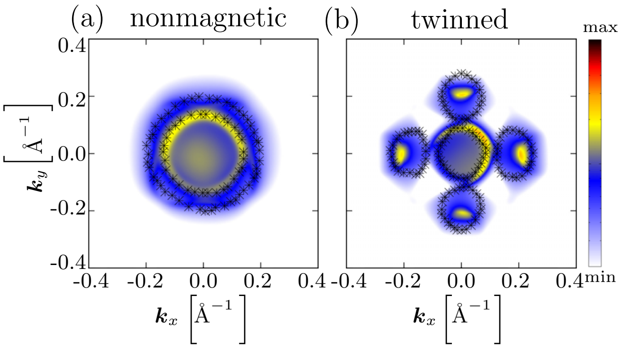

FIG. 4. Calculated Fermi surfaces of $BaFe_2As_2$ as seen by ARPES for the nonmagnetic phase (a) and a hypothetical twinned magnetic phase (b). The twinned calculation is based on a superposition of two antiferromagnetic cells which are rotated by 90° against each other. The overlay of black points is reproduced from the experimental ARPES data of Yi *et al.* [49].

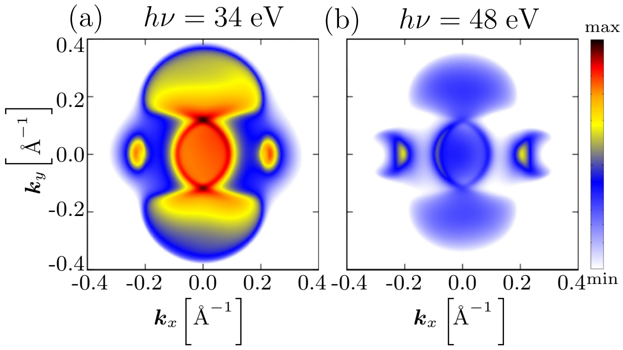

FIG. 6. Calculated Fermi surfaces of $BaFe_2As_2$ for two additional photon energies $h\nu = 34$ eV and $h\nu = 48$ eV, corresponding to either Z (a) or to Γ (b). It can be seen that the topology of interest, namely the anisotropic features, are principally independent of $\boldsymbol{k}_z$.

almost completely for two magnetic domains that are rotated by 90° against each other. This means that although some influence of the magnetic ordering can be seen for twinned crystals, it is not possible to deduce information about the important in-plane anisotropy from the corresponding spectra. This stresses again the importance of ARPES measurements and calculations on detwinned crystals to investigate the magnetic structure correctly. To summarize, the agreement of the calculations with the experimental data is altogether quite good for the nonmagnetic as well as for the twinned magnetic state.

Going back to the original study of detwinned antiferromagnetic crystals the $\boldsymbol{k}_z$ dispersion is shown along the *a* and *b* axes in Fig. 5. The difference between Γ and Z manifests itself mainly by the alternating intensity distributions. We find Γ for photon energies of $h\nu = 22$ eV and $h\nu = 48$ eV, respectively, while Z can be found at $h\nu = 34$ eV. This is in good agreement with literature which reports Z at $h\nu = 35$ eV and Γ at $h\nu = 49$ eV [51]. The anisotropic features, namely the bright spots along $\boldsymbol{k}_x$ and the pedals along $\boldsymbol{k}_y$, seem quite independent of $\boldsymbol{k}_z$, which agrees with the experimental reports on the detwinned crystals [28]. For further discussion the Fermi surfaces for $h\nu = 34$ eV and $h\nu = 48$ eV, respectively, are shown in Fig. 6. The important aspect to note is that the anisotropic features are preserved independently of $\boldsymbol{k}_z$, meaning they are preserved for Γ as well as for Z. However, the most striking anisotropy between the *a* and *b* directions seen in the $\boldsymbol{k}_z$ dispersion is the almost vertical intensity lines along the *a* axis for $\boldsymbol{k}_x \approx \pm 0.2$ Å. They are surprisingly robust concerning the $\boldsymbol{k}_z$ dispersion, already indicating possible surface-related phenomena, as will be discussed later in more detail.

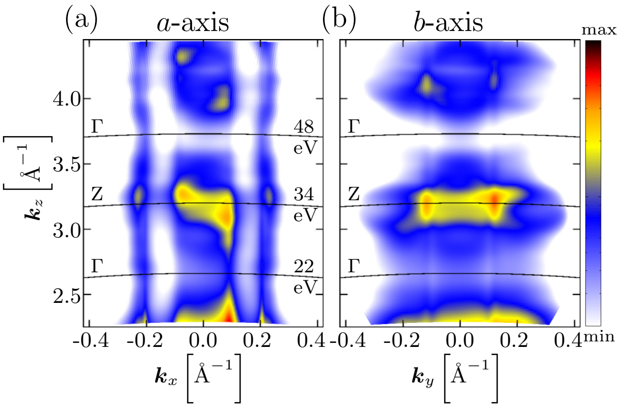

FIG. 5. Calculated $\boldsymbol{k}_z$ dispersion of $BaFe_2As_2$ as seen by ARPES along both the in-plane real-space axes *a* (a) and *b* (b). The black lines mark the photon energies where the alternation of Γ and Z can be seen along $\boldsymbol{k}_z$. Notably, the vertical intensity stripes at $\boldsymbol{k}_x \approx \pm 0.2$ Å in (a) seem almost independent of $\boldsymbol{k}_z$, indicating some connection to a surface-related phenomenon.

To complete the study of the in-plane anisotropy in the undoped compound the spin-dependent bands are investigated polarization-dependently along the two in-plane directions *a* and *b* for $h\nu = 22$ eV and for comparison the isotropic bands of the nonmagnetic case. Anisotropies due to the orthorhombic lattice distortion for the nonmagnetic case are very small and have no significant influence, as shown also in earlier work [33].

The nonmagnetic bands for the polarizations $\boldsymbol{q}_{||\mathrm{FM}}$ and $\boldsymbol{q}_{||\mathrm{AFM}}$ are shown in Figs. 7(b) and 7(e), respectively. Already for the nonmagnetic case it becomes obvious that more information can be deduced for light with a polarization parallel to the ferromagnetic chains. For a perpendicular light polarization the intensity for some bands decreases so strongly that they practically seem to vanish. This is however not due to a vanishing of the bands but only due to the strong intensity variation, i.e., matrix element effects, as already mentioned before and as seen in experiment.

For the spin-polarized band structure with antiferromagnetic order along the *a* axis the corresponding cases for $\boldsymbol{q}_{||\mathrm{FM}}$ and $\boldsymbol{q}_{||\mathrm{AFM}}$ are shown in Figs. 7(a) and 7(d), respectively. The green solid lines are guides to the eye which emphasize the two important anisotropic bands in these spectra. First of all, there is some significant reorientation of the bands compared to the nonmagnetic case. Most striking is the appearance of a steep W-shaped band which was not visible in the nonmagnetic case. This new appearance is most likely due to down-folding of the Brillouin zone when going from the 2-Fe cell to a magnetic

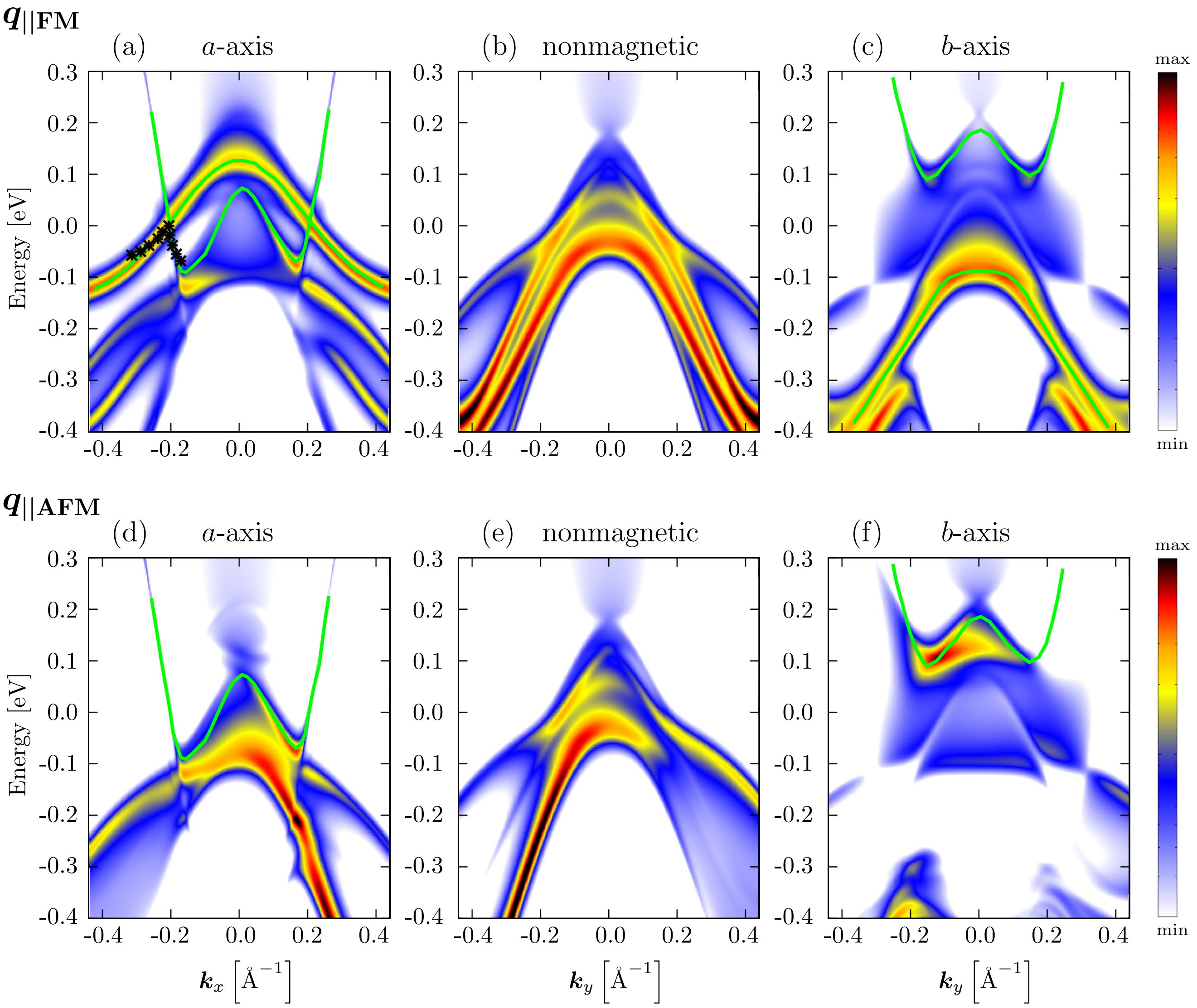

FIG. 7. Calculated bands of $\mathrm{BaFe_2As_2}$ as seen by ARPES depending on the polarization of light, $\boldsymbol{q}_{||\mathrm{FM}}$ [(a)–(c)] and $\boldsymbol{q}_{||\mathrm{AFM}}$ [(d)–(f)], as well as on the orientation of the magnetic phase, either along the antiferromagnetic *a* axis [(a) and (d)] or along the ferromagnetic *b* axis [(c) and (d)]. The band structure of the nonmagnetic phase is shown for comparison in (b) and (e). The solid green lines are guides to the eye for the important anisotropic bands in the magnetic phase. The black points in (a) are reproduced from experimental data of Yi *et al.* [28] indicating the cut at the Fermi level for the two important anisotropic bands along the *a* axis as seen by ARPES.

4-Fe cell. The second important band is a pure hole pocket which is compared to the nonmagnetic case shifted to higher binding energies. It should be noted that the intensity of this band is extremely polarization dependent. It is the dominating band for $\boldsymbol{q}_{||\mathrm{FM}}$ while it is barely visible for $\boldsymbol{q}_{||\mathrm{FM}}$. Comparing with the polarization dependent Fermi surface in Fig. 3 it is obvious that this band is also part of the bright intensity spots in the Fermi surface along the *a* direction and very characteristic for the anisotropy. It is also noteworthy that these two significant bands cross each other exactly at the Fermi level. This crossing is also reported in experiment as can be seen from the black points in Fig. 7(a), which are reproduced from the experimental ARPES data of Yi *et al.* [28]. Thus, the experimental ARPES data could be again well reproduced by the calculations.

The situation for the magnetic bands with ferromagnetic order along the *b* axis as shown in Figs. 7(c) and 7(f) is in many aspects similar to that for the bands along the *a* direction. One can identify two prominent anisotropic bands, one with a W-like shape which has a higher intensity for a light polarization of $\boldsymbol{q}_{||\mathrm{AFM}}$, while the other band marked with the solid green line is the dominating one for light $\boldsymbol{q}_{||\mathrm{FM}}$. The important difference is that these bands do not touch each other as they are significantly shifted away in binding energy. Note that also no crossing is reported in experiment [28]. Why these steep bands with the W shape cannot be seen in experiment for the *b* direction also becomes clear: The responsible band is simply completely shifted above the Fermi level. This observation can in principle be compared to the band splitting in ferromagnets. Note that along the *b* axis there is ferromagnetic coupling while along the *a* axis the magnetic order is antiferromagnetic. Thus, for $BaFe_2As_2$ one sees along the ferromagnetic chains a band splitting of approximately 0.2 eV for a magnetic moment around $0.7\mu_B$. This is comparable for example to Ni which shows a band splitting of approximately 0.3 eV for a moment of approximately $0.6\mu_B$ [52]. Consequently, for decreasing magnetic moments upon alloying one expects a reduced band splitting together with a continuous matching of the anisotropic bands. To investigate this issue in further detail one has to look at the evolution of the ARPES band structure for increasing Co substitution on the Fe position which goes in hand with the reduction of the magnetic moments.

C. Influence of Co substitution on the anisotropy

Substitution of Fe with Co in $Ba(Fe_{1-x}Co_x)_2As_2$ is one of the common ways to induce superconductivity in $BaFe_2As_2$ by electron doping. The substitution does consequently diminish the strength of the antiferromagnetic coupling within this compound until the long-range magnetic order collapses and superconductivity emerges [36,48]. As the strength of the magnetic order decreases with Co doping, in experiment as well as in the calculations, it can be assumed that the strong in-plane anisotropy does also decrease. The breakdown of the long-range antiferromagnetic order in Fig. 1 appears for a somewhat higher Co concentration than in experiment. Thus, the breakdown of the anisotropy is expected at higher doping levels. This is true for a concentration of $x = 0.15$ in $Ba(Fe_{1-x}Co_x)_2As_2$ which is the first substitution level where the magnetic order did completely vanish in the self-consistent calculation. Considering the evolution of the magnetic moments in Fig. 1 one can see that the initial magnetic moment decreased to approximately 75%, 50%, and 25% of the original value for Co substitutions of $x = 0.05$, 0.10, and 0.125, respectively.

To investigate the impact of alloying in detail, the ARPES band structure for these concentrations including the already nonmagnetic $x = 0.15$ for both directions *a* and *b* is presented in Fig. 8. The calculations are performed for $h\nu = 22$ eV

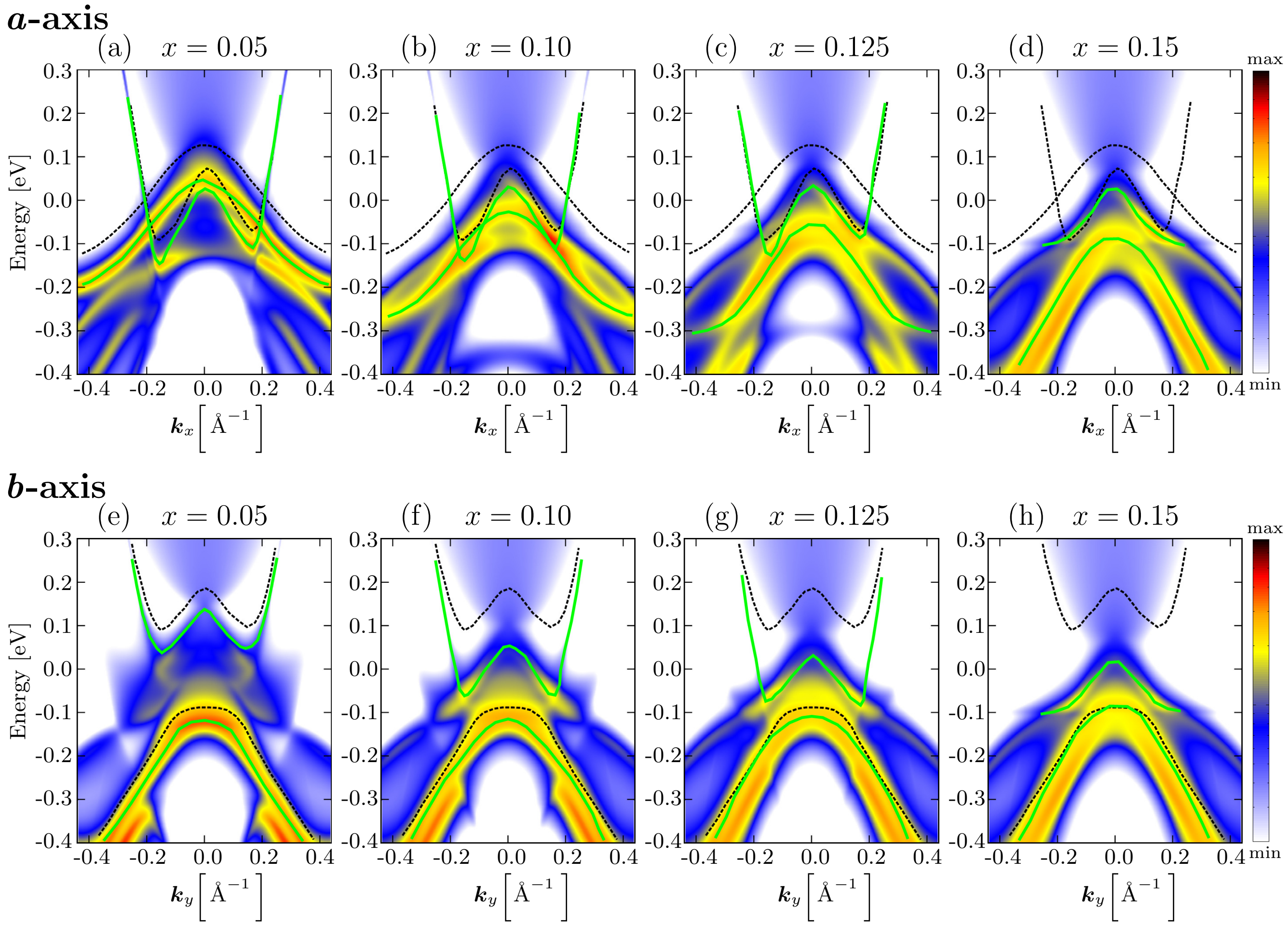

FIG. 8. Calculated bands of $Ba(Fe_{1-x}Co_x)_2As_2$ as seen by ARPES for different Co concentrations *x* depending on the axes *a* [(a)–(d)] and *b* [(e)–(h)] with a constant light polarization of $\boldsymbol{q}_{||FM}$ to easily identify the important bands. The black dashed lines correspond to the initial position of the anisotropic bands in the undoped compound; see Fig. 7. The green solid lines are guides to the eye for the corresponding important anisotropic bands to see their change under increasing Co substitution. Their anisotropy vanishes together with the long-range antiferromagnetic order at $x = 0.15$.

comparable to Fig. 7 but they are only shown for a light polarization of $\boldsymbol{q}_{||\mathrm{FM}}$ because it was already clarified that the anisotropic bands can be best seen with this specific polarization. The black dashed lines in Fig. 8 are shown for comparison and they correspond to the band position of the anisotropic bands in the undoped compound $\mathrm{BaFe_2As_2}$ with the highest anisotropy, seen in Figs. 7(a) and 7(c). The green solid lines are guides to the eye to identify more easily the corresponding anisotropic bands for the specific Co concentrations. The difference between black dashed lines and green solid lines is thus the change of the original anisotropy with increasing Co substitution. For the case of the nonmagnetic $\mathrm{Ba(Fe_{1-\mathit{x}}Co_{\mathit{x}})_2As_2}$ with $x = 0.15$ shown in Figs. 8(d) and 8(h) the anisotropy has completely vanished and the band structures coincide with each other. This could be expected from experiment and is reproduced in the calculations. It should be noted again at this point that the crystal lattice is still orthorhombic; however, the lattice anisotropy is indeed too weak to be visible in the band structure [33].

Some other interesting findings can be deduced from the evolution of the band structure upon Co substitution. First of all the intensity of the W-shaped band decreases continuously; however, it only completely disappears after the collapse of the long-range antiferromagnetic order. The change in anisotropy for the antiferromagnetic order along the a axis is mostly characterized with the consequent shift of the hole pocket to lower binding energies. This is also experimentally reported for a decrease in the magnetic coupling strength, either induced through Co doping or increasing temperature [28]. Concerning this situation for the ferromagnetic order along the b axis the most prominent feature is the shift of the W-shaped band to lower binding energies. What can be seen in Figs. 7(e) to 7(h) is that the energy difference of these two main anisotropic bands does strongly and continuously decrease. This is in agreement with the assumption of a smaller band splitting for decreasing ferromagnetic coupling strength.

In summary one can say that for the antiferromagnetic order along the a axis mostly the hole pocket changes while the W-shaped band stays more or less constant. For the ferromagnetic order along the b axis it is the other way round. The W-shaped band undergoes the strongest change while the other band stays more or less unchanged in energy and shape. The final result is the same in both cases, a matching of the bands and a consequent isotropic in-plane band structure. This detailed analysis allows us to follow the change from the strong in-plane anisotropy of the undoped compound to the isotropic behavior in the Co-substituted system in a continuous way with direct correspondence to ARPES. Thus, this approach based on KKR-CPA proves its advantages for investigating the iron pnictide superconductors at regions of interest which are difficult to evaluate by means of other band structure methods.

D. Surface termination

Using the one-step model of photoemission one can identify different surface states and can thus clarify the origin of surface bands. The reason for the occurrence of surface states has long been developed in multiple scattering theory, which is the underlying basis of the SPR-KKR method [53,54]. The so-called determinant condition uses the reflection matrices of the bulk crystal $\boldsymbol{R}_\mathrm{b}$ and of the surface barrier potential $\boldsymbol{R}_\mathrm{v}$, which connects the inner potential of the bulk crystal with the vacuum level. The appearance of a surface state is given by the following condition:

$$D(E,\boldsymbol{k}) = \det\left[\mathbb{1} - \boldsymbol{R}_\mathrm{b}(E,\boldsymbol{k})\boldsymbol{R}_\mathrm{v}(E,\boldsymbol{k})\right] = 0. \tag{1}$$

For better visualization we plot $1/|D(E,\boldsymbol{k})|$ in the following. If this expression is bigger than approximately 10^3 we speak about a surface state. For values between 10^0 and 10^3 the state is defined as a so-called surface resonance. For values below one has bulk states. More details can be found in the overview by Braun and Donath [55].

The application of this determinant approach is demonstrated in Fig. 9. Here one can see the Fermi surfaces and the band structures along the a axis for an As-terminated and a Ba-terminated surface, respectively, together with the corresponding plot of $1/|D(E,\boldsymbol{k})|$ on the right-hand side of each picture. The bands are shown for $h\nu = 22$ eV and they are averaged over the two light polarizations $\boldsymbol{q}_{||\mathrm{FM}}$ and $\boldsymbol{q}_{||\mathrm{AFM}}$ in order to make all relevant contributions equally visible.

It should be noted that the determinant condition itself and without a high intensity in the corresponding band structure plot is only an indication for a surface state or a surface resonance. Only if a high intensity in the $1/|D(E,\boldsymbol{k})|$ plot coincides with a band in the band structure can one associate this band with a clear surface character. For example, the bright octagon shape of the determinant plot of the Fermi surface in Fig. 9(a) does not have a corresponding counterpart in the band structure plot. The two high-intensity spots along the a axis which are equally visible on the Fermi surface as well as in the determinant condition are in clear contrast to this behavior. Thus, this feature has a surface-related origin, more specifically a surface state as the intensity of $1/|D(E,\boldsymbol{k})|$ is on the order of 10^6.

This surface state can be also identified in the band structure along the a axis as shown in Fig. 9(b) where a strong intensity in the determinant plot coincides with the steep bands that cut the Fermi level and which are part of the already discussed W shape. Consequently, these bands can be identified as surface states. This is in accordance with the earlier findings for the $\boldsymbol{k}_z$ dispersion in Fig. 5(a) where the vertical intensities at $\boldsymbol{k}_x \approx \pm 0.2$ Å were independent of $\boldsymbol{k}_z$, indicating a connection to a surface-related phenomenon.

Another verification for the surface-related origin of these bands is shown in Figs. 9(c) and 9(d), where the corresponding Fermi surface and band structure are shown for a Ba-terminated surface. As already indicated before all other calculations presented in this paper are under the assumption of an As-terminated surface. Obviously, the assumed surface termination has also an influence on surface-related phenomena and surface states might be shifted significantly in energy. Indeed, the surface states discussed for the As-terminated surface have completely vanished in the Ba-terminated case. The corresponding high intensities are missing in the $1/|D(E,\boldsymbol{k})|$ plots and in the band structure of Fig. 9(d) the characteristic steep bands from the As-terminated surface have also vanished. No intensities in the determinant plot coincide with features in the band structure and thus surface effects have been removed

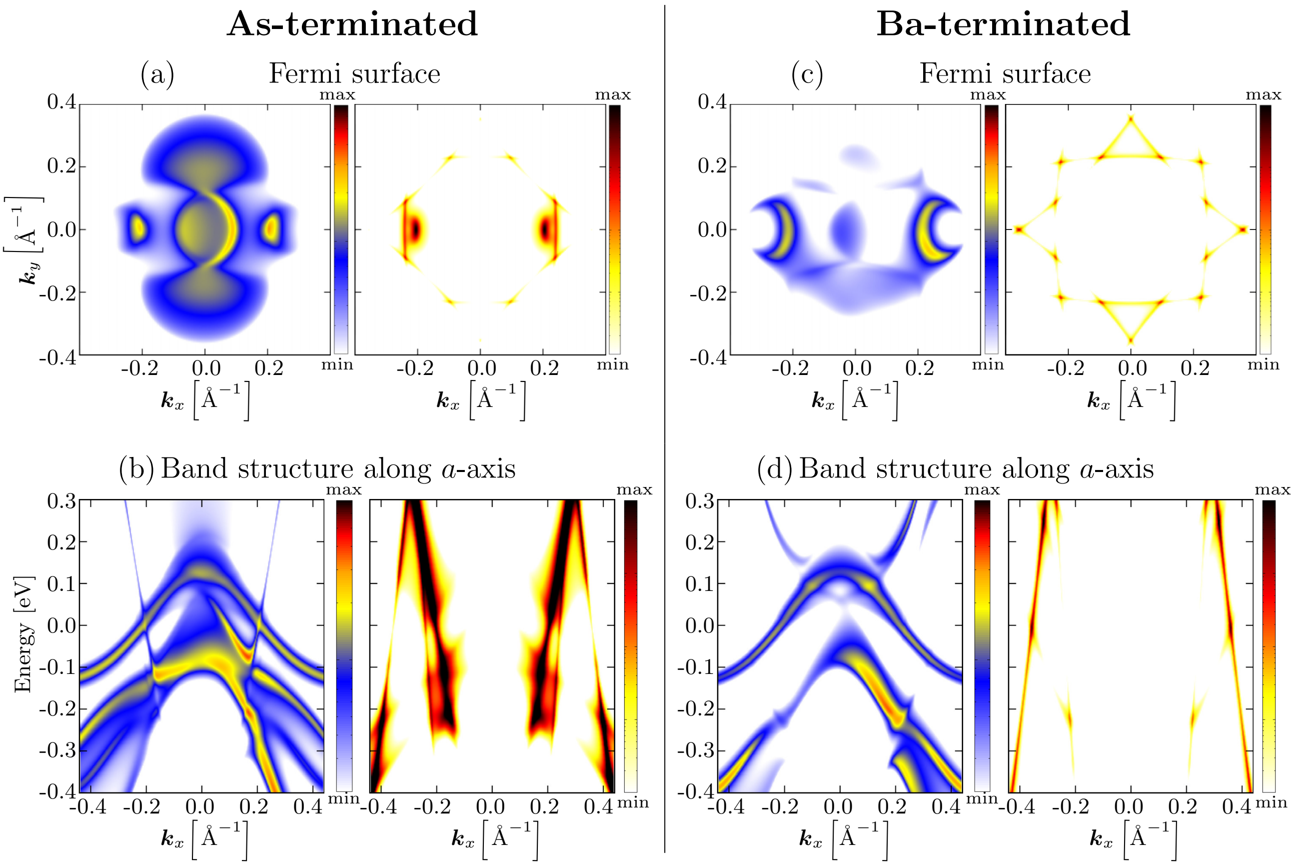

FIG. 9. Calculated Fermi surfaces and band structures of $BaFe_2As_2$ for either an As-terminated surface [(a) and (b)] or a Ba-terminated surface [(c) and (d)]. The right side of each panel shows the corresponding plot of $1/|D(E,\boldsymbol{k})|$, meaning a high intensity indicates a possible surface state if this specific structure can be also identified in the regular electronic structure calculation. Clear surface states can be identified for the As-terminated surface as bright spots in the Fermi surface (a) and as corresponding steep bands in the band structure (b). These surface states are missing for a Ba-terminated surface.

by the Ba termination. Overall, the Fermi surface and the band structure have undergone significant changes for the altered surface termination. The characteristic anisotropic features of the Fermi surface in Fig. 9(a) are hardly visible in the Ba-terminated case in Fig. 9(c). It seems like the Ba layer on top acts as some kind of damping layer which reduces the intensity and blurs the electronic states which are clearly visible in an As-terminated surface. In particular one has to note that the agreement with experimental ARPES data is significantly better for an As-terminated surface compared to the Ba-terminated one. Especially the steep bands along the *a* axis are seen in experiment [28] and they could be successfully identified as surface states which are only visible for an As-terminated surface.

This result can be used for conclusions on the most likely surface termination of $BaFe_2As_2$. Interestingly, the surface termination in this material is still not clear and under debate, although several experimental measurements and theoretical calculations exist [56]. According to first-principles calculations only three possibilities for the surface termination exist, namely a fully As-terminated or a fully Ba-terminated surface as well as an As surface covered with half of the stoichiometric Ba atoms [57]. There are experimental scanning tunneling microscopy (STM) and low-energy electron-diffraction (LEED) measurements which indicate a Ba-terminated surface [58]. However, there are also experimental STM+LEED data which clearly favor an As-terminated surface [59]. The ARPES calculations clearly favor an As-terminated surface as it was shown that agreement with experiment is considerably better compared to the Ba-terminated one. This cannot rule out the possibility of some partial covering with few Ba adatoms but one can state that every Ba atom on top muffles the electronic structure seen in experiment and that this structure is due to an As-terminated compound. So one would expect a more or less clean As-terminated surface as the most probable surface termination for $BaFe_2As_2$. Additional covering with some Ba atoms might be possible but also might have some degrading influence on the quality of the ARPES measurement.

IV. SUMMARY

The Munich SPR-KKR package was used for self-consistent and fully relativistic calculations of orthorhombic $Ba(Fe_{1-x}Co_x)_2As_2$ in its experimentally observed stripe antiferromagnetic ground state for $x = 0.0$ up to $x = 0.15$. The substitutional disorder induced by Co on Fe positions was dealt with on a CPA level which was earlier shown to be fully equal to a comprehensive supercell calculation [33]. Magnetic moments of $0.73\mu_B$ for undoped $BaFe_2As_2$ were reproduced and additionally a reasonable magnetic behavior for increasing Co substitution with a continuous decrease of the magnetic moments until a collapse of the antiferromagnetic order at 15% Co concentration was reached. This is in good agreement with experimental behavior [41,42,48].

Concerning ARPES most experimental data available are actually insufficient to talk about in-plane anisotropy due to twinning effects during the phase transition from the nonmagnetic tetragonal to the antiferromagnetic orthorhombic phase. A complicated detwinning process, typically with uniaxial stress on the single crystal, is necessary to gain anisotropic data of the electronic structure [28,29]. Referring to the available experimental data it was possible to reproduce the electronic structure of $BaFe_2As_2$ in very good agreement with experiment. The Fermi surface shows all important anisotropic features, namely some bright spots of intensity along the antiferromagnetic order along the a axis and more blurred pedals along the ferromagnetic order along the b axis. Also in agreement with experiment a strong dependence on the polarization of light was found, being either parallel to the ferromagnetic or to the antiferromagnetic order, indicating the strong multiorbital character. For comparison the Fermi surface of the nonmagnetic phase as well as a hypothetical Fermi surface for a twinned ARPES measurement as a superposition of two antiferromagnetic cells rotated by 90° to each other was shown. Both were again in agreement with experiment. In addition to the anisotropic $\boldsymbol{k}_z$ dispersion some focus was put on the anisotropic band structure along the a and b axes and it was compared to the nonmagnetic case. One could identify the important anisotropic bands and these could be interpreted in terms of band splitting for the ferromagnetic chains along the b axis, principally comparable to typical ferromagnetic band splitting as observed for example in Ni.

In addition the evolution of these anisotropic bands for small steps of x in $Ba(Fe_{1-x}Co_x)_2As_2$ was presented until the breakdown of long-range antiferromagnetic order. The decreasing band splitting and a continuous matching of the anisotropic bands could be reproduced in great detail and consistent with experimental findings.

Finally the so-called determinant condition $1/|D(E,\boldsymbol{k})|$ was used to evaluate possible surface states of the band structure. It was possible to identify steep bands along the a axis as surface states. These are at least partially responsible for the characteristic bright intensity spots in the electronic structure along the a axis and can also be seen in experiment. Interestingly, these surface states are only visible near the Fermi level for an As-terminated surface. It was shown that a Ba-terminated top layer acts as some kind of damping which moves the surface states far away and blurs the electronic structure. Significantly better agreement with experimental data is found for an As-terminated surface. This leads to the conclusion that an As-terminated surface would be most likely, an issue that is in fact experimentally not convincingly clarified [56,58,59]. Some Ba adatoms might be still possible but one would expect a negative influence on the quality of the measurements.

To conclude, this publication was successful in reproducing the strong in-plane anisotropy of $BaFe_2As_2$ and its behavior under substitution in very good agreement with experiment using ARPES calculations. These calculations allow even predictions on possible surface terminations.

ACKNOWLEDGMENTS

We acknowledge financial support from the Deutsche Forschungsgemeinschaft DFG (Project No. FOR 1346) and from the Bundesministerium für Bildung und Forschung BMBF (Project No. 05K13WMA). We further acknowledge support from CENTEM PLUS (L01402).

[1] Y. Kamihara, T. Watanabe, M. Hirano, and H. Hosono, J. Am. Chem. Soc. **130**, 3296 (2008).

[2] H. Takahashi, K. Igawa, K. Arii, Y. Kamihara, M. Hirano, and H. Hosono, Nature (London) **453**, 376 (2008).

[3] Y. Su, P. Link, A. Schneidewind, T. Wolf, P. Adelmann, Y. Xiao, M. Meven, R. Mittal, M. Rotter, D. Johrendt, T. Brueckel, and M. Loewenhaupt, Phys. Rev. B **79**, 064504 (2009).

[4] Z. P. Yin, S. Lebègue, M. J. Han, B. P. Neal, S. Y. Savrasov, and W. E. Pickett, Phys. Rev. Lett. **101**, 047001 (2008).

[5] D. J. Singh, Phys. Rev. B **78**, 094511 (2008).

[6] I. I. Mazin, D. J. Singh, M. D. Johannes, and M. H. Du, Phys. Rev. Lett. **101**, 057003 (2008).

[7] I. I. Mazin and M. D. Johannes, Nat. Phys. **5**, 141 (2009).

[8] I. I. Mazin, M. D. Johannes, L. Boeri, K. Koepernik, and D. J. Singh, Phys. Rev. B **78**, 085104 (2008).

[9] A. N. Yaresko, G.-Q. Liu, V. N. Antonov, and O. K. Andersen, Phys. Rev. B **79**, 144421 (2009).

[10] I. Opahle, H. C. Kandpal, Y. Zhang, C. Gros, and R. Valentí, Phys. Rev. B **79**, 024509 (2009).

[11] J. Fink, S. Thirupathaiah, R. Ovsyannikov, H. A. Dürr, R. Follath, Y. Huang, S. de Jong, M. S. Golden, Y.-Z. Zhang, H. O. Jeschke, R. Valentí, C. Felser, S. Dastjani Farahani, M. Rotter, and D. Johrendt, Phys. Rev. B **79**, 155118 (2009).

[12] M. J. Han, Q. Yin, W. E. Pickett, and S. Y. Savrasov, Phys. Rev. Lett. **102**, 107003 (2009).

[13] L. X. Yang, Y. Zhang, H. W. Ou, J. F. Zhao, D. W. Shen, B. Zhou, J. Wei, F. Chen, M. Xu, C. He, Y. Chen, Z. D. Wang, X. F. Wang, T. Wu, G. Wu, X. H. Chen, M. Arita, K. Shimada, M. Taniguchi, Z. Y. Lu, T. Xiang, and D. L. Feng, Phys. Rev. Lett. **102**, 107002 (2009).

[14] L. Craco, M. S. Laad, S. Leoni, and H. Rosner, Phys. Rev. B **78**, 134511 (2008).

[15] M. D. Johannes and I. I. Mazin, Phys. Rev. B **79**, 220510 (2009).

[16] A. Sanna, F. Bernardini, G. Profeta, S. Sharma, J. K. Dewhurst, A. Lucarelli, L. Degiorgi, E. K. U. Gross, and S. Massidda, Phys. Rev. B **83**, 054502 (2011).

[17] P. Werner, M. Casula, T. Miyake, F. Aryasetiawan, A. J. Millis, and S. Biermann, Nat. Phys. **8**, 331 (2012).

[18] D. H. Lu, M. Yi, S.-K. Mo, A. S. Erickson, J. Analytis, J.-H. Chu, D. J. Singh, Z. Hussain, T. H. Geballe, I. R. Fisher, and Z.-X. Shen, Nature (London) **455**, 81 (2008).

[19] M. Rotter, M. Tegel, D. Johrendt, I. Schellenberg, W. Hermes, and R. Pöttgen, Phys. Rev. B **78**, 020503 (2008).

[20] H. Gretarsson, A. Lupascu, J. Kim, D. Casa, T. Gog, W. Wu, S. R. Julian, Z. J. Xu, J. S. Wen, G. D. Gu, R. H. Yuan, Z. G. Chen, N.-L. Wang, S. Khim, K. H. Kim, M. Ishikado, I. Jarrige, S. Shamoto, J.-H. Chu, I. R. Fisher, and Y.-J. Kim, Phys. Rev. B **84**, 100509 (2011).

[21] P. Vilmercati, A. Fedorov, F. Bondino, F. Offi, G. Panaccione, P. Lacovig, L. Simonelli, M. A. McGuire, A. S. M. Sefat, D. Mandrus, B. C. Sales, T. Egami, W. Ku, and N. Mannella, Phys. Rev. B **85**, 220503 (2012).

[22] V. B. Zabolotnyy, D. S. Inosov, D. V. Evtushinsky, A. Koitzsch, A. A. Kordyuk, G. L. Sun, J. T. Park, D. Haug, V. Hinkov, A. V. Boris, C. T. Lin, M. Knupfer, A. N. Yaresko, B. Buchner, A. Varykhalov, R. Follath, and S. V. Borisenko, Nature (London) **457**, 569 (2009).

[23] D. V. Evtushinsky, D. S. Inosov, V. B. Zabolotnyy, A. Koitzsch, M. Knupfer, B. Büchner, M. S. Viazovska, G. L. Sun, V. Hinkov, A. V. Boris, C. T. Lin, B. Keimer, A. Varykhalov, A. A. Kordyuk, and S. V. Borisenko, Phys. Rev. B **79**, 054517 (2009).

[24] D. V. Evtushinsky, D. S. Inosov, V. B. Zabolotnyy, M. S. Viazovska, R. Khasanov, A. Amato, H.-H. Klauss, H. Luetkens, C. Niedermayer, G. L. Sun, V. Hinkov, C. T. Lin, A. Varykhalov, A. Koitzsch, M. Knupfer, B. Bchner, A. A. Kordyuk, and S. V. Borisenko, New J. Phys. **11**, 055069 (2009).

[25] D. V. Evtushinsky, V. B. Zabolotnyy, T. K. Kim, A. A. Kordyuk, A. N. Yaresko, J. Maletz, S. Aswartham, S. Wurmehl, A. V. Boris, D. L. Sun, C. T. Lin, B. Shen, H. H. Wen, A. Varykhalov, R. Follath, B. Büchner, and S. V. Borisenko, Phys. Rev. B **89**, 064514 (2014).

[26] Z. P. Yin, K. Haule, and G. Kotliar, Nat. Phys. **7**, 294 (2011).

[27] J. Ferber, K. Foyevtsova, R. Valentí, and H. O. Jeschke, Phys. Rev. B **85**, 094505 (2012).

[28] M. Yi, D. Lu, J.-H. Chu, J. G. Analytis, A. P. Sorini, A. F. Kemper, B. Moritz, S.-K. Mo, R. G. Moore, M. Hashimoto, W.-S. Lee, Z. Hussain, T. P. Devereaux, I. R. Fisher, and Z.-X. Shen, Proc. Natl. Acad. Sci. USA **108**, 6878 (2011).

[29] Y. Kim, H. Oh, C. Kim, D. Song, W. Jung, B. Kim, H. J. Choi, C. Kim, B. Lee, S. Khim, H. Kim, K. Kim, J. Hong, and Y. Kwon, Phys. Rev. B **83**, 064509 (2011).

[30] T.-M. Chuang, M. P. Allan, J. Lee, Y. Xie, N. Ni, S. L. Budko, G. S. Boebinger, P. C. Canfield, and J. C. Davis, Science **327**, 181 (2010).

[31] J.-H. Chu, J. G. Analytis, D. Press, K. De Greve, T. D. Ladd, Y. Yamamoto, and I. R. Fisher, Phys. Rev. B **81**, 214502 (2010).

[32] J. Zhao, D. T. Adroja, D.-X. Yao, R. Bewley, S. Li, X. F. Wang, G. Wu, X. H. Chen, J. Hu, and P. Dai, Nat. Phys. **5**, 555 (2009).

[33] G. Derondeau, S. Polesya, S. Mankovsky, H. Ebert, and J. Minár, Phys. Rev. B **90**, 184509 (2014).

[34] H. Ebert, D. Ködderitzsch, and J. Minár, Rep. Prog. Phys. **74**, 096501 (2011).

[35] H. Ebert *et al.*, The Munich SPR-KKR Package, Version 6.3, http://olymp.cup.uni-muenchen.de/ak/ebert/SPRKKR.

[36] A. S. Sefat, R. Jin, M. A. McGuire, B. C. Sales, D. J. Singh, and D. Mandrus, Phys. Rev. Lett. **101**, 117004 (2008).

[37] L. Vegard, Z. Phys. **5**, 17 (1921).

[38] S. H. Vosko, L. Wilk, and M. Nusair, Can. J. Phys. **58**, 1200 (1980).

[39] J. Minár, J. Braun, and H. Ebert, J. Electron Spectrosc. Relat. Phenom. **189**, 129 (2013).

[40] J. Braun, K. Miyamoto, A. Kimura, T. Okuda, M. Donath, H. Ebert, and J. Minár, New J. Phys. **16**, 015005 (2014).

[41] Q. Huang, Y. Qiu, W. Bao, M. A. Green, J. W. Lynn, Y. C. Gasparovic, T. Wu, G. Wu, and X. H. Chen, Phys. Rev. Lett. **101**, 257003 (2008).

[42] M. Rotter, M. Tegel, I. Schellenberg, F. M. Schappacher, R. Pöttgen, J. Deisenhofer, A. Günther, F. Schrettle, A. Loidl, and D. Johrendt, New J. Phys. **11**, 025014 (2009).

[43] A. A. Aczel, E. Baggio-Saitovitch, S. L. Budko, P. C. Canfield, J. P. Carlo, G. F. Chen, P. Dai, T. Goko, W. Z. Hu, G. M. Luke, J. L. Luo, N. Ni, D. R. Sanchez-Candela, F. F. Tafti, N. L. Wang, T. J. Williams, W. Yu, and Y. J. Uemura, Phys. Rev. B **78**, 214503 (2008).

[44] T. Goko, A. A. Aczel, E. Baggio-Saitovitch, S. L. Bud'ko, P. C. Canfield, J. P. Carlo, G. F. Chen, P. Dai, A. C. Hamann, W. Z. Hu, H. Kageyama, G. M. Luke, J. L. Luo, B. Nachumi, N. Ni, D. Reznik, D. R. Sanchez-Candela, A. T. Savici, K. J. Sikes, N. L. Wang, C. R. Wiebe, T. J. Williams, T. Yamamoto, W. Yu, and Y. J. Uemura, Phys. Rev. B **80**, 024508 (2009).

[45] D. Kasinathan, A. Ormeci, K. Koch, U. Burkhardt, W. Schnelle, A. Leithe-Jasper, and H. Rosner, New J. Phys. **11**, 025023 (2009).

[46] E. Aktürk and S. Ciraci, Phys. Rev. B **79**, 184523 (2009).

[47] C. Lester, J.-H. Chu, J. G. Analytis, S. C. Capelli, A. S. Erickson, C. L. Condron, M. F. Toney, I. R. Fisher, and S. M. Hayden, Phys. Rev. B **79**, 144523 (2009).

[48] J.-H. Chu, J. G. Analytis, C. Kucharczyk, and I. R. Fisher, Phys. Rev. B **79**, 014506 (2009).

[49] M. Yi, D. H. Lu, J. G. Analytis, J.-H. Chu, S.-K. Mo, R.-H. He, M. Hashimoto, R. G. Moore, I. I. Mazin, D. J. Singh, Z. Hussain, I. R. Fisher, and Z.-X. Shen, Phys. Rev. B **80**, 174510 (2009).

[50] M. A. Tanatar, A. Kreyssig, S. Nandi, N. Ni, S. L. Bud'ko, P. C. Canfield, A. I. Goldman, and R. Prozorov, Phys. Rev. B **79**, 180508 (2009).

[51] T. Kondo, R. M. Fernandes, R. Khasanov, C. Liu, A. D. Palczewski, N. Ni, M. Shi, A. Bostwick, E. Rotenberg, J. Schmalian, S. L. Bud'ko, P. C. Canfield, and A. Kaminski, Phys. Rev. B **81**, 060507 (2010).

[52] D. E. Eastman, F. J. Himpsel, and J. A. Knapp, Phys. Rev. Lett. **44**, 95 (1980).

[53] P. M. Echenique and J. B. Pendry, J. Phys. C **11**, 2065 (1978).

[54] E. G. McRae, Rev. Mod. Phys. **51**, 541 (1979).

[55] J. Braun and M. Donath, Europhys. Lett. **59**, 592 (2002).

[56] J. E. Hoffman, Rep. Prog. Phys. **74**, 124513 (2011).

[57] G. Profeta, C. Franchini, K. A. I. L. W. Gamalath, and A. Continenza, Phys. Rev. B **82**, 195407 (2010).

[58] F. Massee, S. de Jong, Y. Huang, J. Kaas, E. van Heumen, J. B. Goedkoop, and M. S. Golden, Phys. Rev. B **80**, 140507 (2009).

[59] V. B. Nascimento, A. Li, D. R. Jayasundara, Y. Xuan, J. O'Neal, S. Pan, T. Y. Chien, B. Hu, X. B. He, G. Li, A. S. Sefat, M. A. McGuire, B. C. Sales, D. Mandrus, M. H. Pan, J. Zhang, R. Jin, and E. W. Plummer, Phys. Rev. Lett. **103**, 076104 (2009).

5.3 Discussion

In this publication it was shown that the applied one-step model of photoemission is able to reproduce the anisotropy in ARPES spectra of the iron pnictide superconductors in great detail and agreement with experiment. In particular, the importance of detwinned ARPES measurements was theoretically emphasized, because only these are able to capture the real anisotropy from an experimental point of view. This has relevant implications for further studies, as only little experimental ARPES data on detwinned samples are available at the moment, due to the complex experimental setup. In order to understand the anisotropic behavior of the iron pnictides in detail it is however mandatory to unveil the full anisotropic electronic structure. Obviously, theory can help in this context as it is easier to calculate the spectra for a full series of different dopant concentrations x then to prepare each sample individually and measure them at low temperatures using a detwinning device.

Another very important result obtained by theory is information about the surface termination. As already stressed, there is a certain discrepancy in the literature concerning this topic from experimental STM and LEED measurements[247,248] and also according to other theoretical work[249] different types of surface termination are possible. The presented publication was unambiguously able to show that only an As-terminated surface can explain the electronic spectra as seen by ARPES measurements which clearly favors the As-terminated surface over a Ba-terminated one. In this context also the general ability of theory to identify surface related states should be emphasized once more. For example, the observed anisotropic bright intensity spots along the antiferromagnetic a axis could be identified as surface states due to an As-terminated surface. This means that surface states in general are quite important for the iron pnictides and cannot be neglected in further studies when discussing the electronic states derived by ARPES.

Thus, the applied theory proved to be very reliable for iron pnictides, even accounting for their complex ARPES spectra. These were hardly investigated theoretically so far having the here presented agreement with experiment. Additional information e.g. on surface related states only accessible by theory can further support experimental measurements by crucial new insights.

Additionally, one should note once more that the presented ARPES data show in agreement with the previous publication that the tetragonal to orthorhombic lattice distortion is negligible and the observed anisotropy stems only from the anisotropic magnetic order.

Chapter 6

Impact of the photoemission response

6.1 Motivation

The motivation for the work presented in this chapter stemmed from a cooperation with the experimentalists Vladimir N. Strocov, Federico Bisti *et al.*[251] from the Swiss Light Source (SLS) of the Paul Scherrer Institute, Villigen, Switzerland. In the beginning, the interest was based on a quite surprising intensity distribution between the $\bar{\Gamma}$ and $\bar{\Gamma}'$ points of neighboring Brillouin zones in the ARPES spectra of the optimally K-doped $(\mathrm{Ba}_{1-x}\mathrm{K}_x)\mathrm{Fe}_2\mathrm{As}_2$ superconductor as shown in Fig. 6.1.

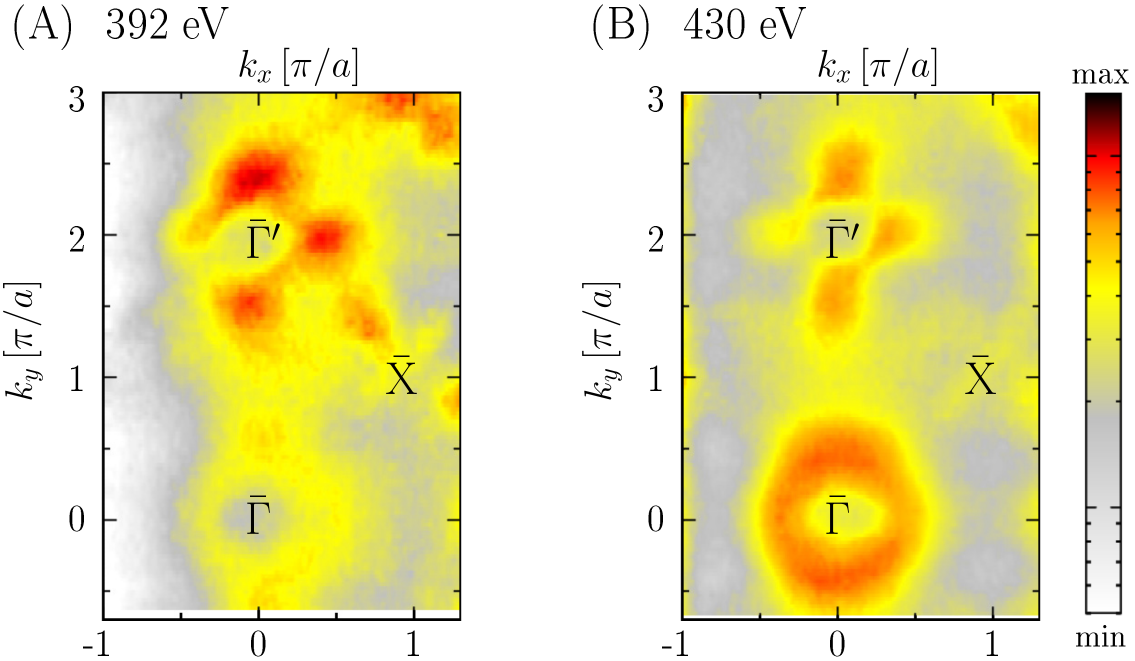

Figure 6.1. Experimental ARPES Fermi surface cuts of $(\mathrm{Ba}_{0.6}\mathrm{K}_{0.4})\mathrm{Fe}_2\mathrm{As}_2$ measured with *p*-polarized light for (A) $h\nu = 392$ eV and for (B) $h\nu = 430$ eV.[251]

The experimental data of $(Ba_{0.6}K_{0.4})Fe_2As_2$ was measured for high photon energies in the soft-X-ray range and is shown in particular for Fig. 6.1 (A) $h\nu = 392$ eV and for (B) $h\nu = 430$ eV.[251] For such high photon energies the electronic structure around $\bar{\mathrm{X}}$ is hardly identifiable, whereas the flower-like topology with four-fold rotational symmetry around $\bar{\Gamma}'$ in comparison to the circle topology around $\bar{\Gamma}$ is the most prominent feature. Such a pronounced difference between neighboring Brillouin zones is rather unexpected. Similar topologies were first discovered by Zabolotnyy *et al.*[33] for lower photon energies around $h\nu = 80$ eV, however, they could not provide an explanation and only stressed that the "apparently different intensity distributions at neighboring $\bar{\Gamma}$ points appear unusual".[33]

The electronic structure of 122-family of iron pnictides has a distinct three-dimensional character and an apparent k_z dispersion with alternating Γ and Z points. This was also verified by a corresponding experimental k_z scan shown in Fig. 6.2 where the two photon energies of the Fermi surface cuts in Fig. 6.1 are marked as black lines.[251]

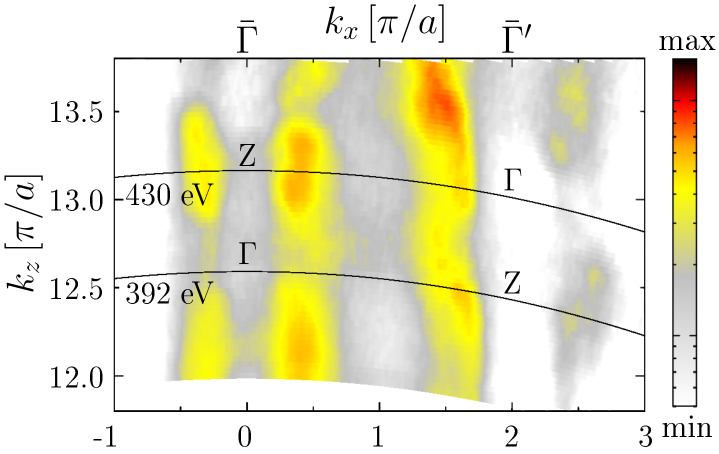

Figure 6.2. Experimental k_z scan with p-polarized light for $(Ba_{0.6}K_{0.4})Fe_2As_2$ showing clearly the k_z dispersion and alternating Γ and Z points at $\bar{\Gamma}$ and $\bar{\Gamma}'$, respectively. The photon energies $h\nu = 392$ eV and $h\nu = 430$ eV are marked with a black line.[251]

One might tend to explain the occurrence of the flower-like topology at $\bar{\Gamma}'$ in terms of this k_z dispersion, however, this is obviously not true. As can be seen from Fig. 6.2 the two photon energies $h\nu = 392$ eV and $h\nu = 430$ eV correspond to transitions at Γ and Z, respectively. Consequently, one should see in Fig. 6.1 the flower like topology for one photon energy at $\bar{\Gamma}$ and for the other photon energy at $\bar{\Gamma}'$, respectively. However, the flower-like feature of the Fermi surface cut can be only observed at $\bar{\Gamma}'$ of the second Brillouin zone and independent on k_z it is never visible at $\bar{\Gamma}$ of the first Brillouin zone. This proved already without doubt that the unexpected flower-like topology at $\bar{\Gamma}'$ is not connected to the k_z dispersion. Thus, it remained an open question how to explain this peculiar phenomenon which was the original motivation to theoretically investigate this system.

However, it proved to be a non-trivial task to capture the individual characteristics of the ARPES spectra of $(\mathrm{Ba}_{1-x}\mathrm{K}_x)\mathrm{Fe}_2\mathrm{As}_2$ correctly. Note, that this compound is one of the most investigated and discussed prototype systems for the iron pnictide superconductors in terms of ARPES.[33,215–217,252–254] A theoretical explanation of the ARPES spectra of iron pnictides is known to be difficult and often it is necessary to consider strong correlation effects in order to obtain reasonable results.[54–59,255–257] Also for the present case it proved to be mandatory to include strong correlations in term of a LDA+DMFT approach. However, it was additionally necessary to combine the LDA+DMFT method with the ARPES one-step model of photoemission in order to finally obtain a satisfactory result. During this long-term investigation in cooperation with experiment the original motivation of understanding the flower-like topology at $\bar{\Gamma}'$ was no longer the only interest. It was possible to discuss two additional spectral features of interest thanks to the subsequently more detailed study.

First, the exceptional propeller-like Fermi surface topology of $(\mathrm{Ba}_{0.6}\mathrm{K}_{0.4})\mathrm{Fe}_2\mathrm{As}_2$ at the $\bar{\mathrm{X}}$ point[33,216,252] could be investigated in detail due to the applied LDA+DMFT approach and by extending the theoretical ARPES study also to lower photon energies. This feature is discussed in terms of a Lifshitz transition[258], meaning topological changes in the Fermi surface which mark the onset of superconductivity. Consequently, the correct explanation of these Lifshitz transitions is of tremendous relevance for the iron pnictides.[35,52]

Secondly, the applied approach could be used to investigate the effective electron masses. Note, that a significant discrepancy between the effective masses derived from experimental ARPES spectra m^*_{exp} and from LDA band structure calculations m^*_{LDA} was reported.[256,257] This observation is typically ascribed to strong correlations and band renormalization as LDA+DMFT calculations for effective masses tend to give better results compared to LDA.[57,259] However, one important point was so far missing in the literature, namely the influence of effects inherent to the photoemission response which can be e.g. surface effects, matrix element effects or final state effects. These phenomena alter the true band dispersion, meaning the apparent mass enhancement seen in the ARPES spectra is not an entirely intrinsic property anymore.

Thus, the following work can discuss several important physics of the iron pnictides concerning the ARPES spectra and correlation effects which can be both adequately described by the applied LDA+DMFT+ARPES approach. Note, that within this chapter the tetragonal, nonmagnetic phase of $(\mathrm{Ba}_{0.6}\mathrm{K}_{0.4})\mathrm{Fe}_2\mathrm{As}_2$ was investigated.

6.2 Publication: arXiv 1606.08977

Fermi surface and effective masses in photoemission response of the $(Ba_{1-x}K_x)Fe_2As_2$ superconductor

Gerald Derondeau,[1] Federico Bisti,[2] Jürgen Braun,[1] Victor A. Rogalev,[2] Masaki Kobayashi,[2,3] Ming Shi,[2] Thorsten Schmitt,[2] Junzhang Ma,[2,4,5] Hong Ding,[4,5] Hubert Ebert,[1] Vladimir N. Strocov,[2] and Ján Minár[1,6]

[1]*Department Chemie, Physikalische Chemie, Universität München, München, Germany*
[2]*Swiss Light Source, Paul Scherrer Institute, CH-5232 Villigen PSI, Switzerland*
[3]*Department of Applied Chemistry, School of Engineering, University of Tokyo, 7-3-1 Hongo, Bunkyo-ku, Tokyo 113-8656, Japan*
[4]*Beijing National Laboratory for Condensed Matter Physics*
[5]*Institute of Physics, Chinese Academy of Sciences, Beijing 100190, China*
[6]*NewTechnologies-Research Center, University of West Bohemia, Pilsen, Czech Republic*

available at: arXiv 1606.08977v2 [cond-mat.supr-con]

submitted to: Scientific Reports on 11th of October 2016 arXiv:1606.08977v2 [cond-mat.supr-con] 14 Sep 2016

Fermi surface and effective masses in photoemission response of the $(\mathrm{Ba}_{1-x}\mathrm{K}_x)\mathrm{Fe}_2\mathrm{As}_2$ superconductor

Gerald Derondeau,[1, *] Federico Bisti,[2] Jürgen Braun,[1] Victor A. Rogalev,[2] Masaki Kobayashi,[2, 3] Ming Shi,[2]
Thorsten Schmitt,[2] Junzhang Ma,[2, 4, 5] Hong Ding,[4, 5] Hubert Ebert,[1] Vladimir N. Strocov,[2, †] and Ján Minár[1, 6, ‡]

[1] *Department Chemie, Physikalische Chemie, Universität München, Butenandtstr. 5-13, 81377 München, Germany*
[2] *Swiss Light Source, Paul Scherrer Institute, CH-5232 Villigen PSI, Switzerland*
[3] *Department of Applied Chemistry, School of Engineering,*
University of Tokyo, 7-3-1 Hongo, Bunkyo-ku, Tokyo 113-8656, Japan
[4] *Beijing National Laboratory for Condensed Matter Physics*
[5] *Institute of Physics, Chinese Academy of Sciences, Beijing 100190, China*
[6] *NewTechnologies-Research Center, University of West Bohemia, Pilsen, Czech Republic*

(Dated: September 15, 2016)

The angle-resolved photoemission spectra of the superconductor $(\mathrm{Ba}_{1-x}\mathrm{K}_x)\mathrm{Fe}_2\mathrm{As}_2$ have been investigated both experimentally and theoretically. Our results explain the previously obscured origins of all salient features of the ARPES response of this paradigm pnictide compound and reveal the origin of the Lifshitz transition. Comparison of calculated ARPES spectra with the underlying DMFT band structure shows an important impact of final state effects, which results for three-dimensional states in a deviation of the ARPES spectra from the true spectral function. In particular, the apparent effective mass enhancement seen in the ARPES response is not an entirely intrinsic property of the quasiparticle valence bands but may have a significant extrinsic contribution from the photoemission process and thus differ from its true value. Because this effect is more pronounced for low photoexcitation energies, soft-X-ray ARPES delivers more accurate values of the mass enhancement due to a sharp definition of the 3D electron momentum.

The iron pnictides are nowadays one of the most studied examples for unconventional superconductivity. Due to their complex properties standard theoretical methods based on a local density approximation (LDA) within density functional theory (DFT) often fail.[1–3] This is especially true if one tries to explain angle-resolved photoemission (ARPES) spectra of the iron pnictides.[4–11] In this context a significant discrepancy between the effective masses derived from experimental ARPES spectra m^*_{exp} and from LDA band structure calculations m^*_{LDA} was reported.[9, 11] Correct trends in the effective masses can be observed using dynamical mean-field theory (DMFT) approaches which quantifies the importance of correlation effects for the iron pnictides.[12, 13]

Various advanced approaches have been applied in the field, accounting for different phenomena. This covers the treatment of disorder in an appropriate way [14–16], the inclusion of spin-orbit coupling (SOC) [17] and in order to calculate ARPES spectra correctly the influence of matrix element effects and surface effects was recently stressed [18, 19]. Finally, electron-electron correlation effects are one of the most important issues discussed.[8, 12, 20–24] All these aspects were shown to play a crucial role for the iron pnictides, yet most approaches so far can deal with only one of these issues at the same time.

In this work we will present a theoretical approach which accounts for all of the above mentioned issues leading in this way to a very satisfactory agreement with experimental ARPES data of the iron pnictides. Here we investigate one of the most prominent prototype systems in the family of iron pnictides, namely the K substituted $(\mathrm{Ba}_{1-x}\mathrm{K}_x)\mathrm{Fe}_2\mathrm{As}_2$ compound [25, 26], which was extensively studied by ARPES.[4–7, 10, 27, 28] There is common agreement, that the Fermi surface (FS) of this compound is quite complex and cannot be obtained from plain DFT calculations. In fact, an exceptional propeller-like FS topology at the $\bar{\mathrm{X}}$ point is found [4–6] which is discussed in terms of a Lifshitz transition, meaning topological changes in the FS which mark the onset of superconductivity.[16, 29] Also a rather puzzling change in the intensity distribution at neighboring $\bar{\Gamma}$ points is known.[4] Until now there is no theoretical work which would explain all the salient features of the ARPES spectra of $(\mathrm{Ba}_{1-x}\mathrm{K}_x)\mathrm{Fe}_2\mathrm{As}_2$.

Results

Impact of correlations on the electronic structure. The crystal structure of $(\mathrm{Ba}_{0.6}\mathrm{K}_{0.4})\mathrm{Fe}_2\mathrm{As}_2$ is shown in Fig. 1 (A), with the corresponding Brillouin zone (BZ) and its two-dimensional counterpart for a (001) orientated surface given in Fig. 1 (B). The electronic structure is represented by means of the Bloch spectral function (BSF), which has the significant advantage that in the presented approach all disorder effects induced through substitution are fully accounted for. The LDA based band structure is shown in Fig. 1 (C) with the corresponding Fermi surface (FS) cut shown in Fig. 1 (D). The topology of this FS cut fails to explain the Fermi surface seen by ARPES.[4] It can neither reproduce the well-known propeller-like features at the $\bar{\mathrm{X}}$ point, nor it can explain the flower-like topology at $\bar{\Gamma}'$.[4] Thus, the applied LDA approach is insufficient to deal accurately

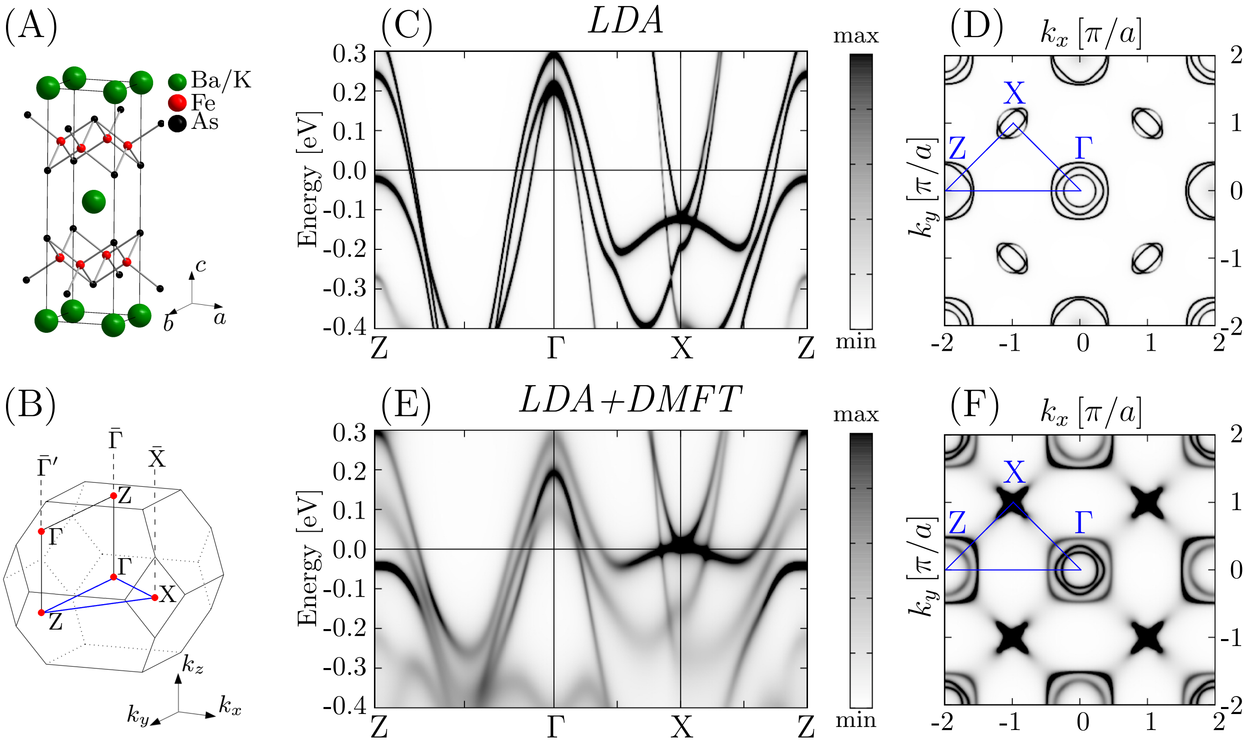

FIG. 1. (A) Crystallographic unit cell of tetragonal $(\mathrm{Ba}_{1-x}\mathrm{K}_x)\mathrm{Fe}_2\mathrm{As}_2$ with (B) corresponding Brillouin zones indicating the important high symmetric points. $\bar{\Gamma}$, $\bar{\Gamma}'$ and $\bar{\mathrm{X}}$ indicate the two-dimensional Brillouin zone for a (001) orientated surface. (C + D) BSF and FS of $(\mathrm{Ba}_{0.6}\mathrm{K}_{0.4})\mathrm{Fe}_2\mathrm{As}_2$ calculated on the basis of LDA. (E + F) Corresponding BSF and FS of $(\mathrm{Ba}_{0.6}\mathrm{K}_{0.4})\mathrm{Fe}_2\mathrm{As}_2$ calculated on the basis of LDA+DMFT. The blue lines always indicate the path chosen for the presented band structure.

with these prominent features. To account for the necessary correlation effects fully self-consistently, we have applied subsequent LDA+DMFT calculations. We used for Fe an averaged on-site Coulomb interaction $U = 3.0$ eV and an exchange interaction $J = 0.9$ eV, which are commonly used for the iron pnictides.[8, 30, 31] The impact of correlation effects represented by the DMFT on the band structure in Fig. 1 (E) and on the Fermi surface cut in Fig. 1 (F) is tremendous. We see strong renormalization of the d_{xy} and $d_{xz/yz}$ bands, in agreement with other literature.[13] However, most prominent are the changes around the X point where a significant upwards shift of the bands towards the Fermi level (E_F) leads to the hole and electron pockets responsible for the appearance of the propeller like topology at $\bar{\mathrm{X}}$ in agreement with experimental ARPES data.[4–6] Note, that a similar upwards shift at X of around 0.1 eV was also observed by Werner *et al.*[8] [32], although the qualitative agreement of our results with experiment seems slightly better. In comparison, Werner *et al.* used a frequency dependent screening which leads to strong incoherence. However, based on suggestions by Tomczak *et al.*[12] and because we look only at energies close to the Fermi level it seems like an acceptable approximation to use a static coulomb interaction U. In particular, we are able to fully account for the chemical disorder of the K-doped compound in terms of the coherent potential approximation (CPA) which seems to be more relevant for the problem at hand. Considering the LDA band structure from Fig. 1 (C) one can already see strong band broadening for the hole band of interest at X. Thus, incoherence due to disorder effects is strongest for explicitly this band and it would be invalid to neglect this. Consequently, strong incoherence at X for the LDA+DMFT band structure makes it difficult to resolve the exact band shape. Based on the ARPES data of Zabolotnyy *et al.*[4] the electron pocket and the hole pocket at X should hybridize even more than in the presented calculations. This effect is covered in our results due to the strong incoherence and it might be also a shortcoming of the applied FLEX DMFT solver.

Still, the consequence of this phenomenon is a topological change in the FS contour, indicating a so-called Lifshitz transition which is crucial for the emergence of superconductivity.[16, 29] This Lifshitz transition was already discussed for high K concentrations ($x \approx 0.9$) within a LDA framework.[16, 28] The present as well as previous experimental work [4–6], however, clearly shows the emergence of the petal topology around $\bar{\mathrm{X}}$ already for optimal doping ($x \approx 0.4$). Based on the latter discussion and by comparing Fig. 1 (C) and (D) one can see that the origin of the Lifshitz transition at

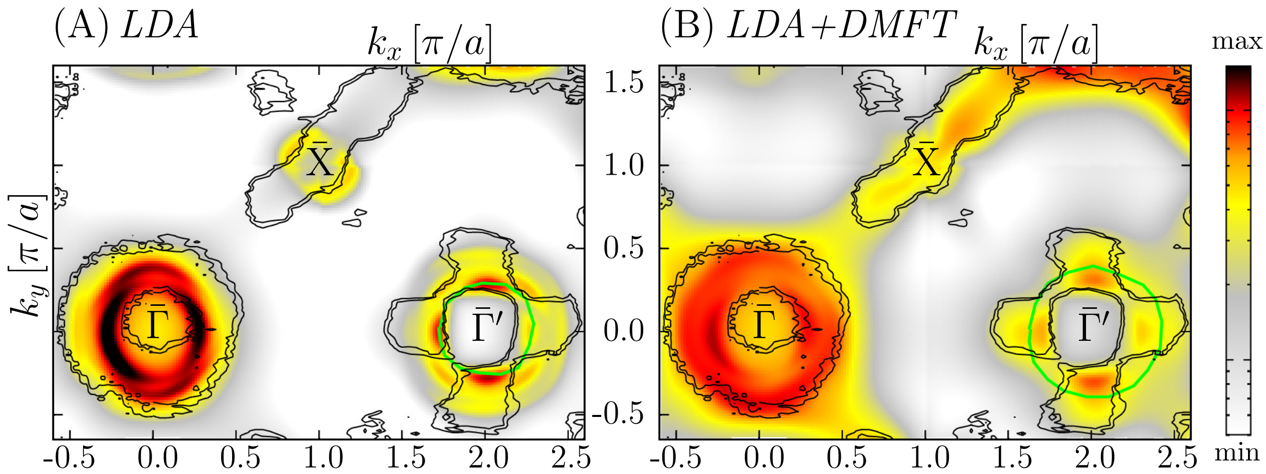

FIG. 2. Fermi surfaces cuts of $(\mathrm{Ba}_{0.6}\mathrm{K}_{0.4})\mathrm{Fe}_2\mathrm{As}_2$ for $h\nu = 75$ eV as seen by one step model ARPES calculations for (A) LDA and (B) LDA+DMFT. The overlay of black isolines always corresponds to experimental ARPES data taken with permission from Zabolotnyy *et al.*[4]. The green solid lines are guides for the eyes to indicate surface state related features.

lower K concentrations is fully controlled by correlation effects accounted for by the applied LDA+DMFT approach. Consequently, the Lifshitz transition can also qualitatively explain the breakdown of magnetic order for $(\mathrm{Ba}_{1-x}\mathrm{K}_x)\mathrm{Fe}_2\mathrm{As}_2$, which takes place at low doping ratios $x < 0.4$ [26], as it destroys the nesting condition [33]. More details showing the clear dependence on the Coulomb interaction U are found in the Supplemental Material.[34] Although, the applied self-consistent DMFT approach has brought important new insights on the topology around $\bar{\mathrm{X}}$, it is not able to reproduce the flower-like intensity distribution observed at $\bar{\Gamma}'$ compared to $\bar{\Gamma}$.[4]

Impact of ARPES response effects. To understand this flower-like feature, additional calculations based on the one-step model of ARPES have been done, accounting for the experimental geometry [35, 36] including surface effects as well as matrix element effects. These calculations were performed using the LDA potentials and within the LDA+DMFT framework. The corresponding spectroscopic Fermi surface cuts obtained from the one-step model ARPES calculations of $(\mathrm{Ba}_{0.6}\mathrm{K}_{0.4})\mathrm{Fe}_2\mathrm{As}_2$ for $h\nu = 75$ eV are shown in Fig. 2 (A) for LDA and in Fig. 2 (B) for the LDA+DMFT calculations. For comparison we show in both pictures the original experimental data from Zabolotnyy *et al.* [4] as an overlay of black isolines, measured at $h\nu = 80$ eV.

The ARPES calculations based on the LDA+DMFT shown in Fig. 2 (B) reveal very good agreement with the experimental data, concerning the Lifshitz transition induced propeller structure at $\bar{\mathrm{X}}$ (only one part of the propeller is clearly visible for the chosen light polarization as was also found in experiment [4]) indicating that the previously discussed electronic structure is correctly reproduced. Furthermore, we obtain good agreement concerning the flower intensity distribution at $\bar{\Gamma}'$. It should be stressed that there is no alternation of this circle and flower topology around $\bar{\Gamma}$ and $\bar{\Gamma}'$, respectively, with alternating Γ and Z points in the k_z direction by changing $h\nu$. Thus, the origin of this interesting topology is not connected to the alternation between Γ and Z points of the bulk Brillouin zone.

The general appearance of two different shapes between $\bar{\Gamma}$ and $\bar{\Gamma}'$ can be explained by the structure factor and the light polarization in terms of a 1-Fe or 2-Fe cell, as discussed by e.g. Moreschini *et al.* [37] or Lin *et al.* [38]. Note, that a correct treatment of the phase difference between two atoms of a unit cell and the light polarization is by construction included in the one-step model of photoemission (see Ref. [39]), thus the theory can sufficiently account for this. However, we find that at the same time other effects can contribute, in order to obtain this flower topology in agreement with experiment. As can be seen from Fig. 2 (A) the intensity distribution at $\bar{\Gamma}'$ has a fourfold rotational symmetry, although the flower-like topology is not adequately reproduced compared to the result in Fig. 2 (B). This difference cannot be explained without additional contributions.

It is known that the intensity distributions in ARPES might change for neighboring Brillouin zones between $\bar{\Gamma}$ and $\bar{\Gamma}'$ due to matrix element effects, however, such a strong change in the intensity distribution as seen in experiment [4] and reproduced in Fig. 2 (B) is rather uncommon and unexpected. Yet, it is also known that the influence of matrix element effects can be enhanced in the vicinity of surface related states. Surface phenomena can be investigated by the applied method, as it is explained in more detail in Ref. [40]. In particular, we have recently shown that surface states have a significant influence on the ARPES spectra of Co-doped $\mathrm{BaFe}_2\mathrm{As}_2$ [19]. Subsequently, one is able to identify

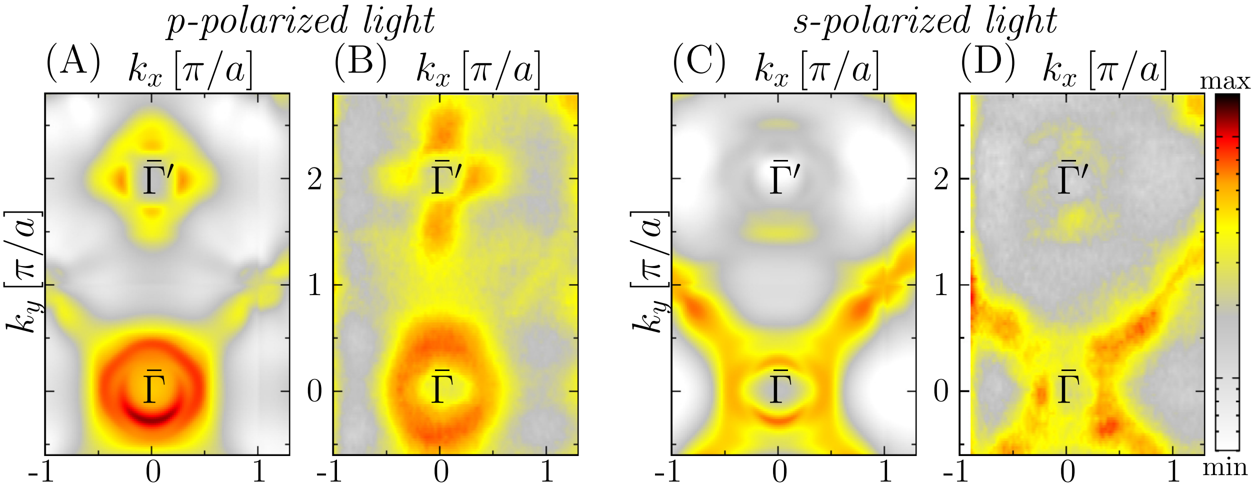

FIG. 3. Fermi surface cuts of $(Ba_{0.6}K_{0.4})Fe_2As_2$ for (A+C) $h\nu = 425$ eV ARPES calculation using LDA+DMFT and (B+D) $h\nu = 430$ eV experimental data. The incoming light was either (A+B) p-polarized or (C+D) s-polarized.

in the spectra of $(Ba_{0.6}K_{0.4})Fe_2As_2$ surface resonance states which wave functions have bulk Bloch asymptotic behavior and exhibit a strong resonance at the vicinity of the surface. This means such surface resonances can show a k_z dispersion and they can be observed also for comparably high photon energies. The positions of these ring-shaped surface resonances is marked with solid green lines as an overlay in Fig. 2. For LDA in Fig. 2 (A) one can see that this surface resonance is compressed and thus its influence on the intensity distribution at $\bar{\Gamma}'$ is less significant. In comparison, the surface resonance is shifted for the LDA+DMFT calculation in Fig. 2 (B) where it cuts precisely through the clearly visible petals of the flower topology, affecting the intensity distribution at this position. We believe, that these contributions from the surface resonances can add up to the commonly discussed explanation based on the 1-Fe/2-Fe scheme, giving finally an overall good agreement with experimental data.

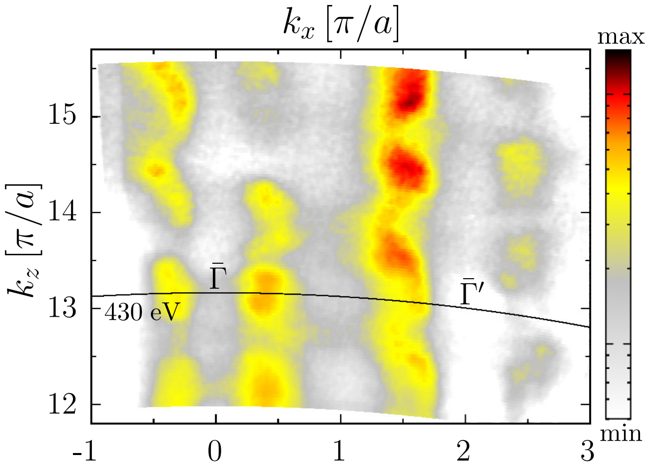

FIG. 4. Experimental k_z scan with p-polarized light for $(Ba_{0.6}K_{0.4})Fe_2As_2$ from 350 eV up to 500 eV. It is showing the clear k_z dispersion at $\bar{\Gamma}$ and $\bar{\Gamma}'$. The photon energy of $h\nu = 430$ eV is marked with a black line.

New bulk sensitive ARPES experiments. Additional bulk sensitive soft-X-ray photoemission measurements for $h\nu = 430$ eV were performed for samples of $(Ba_{0.6}K_{0.4})Fe_2As_2$. The resulting spectra are presented in Figs. 3 (B) and (D) for p-polarized and s-polarized light, respectively. Notably, for p-polarized light the flower shaped topology at $\bar{\Gamma}'$ is enhanced in intensity while for s-polarized light the propeller topologies at $\bar{X}$ are enhanced. Corresponding calculations for $h\nu = 425$ eV are presented in Figs. 3 (A) and (C), which show very good agreement with the experimental data concerning the relevant topologies and the polarization dependence. Thus, these experiments are fully in line with the argumentation of this work so far and further validate our results. Additional extended Fermi surface cuts for higher Brillouin zones can be found in the Supplemental Material.[34]

Furthermore, the experimental k_z scan from 350 eV up to 500 eV is shown in Fig. 4 with the photon energy of $h\nu = 430$ eV explicitly marked with the black line. This shows clearly the k_z dispersion and thus the strong 3D character of the iron pnictides.

Effective masses derived from ARPES spectra Finally, the electronic structure derived from BSF calculations and ARPES calculations was used to analyze the effective masses which are of great actual interest for the iron pnictides.[9, 11–13] The results for the mass ratios of the inner and outer hole pockets around Γ in the ΓZ direction and additionally for the hole pocket at X in the ΓX direction are summarized in Tab. I. More details are found in the Supplemental Material.[34] As

TABLE I. Ratio of effective masses of m^*_{DMFT} to m^*_{LDA} for the Bloch spectral function (BSF) calculations as well as for the ARPES calculations with $h\nu = 75$ eV and 425 eV, respectively. The values correspond to the inner and outer hole pockets around Γ showing strong k_z dispersion and to the hole pocket at X showing weak k_z dispersion.[34]

$\frac{m^*_{\mathrm{DMFT}}}{m^*_{\mathrm{LDA}}}$	BSF	ARPES 75 eV	ARPES 425 eV
Inner pocket Γ	2.59	3.66	2.94
Outer pocket Γ	1.70	2.28	1.98
Hole pocket X	1.43	1.56	1.58

it is commonly done, all values of m^* are normalized to the LDA value m^*_{LDA} deduced from the ground state BSF. First, consider the mass enhancement at Γ only, where the influence of DMFT on the band dispersion can be seen for the BSF, with an average mass enhancement of 2.15 (meaning an average over inner and outer hole pocket Γ), being in good agreement with literature (e.g. 2.04 for $\mathrm{KFe_2As_2}$ [13]). Of more interest is the apparent mass enhancement deduced from the ARPES calculations compared to the BSF band dispersion. The difference is attributed to the fact that the calculated ARPES spectra include not only the correlation effects of DMFT but also final state effects which, as explained below, modify the ARPES spectral shape. On the experimental side, such an apparent mass enhancement has already been observed in ARPES for e.g. the $\mathrm{BaFe_2As_2}$ parent compound and connected with the k_z dispersion of the valence states.[9] The apparent mass enhancement is given by the fact that the ARPES response of the 3D valence states is formed by averaging of their matrix-element weighted k_z dispersion over an interval of the intrinsic final state k_z broadening (Δk_z) determined by the photoelectron mean free path λ.[41, 42] As illustrated in Fig. S5 in the Supplemental Material [34], near the extremes of the valence band k_z dispersions this averaging effectively shifts the ARPES peaks from true k_z dispersions into the band interior (for detailed physical picture see Ref. [41]). In $\boldsymbol{k}_{||}$ dependent ARPES intensities this shift is seen as an apparent bandwidth reduction and corresponding mass enhancement. One can expect a stronger influence of these final state effects at lower photon energies where Δk_z is larger due to a smaller λ. Indeed, our calculations find significant differences in the mass enhancement at Γ depending on $h\nu$. For the low $h\nu$ of 75 eV ($\Delta k_z = 0.2779$ Å^{-1}, which makes about 30% of the perpendicular BZ dimension) we find an average mass enhancement of 2.97 at Γ which is higher than the value of 2.15 obtained from the BSF. The significantly higher $h\nu$ of 425 eV ($\Delta k_z = 0.1228$ Å^{-1}) increases λ and concomitantly improves the k_z definition. The final state effects have therefore a less pronounced contribution, reducing the average mass enhancement at Γ to 2.46. This is true for almost all bands in the iron pnictides as they are 3D materials with most bands showing a clear k_z dispersion. One of the rare exceptions for the $\mathrm{(Ba_{1-x}K_x)Fe_2As_2}$ compound is the hole pocket at X which has almost 2D character and shows hardly a k_z dispersion as can be seen in Fig. 1 (C + E) for the path ΓXZ. In such a case one would expect significantly less influence of the final-state effects and indeed, Tab. I shows that the apparent mass enhancement for high and low $h\nu$ at X is almost the same and very similar to the BSF mass enhancement. This finally explains discrepancies in the observed mass enhancement for the iron pnictides. To reduce these $h\nu$ dependent deviations of the ARPES response from the true 3D valence bands, we justify the use of higher $h\nu$ in the soft-X-ray regime to improve the k_z definition.

Discussion

In conclusion, the presented LDA+DMFT+ARPES study is the first to quantitatively match theoretical description and experimental ARPES data on the paradigm high-temperature superconductor $\mathrm{(Ba_{0.6}K_{0.4})Fe_2As_2}$. These results enable better physical understanding of the unconventional superconductivity in pnictides and will be of great importance for future studies on similar systems. In particular, the origin of the Lifshitz transition in $\mathrm{(Ba_{1-x}K_x)Fe_2As_2}$, crucial for its superconductivity, is identified as fully controlled by electron correlation effects, which we have discussed in detail. Furthermore, we have shown that due to the inherently 3D nature of the iron pnictides their ARPES response is significantly influenced by final state effects, shifting the spectral peaks from the true quasiparticle valence bands. Their mass enhancement apparent in the ARPES spectra is then different from the true value and, moreover, will depend on the photon energy. Thus, the mass renormalization observed in previous ARPES works on iron pnictides is not an entirely intrinsic property of the quasiparticle valence band structure or spectral function, but has a significant contribution due to a peculiarity of the photoemission process extrinsic to the true valence band properties.

Methods

Computational method. Within the present work, the multiple scattering Korringa-Kohn-Rostoker-Green fuction (KKR-GF) method was applied which allows to deal simultaneously with all mentioned spectroscopic and many-body aspects. All calculations have been performed within the fully relativistic four component Dirac formalism [43, 44], accounting this way for all effects induced by spin-orbit coupling. Disorder effects are dealt with by means of the coherent potential approximation (CPA).[16, 19, 45] ARPES calculations are based on the one-step model of photoemission in its spin density matrix formulation using the experimental geometry.[46, 47] Thus, the theory accounts for effects induced by the light polarization, matrix-element effects, final state effects and surface effects. To account for correlation effects fully self-consistently (concerning charge as well as self energy) the LDA+DMFT method using a FLEX solver was applied.[48] For Fe an averaged on-site Coulomb interaction $U = 3.0$ eV and an exchange interaction $J = 0.9$ eV were applied. In the Supplemental Material calculations for different values of U are shown.[34] The lattice constants of the tetragonal cell of $(\mathrm{Ba}_{0.6}\mathrm{K}_{0.4})\mathrm{Fe}_2\mathrm{As}_2$ were taken from experimental data. [26]

ARPES experiments. New ARPES experiments in the soft-X-ray photon energy ($h\nu$) range above 400 eV were performed at the ADRESS beamline of the Swiss Light Source synchrotron facility.[35, 36] By using higher $h\nu$ compared to the conventional ultraviolet ARPES, higher bulk sensitivity is achieved due to an increase of the photoelectron mean free path λ as expected from the well-known "universal curve". Crucial for 3D materials like the iron pnictides is that the increase of λ results, by the Heisenberg uncertainty principle, in a sharp intrinsic definition of the momentum k_z perpendicular to the surface.[41] As explained in the paper, the latter becomes important for the correct evaluation of the true valence band dispersions and effective masses.

In particular, bulk sensitive soft-X-ray photoemission measurements for $h\nu = 430$ eV were performed for in-situ cleaved samples of $(\mathrm{Ba}_{0.6}\mathrm{K}_{0.4})\mathrm{Fe}_2\mathrm{As}_2$ at a temperature of around 12 K and with an overall energy resolution of around 70 meV.

References

[*] gerald.derondeau@cup.uni-muenchen.de
[†] vladimir.strocov@psi.ch
[‡] jan.minar@cup.uni-muenchen.de

[1] I. I. Mazin and M. D. Johannes, Nature Physics **5**, 141 (2009).

[2] I. I. Mazin, D. J. Singh, M. D. Johannes, and M. H. Du, Phys. Rev. Lett. **101**, 057003 (2008).

[3] I. I. Mazin, M. D. Johannes, L. Boeri, K. Koepernik, and D. J. Singh, Phys. Rev. B **78**, 085104 (2008).

[4] V. B. Zabolotnyy, D. S. Inosov, D. V. Evtushinsky, A. Koitzsch, A. A. Kordyuk, G. L. Sun, J. T. Park, D. Haug, V. Hinkov, A. V. Boris, C. T. Lin, M. Knupfer, A. N. Yaresko, B. Büchner, A. Varykhalov, R. Follath, and S. V. Borisenko, Nature **457**, 569 (2009).

[5] D. V. Evtushinsky, D. S. Inosov, V. B. Zabolotnyy, M. S. Viazovska, R. Khasanov, A. Amato, H.-H. Klauss, H. Luetkens, C. Niedermayer, G. L. Sun, V. Hinkov, C. T. Lin, A. Varykhalov, A. Koitzsch, M. Knupfer, B. Büchner, A. A. Kordyuk, and S. V. Borisenko, New Journal of Physics **11**, 055069 (2009).

[6] D. V. Evtushinsky, A. A. Kordyuk, V. B. Zabolotnyy, D. S. Inosov, T. K. Kim, B. Büchner, H. Luo, Z. Wang, H.-H. Wen, G. Sun, C. Lin, and S. V. Borisenko, J. Phys. Soc. Japan **80**, 023710 (2011).

[7] D. V. Evtushinsky, D. S. Inosov, V. B. Zabolotnyy, A. Koitzsch, M. Knupfer, B. Büchner, M. S. Viazovska, G. L. Sun, V. Hinkov, A. V. Boris, C. T. Lin, B. Keimer, A. Varykhalov, A. A. Kordyuk, and S. V. Borisenko, Phys. Rev. B **79**, 054517 (2009).

[8] P. Werner, M. Casula, T. Miyake, F. Aryasetiawan, A. J. Millis, and S. Biermann, Nature Physics **8**, 331 (2012).

[9] V. Brouet, P.-H. Lin, Y. Texier, J. Bobroff, A. Taleb-Ibrahimi, P. Le Fèvre, F. Bertran, M. Casula, P. Werner, S. Biermann, F. Rullier-Albenque, A. Forget, and D. Colson, Phys. Rev. Lett. **110**, 167002 (2013).

[10] D. V. Evtushinsky, V. B. Zabolotnyy, T. K. Kim, A. A. Kordyuk, A. N. Yaresko, J. Maletz, S. Aswartham, S. Wurmehl, A. V. Boris, D. L. Sun, C. T. Lin, B. Shen, H. H. Wen, A. Varykhalov, R. Follath, B. Büchner, and S. V. Borisenko, Phys. Rev. B **89**, 064514 (2014).

[11] V. Brouet, D. LeBoeuf, P.-H. Lin, J. Mansart, A. Taleb-Ibrahimi, P. Le Fèvre, F. Bertran, A. Forget, and D. Colson, Phys. Rev. B **93**, 085137 (2016).

[12] J. M. Tomczak, M. van Schilfgaarde, and G. Kotliar, Phys. Rev. Lett. **109**, 237010 (2012).

[13] S. Backes, D. Guterding, H. O. Jeschke, and R. Valentí, New Journal of Physics **16**, 083025 (2014).

[14] T. Berlijn, C.-H. Lin, W. Garber, and W. Ku, Phys. Rev. Lett. **108**, 207003 (2012).

[15] L. Wang, T. Berlijn, Y. Wang, C.-H. Lin, P. J. Hirschfeld, and W. Ku, Phys. Rev. Lett. **110**, 037001 (2013).

[16] S. N. Khan and D. D. Johnson, Phys. Rev. Lett. **112**, 156401 (2014).

[17] S. V. Borisenko, D. V. Evtushinsky, Z.-H. Liu, I. Morozov, R. Kappenberger, S. Wurmehl, B. Büchner, A. N. Yaresko, T. K. Kim, M. Hoesch, T. Wolf, and N. D. Zhigadlo, Nature Physics **12**, 311 (2016), Letter.

[18] X.-P. Wang, P. Richard, Y.-B. Huang, H. Miao, L. Cevey, N. Xu, Y.-J. Sun, T. Qian, Y.-M. Xu, M. Shi, J.-P. Hu, X. Dai, and H. Ding, Phys. Rev. B **85**, 214518 (2012).

[19] G. Derondeau, J. Braun, H. Ebert, and J. Minár, Phys. Rev. B **93**, 144513 (2016).

[20] Z. P. Yin, K. Haule, and G. Kotliar, Nature Physics **7**, 294 (2011).

[21] Y.-Z. Zhang, H. Lee, I. Opahle, H. O. Jeschke, and R. Valentí, J. Phys. Chem. Sol. **72**, 324 (2011).

[22] J. Ferber, H. O. Jeschke, and R. Valentí, Phys. Rev. Lett. **109**, 236403 (2012).

[23] N. Xu, P. Richard, A. van Roekeghem, P. Zhang, H. Miao, W.-L. Zhang, T. Qian, M. Ferrero, A. S. Sefat, S. Biermann, and H. Ding, Phys. Rev. X **3**, 011006 (2013).

[24] Z. P. Yin, K. Haule, and G. Kotliar, Nature Physics **10**, 845 (2014).

[25] M. Rotter, M. Tegel, D. Johrendt, I. Schellenberg, W. Hermes, and R. Pöttgen, Phys. Rev. B **78**, 020503 (2008).

[26] M. Rotter, M. Tegel, and D. Johrendt, Phys. Rev. Lett. **101**, 107006 (2008).

[27] K. Nakayama, T. Sato, P. Richard, Y.-M. Xu, T. Kawahara, K. Umezawa, T. Qian, M. Neupane, G. F. Chen, H. Ding, and T. Takahashi, Phys. Rev. B **83**, 020501 (2011).

[28] N. Xu, P. Richard, X. Shi, A. van Roekeghem, T. Qian, E. Razzoli, E. Rienks, G.-F. Chen, E. Ieki, K. Nakayama, T. Sato, T. Takahashi, M. Shi, and H. Ding, Phys. Rev. B **88**, 220508 (2013).

[29] C. Liu, T. Kondo, R. M. Fernandes, A. D. Palczewski, E. D. Mun, N. Ni, A. N. Thaler, A. Bostwick, E. Rotenberg, J. Schmalian, S. L. Bud'ko, P. C. Canfield, and

A. Kaminski, Nature Physics **6**, 419 (2010).
[30] J. Ferber, K. Foyevtsova, R. Valentí, and H. O. Jeschke, Phys. Rev. B **85**, 094505 (2012).
[31] M. Aichhorn, L. Pourovskii, V. Vildosola, M. Ferrero, O. Parcollet, T. Miyake, A. Georges, and S. Biermann, Phys. Rev. B **80**, 085101 (2009).
[32] Note, that the X point in our notation corresponds to the M point in the notation used by Werner *et al.*
[33] M. G. Kim, J. Lamsal, T. W. Heitmann, G. S. Tucker, D. K. Pratt, S. N. Khan, Y. B. Lee, A. Alam, A. Thaler, N. Ni, S. Ran, S. L. Bud'ko, K. J. Marty, M. D. Lumsden, P. C. Canfield, B. N. Harmon, D. D. Johnson, A. Kreyssig, R. J. McQueeney, and A. I. Goldman, Phys. Rev. Lett. **109**, 167003 (2012).
[34] Supplemantal Material.
[35] V. N. Strocov, X. Wang, M. Shi, M. Kobayashi, J. Krempasky, C. Hess, T. Schmitt, and L. Patthey, Synchrotron Radiat. News **21**, 32 (2014).
[36] V. N. Strocov, M. Kobayashi, X. Wang, L. L. Lev, J. Krempasky, V. V. Rogalev, T. Schmitt, C. Cancellieri, and M. L. Reinle-Schmitt, Synchrotron Radiat. News **27**, 31 (2014).
[37] L. Moreschini, P.-H. Lin, C.-H. Lin, W. Ku, D. Innocenti, Y. J. Chang, A. L. Walter, K. S. Kim, V. Brouet, K.-W. Yeh, M.-K. Wu, E. Rotenberg, A. Bostwick, and M. Grioni, Phys. Rev. Lett. **112**, 087602 (2014).
[38] C.-H. Lin, T. Berlijn, L. Wang, C.-C. Lee, W.-G. Yin, and W. Ku, Phys. Rev. Lett. **107**, 257001 (2011).
[39] L. L. Lev, J. Krempaský, U. Staub, V. A. Rogalev, T. Schmitt, M. Shi, P. Blaha, A. S. Mishchenko, A. A. Veligzhanin, Y. V. Zubavichus, M. B. Tsetlin, H. Volfová, J. Braun, J. Minár, and V. N. Strocov, Phys. Rev. Lett. **114**, 237601 (2015).
[40] J. Braun and M. Donath, Europhys. Lett. **59**, 592 (2002).
[41] V. N. Strocov, J. Electron. Spectrosc. Relat. Phenom. **130**, 65 (2003).
[42] R. L. Kurtz, D. A. Browne, and G. J. Mankey, J. Phys.: Cond. Mat. **19**, 355001 (2007).
[43] H. Ebert, D. Ködderitzsch, and J. Minár, Rep. Prog. Phys. **74**, 096501 (2011).
[44] H. Ebert et al., *The Munich SPR-KKR package*, version 6.3, http://olymp.cup.uni-muenchen.de/ak/ebert/SPRKKR, 2012.
[45] G. Derondeau, S. Polesya, S. Mankovsky, H. Ebert, and J. Minár, Phys. Rev. B **90**, 184509 (2014).
[46] J. Minár, J. Braun, and H. Ebert, J. Electron. Spectrosc. Relat. Phenom. **189**, 129 (2013).
[47] J. Braun, K. Miyamoto, A. Kimura, T. Okuda, M. Donath, H. Ebert, and J. Minár, New Journal of Physics **16**, 015005 (2014).
[48] J. Minár, J. Phys.: Cond. Mat. **23**, 253201 (2011).

Acknowledgments

We thank V. Zabolotnyy and S. Borisenko for allowing us to use their experimental data. Special thanks goes to S. Biermann for discussions and ideas. We acknowledge financial support from the Deutsche Forschungsgemeinschaft DFG (projects FOR 1346) and from the Bundesministerium für Bildung und Forschung BMBF (project 05K13WMA). We further thank for the support from CENTEM PLUS (L01402). F. Bisti acknowledges the funding from the Swiss National Science Foundation under the grant agreement n.200021_146890 and European Community's Seventh Framework Programme (FP7/2007-2013) under the grant agreement n.290605 (PSI-FELLOW/COFUND).

Author contributions

G.D., V.N.S. and J.Mi. wrote the manuscript. F.B. V.A.R., M.K., T.S., J.Ma and V.N.S. performed the experiments and analyzed the data. G.D. performed the calculations. G.D., F.B., J.B., M.S., H.D., H.E., V.N.S. and J.Mi. participated at the discussions. J.Mi. supervised the theoretical part, V.N.S. supervised the experimental part.

Additional information

Supplemental Material accompanies this paper.

Competing financial interests: The authors declare no competing financial interests.

Supplemental Material for

Fermi surface and effective masses in photoemission response of the $(\mathbf{Ba_{1-x}K_x})\mathbf{Fe_2As_2}$ superconductor

Gerald Derondeau,[1,*] Federico Bisti,[2] Jürgen Braun,[1] Victor A. Rogalev,[2]
Masaki Kobayashi,[2,3] Ming Shi,[2] Thorsten Schmitt,[2] Junzhang Ma,[2,4,5]
Hong Ding,[4,5] Hubert Ebert,[1] Vladimir N. Strocov,[2,†] and Ján Minár[1,6,‡]

[1]*Department Chemie, Physikalische Chemie, Universität München,*
Butenandtstr. 5-13, 81377 München, Germany
[2]*Swiss Light Source, Paul Scherrer Institute, CH-5232 Villigen PSI, Switzerland*
[3]*Department of Applied Chemistry, School of Engineering,*
University of Tokyo, 7-3-1 Hongo, Bunkyo-ku, Tokyo 113-8656, Japan
[4]*Beijing National Laboratory for Condensed Matter Physics*
[5]*Institute of Physics, Chinese Academy of Sciences, Beijing 100190, China*
[6]*NewTechnologies-Research Center, University of West Bohemia, Pilsen, Czech Republic*

(Dated: September 15, 2016)

1. LIFSHITZ TRANSITION

A Lifshitz transition is characterized as a topological change of the Fermi surface.[1] For the iron pnictide superconductors this type of transition is of crucial importance as it is believed to mark the onset of superconductivity.[2–5] The K-doped $(\mathrm{Ba}_{1-x}\mathrm{K}_x)\mathrm{Fe}_2\mathrm{As}_2$ is a famous example for such a Lifshitz transition around the X point, leading to the discussed propeller topologies seen in ARPES experiments.[5–8] As known from experimental data [6–8] and the experiments performed within this work these topological features are already clearly visible for the optimally doped $(\mathrm{Ba}_{0.6}\mathrm{K}_{0.4})\mathrm{Fe}_2\mathrm{As}_2$. This is expected, following the argumentation that the Lifshitz transition suppresses the magnetic order due to a reduced nesting and thus induces superconductivity.[2, 9] However, the observed Lifshitz transition on the basis of the LDA was so far discussed only for high doping concentrations $x \approx 0.9$. [5, 10] It is also known that it is difficult to prepare homogeneous samples of over-doped $(\mathrm{Ba}_{1-x}\mathrm{K}_x)\mathrm{Fe}_2\mathrm{As}_2$ [5] which might explain discrepancies between various experiments about the onset of the Lifshitz transition.[6, 8, 10, 11] One remarkable and important paper from Khan and Johnson used the CPA to investigate the Lifshitz transition for $(\mathrm{Ba}_{1-x}\mathrm{K}_x)\mathrm{Fe}_2\mathrm{As}_2$ and they found a similar emergence of these propeller-like topologies for the heavily over-doped $(\mathrm{Ba}_{0.1}\mathrm{K}_{0.9})\mathrm{Fe}_2\mathrm{As}_2$.[5] However, with our new findings this result is now fully understandable. Using only a LDA based approach the relevant bands around X are still around 0.1 eV below the Fermi level (E_F). One can use over-doping with K in order to decrease E_F. The disadvantage of this approach is however that not only the relevant bands around X but the whole band structure is moved. Using a LDA+DMFT based approach one can see that correlation effects alter the electronic structure around X already for optimally doped $(\mathrm{Ba}_{0.6}\mathrm{K}_{0.4})\mathrm{Fe}_2\mathrm{As}_2$ so that the Lifshitz transition can emerge for lower doping concentration, in agreement with experiments.[6–8]

In order to show how this topology is affected by the correlation strength we show the corresponding BSF and FS in Fig. S1 for (A) LDA and LDA+DMFT with a varying on-site Coulomb interaction of (B) $U = 2.0$ eV, (C) $U = 3.0$ eV and (D) $U = 4.0$ eV with a constant exchange interaction $J = 0.9$ eV for Fe. Best agreement with experiment can be found for $U = 3.0$ eV as used and discussed in the main paper but it is also obvious that bands responsible for the Lifshitz transition are directly controlled by the Coulomb interaction U. Thus, we show that the origin of the important Lifshitz transition in $(\mathrm{Ba}_{1-x}\mathrm{K}_x)\mathrm{Fe}_2\mathrm{As}_2$ can be fully explained by correlation effects.

Still, it is also interesting to note that recent work on the ARPES spectra of the electron doped $\mathrm{Ba}(\mathrm{Fe}_{1-x}\mathrm{Co}_x)_2\mathrm{As}_2$ was successful using only a LDA approach.[12] The strength of correlation effects in the iron pnictides seem to vary with electron or hole doping.

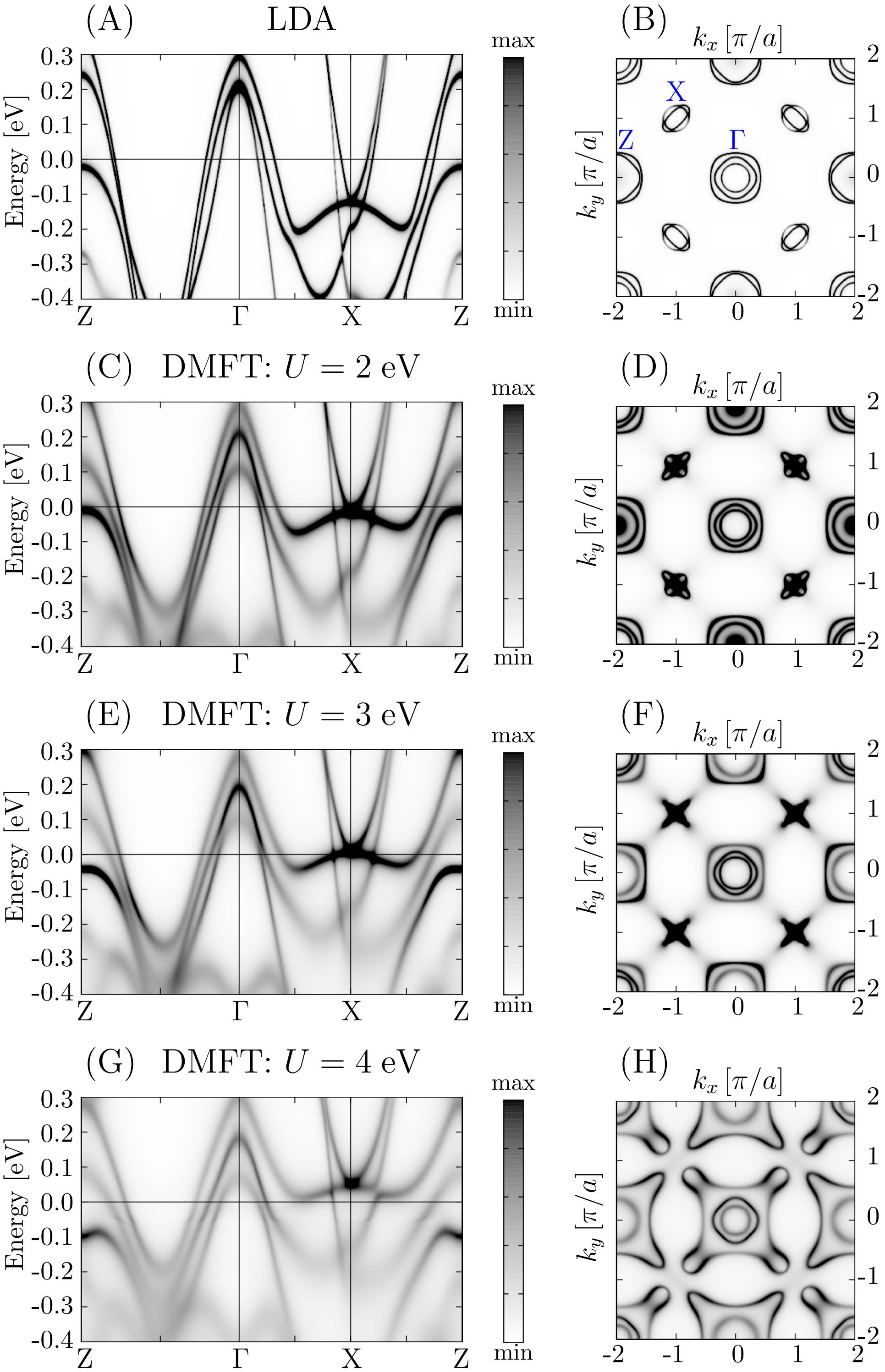

FIG. S1. (Color online) (A + B) BSF and FS of $(\mathrm{Ba}_{0.6}\mathrm{K}_{0.4})\mathrm{Fe}_2\mathrm{As}_2$ calculated on the basis of LDA. Corresponding BSF and FS of $(\mathrm{Ba}_{0.6}\mathrm{K}_{0.4})\mathrm{Fe}_2\mathrm{As}_2$ calculated on the basis of LDA+DMFT with (C + D) $U = 2.0$ eV, (E + F) $U = 3.0$ eV and (G + H) $U = 4.0$ eV for Fe ($J = 0.9$ eV).

2. EXTENDED FERMI SURFACE CUT

In correspondence to Fig. 3 of the main manuscript we present additionally extended Fermi surface cuts of $(Ba_{0.6}K_{0.4})Fe_2As_2$ for experimental data and theoretical calculations, respectively. Thus, Fig. S2 (A) shows the experimental data up to the second Brillouin zone and (B) the calculated Fermi surface cut up to the forth Brillouin zone, both images for p-polarized light and $h\nu = 430$ eV. This verifies that the alternating symmetry of the flower-like topology at $\bar{\Gamma}'$ compared to $\bar{\Gamma}$ is preserved over the whole k-space, in agreement with the data of Zabolotnyy *et al.* [6]. Interestingly, the flower-like topology changes a little bit for the third and forth Brillouin zone in Fig. S2 (B) which is connected to the k_z dispersion. Note, that the calculation is shown for a fixed photon energy of $h\nu = 430$ eV, thus, the effect of the k_z dispersion increases for higher Brillouin zones (see also the k_z scan in Fig. 4). In the experimental data of Fig. S2 (A) the value of k_z is corrected on the other hand. The blue square in (B) corresponds to the part of the Fermi surface shown in (A).

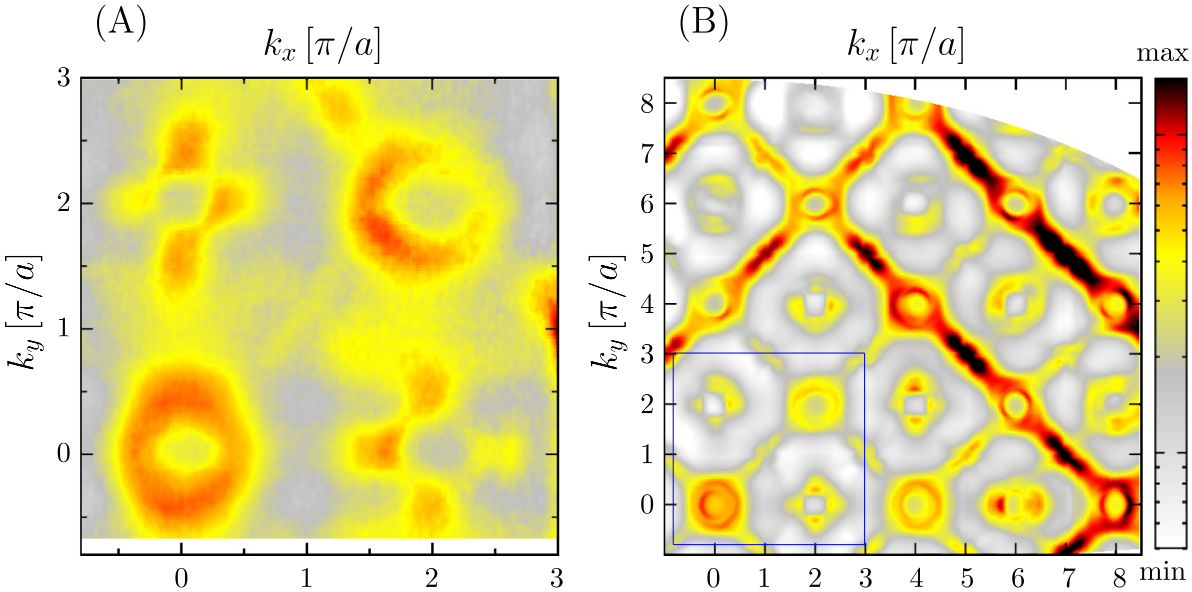

FIG. S2. Fermi surface cuts of $(Ba_{0.6}K_{0.4})Fe_2As_2$ with a fixed $h\nu = 430$ eV and for p-polarized light extending over several Brillouin zones. This is shown for (A) experimental data and (B) ARPES calculations using LDA+DMFT. The blue square in (B) corresponds to the part seen in (A).

3. DERIVED EFFECTIVE MASS ENHANCEMENT

In order to derive the mass enhancements shown in Tab. I the corresponding bands shown in Fig. S3 were used with the applied parabolic fits shown as solid green and red lines on top. For the BSF in Fig. S3 (A + B) and (E + F) the band dispersion can be fitted very reasonably by parabolic functions. For the ARPES response however, final state effects, matrix element effects and surface effects alter the true band dispersion which results in bands showing more deviation from the perfect parabolic behavior. As discussed in the main paper, this is mainly due to final state effects which have a stronger impact the more pronounced the k_z dispersion of the corresponding bands is. Thus, the deviations from the perfect parabolic behavior are stronger in Fig. S3 (C + D) at the Γ point, compared to Fig. S3 (G + H) at the X point, because the bands at Γ have stronger 3D character whereas the band at X considered here is almost a 2D band. Furthermore, one should note that in the ARPES spectra the two outer bands around Γ are hardly distinguishable due to intensity loss connected to the ARPES response. As a technical detail, the calculations used an imaginary energy of 0.025 eV for the initial states and of 5.0 eV for the final states.

The resulting mass renormalization is shown in Fig. S4 (A - C) with the LDA bands from Fig. S3 (A) on top of the respective DMFT BSF and the DMFT ARPES response as dashed green and red lines. In addition, the DMFT bands of Fig. S3 (B) are shown on top of the ARPES spectra in Fig. S4 (D - E). This shows explicitly the deviation of the ARPES response from the true band dispersion derived from DMFT BSF. Consequently, the apparent mass enhancement seen in

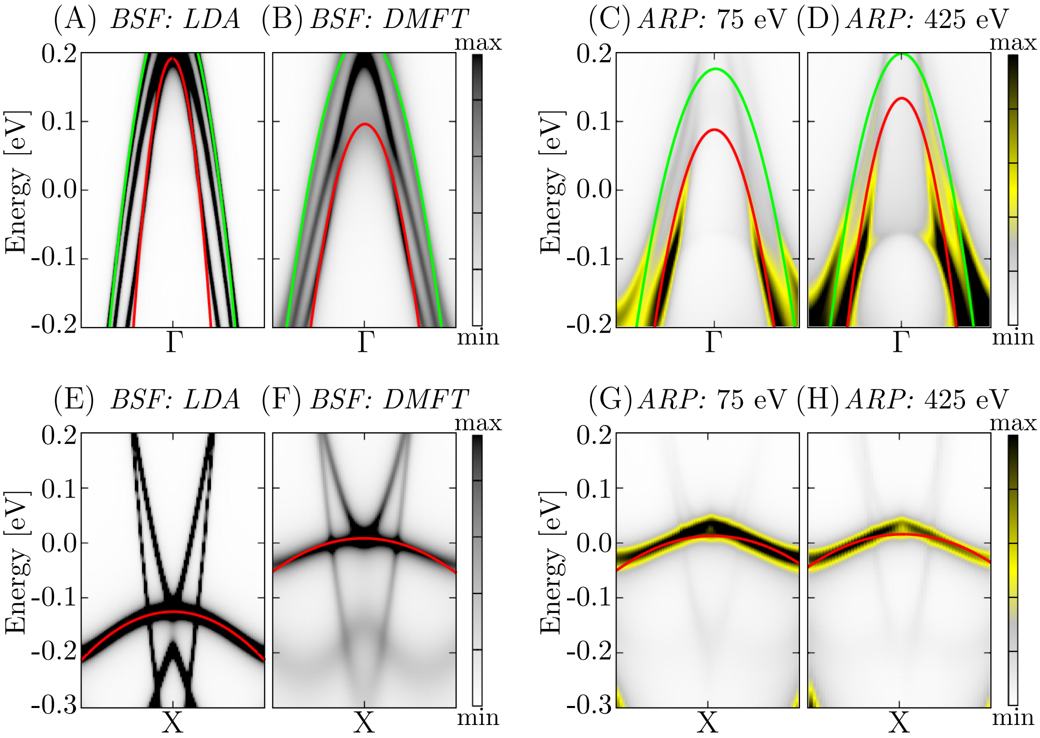

FIG. S3. Bands for which the mass enhancement is shown in Tab I. The solid red and green lines correspond to the applied parabolic plot fit. They are shown for (A - D) the Γ point having a strong k_z dispersion and for (E - H) the X point having a weak k_z dispersion. (A + E) BSF based on LDA, (B + F) BSF based on LDA+DMFT and (C + G) ARPES calculations based on DMFT for $h\nu = 75$ eV and (D + H) the same for $h\nu = 425$ eV.

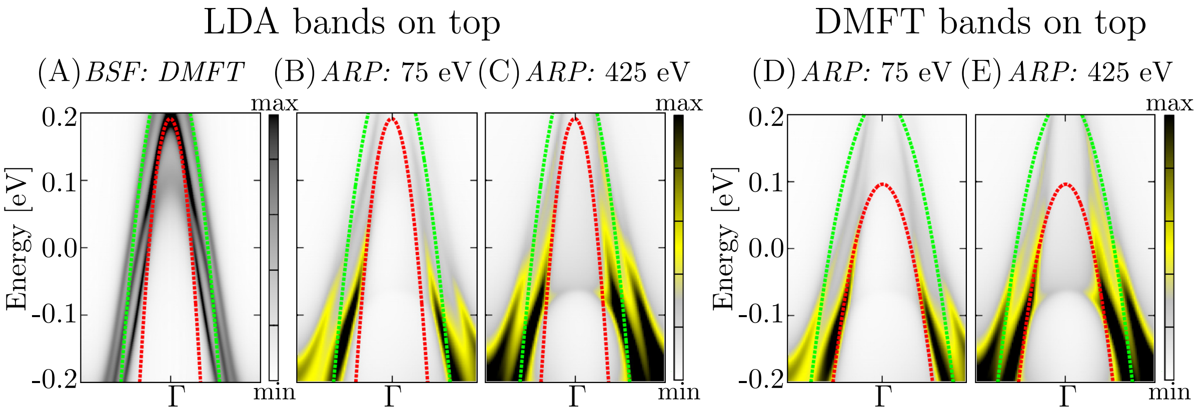

FIG. S4. (A - C) Band renormalization for BSF DMFT and the ARPES response with the LDA bands of Fig. S3 (A) on top. (D - E) The same ARPES spectra but with the DMFT bands of Fig. S3 (B) on top in order to show the effect only due to the ARPES response.

ARPES is affected by these ARPES response effects and thus it is not an intrinsic property of the quasiparticle valence band structure or spectral function. Why the ARPES response is affected by the k_z broadening Δk_z is depicted schematically in Fig. S5. As discussed in the main paper, Δk_z can be reduced by choosing a higher photon energy, although the resulting effects can be never fully avoided for 3D materials like the iron pnictides.

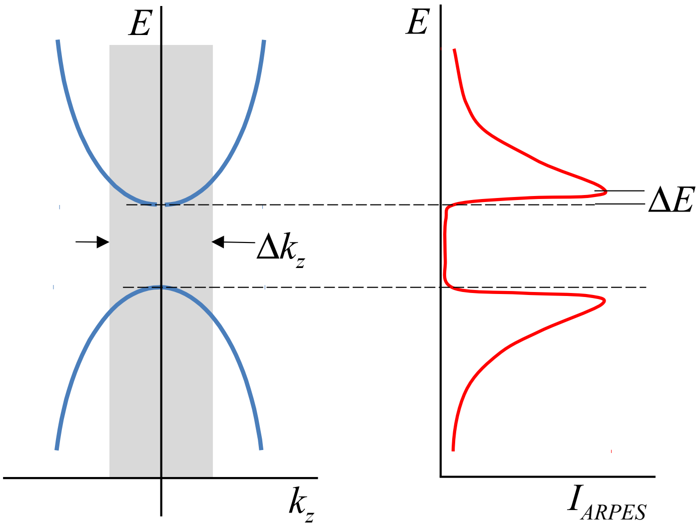

FIG. S5. Mechanism of the apparent mass enhancement (assuming a constant matrix element). The ARPES signal is formed by averaging of the valence band dispersion within the Δk_z broadening interval. Near the extremes of the k_z dispersion, this averaging results in asymmetry of the ARPES weight and shifting of the resulting spectral peak away from the extreme towards the band interior (for a more detailed picture including lifetime broadening of the valence states see Ref. [13]). Concerning its $\boldsymbol{k}_{||}$ dependence of the ARPES spectra this shift causes an apparent reduction of the bandwidth and an increase of m^*.

---

[*] gerald.derondeau@cup.uni-muenchen.de

[†] vladimir.strocov@psi.ch

[‡] jan.minar@cup.uni-muenchen.de

[1] I. M. Lifshitz, Sov. Phys. J.E.T.P. **11**, 1130 (1960).

[2] C. Liu, T. Kondo, R. M. Fernandes, A. D. Palczewski, E. D. Mun, N. Ni, A. N. Thaler, A. Bostwick, E. Rotenberg, J. Schmalian, S. L. Bud'ko, P. C. Canfield, and A. Kaminski, Nature Physics **6**, 419 (2010).

[3] K. Matan, S. Ibuka, R. Morinaga, S. Chi, J. W. Lynn, A. D. Christianson, M. D. Lumsden, and T. J. Sato, Phys. Rev. B **82**, 054515 (2010).

[4] C. Liu, A. D. Palczewski, R. S. Dhaka, T. Kondo, R. M. Fernandes, E. D. Mun, H. Hodovanets, A. N. Thaler, J. Schmalian, S. L. Bud'ko, P. C. Canfield, and A. Kaminski, Phys. Rev. B **84**, 020509 (2011).

[5] S. N. Khan and D. D. Johnson, Phys. Rev. Lett. **112**, 156401 (2014).

[6] V. B. Zabolotnyy, D. S. Inosov, D. V. Evtushinsky, A. Koitzsch, A. A. Kordyuk, G. L. Sun, J. T. Park, D. Haug, V. Hinkov, A. V. Boris, C. T. Lin, M. Knupfer, A. N. Yaresko, B. Büchner, A. Varykhalov, R. Follath, and S. V. Borisenko, Nature **457**, 569 (2009).

[7] D. V. Evtushinsky, D. S. Inosov, V. B. Zabolotnyy, M. S. Viazovska, R. Khasanov, A. Amato, H.-H. Klauss, H. Luetkens, C. Niedermayer, G. L. Sun, V. Hinkov, C. T. Lin, A. Varykhalov, A. Koitzsch, M. Knupfer, B. Büchner, A. A. Kordyuk, and S. V. Borisenko, New Journal of Physics **11**, 055069 (2009).

[8] D. V. Evtushinsky, A. A. Kordyuk, V. B. Zabolotnyy, D. S. Inosov, T. K. Kim, B. Büchner, H. Luo, Z. Wang, H.-H. Wen, G. Sun, C. Lin, and S. V. Borisenko, J. Phys. Soc. Japan **80**, 023710 (2011).

[9] M. G. Kim, J. Lamsal, T. W. Heitmann, G. S. Tucker, D. K. Pratt, S. N. Khan, Y. B. Lee, A. Alam, A. Thaler, N. Ni, S. Ran, S. L. Bud'ko, K. J. Marty, M. D. Lumsden, P. C. Canfield, B. N. Harmon, D. D. Johnson, A. Kreyssig, R. J. McQueeney, and A. I. Goldman, Phys. Rev. Lett. **109**, 167003 (2012).

[10] N. Xu, P. Richard, X. Shi, A. van Roekeghem, T. Qian, E. Razzoli, E. Rienks, G.-F. Chen, E. Ieki, K. Nakayama, T. Sato, T. Takahashi, M. Shi, and H. Ding, Phys. Rev. B **88**, 220508 (2013).

[11] K. Nakayama, T. Sato, P. Richard, Y.-M. Xu, T. Kawahara, K. Umezawa, T. Qian, M. Neupane, G. F. Chen, H. Ding, and T. Takahashi, Phys. Rev. B **83**, 020501 (2011).

[12] G. Derondeau, J. Braun, H. Ebert, and J. Minár, Phys. Rev. B **93**, 144513 (2016).

[13] V. N. Strocov, J. Electron. Spectrosc. Relat. Phenom. **130**, 65 (2003).

6.3 Additional calculations

Due to the extensive long-term study, which resulted in a huge amount of data, only a small part of the performed calculations could be shown in the published manuscript. Especially parts which were too technical had to be skipped. In the following some additional calculations on this topic will be presented for the sake of completeness and in order to further support the presented work. This will focus especially on the flower-like Fermi surface topology seen at $\bar{\Gamma}'$.

The k_z dispersion

The original motivation was based on the unexpected flower-like topology which was found by experiment to be always at $\bar{\Gamma}'$ independent on k_z. The clear k_z dispersion of the compound was mentioned in the presented work and shown for experiment, however, it was not explicitly shown for the calculations due to lack of space. For the sake of consistency, the corresponding calculated Fermi surface cuts are shown in Fig. 6.3 for (A) $h\nu = 392$ eV and (B) $h\nu = 430$ eV in comparison to the experimental data presented in Fig. 6.1.

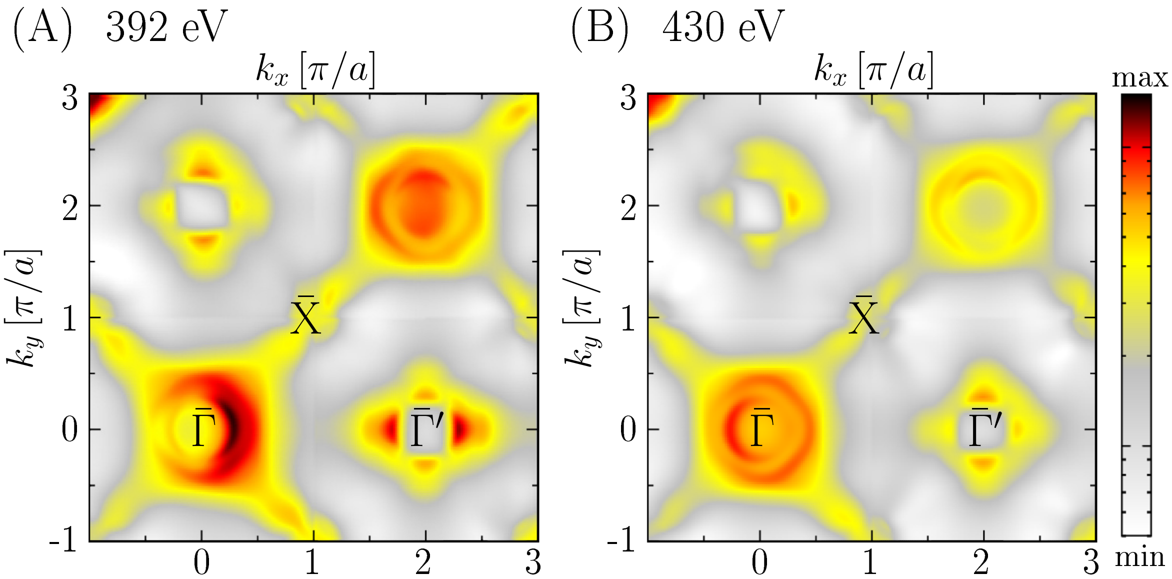

Figure 6.3. Calculated ARPES Fermi surface cuts of $(\mathrm{Ba}_{0.6}\mathrm{K}_{0.4})\mathrm{Fe}_2\mathrm{As}_2$ measured with p-polarized light for (A) $h\nu = 392$ eV and for (B) $h\nu = 430$ eV, in comparison to Fig. 6.1.

It is obvious that the flower-like topology of interest can be found in both calculations at $\bar{\Gamma}'$ and is thus independent on k_z as one should expect from experiment. In addition, the calculated k_z dispersion is shown in Fig. 6.4, corresponding to the experimental result from Fig. 6.2.

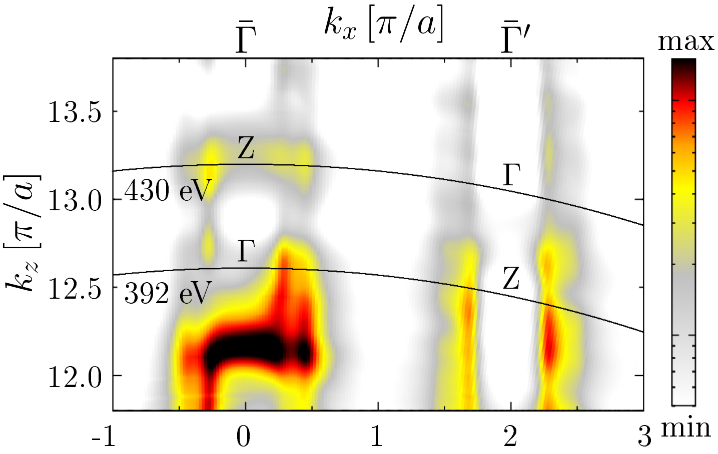

Figure 6.4. Calculated k_z scan, in comparison to Fig. 6.2, with p-polarized light for $(Ba_{0.6}K_{0.4})Fe_2As_2$ showing k_z dispersion and alternating Γ and Z points. The photon energies $h\nu = 392$ eV and $h\nu = 430$ eV are marked by black lines.

Minor details in the intensity distribution of the calculated k_z scan deviate from experiment, which might be due to small deviations in the angle of the incident light. However, more important is the obvious k_z dispersion and the alternating points of high and low intensities, representing Z and Γ, respectively. This is reproduced in good agreement with experimental data. Furthermore, one can see that $h\nu = 392$ eV and $h\nu = 430$ eV correspond in experiment and in the calculations to approximately the same lines in $\boldsymbol{k}$-space.

Impact of the surface barrier

It was explicitly shown that the unexpected topologies in the ARPES spectra of $(Ba_{0.6}K_{0.4})Fe_2As_2$ as presented in the original motivation in section 6.1 could be reproduced concerning all aspects by the applied method. However, the details of the surface resonance states, which are believed to be crucial for the flower-like topology at $\bar{\Gamma}'$, were not discussed in the published manuscript, as this would have been too technical for the general reader.

Thus, we show in Fig. 6.5 the calculated Fermi surface cuts with $h\nu = 80$ eV for three different values of the surface barrier in (A) – (C), respectively. As explained in subsection 2.2.3, the surface potential is described by the spin-dependent Rundgren-Malmström barrier, which connects the asymptotic region $\sim \frac{1}{z}$ to the bulk muffin-tin zero by a third-order polynomial in z.[139] The surface barrier parameter, given in atomic units, now specifies the distance between the crystal and the image plane. Thus, it is connected to the width of the third-order polynomial and parameterizes the

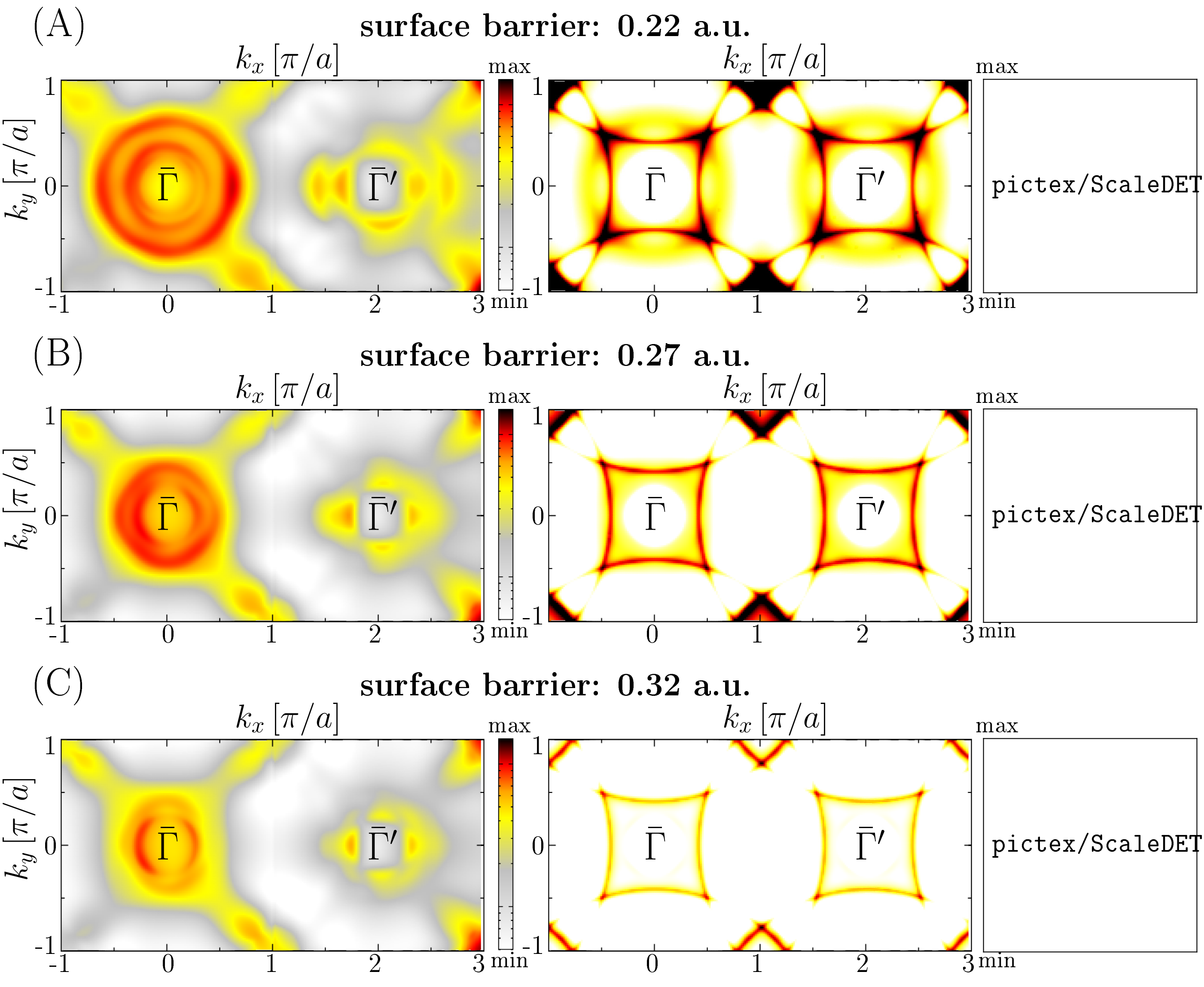

Figure 6.5. Fermi surfaces cuts of $(\mathrm{Ba}_{0.6}\mathrm{K}_{0.4})\mathrm{Fe}_2\mathrm{As}_2$ for $h\nu = 80$ eV as obtained by one step model ARPES calculations for (A) LDA and (B) LDA+DMFT. The overlay of black isolines always corresponds to experimental ARPES data taken with permission from Zabolotnyy *et al.*[33]. The green solid lines are guides for the eyes to indicate surface state related features.

impact of the surface. Changing the surface barrier will consequently shift states which have a surface character. To identify such states, the already described determinant condition is used, as explained in subsection 2.2.3.

The right panel of Fig. 6.5 corresponds to the respective plot of the determinant condition, equal to the discussion of surface states in Chapter 5. One can see that the dark areas of the determinant condition do not correspond to real features of the Fermi surface, meaning these indications show no real surface states. On the other hand, the dark yellow rings around $\bar{\Gamma}$ and $\bar{\Gamma}'$ correspond directly to the respective outer ring of the Fermi surface cut. Thus, the outer ring around $\bar{\Gamma}$ can be clearly identified as a surface resonance state.

Assuming different values for the surface barrier does shift these surface resonances in their binding energy, meaning they will cut the Fermi surface at different positions, respectively. This effect can be also observed in the Fermi surface cuts on the left panel, meaning the outer ring around $\bar{\Gamma}$ gets continuously more compressed for higher values of the surface barrier. Thus, the position of these surface resonances has a significant impact on the resulting spectrum and also on the flower-like topology at $\bar{\Gamma}'$. As mentioned in the main paper the difference between two Brillouin zones can be understood based on the structure factor, meaning the phase difference between different atoms of one unit cell has to be accounted for. Based on the light polarization, now different orbitals are exited for the first and the second Brillouin zone, as explained e.g. by Moreschini *et al.*[260]. Note, that using the multiple scattering approach within SPR-KKR accounts by construction correctly for the structure factor. Thus, the correct polarization-depend intensities at $\bar{\Gamma}$ and $\bar{\Gamma}'$ are reproduced by the presented calculations in good agreement with the work of Moreschini *et al.*[260]. However, as shown in Fig. 6.5, one finds that the correct treatment of the structure factor alone is not sufficient to explain completely the topology observed in the experimental ARPES spectra of $(Ba_{0.6}K_{0.4})Fe_2As_2$. Additionally, the ring-shaped surface resonance influences and enhances the flower-like topology at $\bar{\Gamma}'$. Best agreement with experiment can be observed in Fig. 6.5 (B) for a surface barrier of 0.27 a.u., where the surface resonance is precisely enhancing the four petals at $\bar{\Gamma}'$. Note, that all calculations shown in the manuscript thus used a surface barrier of 0.27 a.u., corresponding to (B).

6.4 Discussion

The original phenomenon of interest, namely the flower-like Fermi surface topology at $\bar{\Gamma}'$ of the second Brillouin zone, could be successfully reproduced by theory. It was shown that the presented ARPES calculations which by construction include the correct treatment of the structure factor and the light polarization are able to capture all effects which are necessary to reproduce this four-fold flower pattern for the second Brillouin zone. Thus, all effects which are discussed e.g. by Moreschini *et al.*[260] can be correctly described by the applied SPR-KKR method combined with the one-step model of photoemission. Additionally, it was shown that surface resonances play an important role in the spectra of $(\mathrm{Ba}_{0.6}\mathrm{K}_{0.4})\mathrm{Fe}_2\mathrm{As}_2$ and they have a significant influence on the shape of the flower-like topologies. Only if these surface resonances are correctly accounted for, an overall good agreement with experiment could be reached. Thus, future studies on the iron pnictides have to account for surface related effects, as it was already stressed for $\mathrm{Ba}(\mathrm{Fe}_{1-x}\mathrm{Co}_x)_2\mathrm{As}_2$ in Chapter 5.

Apart from this, other relevant results of this chapter should be emphasized. Without doubt ARPES is the most informative experimental tool for the electronic structure of the iron pnictides, however, a comprehensive theoretical study of their ARPES spectra is up to now rarely successful. On the other hand, the present work has exhaustively explained all salient features of the ARPES spectra in $(\mathrm{Ba}_{0.6}\mathrm{K}_{0.4})\mathrm{Fe}_2\mathrm{As}_2$ by using a combination of LDA+DMFT+ARPES calculations, which was not achieved so far. One should also note, that the applied approach can handle low photon energies in the UV regime as well as high photon energies in the soft-X-ray region at the same time. This correct treatment of ARPES is obviously very important, as two points obtained with the presented approach will significantly affect future ARPES studies on the iron pnictides.

First, this work could identify the origin of the Lifshitz transition in the K-doped $(\mathrm{Ba}_{0.6}\mathrm{K}_{0.4})\mathrm{Fe}_2\mathrm{As}_2$ superconductor for a reasonable doping concentration x, which is crucial for the emergence of superconductivity. It was shown that this Lifshitz transition seems to be fully controlled by electron correlation effects accounted for within the DMFT framework. This emphasizes the impact strong correlations can have on the iron pnictides and it should help further research in order to control the emergence of superconductivity. At this point one should also note, that the importance of strong correlations seem to vary for different compounds. The ARPES spectra of antiferromagnetic $\mathrm{Ba}(\mathrm{Fe}_{1-x}\mathrm{Co}_x)_2\mathrm{As}_2$ in Chapter 5 could be obviously well described by using only a LDA approach. On the other hand, correlations as accounted for by the LDA+DMFT method were mandatory to obtain correct results for nonmagnetic $(Ba_{0.6}K_{0.4})Fe_2As_2$ as shown in this chapter. This behavior seems to be connected to the difference concerning electron or hole doping. There is work in the literature which supports this idea, indicating indeed that the hole-doped iron pnictides might be stronger affected by correlations.[55,261] However, the results obtained in this publication cannot exclude that a difference in the correlation strength might be also due to the antiferromagnetic to nonmagnetic transition.

Secondly, it was shown that there is an inevitable difference between the spectra seen in ARPES and the band dispersion derived from DMFT. This traces back to the photoemission response, including final state effects or also surface effects and matrix element effects. In particular, it was discovered that the effective mass renormalization observed in all previous ARPES studies on iron pnictides is actually not an entirely intrinsic property of the quasiparticle valence band structure, but has a significant extrinsic contribution due to the photoemission process itself. This phenomenon is essentially determined by the three-dimensional momentum definition of the photoemission final states, resulting in a k_z broadening of the electronic structure. This Δk_z has a stronger impact at lower photon energies in the ultraviolet energy range, which is commonly used in ARPES experiments. Thus, higher photon energies in the soft-X-ray region should provide better results for the mass renormalization. However, one should keep in mind that a higher $h\nu$ also goes in hand with a reduced resolution. Still, the here published information is crucial to know because it affects all published experimental results on the effective mass renormalization so far. Consequently, it has also a significant impact on theoretical models discussing strong correlations in the iron pnictides based on the obtained effective mass renormalization.

Chapter 7

Anisotropic magnetoresistance

7.1 Motivation

The idea for the work presented in the following started already with the first investigation of the doping dependent behavior of Ba(Fe$_{1-x}$Co$_x$)$_2$As$_2$ in Chapter 4. It was observed, that not only the electronic structure shows a prominent in-plane anisotropy, but also the strength of disorder effects varied between the a and b axes, respectively. Consequently, it was noted in the published manuscript:

> “Additionally, the in-plane anisotropy of the disorder [...] may be an interesting first indication for anisotropic effects in the transport properties at the proximity of the magnetic phase. [...] Still, an investigation of only the Fermi surface is insufficient [...] and specific calculations of the linear-response properties of these systems are necessary and planned for the future.”[262]

It turned out that an extensive study was mandatory to investigate this issue in more detail to get satisfactory results. However, the interest was certainly justified. The in-plane resistivity anisotropy of the 122-family of iron pnictides was since its discovery in 2010 for BaFe$_2$As$_2$[38] and Ba(Fe$_{1-x}$Co$_x$)$_2$As$_2$[39] one of the most discussed and investigated issues of the following years. This interest was mainly due to the unexpected behavior, meaning a higher resistivity along the shorter ferromagnetically coupled b axis was reported, while the lower resistance was found along the antiferromagnetically coupled a axis.[38,39,42] Furthermore, significant deviations in the resistivity were reported for different kinds of substitution in BaFe$_2$As$_2$.[43,192,222,263] Altogether, it is quite difficult to find a reasonable explanation for this confusing resistivity behavior and several sometimes contradicting theories were developed on this topic.

From the experimental site, scanning tunneling microscope (STM) experiments had observed local anisotropic defect states with a size of approximately 22 Å, extending over several unit cells.[40,195,196] Thus, several experimentalists assumed such anisotropic scattering states as origin of the resistivity anisotropy[42,263], however, other experimental work argued vigorously against such extrinsic sources in favor of the intrinsic band structure[44] as origin. From theory, the issue was extensively investigated, although mainly based on model Hamiltonian approaches.[155,264–270] Some work stressed the importance of spin fluctuations[269,270], while other was able to reproduce so-called nematogen impurity states which explain the origin of the resistivity anisotropy by means of extended impurity states similar to the already mentioned STM experiments.[155,266,267]

In any case, the majority of nowadays theories on the topic of the resistivity anisotropy has abandoned the idea of linking this phenomenon to the anisotropic band structure, except of e.g. Kuo and Fisher[44]. The idea was suggested in the beginning from ARPES measurements[36] but it was never really quantified how the electronic band structure and the resistivity anisotropy might be related to each other. Thus, it was striking to observe an in-plane anisotropy of the disorder induced band broadening of the electronic structure in $\mathrm{Ba(Fe_{1-x}Co_x)_2As_2}$ as presented in Chapter 4. After all, the influence of the anisotropic band structure to this controversial phenomenon was never investigated on a first-principles level so far. Thus, the Kubo-Greenwood formalism as available within the SPR-KKR package provided the necessary technical opportunity.

7.2 Publication: arXiv 1608.08077

In-plane anisotropic magnetoresistance in antiferromagnetic $Ba(Fe_{1-x}Co_x)_2As_2$, $(Ba_{1-x}K_x)Fe_2As_2$ and $Ba(Fe_{1-x}Ru_x)_2As_2$

Gerald Derondeau,[1] Ján Minár,[1,2] Sebastian Wimmer,[1] Hubert Ebert[1]

[1] *Department Chemie, Physikalische Chemie, Universität München, München, Germany*
[2] *NewTechnologies-Research Center, University of West Bohemia, Pilsen, Czech Republic*

available at: arXiv 1608.08077 [cond-mat.supr-con]

submitted to: Physical Review Letters on 31st of August 2016

In-plane anisotropic magnetoresistance in antiferromagnetic $\mathbf{Ba(Fe_{1-x}Co_x)_2As_2}$, $\mathbf{(Ba_{1-x}K_x)Fe_2As_2}$ and $\mathbf{Ba(Fe_{1-x}Ru_x)_2As_2}$

Gerald Derondeau,[1, *] Ján Minár,[1, 2] Sebastian Wimmer,[1] and Hubert Ebert[1]
[1] *Department Chemie, Physikalische Chemie, Universität München, Butenandtstr. 5-13, 81377 München, Germany*
[2] *NewTechnologies-Research Center, University of West Bohemia, Pilsen, Czech Republic*

(Dated: August 30, 2016)

Using the Kubo-Greenwood formalism the resistivity anisotropy for electron doped $Ba(Fe_{1-x}Co_x)_2As_2$, hole doped $(Ba_{1-x}K_x)Fe_2As_2$ and isovalently doped $Ba(Fe_{1-x}Ru_x)_2As_2$ in their antiferromagnetic state has been calculated in order to clarify the origin of this important phenomenon. The results show good agreement with experiment for all cases without considering impurity states extending over several unit cells or temperature induced spin fluctuations. From this it is concluded that the resistivity anisotropy at low temperatures is primarily caused by an in-plane anisotropic magnetoresistance. Accounting for the band dispersion with respect to k_z is however mandatory to explain the results, showing the importance of the three-dimensional character of the electronic structure for the iron pnictides. Furthermore, it is shown that the counterintuitive sign of the resistivity anisotropy is no fundamental property but just a peculiarity of the anisotropic band structure.

The iron pnictide superconductors are one of most important examples for unconventioanl superconductivity, with the physical interest of the last few years mainly focused on their strong in-plane anisotropy which emerges for various physical properties [1–6]. This anisotropy is prominent in electrical transport [1–3, 7–11] but also shows up in angle-resolved photoemission spectroscopy (ARPES) [4, 12], neutron diffraction [5] or optical spectroscopy [6, 13]. Of special interest is the in-plane resistivity anisotropy ($\Delta\rho = \rho_a - \rho_b$) for the $BaFe_2As_2$ family as it seems to involve several physical phenomena. Notably, the higher resistivity was observed along the shorter b axis (ρ_b) which corresponds to ferromagnetically coupled chains, while the lower resistivity was found along the a axis (ρ_a) along which the spins couple antiferromagnetically [1, 2]. A quite different behavior is reported for different kinds of substitution in $BaFe_2As_2$ [9, 10, 14, 15]. Compared to electron doped $Ba(Fe_{1\text{-}x}Co_x)_2As_2$ [1, 3] a smaller resistivity and anisotropy is seen in isovalent $Ba(Fe_{1\text{-}x}Ru_x)_2As_2$ [15] and an almost negligible resistivity and possibly inverted anisotropy is reported for hole doped $(Ba_{1\text{-}x}K_x)Fe_2As_2$ [7, 10].

Obviously, it turned out to be non-trivial to find a theoretical explanation which can account for all these findings. There is recent theoretical work by several groups based on model Hamiltonian approaches [16–22] and little numerical work based on Monte Carlo simulations [23]. However, the origin of $\Delta\rho$ is still under discussion. For example Kuo and Fisher [11] ascribe $\Delta\rho$ exclusively to contributions of the intrinsic anisotropic band structure. Another approach is to assume extrinsic defect states which extend over several unit cells [3, 15]. These can be explained theoretically [17–19] and monitored by scanning tunneling microscope (STM) experiments which see local anisotropic defect states with a size of approximately 22 Å [24–26]. What is missing so far is theoretical work that is not based on a model Hamiltonian but on a parameter-free application of density functional theory (DFT) or a comparable scheme, showing whether and how the intrinsic band structure can explain the observed resistivity anisotropy $\Delta\rho$.

With this work we present a first principles DFT-based study on $\Delta\rho$ in three exemplary iron pnictides: electron doped $Ba(Fe_{1\text{-}x}Co_x)_2As_2$ (Co-122), hole doped $(Ba_{1\text{-}x}K_x)Fe_2As_2$ (K-122) and isovalent doped $Ba(Fe_{1\text{-}x}Ru_x)_2As_2$ (Ru-122). In order to reliably account for the disorder induced by substitution we use the Korringa-Kohn-Rostoker-Green function (KKR-GF) approach together with the coherent potential approximation (CPA) alloy theory, which proved already to be a very powerful and accurate tool to study the electronic structure of the substitutional iron pnictides [27–29]. Access to the longitudinal resistivity is given by the Kubo-Greenwood equation [30, 31], which allows for a direct comparison with experiment. All calculations have been performed self-consistently and fully relativistically within the four component Dirac formalism based on the local density approximation (LDA) [32, 33]. The applied theory thus accounts for all effects of the intrinsic band structure and of disorder induced impurity scattering in terms of the CPA. On the other hand, it does not account for anisotropic impurity states extending over several unit cells or for temperature induced spin fluctuations. More details are found in the Supplemental Material.[34]

The magnetic properties of the investigated compounds are summarized in Fig. 1 together with the orthorhombic unit cell in its experimental magnetic configuration. The obtained magnetic moment of undoped $BaFe_2As_2$ is 0.73 μ_B and thus in good agreement with experimental data (0.87 μ_B [35]). Using the CPA allows for a site resolved investigation of the magnetic moments, thus, the solid lines correspond to the average magnetic

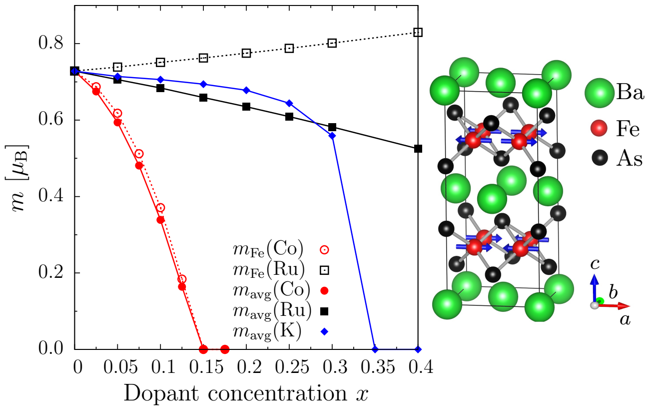

FIG. 1. (Left) Magnetic moments for Co-122 (red), K-122 (blue) and Ru-122 (black) depending on the dopant concentration x. The solid lines correspond to m_avg, meaning the substitutional dependent average, while the dashed lines correspond to the pure Fe moment m_Fe. (Right) Orthorhombic unit cell with the experimental magnetic configuration.

moment while the dashed lines give the Fe contribution only. The collapse of long range antiferromagnetic order at the critical concentration x_crit for Co-122 and K-122 is in reasonable agreement with experiment, although it is slightly shifted to higher x values when compared with experiment (Co-122: $x_\mathrm{crit}^\mathrm{exp} \approx 0.07$ [36]; K-122: $x_\mathrm{crit}^\mathrm{exp} \approx 0.25$ [37]). Yet, for isovalent doped Ru-122 the average magnetic moments decrease due to the increasing Ru concentration which has a low magnetic moment in the order of 0.07 μ_B (not shown in Fig. 1), however, the individual Fe magnetic moments surprisingly increase. In the literature magnetic dilution was already discussed as the main driving force for the magnetic breakdown in Ru-122 [38, 39], yet in the investigated regime of x the magnetic order did not disappear, i.e. x_crit should be higher than 0.4 (see Fig. 1).

Accounting for the magnetic configuration the in-plane longitudinal resistivity was calculated, with the main results shown in Fig. 2. First consider Co-122 in (A), where the resistivity of the antiferromagnetic (AFM) configuration has a dome-like variation with increasing dopant concentration x until the collapse of the AFM order takes place at x_crit. Note that the resistivity ρ_b AFM along the ferromagnetic b axis (red) is always larger than the resistivity ρ_a AFM along the antiferromagnetic a axis (blue) with a maximum of the anisotropy roughly at $x_\mathrm{crit}/2$. This behavior is in full agreement with experiment [1, 3]. In Fig. 2 (A) we also give the experimental data of Ishida *et al.*[3] for ρ_a and ρ_b using specifically adapted scales to the right and top of the figure. A direct comparison of the theoretical and experimental data seems nevertheless justified for two reasons. First of all, the self-consistently calculated collapse of the AFM order takes place at a higher x_crit compared to experiment, thus one should account for that by adjusting the experimental and theoretical x axis in a way that the breakdown of magnetic order coincides. Secondly, it is known that the resistivity decreases significantly for annealed crystals, indicating a strong contribution of crystal defects [3, 9]. Thus it is expected to find the calculated resistivity to be lower than the experimental one, consequently the axis to the right for the experimental resistivity is adjusted by a factor of 2. Most important are the order of magnitude and the dependency of $\Delta\rho$ on the doping, which are rather well reproduced by the presented calculations. For comparison we show also the calculated resistivity of the same orthorhombic crystal but for the nonmagnetic (NM) state, using green (a axis) and purple (b axis) lines in Fig. 2. Notably, the resistivity of the orthorhombic NM Co-122 is almost by a factor of 10 reduced compared to the AFM case and it shows neither a dome-like behavior nor a significant anisotropy due to the lattice distortion. This unambiguously shows that the lattice has a negligible contribution to the anisotropic behavior compared to the magnetic structure, as was stressed before in Refs [27, 29].

Next, consider K-122 in Fig. 2 (B), where we show no experimental data because $\Delta\rho$ is reported to be almost immeasurably small with even possible sign changes [7, 10]. Indeed, the calculations find an in-plane resistivity always below 8 $\mu\Omega$ cm which is reduced by a factor of 15 compared to Co-122. Replacing Fe with Co or Ru affects the d-electronic states which are dominating at the Fermi level (E_F) for the iron pnictides. Thus, disorder introduced for sp-elements like Ba or K hardly affects the resistivity of the compound. The calculations further support the possibility of sign changes in $\Delta\rho$ with x.

Finally, consider Ru-122 in Fig. 2 (C), with recent experimental data taken from Liu *et al.* [15] shown as for the Co-122 case with axes at the top and on the right adjusted the same way. The sign of $\Delta\rho$ is the same as for Co-122, however, the anisotropy does not disappear as the magnetic order in Ru-122 (see Fig. 1) also does not disappear for the investigated regime of substitution. In addition, one has to note that for comparable dopant concentrations the resistivity in Ru-122 is reduced compared to Co-122, as it was also observed in experiment [15]. Thus, again the trends and the order of magnitude for the resistivity are in reasonable agreement with recent experimental data.

In summary, in all three representative iron pnictides it was possible to reproduce the qualitative behavior of $\Delta\rho$ in the antiferromagnetic phase based on a LDA approach without considering spatially extended impurity states or spin fluctuations. Thus, the resistivity anisotropy of the iron pnictides at low temperatures can be well understood in terms of an in-plane anisotropic magnetoresistance (AMR) [40]. This leads to the question how the anisotropic band structure can influence this AMR. The idea of linking $\Delta\rho$ to the band structure as seen e.g. by ARPES was already proposed by Yi *et*

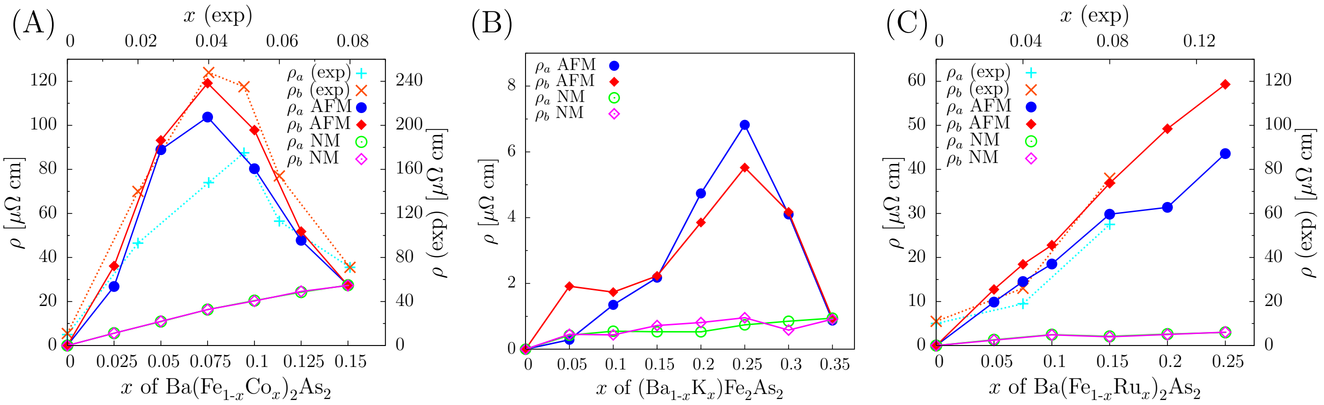

FIG. 2. In-plane resistivity calculated for (A) Co-122, for (B) K-122 and for (C) Ru-122 up to x_{crit} as a function of the concentration x. The blue and red curves correspond to the antiferromagnetic (AFM) state, while the green and purple lines correspond to the same orthorhombic lattice but for the nonmagnetic (NM) case. The pluses and crosses are experimental data [3, 15] with the corresponding concentration x (exp) and resistivity ρ (exp) axes given at the top and right of the figure.

al. [4], however, corresponding explanations were hardly successful so far [15]. The main reason for this apparent incompatibility is due to the fact that ARPES is a surface sensitive method. For the iron pnictides, however, it is absolutely mandatory to account for the dispersion of bands with k_z as was also recently stressed in the context of the effective mass enhancement seen in ARPES [41]. Accounting for the k_z dispersion of the anisotropic bands will thus allow for more meaningful results and an at least qualitative understanding of the observed trends.

Discussing the presented resistivity data, one should first note that the resistivity anisotropy is also observed for the parent compound $\mathrm{BaFe_2As_2}$, although it is reported to be small after annealing [2, 9]. Still, the Lifshitz transition [42], i.e. the topological change of the Fermi surface when going from the nonmagnetic to the antiferromagnetic state, should influence the resistivity behavior. Indeed, the formerly almost isotropic bands in the NM state undergo a significant band splitting resulting in a considerable anisotropy after the Lifshitz transition to the AFM state [27, 29, 42]. When accounting for the k_z dispersion, one can qualitatively understand the higher resistivity along b in terms of a hybridization of hole and electron pockets seen also in ARPES [42]. This leads to the formation of a band gap and of minima from electron pockets at the Fermi level only along the b axis. This Lifshitz transition of $\mathrm{BaFe_2As_2}$ and the implications for $\Delta\rho$ are discussed in more detail in the Supplemental Material.[34]

A qualitative discussion of $\Delta\rho$ for the investigated compounds will be exemplarily done for Co-122 with $x = 0.075$, having the highest value of $\Delta\rho$ for Co substitution and for Ru-122 with $x = 0.10$ as an example of isovalent doping. The band structures are shown for different k_z values in Fig. 3 with the paths $\overline{\Gamma \mathrm{Y}}$ and $\overline{\Gamma \mathrm{X}}$ corresponding to directions in $\boldsymbol{k}$-space parallel to the b and a axes, respectively. First consider the Co-122 case in panels (A - E), where a strong dependence of the bands on k_z is obvious. Of most interest are the W- or S-shaped bands (W-band: two minima along both directions $\overline{\Gamma \mathrm{Y}}$ and $\overline{\Gamma \mathrm{X}}$; S-band: only one minimum along $\overline{\Gamma \mathrm{Y}}$) which are a result of the previously discussed hybridization with significant band broadening due to the disorder. The highest $\Delta\rho$ is observed for $x = 0.075$ in Co-122 because for exactly this concentration most of these W- and S-bands have their minimum precisely at E_F. Approaching these extrema, the slope of the bands is decreasing, leading to a decrease of the quasiparticle velocities and thus to an increase of the resistivity. Additionally, the apparently strong disorder-induced broadening of the W- and S-bands leads to a decreased quasiparticle lifetime which again increases the resistivity. It would be difficult to explain $\Delta\rho$ based on their contribution at E_F in Co-122 for some values of k_z, e.g. for Fig. 3 (A) $k_z = 0.0$, (B) 0.25 and (D) 0.75. However, for (C) $k_z = 0.5$ and (E) 1.0 the contribution at E_F is clearly anisotropic with a higher impact along the $\overline{\Gamma \mathrm{Y}}$ path, leading to a higher resistivity ρ_b compared to ρ_a.

Analogously, $\Delta\rho$ can be explained for the Ru-122 compound with $x = 0.1$, but now the strong anisotropic contribution can be seen for Fig. 3 (F) $k_z = 0.0$ and (I) 0.75, where one has either a band gap along $\overline{\Gamma \mathrm{Y}}$, or the minimum of a S-shaped band at E_F. The Ru-122 system is an interesting prototype system for isovalent doping because the Ru substitution induces disorder but E_F is only marginally changed. The crucial impact of the anisotropic band structure can be easily shown by artificially changing the Fermi energy by ΔE_F and recalculating the resistivity $\rho_{a(b)}$ for $\mathrm{Ba(Fe_{0.9}Ru_{0.1})_2As_2}$. The results are presented in Fig. 4 where some exemplary values are highlighted by the cyan, black, green and purple lines. The corresponding energies are indicated in Fig. 3 (F - J) for comparison. It becomes immediately obvious, that the magnitude and the sign of $\Delta\rho = \rho_a - \rho_b$ depends

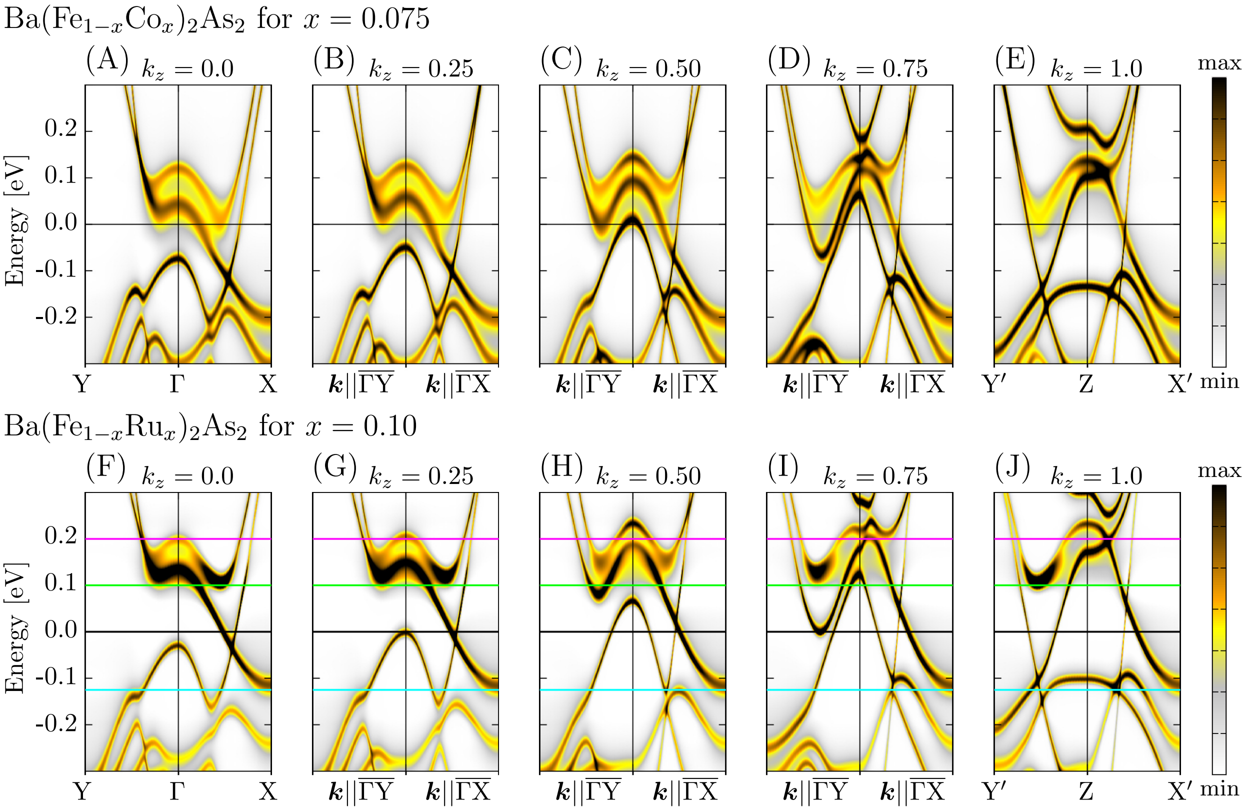

FIG. 3. Bloch spectral functions for different values of k_z in units of $\frac{2\pi}{c}$, with $\overline{\Gamma \mathrm{Y}}$ and $\overline{\Gamma \mathrm{X}}$ corresponding to paths parallel to the b and a axes, respectively. The panels (A - E) and (F - J) show results for Co-122 with $x = 0.075$ and Ru-122 with $x = 0.10$, respectively, with the colored cuts corresponding to the cuts in Fig. 4.

strongly on the chosen energy. For $\Delta E_F = -0.125$ eV (cyan line) one arrives at the minimum of a band at X, whose impact is strong enough to change the sign of $\Delta\rho$, meaning a higher resistivity ρ_a compared to ρ_b. This is comparable to K-122, where the hole doping induces this energy shift and explains the possible sign change in $\Delta\rho$. Increasing the energy to $\Delta E_F = 0.10$ eV (green line) significantly increases $\Delta\rho$ that gets comparable to the Co-122 case for $x = 0.075$ in Fig. 3 (A - E). Further increasing the shift to $\Delta E_F = 0.20$ eV (purple line) moves again away from this peculiar band situation, decreasing $\Delta\rho$ as it is the case for overdoped Co-122 with $x > 0.1$.

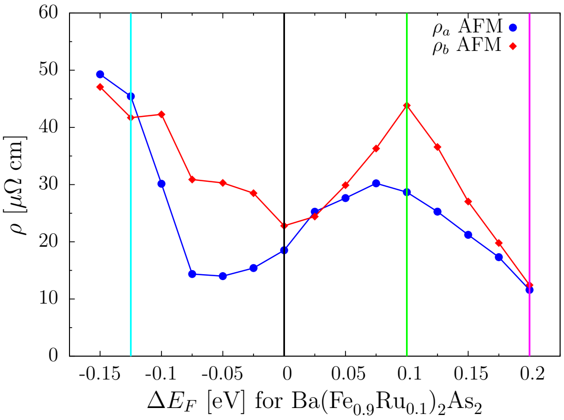

FIG. 4. Change in $\rho_{a(b)}$ for Ru-122 with $x = 0.1$ depending on an artificial shift ΔE_F of the Fermi energy. The cyan, black, green and purple cuts correspond to the cuts in the band structures in Fig. 3.

Altogether, we have shown that $\Delta\rho$ in the low temperature phase of the iron pnictides can be explained in terms of an in-plane AMR. Additional contributions of extended impurity states obviously cannot be ruled out. Furthermore, we do not disagree with work considering the impact of higher temperatures in the nematic phase [17–19, 21], rather we provide new insights from first-principles calculations on real materials. These disproved in particular recent suggestions that the anisotropic band structure has no impact on $\Delta\rho$ [15] and highlighted the importance of the dispersion with k_z.

In conclusion, this work is the first to present first principles transport calculations of the resistivity anisotropy in the low temperature antiferromagnetic phase of the iron pnictide superconductors. We show for three exemplary systems resistivity values in good agreement with experiment. It turned out that it is sufficient to discuss $\Delta\rho$ in the antiferromagnetic phase in terms of an anisotropic magnetoresistance. This AMR can be tuned by either disorder scattering from impurities or by an energy shift due to respective electron or hole doping. Most important, it was mandatory to account for the k_z dispersion in order to understand the results based on the anisotropic band structure, showing the crucial impact of the three-dimensional character of the electronic structure for the iron pnictides which future studies have to account for. Furthermore, resistivity calculations for varying energy reveal that the sign of $\Delta\rho$ is no fundamental property of the pnictides but rather a peculiarity of the anisotropic band structure.

We thank Ilja Turek for valuable discussions. We acknowledge financial support within the research group FOR 1346, within priority program SPP 1538 and from CENTEM PLUS (L01402).

---

* gerald.derondeau@cup.uni-muenchen.de

[1] J.-H. Chu, J. G. Analytis, K. De Greve, P. L. McMahon, Z. Islam, Y. Yamamoto, and I. R. Fisher, Science **329**, 824 (2010).

[2] M. A. Tanatar, E. C. Blomberg, A. Kreyssig, M. G. Kim, N. Ni, A. Thaler, S. L. Bud'ko, P. C. Canfield, A. I. Goldman, I. I. Mazin, and R. Prozorov, Phys. Rev. B **81**, 184508 (2010).

[3] S. Ishida, M. Nakajima, T. Liang, K. Kihou, C. H. Lee, A. Iyo, H. Eisaki, T. Kakeshita, Y. Tomioka, T. Ito, and S. Uchida, Phys. Rev. Lett. **110**, 207001 (2013).

[4] M. Yi, D. Lu, J.-H. Chu, J. G. Analytis, A. P. Sorini, A. F. Kemper, B. Moritz, S.-K. Mo, R. G. Moore, M. Hashimoto, W.-S. Lee, Z. Hussain, T. P. Devereaux, I. R. Fisher, and Z.-X. Shen, Proc. Nat. Ac. Sci. US. **108**, 6878 (2011).

[5] J. Zhao, D. T. Adroja, D.-X. Yao, R. Bewley, S. Li, X. F. Wang, G. Wu, X. H. Chen, J. Hu, and P. Dai, Nature Physics **5**, 555 (2009).

[6] M. Nakajima, S. Ishida, Y. Tomioka, K. Kihou, C. H. Lee, A. Iyo, T. Ito, T. Kakeshita, H. Eisaki, and S. Uchida, Phys. Rev. Lett. **109**, 217003 (2012).

[7] J. J. Ying, X. F. Wang, T. Wu, Z. J. Xiang, R. H. Liu, Y. J. Yan, A. F. Wang, M. Zhang, G. J. Ye, P. Cheng, J. P. Hu, and X. H. Chen, Phys. Rev. Lett. **107**, 067001 (2011).

[8] J.-H. Chu, H.-H. Kuo, J. G. Analytis, and I. R. Fisher, Science **337**, 710 (2012).

[9] S. Ishida, M. Nakajima, T. Liang, K. Kihou, C.-H. Lee, A. Iyo, H. Eisaki, T. Kakeshita, Y. Tomioka, T. Ito, and S. Uchida, J. Amer. Chem. Soc. **135**, 3158 (2013).

[10] E. C. Blomberg, M. A. Tanatar, R. M. Fernandes, I. I. Mazin, B. Shen, H.-H. Wen, M. D. Johannes, J. Schmalian, and R. Prozorov, Nat. Commun. **4**, 1914 (2013), Article.

[11] H.-H. Kuo and I. R. Fisher, Phys. Rev. Lett. **112**, 227001 (2014).

[12] Y. Kim, H. Oh, C. Kim, D. Song, W. Jung, B. Kim, H. J. Choi, C. Kim, B. Lee, S. Khim, H. Kim, K. Kim, J. Hong, and Y. Kwon, Phys. Rev. B **83**, 064509 (2011).

[13] A. Dusza, A. Lucarelli, F. Pfuner, J.-H. Chu, I. R. Fisher, and L. Degiorgi, Europhys. Lett. **93**, 37002 (2011).

[14] H.-H. Kuo, J.-H. Chu, S. C. Riggs, L. Yu, P. L. McMahon, K. De Greve, Y. Yamamoto, J. G. Analytis, and I. R. Fisher, Phys. Rev. B **84**, 054540 (2011).

[15] L. Liu, T. Mikami, S. Ishida, K. Koshiishi, K. Okazaki, T. Yoshida, H. Suzuki, M. Horio, L. C. C. Ambolode, J. Xu, H. Kumigashira, K. Ono, M. Nakajima, K. Kihou, C. H. Lee, A. Iyo, H. Eisaki, T. Kakeshita, S. Uchida, and A. Fujimori, Phys. Rev. B **92**, 094503 (2015).

[16] R. M. Fernandes, E. Abrahams, and J. Schmalian, Phys. Rev. Lett. **107**, 217002 (2011).

[17] M. N. Gastiasoro, I. Paul, Y. Wang, P. J. Hirschfeld, and B. M. Andersen, Phys. Rev. Lett. **113**, 127001 (2014).

[18] M. N. Gastiasoro, P. J. Hirschfeld, and B. M. Andersen, Phys. Rev. B **89**, 100502 (2014).

[19] Y. Wang, M. N. Gastiasoro, B. M. Andersen, M. Tomić, H. O. Jeschke, R. Valentí, I. Paul, and P. J. Hirschfeld, Phys. Rev. Lett. **114**, 097003 (2015).

[20] K. Sugimoto, P. Prelovšek, E. Kaneshita, and T. Tohyama, Phys. Rev. B **90**, 125157 (2014).

[21] M. Breitkreiz, P. M. R. Brydon, and C. Timm, Phys. Rev. B **90**, 121104 (2014).

[22] M. Breitkreiz, P. M. R. Brydon, and C. Timm, Phys. Rev. B **89**, 245106 (2014).

[23] S. Liang, G. Alvarez, C. Şen, A. Moreo, and E. Dagotto, Phys. Rev. Lett. **109**, 047001 (2012).

[24] T.-M. Chuang, M. P. Allan, J. Lee, Y. Xie, N. Ni, S. L. Bud'ko, G. S. Boebinger, P. C. Canfield, and J. C. Davis, Science **327**, 181 (2010).

[25] M. P. Allan, T.-M. Chuang, F. Massee, Y. Xie, N. Ni, S. L. Bud'ko, G. S. Boebinger, Q. Wang, D. S. Dessau, P. C. Canfield, M. S. Golden, and J. C. Davis, Nature Physics **9**, 220 (2013).

[26] E. P. Rosenthal, E. F. Andrade, C. J. Arguello, R. M. Fernandes, X. C. Xing, L. Y.and Wang, C. Q. Jin, A. J. Millis, and A. N. Pasupathy, Nature Physics **10**, 225 (2014).

[27] G. Derondeau, S. Polesya, S. Mankovsky, H. Ebert, and J. Minár, Phys. Rev. B **90**, 184509 (2014).

[28] S. N. Khan and D. D. Johnson, Phys. Rev. Lett. **112**, 156401 (2014).

[29] G. Derondeau, J. Braun, H. Ebert, and J. Minár, Phys. Rev. B **93**, 144513 (2016).

[30] D. Ködderitzsch, S. Lowitzer, J. B. Staunton, and H. Ebert, phys. stat. sol. (b) **248**, 2248 (2011).

[31] D. Ködderitzsch, K. Chadova, and H. Ebert, Phys. Rev. B **92**, 184415 (2015).

[32] H. Ebert, D. Ködderitzsch, and J. Minár, Rep. Prog. Phys. **74**, 096501 (2011).

[33] H. Ebert et al., *The Munich SPR-KKR package*, version 6.3, http://olymp.cup.uni-muenchen.de/ak/ebert/SPRKKR, 2012.

[34] Supplemantal Material.

[35] Q. Huang, Y. Qiu, W. Bao, M. A. Green, J. W. Lynn, Y. C. Gasparovic, T. Wu, G. Wu, and X. H. Chen, Phys. Rev. Lett. **101**, 257003 (2008).

[36] C. Lester, J.-H. Chu, J. G. Analytis, S. C. Capelli, A. S. Erickson, C. L. Condron, M. F. Toney, I. R. Fisher, and S. M. Hayden, Phys. Rev. B **79**, 144523 (2009).

[37] M. Rotter, M. Pangerl, M. Tegel, and D. Johrendt, Angew. Chem. Int. Ed. **47**, 7949 (2008).

[38] R. S. Dhaka, C. Liu, R. M. Fernandes, R. Jiang, C. P. Strehlow, T. Kondo, A. Thaler, J. Schmalian, S. L.

Bud'ko, P. C. Canfield, and A. Kaminski, Phys. Rev. Lett. **107**, 267002 (2011).

[39] R. S. Dhaka, S. E. Hahn, E. Razzoli, R. Jiang, M. Shi, B. N. Harmon, A. Thaler, S. L. Bud'ko, P. C. Canfield, and A. Kaminski, Phys. Rev. Lett. **110**, 067002 (2013).

[40] X. Marti, I. Fina, C. Frontera, J. Liu, P. Wadley, Q. He, R. J. Paull, J. D. Clarkson, J. Kudrnovský, I. Turek, J. Kuneš, D. Yi, J.-H. Chu, C. T. Nelson, L. You, E. Arenholz, S. Salahuddin, J. Fontcuberta, T. Jungwirth, and R. Ramesh, Nature Materials **13**, 367 (2014).

[41] G. Derondeau, F. Bisti, J. Braun, V. A. Rogalev, M. Shi, T. Schmitt, J. Ma, H. Ding, H. Ebert, V. N. Strocov, and J. Minár, arXiv:1606.08977, 2016.

[42] C. Liu, T. Kondo, R. M. Fernandes, A. D. Palczewski, E. D. Mun, N. Ni, A. N. Thaler, A. Bostwick, E. Rotenberg, J. Schmalian, S. L. Bud'ko, P. C. Canfield, and A. Kaminski, Nature Physics **6**, 419 (2010).

Supplemental Material for

In-plane anisotropic magnetoresistance in antiferromagnetic $\mathrm{Ba(Fe_{1-x}Co_x)_2As_2}$, $\mathrm{(Ba_{1-x}K_x)Fe_2As_2}$ and $\mathrm{Ba(Fe_{1-x}Ru_x)_2As_2}$

Gerald Derondeau,[1,*] Ján Minár,[1,2] Sebastian Wimmer,[1] and Hubert Ebert[1]

[1]*Department Chemie, Physikalische Chemie, Universität München,*
Butenandtstr. 5-13, 81377 München, Germany
[2]*NewTechnologies-Research Center, University of West Bohemia, Pilsen, Czech Republic*

(Dated: August 30, 2016)

1. COMPUTATIONAL DETAILS

All calculations have been performed self-consistently and fully relativistically within the four component Dirac formalism using the coherent potential approximation (CPA) alloy theory as implemented in the Munich SPR-KKR program package [1, 2]. The treatment of disorder via the CPA was already shown to be a powerful and accurate tool, fully comparable to recent supercell calculations that have to take the average over many configurations [3, 4]. Doing so, would however give no direct access to the in-plane resistivity anisotropy as it is possible within the presented approach. Furthermore, the CPA allows for an investigation of isovalent doped Ru-122 which is not accessible by e.g. a virtual crystal approximation (VCA). Furthermore, the Dirac formalism implies by construction a full inclusion of effects induced by spin-orbit coupling, which was recently shown to be important for the iron pnictides [5]. The crystal structure is based on the orthorhombic 4-Fe unit cell in its experimental magnetic configuration [6], implying antiferromagnetic chains along the a and c axes and ferromagnetic chains along the b axis. The magnetic moments are oriented in-plane along the a axis. The lattice parameters where chosen according to experimental X-ray data and using a linear interpolation to account for the influence of substitution based on available data [7–10]. More details on the procedure can be found in a previous publication [3]. For all electronic structure calculations the local density approximation (LDA) exchange-correlation potential was applied, using the parameterization of Vosko, Wilk and Nusair [11]. The longitudinal resistivity was calculated using the Kubo-Greenwood equation within KKR-CPA [12, 13], for the symmetric part of the conductivity tensor (1):

$$\sigma_{\mu\mu} \; = \; \frac{\hbar}{\pi V}\,\mathrm{Tr}\langle\hat{j}_{\mu}\mathrm{Im}G^{+}\hat{j}_{\mu}\mathrm{Im}G^{+}\rangle_{c}\;, \tag{1}$$

with G^{+} being the retarded Green's functions, V the cell volume and $\hat{j}_{\mu}$ the μ component of the electric current operator. In the relativistic formulation the latter reads $\hat{j}_{\mu} = -|e|c\alpha_{\mu}$, with the elementary charge e, the speed of light c and α_{μ} being one of the 4×4 Dirac α matrices. The brackets $\langle\;\rangle_{c}$ indicate a configurational average with respect to an alloy in terms of the CPA.

2. VERTEX CORRECTIONS

The CPA vertex corrections [12, 13] are included in all resistivity calculations, ensuring proper averaging of the product of two Green's functions in equation (1). Still, the overall impact of the vertex corrections is comparably small (in the order of at most 7 %) which indicates that incoherent scattering processes are less important. This is in agreement with having mainly d character for the electrons at the Fermi level. Furthermore, this means that it is a reasonable approximation to look at the effective single particle Bloch spectral function in order to investigate this resistivity anisotropy [14]. However, it is interesting to note that the vertex corrections itself are also highly anisotropic as can be seen in Fig. S1. Here, ρ_a and ρ_b of the AFM state are shown for all investigated compounds, including vertex corrections (VC) and also without vertex corrections (nVC). It is obvious that the impact of vertex corrections on ρ_a is almost zero in all cases while the influence on ρ_b is especially for Co-122 and Ru-122 much more pronounced. This finding is consistent with a stronger impact of disorder on the AFM coupling along b.

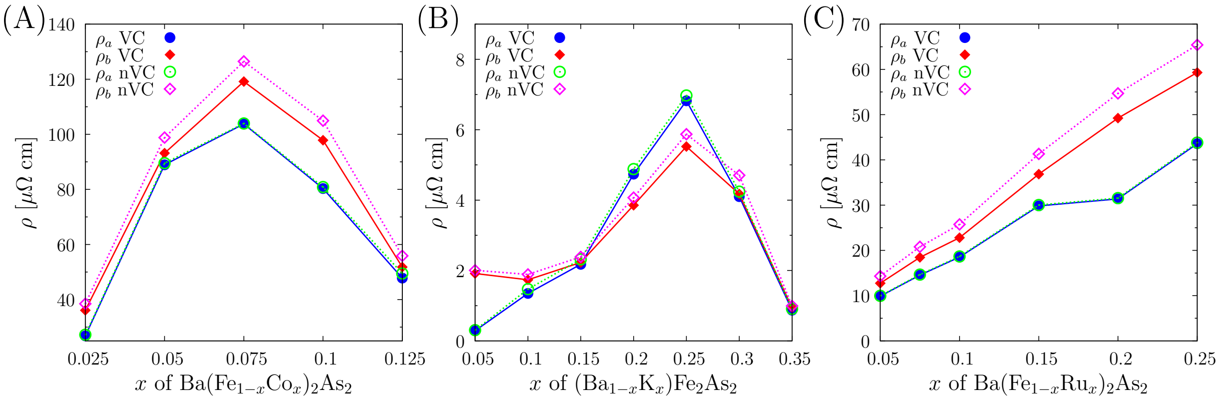

FIG. S1. In-plane resistivity of the AFM state for (A) Co-122, for (B) K-122 and for (C) Ru-122 depending on the substitution level x. The results are split into ρ_a and ρ_b either including vertex corrections (VC) with solid lines or without any vertex corrections (nVC) shown in dashed lines.

3. LIFSHITZ TRANSITION OF THE PARENT COMPOUND

Lifshitz transitions are characterized as a topological change of the Fermi surface.[15] There are several kinds of Lifshitz transitions discussed for the iron pnictides and these are of significant importance for the underlying physics and superconductivity.[16–19] The topological change of the Fermi surface for the $BaFe_2As_2$ mother compound when going from the nonmagnetic to the antiferromagnetic state can be also understood in terms of a Lifshitz transition, introducing strong anisotropy into the AFM electronic structure.[3, 4] The corresponding electronic structure for $BaFe_2As_2$ is shown in Fig. S2 for the (A - E) AFM state and the (F - J) nonmagnetic case. For comparison, all calculations are presented with respect to the same orthorhombic 4-Fe unit cell which implies a back-folding of bands into a smaller Brillouin zone, compared to the 2-Fe cell. See also Ref. [20] for further information on the magnetic Brillouin zone in $BaFe_2As_2$. The upper rows show the band structure for different values of k_z, while the lower rows depict the respective Fermi surface cuts. As in the main paper, the paths ΓY and ΓX correspond to paths in $\boldsymbol{k}$-space which are parallel the b and a axes, respectively.

BaFe$_2$As$_2$ - antiferromagnetic AFM

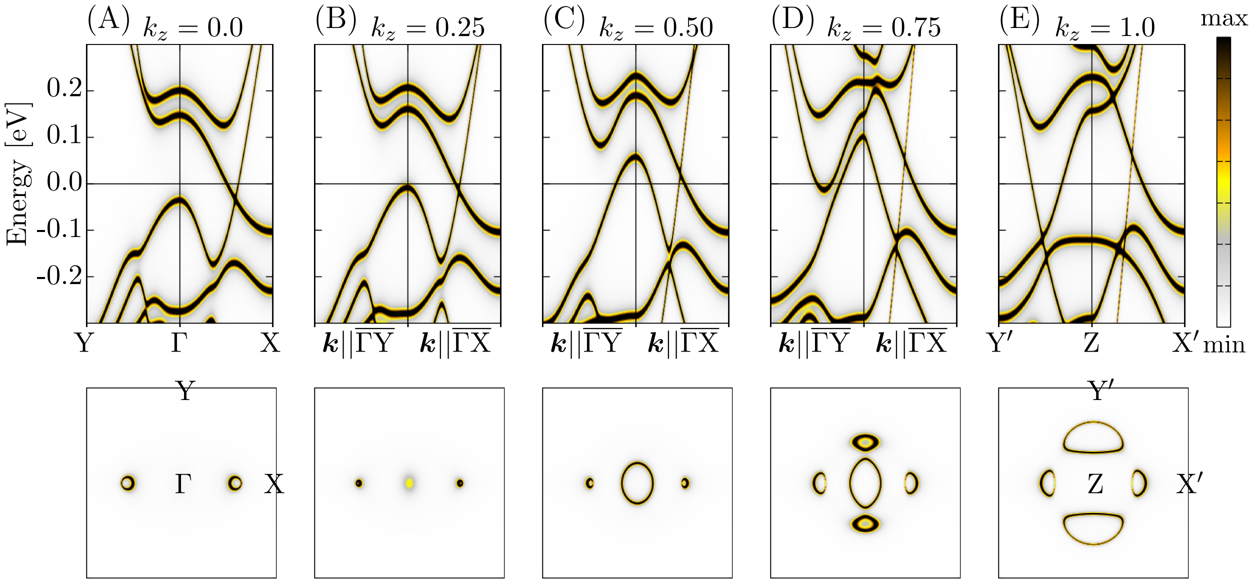

BaFe$_2$As$_2$ - nonmagnetic NM

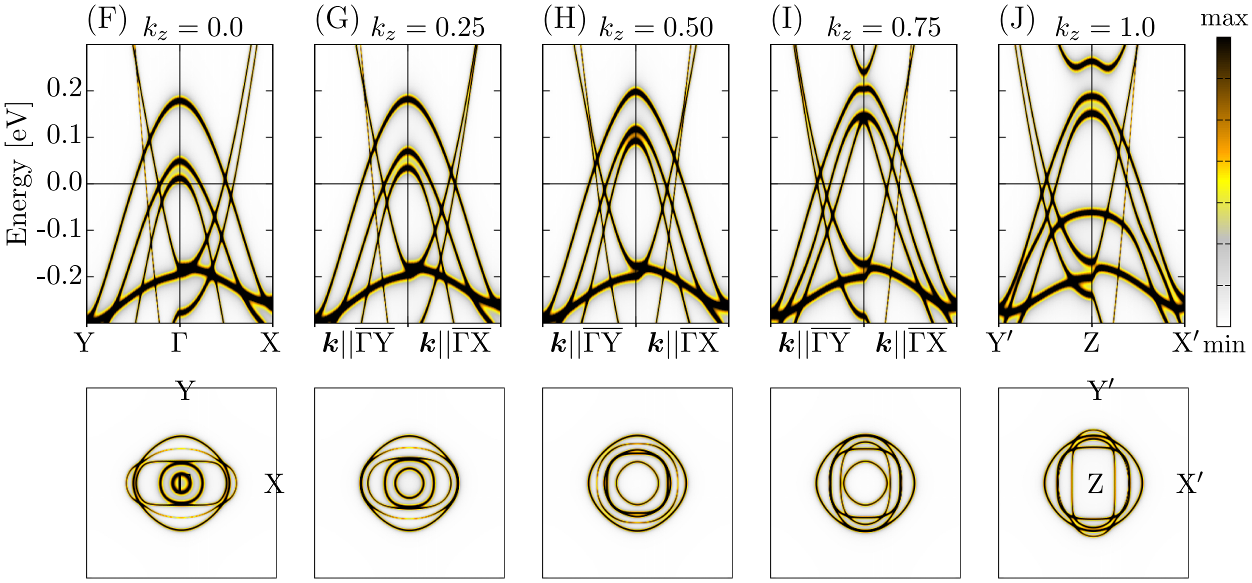

FIG. S2. Bloch spectral functions of orthorhombic BaFe$_2$As$_2$ for different values of k_z in $\frac{2\pi}{c}$, with ΓY and ΓX corresponding to paths parallel to the b and a axes, respectively. Shown for (A - E) the AFM state and for (F - J) the nonmagnetic case. The upper panel presents the band structure and the lower panel shows the corresponding cut of the Fermi surface. In order to allow direct comparison, all images are shown for the 4-Fe unit cell with a back-folding of bands onto Γ.

Going from a 2-Fe unit cell to the 4-Fe cell implies that the hole pockets and the electron pockets of the 2-Fe cell are back folded onto each other in one Γ point as can be seen for the nonmagnetic band structure of a 4-Fe unit cell in Fig. S2 (F - J). An additionally emerging antiferromagnetic order leads to a hybridization of these hole- and electron pockets as shown in Fig. S2 (A - E), which was discussed in detail by e.g. Liu *et al.* [16] in terms of a Lifshitz transition. It is possible to discuss the emergence of a non-zero $\Delta\rho$ already at this point, although earlier attempts were less fruitful.[21, 22] The reason for this apparent incompatibility is that the iron pnictides are clearly 3D materials whose bands show typically a strong k_z dispersion, which is often not sufficiently accounted for.[23] This becomes obvious in Fig. S2 where especially in the AFM case a strong electronic anisotropy emerges which does significantly depend on the value of k_z. For the nonmagnetic case in Fig. S2 (F - J) the corresponding electronic structure is, when considering the k_z dispersion, more or less isotropic. The situation is completely different for the AFM state in Fig. S2 (A - E). With a similar argumentation as used in the main paper one can qualitatively expect a $\Delta\rho$ with a higher ρ_b along the path ΓY for e.g. $k_z = 0.0$ and 0.75. The hybridization does lead first of all to the opening of a band gap only along the ΓY path for $k_z = 0.0$. For $k_z = 0.75$ a minimum of an electron pocket at E_F leads to a minimum of the quasiparticle velocity, increasing the resistivity. Using an even higher resolution in the k_z dispersion (45 different values were calculated) shows clearly that these two distinct features emerge only along ΓY and never along ΓX. This can already qualitatively explain the occurrence of $\Delta\rho$ in the undoped $BaFe_2As_2$. This effect increases with substitution, as disorder-induced anisotropic band broadening leads to a simultaneous reduction of the quasiparticle lifetime as discussed in the main paper. Electron or hole doping do further move the Fermi level and can either increase or decrease the anisotropy, as was shown in Fig. 4.

---

[*] gerald.derondeau@cup.uni-muenchen.de

[1] H. Ebert, D. Ködderitzsch, and J. Minár, Rep. Prog. Phys. **74**, 096501 (2011).

[2] H. Ebert et al., *The Munich SPR-KKR package*, version 6.3, http://olymp.cup.uni-muenchen.de/ak/ebert/SPRKKR, 2012.

[3] G. Derondeau, S. Polesya, S. Mankovsky, H. Ebert, and J. Minár, Phys. Rev. B **90**, 184509 (2014).

[4] G. Derondeau, J. Braun, H. Ebert, and J. Minár, Phys. Rev. B **93**, 144513 (2016).

[5] S. V. Borisenko, D. V. Evtushinsky, Z.-H. Liu, I. Morozov, R. Kappenberger, S. Wurmehl, B. Büchner, A. N. Yaresko, T. K. Kim, M. Hoesch, T. Wolf, and N. D. Zhigadlo, Nature Physics **12**, 311 (2016).

[6] Q. Huang, Y. Qiu, W. Bao, M. A. Green, J. W. Lynn, Y. C. Gasparovic, T. Wu, G. Wu, and X. H. Chen, Phys. Rev. Lett. **101**, 257003 (2008).

[7] M. Rotter, M. Tegel, D. Johrendt, I. Schellenberg, W. Hermes, and R. Pöttgen, Phys. Rev. B **78**, 020503 (2008).

[8] M. Rotter, M. Pangerl, M. Tegel, and D. Johrendt, Angew. Chem. Int. Ed. **47**, 7949 (2008).

[9] A. S. Sefat, R. Jin, M. A. McGuire, B. C. Sales, D. J. Singh, and D. Mandrus, Phys. Rev. Lett. **101**, 117004 (2008).

[10] A. Thaler, N. Ni, A. Kracher, J. Q. Yan, S. L. Bud'ko, and P. C. Canfield, Phys. Rev. B **82**, 014534 (2010).

[11] S. H. Vosko, L. Wilk, and M. Nusair, Can. J. Phys. **58**, 1200 (1980).

[12] W. H. Butler, Phys. Rev. B **31**, 3260 (1985).

[13] J. Banhart, H. Ebert, P. Weinberger, and J. Voitländer, Phys. Rev. B **50**, 2104 (1994).

[14] B. Velický, Phys. Rev. **184**, 614 (1969).

[15] I. M. Lifshitz, Sov. Phys. J.E.T.P. **11**, 1130 (1960).

[16] C. Liu, T. Kondo, R. M. Fernandes, A. D. Palczewski, E. D. Mun, N. Ni, A. N. Thaler, A. Bostwick, E. Rotenberg, J. Schmalian, S. L. Bud'ko, P. C. Canfield, and A. Kaminski, Nature Physics **6**, 419 (2010).

[17] K. Matan, S. Ibuka, R. Morinaga, S. Chi, J. W. Lynn, A. D. Christianson, M. D. Lumsden, and T. J. Sato, Phys. Rev. B **82**, 054515 (2010).

[18] C. Liu, A. D. Palczewski, R. S. Dhaka, T. Kondo, R. M. Fernandes, E. D. Mun, H. Hodovanets, A. N. Thaler, J. Schmalian, S. L. Bud'ko, P. C. Canfield, and A. Kaminski, Phys. Rev. B **84**, 020509 (2011).

[19] S. N. Khan and D. D. Johnson, Phys. Rev. Lett. **112**, 156401 (2014).

[20] M. Yi, D. H. Lu, J. G. Analytis, J.-H. Chu, S.-K. Mo, R.-H. He, M. Hashimoto, R. G. Moore, I. I. Mazin, D. J. Singh, Z. Hussain, I. R. Fisher, and Z.-X. Shen, Phys. Rev. B **80**, 174510 (2009).

[21] M. Yi, D. Lu, J.-H. Chu, J. G. Analytis, A. P. Sorini, A. F. Kemper, B. Moritz, S.-K. Mo, R. G. Moore, M. Hashimoto, W.-S. Lee, Z. Hussain, T. P. Devereaux, I. R. Fisher, and Z.-X. Shen, Proc. Nat. Ac. Sci. US. **108**, 6878 (2011).

[22] L. Liu, T. Mikami, S. Ishida, K. Koshiishi, K. Okazaki, T. Yoshida, H. Suzuki, M. Horio, L. C. C. Ambolode, J. Xu, H. Kumigashira, K. Ono, M. Nakajima, K. Kihou, C. H. Lee, A. Iyo, H. Eisaki, T. Kakeshita, S. Uchida, and A. Fujimori, Phys. Rev. B **92**, 094503 (2015).

[23] G. Derondeau, F. Bisti, J. Braun, V. A. Rogalev, M. Shi, T. Schmitt, J. Ma, H. Ding, H. Ebert, V. N. Strocov, and J. Minár, arXiv:1606.08977, 2016.

7.3 Discussion

The original question was whether it is possible to use the Kubo-Greenwood formalism as implemented within the SPR-KKR program package in order to reasonably describe the resistivity anisotropy of the 122 iron pnictides. This goal could have been definitely realized. Therefore, not only electron doped $\mathrm{Ba(Fe_{1-x}Co_x)_2As_2}$ was investigated, but also hole doped $\mathrm{(Ba_{1-x}K_x)Fe_2As_2}$ and the isovalently doped $\mathrm{Ba(Fe_{1-x}Ru_x)_2As_2}$ in order to account for every relevant scenario. All three cases could be well described by the applied method and showed good agreement with experimental data. This direct comparison of experimental data of real materials with resistivity calculations was a major achievement which could be only realized thanks to the applied first-principles approach.

It is very important to note, that this good agreement was obtained without considering for spin fluctuations or extended impurity states in our theory, but only by correctly accounting for the electronic band structure. This information is a crucial discovery, because most recent studies argue in either of these two ways. Recent work by Liu *et al.*[263] even claims that the anisotropic band structure has no impact at all on the resistivity anisotropy, which was clearly disproved by the presented work. Quite on the contrary, the results were explained based on the anisotropic band structure and it was shown that previous attempts in this direction were less fruitful because the three-dimensional character of the band structure was not sufficiently accounted for. Note, that this crucial importance of the three-dimensional electronic structure is perfectly in line with the last publication presented in Chapter 6. Thus, one should stress once more that the iron pnictides are clearly no two-dimensional materials and it is absolutely mandatory to fully account for the three-dimensional electronic structure is order to capture their properties correctly.

Interestingly, the presented results mean at the same time that the counterintuitive sign of the resistivity anisotropy is no fundamental property of the iron pnictides, but just a peculiarity of the anisotropic band structure. In particular, one should stress that this work provides a new interpretation of this important phenomenon in terms of an anisotropic magnetoresistance (AMR), meaning this property can be well described by nothing more than its anisotropic magnetic ordering. This calls for an extensive reinterpretation of the resistivity anisotropy in the iron pnictides for the future.

Chapter 8

Relativistic hyperfine interactions

8.1 Motivation

It was mentioned in subsection 3.2.1 that a discrepancy is reported in the magnitude of the Fe magnetic moment in $BaFe_2As_2$, depending on the chosen experimental method. Neutron diffraction data predicts a magnetic moment of 0.87 μ_B[24] from powder samples, while from ^{57}Fe Mössbauer spectroscopy a value between 0.4 – 0.5 μ_B[22,45] was estimated in the literature. The motivation for this work was to explain and resolve this issue.

In experiment, it is a common practice to use the measured total hyperfine field $B_{\rm hf}$ and estimate with it the average magnetic moment μ of the compound. This procedure is based on assuming a linear relationship between $B_{\rm hf}$ and μ, which would result in a constant ratio $A = -B_{\rm hf}/\mu$. Commonly applied are the ratios based on bulk Fe, $A(\mathrm{Fe}) = 15\ \mathrm{T}/\mu_B$ or based on Fe^{3+} ions in Fe_2O_3, $A(\mathrm{Fe}^{3+}) = 11\ \mathrm{T}/\mu_B$. Using these values for $BaFe_2As_2$ with a measured hyperfine field of -5.47 T[22,45] would result in a magnetic moment in the order of 0.4 – 0.5 μ_B. However, one can question whether these proportionality ratios of Fe or Fe_2O_3 are really appropriate for the iron pnictides.[271] As it was described in subsection 2.1.7 the total hyperfine field is formed by contributions not only from the Fermi contact term but also from orbital or dipolar parts. If these terms are neglected this can reasonably explain huge deviations from the expected relation. Indeed, it was already suggested that a non-zero contribution of d-orbitals to the hyperfine field with an opposite sign to that of the Fermi contact field might have a significant impact for $BaFe_2As_2$.[46] This would imply that a more reliable estimation of the magnetic moments based on ^{57}Fe Mössbauer spectroscopy is not referring to bulk Fe and thus lies not between 0.4 and 0.5 μ_B, explaining the discrepancy from neutron diffraction. However, this issue could not be quantified so far as it requires a fully relativistic treatment in order to calculate B_{hf} including d-orbital contributions. Although there is theoretical work available on the issue of hyperfine fields in the $BaFe_2As_2$ family it was not performed relativistically and thus it could not capture the necessary effects.[272]

In order to finally solve this long standing problem it was the idea to calculate the hyperfine field B_{hf} with its various contributions for the $BaFe_2As_2$ family in a fully relativistic way. Numerous ^{57}Fe Mössbauer spectroscopy data are available for different $BaFe_2As_2$ compounds covering several types of substitution[45–48], which means the calculations can be compared to experimental values in order to verify the applicability. At this point one can make use of the CPA in order to investigate the magnetic moments and the corresponding hyperfine fields of not only the mother compound $BaFe_2As_2$, but of a wide variety of different dopants. Thus, five different kinds of substitution were studied, covering electron doped $Ba(Fe_{1-x}Co_x)_2As_2$ and $Ba(Fe_{1-x}Ni_x)_2As_2$, hole doped $(Ba_{1-x}K_x)Fe_2As_2$ and also isovalently doped $Ba(Fe_{1-x}Ru_x)_2As_2$ and $BaFe_2(As_{1-x}P_x)_2$. This way a comprehensive study of the hyperfine fields and its relation to the magnetic moments is possible, depending on the concentration x.

8.2 Publication: Physical Review B 94, 214508

Hyperfine fields in the $BaFe_2As_2$ family and their relation to the magnetic moment

Gerald Derondeau,[1] Ján Minár,[1,2] Hubert Ebert[1]

[1]*Department Chemie, Physikalische Chemie, Universität München, München, Germany*
[2]*NewTechnologies-Research Center, University of West Bohemia, Pilsen, Czech Republic*

published in: Physical Review B **94**, 214508 (2016).

This publication was selected as Editors' Suggestion.

PHYSICAL REVIEW B **94**, 214508 (2016)

Hyperfine fields in the $BaFe_2As_2$ family and their relation to the magnetic moment

Gerald Derondeau,[1,*] Ján Minár,[1,2] and Hubert Ebert[1]

[1]*Department Chemie, Physikalische Chemie, Universität München, Butenandtstrasse 5-13, 81377 München, Germany*

[2]*New Technologies Research Center, University of West Bohemia, Pilsen, Czech Republic*

(Received 29 September 2016; published 12 December 2016)

The hyperfine field B_{hf} and the magnetic properties of the $BaFe_2As_2$ family are studied using the fully relativistic Dirac formalism for different types of substitution. The study covers electron doped $Ba(Fe_{1-x}Co_x)_2As_2$ and $Ba(Fe_{1-x}Ni_x)_2As_2$, hole doped $(Ba_{1-x}K_x)Fe_2As_2$, and also isovalently doped $Ba(Fe_{1-x}Ru_x)_2As_2$ and $BaFe_2(As_{1-x}P_x)_2$ for a wide range of the concentration x. For the substituted compounds the hyperfine fields show a very strong dependence on the dopant type and its concentration x. Relativistic contributions were found to have a significantly stronger impact for the iron pnictides when compared to bulk Fe. As an important finding, we demonstrate that it is not sensible to relate the hyperfine field B_{hf} to the average magnetic moment μ of the compound, as it was done in earlier literature.

DOI: 10.1103/PhysRevB.94.214508

I. INTRODUCTION

Since the discovery of high-temperature superconductivity in $La(O_{1-x}F_x)FeAs$ [1,2] the iron pnictides are currently one of the most important prototype systems for unconventional superconductivity. The mechanism of superconductivity is more than likely connected to magnetic fluctuations [3–5], which makes the magnetic behavior of the iron pnictides a crucial property [6,7]. Despite tremendous research over the last years the complex magnetism of these compounds is still nontrivial to explain and some problems remain unsolved.

For example, a discrepancy is observed concerning the magnitude of the magnetic moment, depending on the chosen experimental method. Neutron diffraction data predict for the low-temperature phase of $BaFe_2As_2$ a total magnetic moment of $0.87\,\mu_{\mathrm{B}}$ per Fe from powder samples [8], while from ^{57}Fe Mössbauer spectroscopy [9,10] a value between $0.4\,\mu_{\mathrm{B}}$ and $0.5\,\mu_{\mathrm{B}}$ was estimated. One should note that the magnetic moments in the iron pnictides are generally considered to behave nearly itinerant [4,6,11–13], although sometimes a localized picture might be more appropriate [14–16]. Furthermore, density functional theory (DFT) calculations often overestimate the magnitude of the magnetic moments, ranging from approximately $1.2\,\mu_{\mathrm{B}}$ up to $2.6\,\mu_{\mathrm{B}}$ [7,11,17–19]. Thus, the magnetic moments are known to be highly sensitive to the system and computational parameters, which makes estimations difficult and leads sometimes to seemingly contradicting reports [7,9,20–22]. Furthermore, the importance of spin-orbit coupling for the iron pnictides was only recently stressed [23].

Nowadays, a lot of ^{57}Fe Mössbauer spectroscopy data are available for the $BaFe_2As_2$ family with different types of substitution and doping [10,24–27]. The previously mentioned discrepancy between neutron diffraction and ^{57}Fe Mössbauer spectroscopy is often ascribed to possible nonzero contributions of d orbitals to the hyperfine field with an opposite sign to that of the Fermi contact field [24]. This would explain why the suggested hyperfine proportionality constant A between the experimentally measured hyperfine field B_{exp} and the underlying magnetic moment μ(Fe) has a nonlinear behavior and is in particular not comparable to the corresponding value for bulk Fe. This would imply that a more reliable estimation of magnetic moments based on ^{57}Fe Mössbauer spectroscopy lies not between $0.4\,\mu_{\mathrm{B}}$ and $0.5\,\mu_{\mathrm{B}}$ but has a higher value. Although such aspects were already suggested as a most likely explanation for this discrepancy [24], a quantitative study of the theoretical hyperfine fields including relativistic contributions is still missing [28].

To clarify this situation, we address in this paper the antiferromagnetic state of the undoped mother compound $BaFe_2As_2$ together with a large variety of different types of substitution. These include electron doping in the case of $Ba(Fe_{1-x}Co_x)_2As_2$ and $Ba(Fe_{1-x}Ni_x)_2As_2$, hole doping as in $(Ba_{1-x}K_x)Fe_2As_2$, and also isovalently doped compounds such as $Ba(Fe_{1-x}Ru_x)_2As_2$ and $BaFe_2(As_{1-x}P_x)_2$. To deal adequately with substitutional systems the fully relativistic Korringa-Kohn-Rostoker-Green's function (KKR-GF) approach is used, which was already shown to be an appropriate tool to investigate various properties of the iron pnictides [29–31]. Chemical disorder due to substitution is dealt by means of the coherent potential approximation (CPA), which effectively gives results comparable to the tedious average over many supercell configurations and is much more reliable than the virtual crystal approximation (VCA) [29,32]. Application of the CPA to the iron pnictides was already shown to be quite successful [29,30,33–35]. Using this approach, one can not only investigate the type-resolved evolution of magnetic moments with composition, but also the doping dependence of the hyperfine fields. Furthermore, all contributions to the total hyperfine field B_{hf} can be separated, revealing the direct impact of orbital non-s-electron parts within the fully relativistic approach.

II. COMPUTATIONAL DETAILS

All calculations have been performed self-consistently and fully relativistically within the four component Dirac formalism, using the Munich SPR-KKR program package [36,37]. The crystal structure is based on the orthorhombic, antiferromagnetic phase of $BaFe_2As_2$ in its experimentally observed stripe spin state using a 4-Fe unit cell. This implies

---

[*] gerald.derondeau@cup.uni-muenchen.de

antiferromagnetically ordered chains along the a and c axes and ferromagnetically ordered chains along the b axis. With spin-orbit coupling included within the relativistic approach the orientation of the magnetic moments was chosen to be in plane along the a axis, in line with experiment [20]. The lattice parameters and As position z where chosen according to experimental x-ray data [9]. To account for the influence of different substitutions, a linear interpolation of the lattice parameters with respect to the concentration x was performed based on Vegard's law [38]. This interpolation was individually done for each type of substitution, based on available experimental data [9,39–43]. More details on this procedure can be found in previous publications [29,30]. The treatment of disorder introduced by substitution is dealt with by means of the CPA. For the angular momentum expansion of the KKR Green's function an upper limit $\ell_{\rm max} = 4$ was used, i.e., s, p, d, f, and g orbitals were included in the basis set, although contributions to the hyperfine field of Fe from f and g orbitals are zero, as one would expect. All DFT calculations used the local spin-density approximation (LSDA) exchange-correlation potential with the parametrization as given by Vosko, Wilk, and Nusair [44]. The calculation and decomposition of the hyperfine field $B_{\rm hf}$ is done in its fully relativistic form as discussed in detail in Ref. [45].

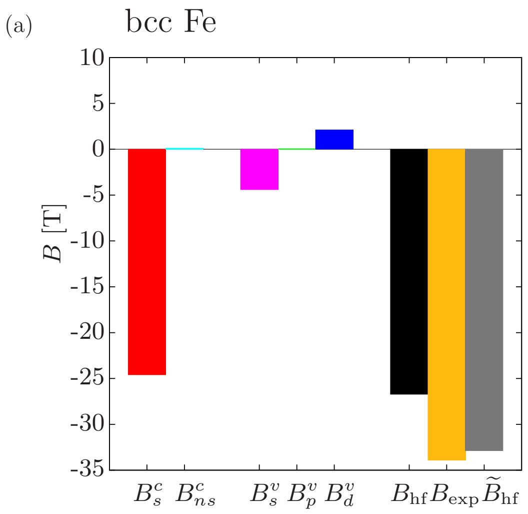

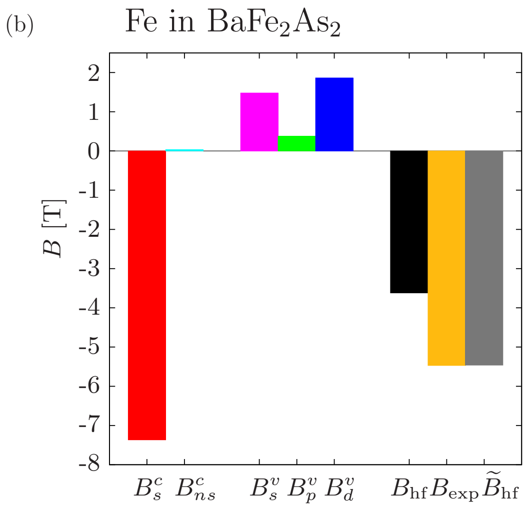

FIG. 1. Contributions to the hyperfine field $B_{\rm hf}$ for (a) bcc Fe and for (b) Fe in antiferromagnetic BaFe$_2$As$_2$. For comparison, experimental values are shown as $B_{\rm exp}$ [9,10,51]. $\widetilde{B}_{\rm hf}$ is based on Eq. (2) and includes an enhancement of the core polarization B_s^c of 25%.

III. RESULTS AND DISCUSSION

A. Undoped mother compound

The calculated total magnetic moment of Fe in the undoped mother compound BaFe$_2$As$_2$ is $\mu({\rm Fe}) = 0.73\,\mu_{\rm B}$, as was already published in earlier work [30]. This moment splits into a spin magnetic moment of $\mu_{\rm spin}({\rm Fe}) = 0.70\,\mu_{\rm B}$ and an orbital magnetic moment of $\mu_{\rm orb}({\rm Fe}) = 0.03\,\mu_{\rm B}$. Obviously, this is in good agreement with experimental neutron diffraction data of pure BaFe$_2$As$_2$ being $0.87\,\mu_{\rm B}$ [8].

If the finite size of the atomic core is ignored, as usually done, the fully relativistic approach described in Ref. [45] splits $B_{\rm hf}$ into five contributions. There are two contributions due to the s electrons that are conventionally ascribed to the Fermi contact interaction. The larger part is the core polarization contribution B_s^c that was demonstrated in numerous studies to be proportional to the local spin magnetic moment $\mu_{\rm spin}$ [46–48]. In addition, there is a s-electron contribution from the valence band B_s^v that is due to the polarization and also dominantly due to the population mechanism [49]. For systems with low symmetry there may be a spin dipolar contribution to $B_{\rm hf}$ for the non-s electrons [45,50]. Apart from $p_{1/2}$ states, states with higher angular momentum such as p and d states have zero probability density at the core and for that reason do not contribute to $B_{\rm hf}$ via the Fermi contact term. If spin-orbit coupling is accounted for, as done here, there is an additional contribution due to the spin-orbit induced orbital magnetization [45,50]. As the orbital contribution is in general dominating compared to the spin-dipolar one [45], we use in the following the term orbital for the total field connected with non-s electrons. Thus, for a transition metal, the remaining three contributions are the orbital field B_{ns}^c of the non-s core states and the orbital fields B_p^v and B_d^v of the valence electrons with p and d character, respectively. One arrives for the hyperfine field $B_{\rm hf}$ at the following decomposition [45]:

$$B_{\rm hf} = B_s^c + B_{ns}^c + B_s^v + B_p^v + B_d^v. \tag{1}$$

Figure 1(a) shows for bcc Fe numerical results for the various contributions to the hyperfine field. As it is well known, $B_{\rm hf}$ of bcc Fe is dominated by its large core polarization contribution B_s^c. This is enhanced by the field B_s^v, which is also negative. All other contributions are much smaller and positive. Comparing the total calculated hyperfine field $B_{\rm hf} = -26.7$ T with the corresponding experimental value $B_{\rm exp} = -33.9$ T, one finds the theoretical values too small by about 25% [52]. This well known problem is primarily to be ascribed to shortcomings of LSDA when dealing with the core polarization cased by the spin polarization of the valence electrons [53–55]. To cure this problem it is common to enhance B_s^c by about 25% [53–56]. Using this empirical approach one has for the enhanced hyperfine field $\widetilde{B}_{\rm hf}$ the

TABLE I. Different contributions to the hyperfine field $B_{\rm hf}$ for $\mathrm{BaFe_2As_2}$, depending on the magnetization direction axis. Consistent with experiment is an orientation of magnetic moments along the a axis, which was applied throughout this work.

Axis	$\mu_{\rm spin}$ (μ_B)	B_s^c (T)	B_{ns}^c (T)	B_s^v (T)	B_p^v (T)	B_d^v (T)	$B_{\rm hf}$ (T)
a	0.696	−7.37	0.035	1.48	0.37	1.86	−3.62
b	0.698	−7.39	0.036	1.48	−0.34	2.66	−3.55
c	0.695	−7.36	0.035	1.48	−0.10	−0.13	−6.08

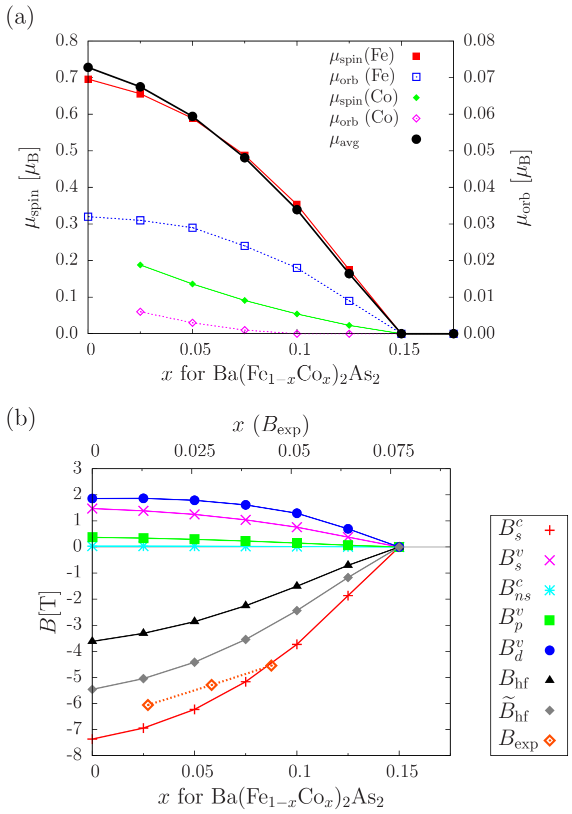

FIG. 2. (a) Component-resolved magnetic moments for Co-122 depending on the concentration x. The left (right) scale refers to the spin (orbital) magnetic moment. (b) Corresponding hyperfine field contributions for Fe in Co-122. The experimental data $B_{\rm exp}$ (dashed orange lines) [24] refer to the upper axis, with the upper and lower axes for the concentration x chosen such that $x_{\rm crit} = x_{\rm crit,exp}$.

relation

$$\widetilde{B}_{\rm hf} = 1.25\, B_s^c + B_{ns}^c + B_s^v + B_p^v + B_d^v. \qquad (2)$$

As can be seen in Fig. 1(a), this leads to $\widetilde{B}_{\rm hf} = -32.9$ T for bcc Fe, in good agreement with experiment. Next, consider Fe in the undoped mother compound $\mathrm{BaFe_2As_2}$ as presented in Fig. 1(b). Comparing the calculated $B_{\rm hf} = -3.62$ T with the experimental one $B_{\rm exp} = -5.47$ T [9,10], the shortcomings of LSDA are obviously the same as for bcc Fe, as one would expect. However, the enhanced field $\widetilde{B}_{\rm hf} = -5.46$ T is in perfect agreement with experiment, confirming the transferability of the enhancement factor in Eq. (2). Compared with bcc Fe, the various contributions to $\widetilde{B}_{\rm hf}$ of Fe in $\mathrm{BaFe_2As_2}$ show two major differences. First, the sign of the valence band s-electron contribution B_s^v is different, and, second, the spin-orbit induced contribution of d electrons B_d^v is considerably higher in the latter case. Both features lead to a very different relation between the enhanced hyperfine field $\widetilde{B}_{\rm hf}$ and the local spin magnetic moment $\mu_{\rm spin}$ for the two systems. As $\widetilde{B}_{\rm hf}$ of bcc Fe is dominated by its enhanced core polarization contribution $\widetilde{B}_s^c$ ($\widetilde{B}_{\rm hf}/\widetilde{B}_s^c \approx 1.07$), which is proportional to $\mu_{\rm spin}$, it seems justified to assume that the experimental field $B_{\rm exp}$ reflects in a one-to-one manner the local spin moment. For Fe in $\mathrm{BaFe_2As_2}$, on the other hand, we find $\widetilde{B}_{\rm hf}/\widetilde{B}_s^c \approx 0.59$, i.e., the total field $\widetilde{B}_{\rm hf}$ can by no means be used to monitor the local spin magnetic moment of Fe.

It was found that this unexpected behavior of $\mathrm{BaFe_2As_2}$ compared to bcc Fe is mainly due to its in-plane orientation of magnetic moments along the a axis. It was already stressed that this magnetization direction is conform with experiment [20] and can be theoretically described by the applied inclusion of spin-orbit coupling. For comparison, we show in Table I the components of the hyperfine field of $\mathrm{BaFe_2As_2}$ depending on the magnetization direction. It is obvious that the contributions B_p^v and B_d^v depend strongly on the chosen orientation, although the spin magnetic moment of Fe $\mu_{\rm spin}$ and the other contributions to the hyperfine field only marginally change. This has naturally an impact on the total hyperfine field $B_{\rm hf}$ which thus depends on the magnetization direction in $\mathrm{BaFe_2As_2}$.

B. Electron and hole doping

Having investigated the hyperfine field contributions of the undoped $\mathrm{BaFe_2As_2}$ including relativistic effects, an interesting issue is their variation under different types of substitution in the $\mathrm{BaFe_2As_2}$ family.

Two examples of electron doping were investigated, namely, $\mathrm{Ba(Fe_{1-x}Co_x)_2As_2}$ (Co-122) and $\mathrm{Ba(Fe_{1-x}Ni_x)_2As_2}$ (Ni-122), with the corresponding data shown in Figs. 2 and 3, respectively. Furthermore, one case of hole doping, $\mathrm{(Ba_{1-x}K_x)Fe_2As_2}$ (K-122), has been considered (see Fig. 4). In all cases, the magnetic moments of the components are presented in Figs. 2(a), 3(a), and 4(a), respectively, as a function of the concentration. The magnetic moments for Co-122 in Fig. 2(a) were published before [30], and are reproduced here to supply a reference for the hyperfine field and to allow for direct comparison with other systems. The various figures give in a component-resolved manner the spin magnetic moments $\mu_{\rm spin}$ (left axis) and the orbital magnetic moments $\mu_{\rm orb}$ (right axis). The concentration dependent average of the system with composition $\mathrm{Ba(Fe_{1-x}}TM_x\mathrm{)_2As_2}$ is shown as $\mu_{\rm avg} = (1-x)[\mu_{\rm spin}(\mathrm{Fe}) + \mu_{\rm orb}(\mathrm{Fe})] + x[\mu_{\rm spin}(TM) + \mu_{\rm orb}(TM)]$.

First consider the electron doped compounds Co-122 and Ni-122. Both systems show a similar decrease in $\mu_{\rm avg}$ until the breakdown of long range antiferromagnetic (AFM) order at $x_{\rm crit}$ is reached, with $x_{\rm crit}(\text{Co-122}) = 0.125$ and $x_{\rm crit}(\text{Ni-122}) = 0.075$, respectively. This is in reasonable agreement with experiment, with the experimental $x_{\rm crit,exp}$ being lower [$x_{\rm crit,exp}(\text{Co-122}) \approx 0.075$ [57], $x_{\rm crit,exp}(\text{Ni-122}) \approx 0.0375$ [58]]. Concerning the instability of the antiferromagnetic order, the electronic structure calculations account for a change in the nesting condition due to a shift of the Fermi level

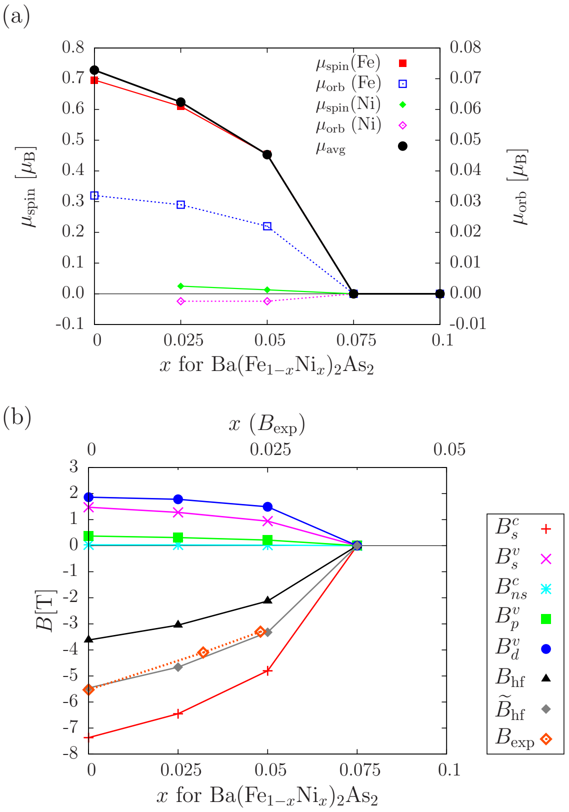

FIG. 3. Same as for Fig. 2, but for Ni-122 with experimental data from Ref. [25].

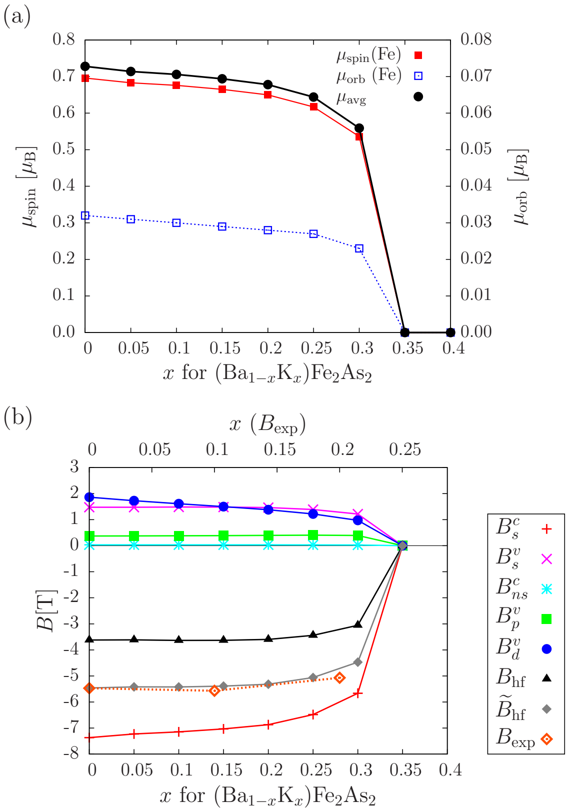

FIG. 4. Same as for Fig. 2, but for K-122 with experimental data from Ref. [10].

due to doping but they do not explicitly account for fluctuating magnetic moments or incommensurate spin-density waves [59]. This might explain the observed discrepancies between x_{crit} and $x_{crit,exp}$, implying that these aspects should be accounted for in order to get better agreement.

In line with experiment, x_{crit} for Ni-122 is found to be only half of Co-122. This had to be expected because of the formal doubling of electron doping by Ni compared to Co substitution of Fe. Another difference between these two compounds is the lower Ni moment in Ni-122 compared to that of Co in Co-122. In this context one should also note that the rather small orbital moment of Ni has a different sign compared to its spin moment. The various hyperfine field contributions for Fe in Co-122 and Ni-122 are shown in Figs. 2(b) and 3(b), respectively. The trends of the Fe magnetic moments and in the hyperfine field contributions behave in a similar way. The figures show also experimental data for the hyperfine field B_{exp} [24,25]. These has been plotted using a different scale for the concentration x at the top of the figure that was chosen such that theoretical and experimental critical concentrations agree ($x_{crit} = x_{crit,exp}$). With the aforementioned enhancement of the core polarization field by 25% and the rescaling of the x axis, one finds a very satisfying agreement for $\widetilde{B}_{hf}$ and B_{exp} for Co-122 [Fig. 2(b)] as well as Ni-122 [Fig. 3(b)].

Next, the K-122 compound is discussed with its magnetic moments shown in Fig. 4(a) (see also Ref. [60]). A breakdown of the AFM order is found from the calculations at x_{crit}(K-122) $= 0.35$, while a lower $x_{crit,exp}$(K-122) ≈ 0.25 [40] is observed in experiment. It should be noted that the substituted K does not have a noteworthy magnetic moment. As the Fe concentration does not change with substitution on the Ba position, the average moment is therefore equal to the Fe moment, leading in this case to $\mu_{avg} = \mu(\text{Fe}) = \mu_{spin}(\text{Fe}) + \mu_{orb}(\text{Fe})$. One can see that for K-122 the magnetic moments change only marginally over a wide concentration range x and undergo a sharp drop for $x > 0.25$. The same behavior can be seen in the hyperfine field contributions of K-122, as shown in Fig. 4(b). Experimental data for B_{exp} [10], referring again to the upper axis, are in good agreement with the enhanced theoretical field $\widetilde{B}_{hf}$. In particular, the experimental B_{exp} is also nearly constant over a large range of concentration, in variance to the electron doped systems considered above.

C. Isovalent doping

The subsequently discussed Ba(Fe$_{1-x}$Ru$_x$)$_2$As$_2$ (Ru-122) and BaFe$_2$(As$_{1-x}$P$_x$)$_2$ (P-122) compounds are fundamentally different from the systems considered above because of the isovalent doping. This means, in particular, that the VCA is inappropriate to deal with these systems in a meaningful way. Still, a supercell approach could be applied to deal with the substitution [61]. However, the large computational effort makes theoretical work on these compounds rare and difficult. On the other hand, CPA-based approaches provide an efficient and powerful framework for this task.

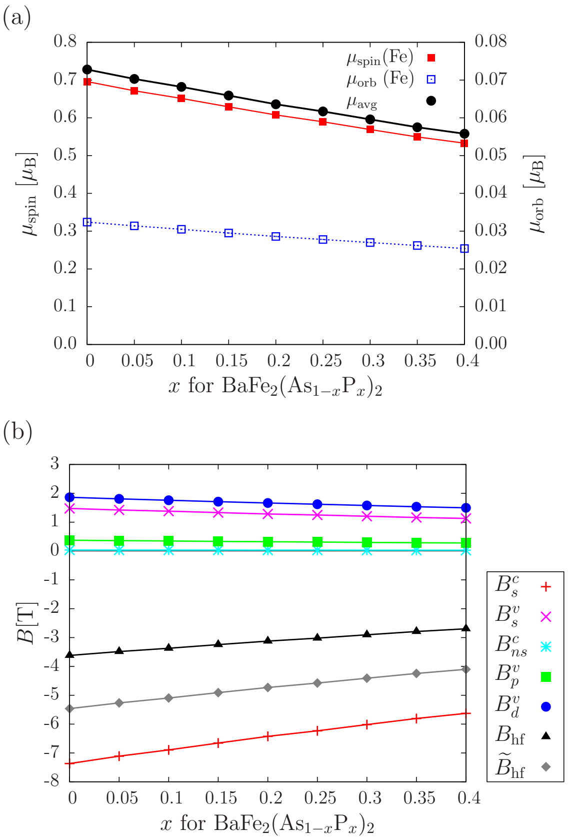

FIG. 5. Same as for Fig. 2, but for P-122.

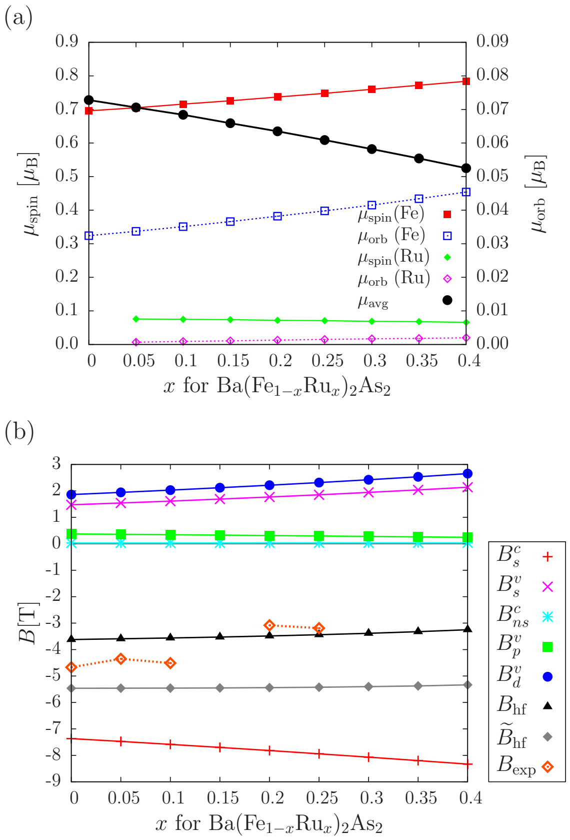

FIG. 6. Same as for Fig. 2, but for Ru-122 with experimental data from Ref. [26].

We show the component-resolved magnetic moments of P-122 and Ru-122 in Figs. 5(a) and 6(a), respectively. The first point to note is that the calculations do not lead to a critical concentration $x_{\rm crit}$ within the investigated regime of substitution, while on the experimental side one has $x_{\rm crit,exp}$(Ru-122) $\approx x_{\rm crit,exp}$(P-122) ≈ 0.3 [62,63]. Isovalent doping should in general shift the Fermi level E_F only marginally, leading to an unchanged nesting behavior. Thus, magnetic ordering may be preserved as long as the substitutional limit $x \to 1$ has a finite magnetic moment. In the case of electron or hole doping of BaFe$_2$As$_2$ the breakdown of magnetic order at a critical concentration $x_{\rm crit}$ can be understood solely by the nesting condition when the Fermi energy E_F changes due to substitution. Note that also K-122 shows a finite $x_{\rm crit}$ with good agreement to experiment, although the substitution happens not on the Fe position but within the Ba layer. On the other hand, isovalent substitution either within (Ru-122) or outside (P-122) the Fe layer cannot explain the magnetic breakdown by the substitution alone. This indicates that other phenomena not accounted for within the CPA mean field approach influence the stability of the magnetic structure. In the literature, e.g., magnetic dilution was discussed as the main driving force for the magnetic breakdown in Ru-122 [64,65]. Although we find a decrease in the magnetic moments due to the decrease in the Fe content, it seems not sufficient to cause a breakdown of the magnetic order without further reasons. Spin fluctuations and incommensurate spin-density waves can have an impact on the stability of the antiferromagnetic order, but also the emergence of a competing superconducting state might play a role. In any case, it becomes obvious that the isovalently doped compounds of the BaFe$_2$As$_2$ family are even more difficult to understand than the electron and hole doped variants. Nevertheless, LSDA-based calculations can reproduce the decrease of the average magnetic moment $\mu_{\rm avg}$ for Ru-122 as well as for P-122, although the details of this reduction in the magnetic moments are fundamentally different.

The magnetic moments and the hyperfine field contributions of Fe in P-122 shown in Fig. 5 behave in a similar way as those of K-122 (Fig. 4). In both cases the substitution takes place outside the Fe layer; i.e., although the Fe concentration does not change the total Fe moment, μ(Fe) does. The hyperfine field contributions of Fe in P-122 vary again similar with composition as the magnetic moments do. Of course, this has to be expected as the hyperfine field reflects the magnetization of the Fe atoms, which are the only magnetic components of these systems.

For Ru-122 the average moment $\mu_{\rm avg}$ shown in Fig. 6(a) decreases due to the increasing concentration of Ru which has a small induced magnetic moment of around $\mu({\rm Ru}) \approx 0.07\mu_{\rm B}$, independent on the concentration x. However, the local Fe spin magnetic moment $\mu_{\rm spin}$(Fe) and orbital $\mu_{\rm orb}$(Fe) magnetic moments surprisingly increase. This is a rather unexpected finding as it was not observed so far within theoretical investigations on the iron pnictides. Accordingly, the corresponding relation to the directly measurable hyperfine field B_{hf} of Fe is of interest as it provides an element specific probe of the magnetic properties. As can be seen in Fig. 6(b), B_{hf} stays more or less constant over the whole investigated regime of substitution, although μ(Fe) increases. This is due to the fact that μ_{spin}(Fe) and μ_{orb}(Fe) simultaneously increase, leading to a subsequent increase of the absolute values of B_s^c and B_d^v. Because the sign of both contributions is different, their changes essentially compensate each other. This does not contradict with experimental findings of Reddy *et al.* [26] depicted in Fig. 6(b) which show a more or less constant B_{hf} for Ru concentrations $x \leqslant 0.1$. The rapid drop to lower B_{hf} values for Ru-122 for $x \geqslant 0.2$ is most likely connected to the proximity to the critical concentration x_{crit}, which could not be reproduced by our LSDA-based calculations.

In conclusion, a quite unexpected and interesting variation of the magnetic moments and the hyperfine field with the concentration x of the Ru-122 compound was found which is consistent with experimental findings. This shows, in particular, that Ru-122 and P-122 differ more from each other with respect to their magnetic properties, as one might expect for two isovalently doped pnictides.

D. Relation to the magnetic moment

Finally, the results can be used to clarify the relation between B_{hf} and the average magnetic moment μ_{avg}. It is quite common to assume that the ratio $A_{\mathrm{hf}}^{\mathrm{avg}} = -B_{\mathrm{hf}}/\mu_{\mathrm{avg}}$ or $A_{\mathrm{hf}} = -B_{\mathrm{hf}}/\mu_{\mathrm{spin}}(\mathrm{Fe})$ is constant and use this value in order to obtain the magnetic moments in related compounds from the Fe hyperfine fields. For example, $A_{\mathrm{hf}}^{\mathrm{avg}}(\mathrm{Fe}) = 15\ \mathrm{T}/\mu_{\mathrm{B}}$ was given for bulk Fe and $A_{\mathrm{hf}}^{\mathrm{avg}}(\mathrm{Fe}^{3+}) = 11\ \mathrm{T}/\mu_{\mathrm{B}}$ for Fe^{3+} ions in $\mathrm{Fe_2O_3}$ [25]. These values give for $\mathrm{BaFe_2As_2}$ with an experimental hyperfine field $B_{\mathrm{exp}} = -5.47$ T a magnetic moment $\mu_{\mathrm{avg}} \sim 0.4$–$0.5\,\mu_{\mathrm{B}}$ [9,10]. Later on it was questioned whether these ratios $A_{\mathrm{hf}}^{\mathrm{avg}}$ are applicable to the iron pnictides [24,25]. In addition, there is general work showing that a scaling of B_{hf} with the corresponding magnetic moment μ_{avg} cannot be assumed *a priori* because $A_{\mathrm{hf}}^{\mathrm{avg}}$ varies strongly for different materials [51]. This is in line with our results that can be used to quantify $A_{\mathrm{hf}}^{\mathrm{avg}}$. Additionally, the assumption of a constant ratio $A_{\mathrm{hf}}^{\mathrm{avg}}$ for doped systems can be disproved, supporting other work [24] which concludes that B_{hf} is indeed not proportional to μ_{avg} for $\mathrm{BaFe_2As_2}$-based substitutional systems.

As stressed already, the core s-electron contribution B_s^c is indeed proportional to μ_{spin}(Fe), which is quantified for our calculations in Fig. 7(a), where we show the ratio $A_c = -B_s^c/\mu_{\mathrm{spin}}(\mathrm{Fe})$ for all investigated compounds depending on the concentration x. Independent on x, we find the value of A_c is nearly constant, $10.6\ \mathrm{T}/\mu_{\mathrm{B}}$. This is in reasonable agreement with earlier work of Lindgren and Sjøstrøm where a value around $12.6\ \mathrm{T}/\mu_{\mathrm{B}}$ was calculated [48]. However, B_s^c can obviously vary significantly from B_{hf}, as was extensively shown in the literature.

At least for the undoped $\mathrm{BaFe_2As_2}$, the average moment equals the total Fe moment and is close to the spin magnetic moment of iron, $\mu_{\mathrm{avg}} = \mu_{\mathrm{spin}}(\mathrm{Fe}) + \mu_{\mathrm{orb}}(\mathrm{Fe}) \approx \mu_{\mathrm{spin}}(\mathrm{Fe})$. Based on the calculations, one gets for $\mathrm{BaFe_2As_2}$ a ratio $A_{\mathrm{hf}} = -B_{\mathrm{hf}}/\mu_{\mathrm{spin}}(\mathrm{Fe}) = 5.2\ \mathrm{T}/\mu_{\mathrm{B}}$, or based on the enhanced hyperfine field $\widetilde{B}_{\mathrm{hf}}$, a ratio $\widetilde{A}_{\mathrm{hf}} = 7.8\ \mathrm{T}/\mu_{\mathrm{B}}$. This is by a factor of 2–3 different from the ratio $A_{\mathrm{hf}}^{\mathrm{avg}}$(Fe) applied in previous publications [9,10]. Consequently, the magnetic moment of $\mathrm{BaFe_2As_2}$ based on the measured hyperfine field of 5.47 T should be not between $0.4\,\mu_{\mathrm{B}}$ and $0.5\,\mu_{\mathrm{B}}$ but rather in the range between $0.7\,\mu_{\mathrm{B}}$ and $1.0\,\mu_{\mathrm{B}}$, which is in better qualitative agreement with neutron diffraction, reporting

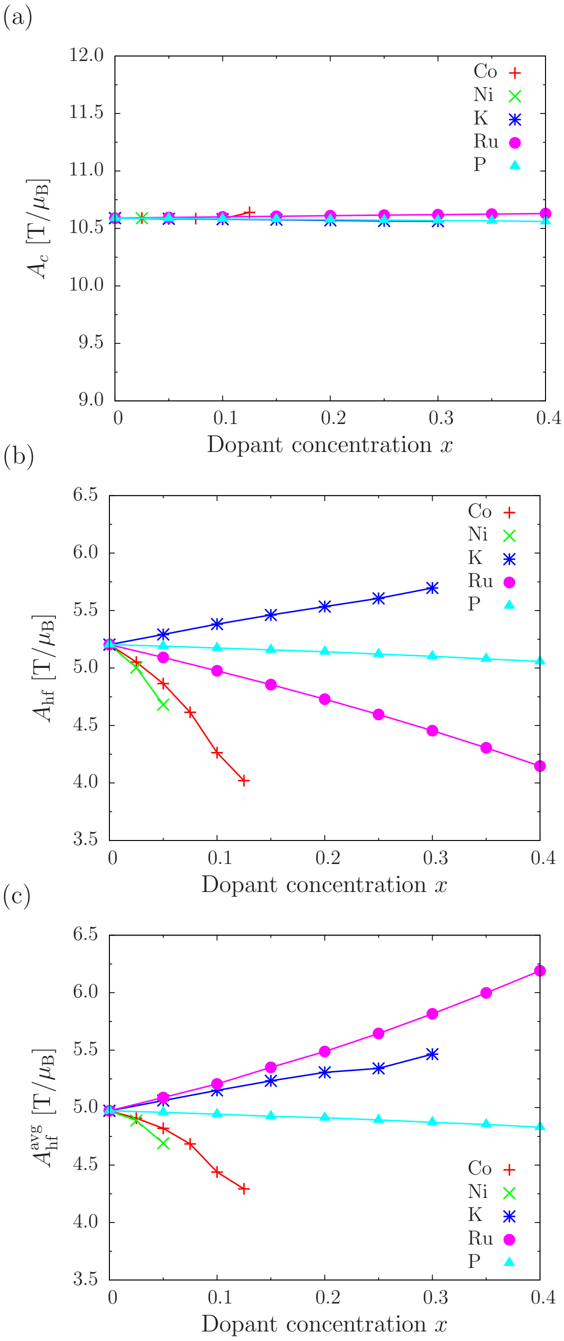

FIG. 7. (a) The ratio $A_c = -B_s^c/\mu_{\mathrm{spin}}(\mathrm{Fe})$ is shown for all investigated compounds, depending on the respective dopant and its concentration x. The constant behavior shows a reasonable relation to the magnetic moment μ. However, the same ratios are shown for (b) $A_{\mathrm{hf}} = -B_{\mathrm{hf}}/\mu_{\mathrm{spin}}(\mathrm{Fe})$ and for (c) $A_{\mathrm{hf}}^{\mathrm{avg}} = -B_{\mathrm{hf}}/\mu_{\mathrm{avg}}$, having huge deviations for an constant A_{hf} behavior, depending on x and on the chosen dopant.

$0.87\,\mu_B$ [8]. Nevertheless, one should keep in mind that this is a qualitative estimation and it is clear from the literature [24,51] and from our work that an estimation of μ_{avg} based on B_{hf} should be avoided as far as possible.

However, for the doped iron pnictides there is a significant difference between μ_{avg} and μ_{spin}(Fe). Thus, the relation between B_{hf} and μ_{avg} leads to an unpredictable, nonlinear behavior of the ratio A_{hf}^{avg}. To quantify our claim we plot the obtained values of $A_{hf} = -B_{hf}/\mu_{spin}(\text{Fe})$ and $A_{hf}^{avg} = -B_{hf}/\mu_{avg}$ depending on the concentration x for all investigated compounds in Figs. 7(b) and 7(c), respectively. Already the ratio A_{hf}, which is coupled to the spin magnetic moment of Fe, depends strongly on the respective dopant and on the concentration x. It becomes apparent that for such a behavior no reasonable relation between B_{hf} and μ_{spin}(Fe) is possible. This problem becomes even more obvious when considering A_{hf}^{avg}. Here, the Ru-122 compound is interesting to mention because A_{hf} decreases with x while A_{hf}^{avg} increases with the concentration. This is due to the fact that the Fe moment in Ru-122 increases while the average moment decreases (see also Fig. 6). Thus, it can be crucially misleading to relate B_{hf} to the average magnetic moment μ_{avg} in doped iron pnictides. Consequently, the presented study clearly shows that the hyperfine fields B_{hf} of Fe obtained from ^{57}Fe Mössbauer spectroscopy are not suitable to make predictions about the respective magnetic moment μ_{avg} in doped iron pnictide superconductors for different substitutions.

IV. SUMMARY

To summarize, this work presented a comprehensive theoretical study of the hyperfine fields in the iron pnictide superconductor family of $BaFe_2As_2$ with good agreement with experiment. The CPA was applied to a variety of compounds, dealing accurately with the substitutional disorder and accounting for all variants of doping. This includes electron doped $Ba(Fe_{1-x}Co_x)_2As_2$ and $Ba(Fe_{1-x}Ni_x)_2As_2$, hole doped $(Ba_{1-x}K_x)Fe_2As_2$, and also isovalently doped $Ba(Fe_{1-x}Ru_x)_2As_2$ and $BaFe_2(As_{1-x}P_x)_2$. All systems were investigated in their antiferromagnetic state which was used to study the magnetic moments depending on the concentration x in detail. In order to get meaningful results the fully relativistic Dirac formalism was applied, which ensured that all relativistic contributions to B_{hf} were accurately dealt with. Indeed, spin-orbit induced contributions were found to have a significantly higher influence on Fe in $BaFe_2As_2$, as found for bulk Fe. In particular, the orientation of magnetic moments along the a axis, consistent with experiment, plays a significant role for the hyperfine field. Consequently, we have quantified in detail why it is not sensible to apply the bulk Fe ratio $A_{hf}^{avg}(\text{Fe}) = 15\,\text{T}/\mu_B$ to the iron pnictides in order to obtain estimations for the magnetic moment from ^{57}Fe Mössbauer spectroscopy. As a crude estimate, one might rather expect for undoped $BaFe_2As_2$ ratios around 5.0–7.5 T/μ_B, leading to a magnetic moment of roughly 0.7–1.0 μ_B, which is more consistent with neutron diffraction reporting $0.87\,\mu_B$ [8]. However, it is best to avoid such estimations, as was shown for the substituted iron pnictide systems. Here, the behavior of A_{hf}^{avg} with the concentration x is clearly unpredictable and might lead to wrong conclusions. Thus, relating the hyperfine fields B_{hf} of Fe obtained via ^{57}Fe Mössbauer spectroscopy with the magnetic moments should be avoided for substituted iron pnictides.

ACKNOWLEDGMENT

We acknowledge financial support from the DFG Project FOR 1346. J.M. acknowledges project CENTEM PLUS (LO1402) and VEDPMNF (CZ.02.1.01/15.003/358) of Czech ministerium MSMT.

[1] Y. Kamihara, T. Watanabe, M. Hirano, and H. Hosono, J. Am. Chem. Soc. **130**, 3296 (2008).

[2] H. Takahashi, K. Igawa, K. Arii, Y. Kamihara, M. Hirano, and H. Hosono, Nature (London) **453**, 376 (2008).

[3] D. J. Singh, Phys. Rev. B **78**, 094511 (2008).

[4] I. I. Mazin, D. J. Singh, M. D. Johannes, and M. H. Du, Phys. Rev. Lett. **101**, 057003 (2008).

[5] R. M. Fernandes, D. K. Pratt, W. Tian, J. Zarestky, A. Kreyssig, S. Nandi, M. G. Kim, A. Thaler, N. Ni, P. C. Canfield, R. J. McQueeney, J. Schmalian, and A. I. Goldman, Phys. Rev. B **81**, 140501 (2010).

[6] I. I. Mazin and M. D. Johannes, Nat. Phys. **5**, 141 (2009).

[7] I. I. Mazin, M. D. Johannes, L. Boeri, K. Koepernik, and D. J. Singh, Phys. Rev. B **78**, 085104 (2008).

[8] Q. Huang, Y. Qiu, W. Bao, M. A. Green, J. W. Lynn, Y. C. Gasparovic, T. Wu, G. Wu, and X. H. Chen, Phys. Rev. Lett. **101**, 257003 (2008).

[9] M. Rotter, M. Tegel, D. Johrendt, I. Schellenberg, W. Hermes, and R. Pöttgen, Phys. Rev. B **78**, 020503 (2008).

[10] M. Rotter, M. Tegel, I. Schellenberg, F. M. Schappacher, R. Pöttgen, J. Deisenhofer, A. Günther, F. Schrettle, A. Loidl, and D. Johrendt, New J. Phys. **11**, 025014 (2009).

[11] A. N. Yaresko, G.-Q. Liu, V. N. Antonov, and O. K. Andersen, Phys. Rev. B **79**, 144421 (2009).

[12] I. Opahle, H. C. Kandpal, Y. Zhang, C. Gros, and R. Valentí, Phys. Rev. B **79**, 024509 (2009).

[13] J. Fink, S. Thirupathaiah, R. Ovsyannikov, H. A. Dürr, R. Follath, Y. Huang, S. de Jong, M. S. Golden, Y.-Z. Zhang, H. O. Jeschke, R. Valentí, C. Felser, S. Dastjani Farahani, M. Rotter, and D. Johrendt, Phys. Rev. B **79**, 155118 (2009).

[14] M. J. Han, Q. Yin, W. E. Pickett, and S. Y. Savrasov, Phys. Rev. Lett. **102**, 107003 (2009).

[15] L. X. Yang, Y. Zhang, H. W. Ou, J. F. Zhao, D. W. Shen, B. Zhou, J. Wei, F. Chen, M. Xu, C. He, Y. Chen, Z. D. Wang, X. F. Wang, T. Wu, G. Wu, X. H. Chen, M. Arita, K. Shimada, M. Taniguchi, Z. Y. Lu, T. Xiang, and D. L. Feng, Phys. Rev. Lett. **102**, 107002 (2009).

[16] L. Craco, M. S. Laad, S. Leoni, and H. Rosner, Phys. Rev. B **78**, 134511 (2008).

[17] D. Kasinathan, A. Ormeci, K. Koch, U. Burkhardt, W. Schnelle, A. Leithe-Jasper, and H. Rosner, New J. Phys. **11**, 025023 (2009).

[18] A. Sanna, F. Bernardini, G. Profeta, S. Sharma, J. K. Dewhurst, A. Lucarelli, L. Degiorgi, E. K. U. Gross, and S. Massidda, Phys. Rev. B **83**, 054502 (2011).

[19] E. Aktürk and S. Ciraci, Phys. Rev. B **79**, 184523 (2009).

[20] Y. Su, P. Link, A. Schneidewind, T. Wolf, P. Adelmann, Y. Xiao, M. Meven, R. Mittal, M. Rotter, D. Johrendt, T. Brueckel, and M. Loewenhaupt, Phys. Rev. B **79**, 064504 (2009).

[21] H. Gretarsson, A. Lupascu, J. Kim, D. Casa, T. Gog, W. Wu, S. R. Julian, Z. J. Xu, J. S. Wen, G. D. Gu, R. H. Yuan, Z. G. Chen, N.-L. Wang, S. Khim, K. H. Kim, M. Ishikado, I. Jarrige, S. Shamoto, J.-H. Chu, I. R. Fisher, and Y.-J. Kim, Phys. Rev. B **84**, 100509 (2011).

[22] P. Vilmercati, A. Fedorov, F. Bondino, F. Offi, G. Panaccione, P. Lacovig, L. Simonelli, M. A. McGuire, A. S. M. Sefat, D. Mandrus, B. C. Sales, T. Egami, W. Ku, and N. Mannella, Phys. Rev. B **85**, 220503 (2012).

[23] S. V. Borisenko, D. V. Evtushinsky, Z.-H. Liu, I. Morozov, R. Kappenberger, S. Wurmehl, B. Büchner, A. N. Yaresko, T. K. Kim, M. Hoesch, T. Wolf, and N. D. Zhigadlo, Nat. Phys. **12**, 311 (2016).

[24] P. Bonville, F. Rullier-Albenque, D. Colson, and A. Forget, Europhys. Lett. **89**, 67008 (2010).

[25] I. Nowik, I. Felner, N. Ni, S. L. Bud'ko, and P. C. Canfield, J. Phys.: Condens. Matter **22**, 355701 (2010).

[26] V. R. Reddy, A. Bharathi, A. Gupta, K. Sharma, S. Chandra, S. Sharma, K. Vinod, and C. S. Sundar, J. Phys.: Condens. Matter **26**, 356002 (2014).

[27] J. M. Allred, K. M. Taddei, D. E. Bugaris, M. J. Krogstad, S. H. Lapidus, D. Y. Chung, H. Claus, M. G. Kanatzidis, D. E. Brown, J. Kang, R. M. Fernandes, I. Eremin, S. Rosenkranz, O. Chmaissem, and R. Osborn, Nat. Phys. **12**, 493 (2016).

[28] H. Pang, Y. Fang, and F. Li, Hyperfine Interact. **199**, 387 (2011).

[29] G. Derondeau, S. Polesya, S. Mankovsky, H. Ebert, and J. Minár, Phys. Rev. B **90**, 184509 (2014).

[30] G. Derondeau, J. Braun, H. Ebert, and J. Minár, Phys. Rev. B **93**, 144513 (2016).

[31] G. Derondeau, F. Bisti, J. Braun, V. A. Rogalev, M. Kobayashi, M. Shi, T. Schmitt, J. Ma, H. Ding, H. Ebert, V. N. Strocov, and J. Minár, arXiv:1606.08977.

[32] T. Berlijn, C.-H. Lin, W. Garber, and W. Ku, Phys. Rev. Lett. **108**, 207003 (2012).

[33] S. N. Khan and D. D. Johnson, Phys. Rev. Lett. **112**, 156401 (2014).

[34] S. N. Khan, A. Alam, and D. D. Johnson, Phys. Rev. B **89**, 205121 (2014).

[35] A. Herbig, R. Heid, and J. Schmalian, Phys. Rev. B **94**, 094512 (2016).

[36] H. Ebert, D. Ködderitzsch, and J. Minár, Rep. Prog. Phys. **74**, 096501 (2011).

[37] H. Ebert *et al.*, *The Munich SPR-KKR Package*, version 6.3, http://olymp.cup.uni-muenchen.de/ak/ebert/SPRKKR, 2012.

[38] L. Vegard, Z. Phys. **5**, 17 (1921).

[39] A. S. Sefat, R. Jin, M. A. McGuire, B. C. Sales, D. J. Singh, and D. Mandrus, Phys. Rev. Lett. **101**, 117004 (2008).

[40] M. Rotter, M. Pangerl, M. Tegel, and D. Johrendt, Angew. Chem. Int. Ed. **47**, 7949 (2008).

[41] A. Thaler, N. Ni, A. Kracher, J. Q. Yan, S. L. Bud'ko, and P. C. Canfield, Phys. Rev. B **82**, 014534 (2010).

[42] M. Rotter, Ph.D. thesis, LMU München, 2010.

[43] M. Merz, P. Schweiss, P. Nagel, M.-J. Huang, R. Eder, T. Wolf, H. von Löhneysen, and S. Schuppler, J. Phys. Soc. Jpn. **85**, 044707 (2016).

[44] S. H. Vosko, L. Wilk, and M. Nusair, Can. J. Phys. **58**, 1200 (1980).

[45] M. Battocletti and H. Ebert, Phys. Rev. B **64**, 094417 (2001).

[46] H. Akai, M. Akai, S. Blügel, R. Zeller, and P. H. Dederichs, J. Magn. Magn. Mater. **45**, 291 (1984).

[47] M. E. Elzain, D. E. Ellis, and D. Guenzburger, Phys. Rev. B **34**, 1430 (1986).

[48] B. Lindgren and J. Sjostrom, J. Phys. F: Met. Phys. **18**, 1563 (1988).

[49] H. Ebert, H. Winter, D. D. Johnson, and F. J. Pinski, Hyperfine Interact. **51**, 925 (1989).

[50] G. Y. Guo and H. Ebert, Phys. Rev. B **53**, 2492 (1996).

[51] S. Dubiel, J. Alloys Compd. **488**, 18 (2009).

[52] H. Akai and T. Kotani, Hyperfine Interact. **120**, 3 (1999).

[53] S. Blügel, H. Akai, R. Zeller, and P. H. Dederichs, Phys. Rev. B **35**, 3271 (1987).

[54] H. Ebert, P. Strange, and B. L. Gyorffy, J. Phys. (Paris) **49**, 31 (1988).

[55] D. Benea, O. Isnard, J. Minár, H. Ebert, and V. Pop, J. Appl. Phys. **109**, 083909 (2011).

[56] H. Ebert and H. Akai, Hyperfine Interact. **78**, 361 (1993).

[57] C. Lester, J.-H. Chu, J. G. Analytis, S. C. Capelli, A. S. Erickson, C. L. Condron, M. F. Toney, I. R. Fisher, and S. M. Hayden, Phys. Rev. B **79**, 144523 (2009).

[58] N. Ni, A. Thaler, J. Q. Yan, A. Kracher, E. Colombier, S. L. Bud'ko, P. C. Canfield, and S. T. Hannahs, Phys. Rev. B **82**, 024519 (2010).

[59] D. K. Pratt, M. G. Kim, A. Kreyssig, Y. B. Lee, G. S. Tucker, A. Thaler, W. Tian, J. L. Zarestky, S. L. Bud'ko, P. C. Canfield, B. N. Harmon, A. I. Goldman, and R. J. McQueeney, Phys. Rev. Lett. **106**, 257001 (2011).

[60] G. Derondeau, J. Minár, S. Wimmer, and H. Ebert, arXiv:1608.08077.

[61] L. Wang, T. Berlijn, Y. Wang, C.-H. Lin, P. J. Hirschfeld, and W. Ku, Phys. Rev. Lett. **110**, 037001 (2013).

[62] M. G. Kim, D. K. Pratt, G. E. Rustan, W. Tian, J. L. Zarestky, A. Thaler, S. L. Bud'ko, P. C. Canfield, R. J. McQueeney, A. Kreyssig, and A. I. Goldman, Phys. Rev. B **83**, 054514 (2011).

[63] D. Hu, X. Lu, W. Zhang, H. Luo, S. Li, P. Wang, G. Chen, F. Han, S. R. Banjara, A. Sapkota, A. Kreyssig, A. I. Goldman, Z. Yamani, C. Niedermayer, M. Skoulatos, R. Georgii, T. Keller, P. Wang, W. Yu, and P. Dai, Phys. Rev. Lett. **114**, 157002 (2015).

[64] R. S. Dhaka, C. Liu, R. M. Fernandes, R. Jiang, C. P. Strehlow, T. Kondo, A. Thaler, J. Schmalian, S. L. Bud'ko, P. C. Canfield, and A. Kaminski, Phys. Rev. Lett. **107**, 267002 (2011).

[65] R. S. Dhaka, S. E. Hahn, E. Razzoli, R. Jiang, M. Shi, B. N. Harmon, A. Thaler, S. L. Bud'ko, P. C. Canfield, and A. Kaminski, Phys. Rev. Lett. **110**, 067002 (2013).

8.3 Discussion

The original motivation was to explain quantitatively why there is a difference in the reported magnitude of the magnetic moment in $BaFe_2As_2$ between neutron diffraction and ^{57}Fe Mössbauer spectroscopy. This question could be satisfactory answered by discussing the relation between the measured hyperfine field B_{hf} and the magnetic moment μ. It was found that the commonly applied hyperfine field proportionality ratio of around 15 T/μ_{B}, stemming from bulk Fe, cannot be applied to $BaFe_2As_2$. This is due to considerably stronger relativistic effects in $BaFe_2As_2$, which lead to a significant contribution of d-electrons to the hyperfine field. Thus, the previous approximation of the magnetic moment in $BaFe_2As_2$ of 0.4 – 0.5 μ_{B} was based on wrong assumptions concerning the proportionality parameter A. For undoped $BaFe_2As_2$ values around 5.0 – 7.5 T/μ_{B} would be more appropriate, leading to a magnetic moment of roughly 0.7 – 1.0 μ_{B} per Fe in $BaFe_2As_2$, which is more consistent with neutron diffraction reporting 0.87 μ_{B}.[24]

However, one should stress once more that such proportionality relations are clearly not justified for substituted iron pnictide compounds. We have quantified that the hyperfine field shows a strong dependence on the dopant type and the concentration x. Thus, estimations of the magnetic moment based on the hyperfine field should be preferably avoided for the iron pnictides because the behavior of A with the concentration x is too unpredictable and might lead to wrong conclusions. These findings should be accounted for in future studies.

Finally, the presented work has demonstrated the wide applicability of the CPA for different substitutions in the iron pnictides. Two different types of electron doping, namely by Co and Ni, could have been compared to each other in good agreement with experiment. Furthermore, the behavior of the magnetic moments with the concentration x was well reproduced for all investigated electron or hole doped compounds. In this context one should note the striking results for the isovalent compounds $Ba(Fe_{1-x}Ru_x)_2As_2$ and $BaFe_2(As_{1-x}P_x)_2$. Both did not show a critical concentration x_{crit} in the calculations which indicates that their magnetic properties might be different from the electron and hole doped scenarios. In particular, we have found that the magnetic moments evolve already for these two compounds completely different with x. Although for both systems the average magnetic moments do decrease, this change is related to a decrease of the Fe moment in $BaFe_2(As_{1-x}P_x)_2$ and a surprising increase of the local Fe moment in $Ba(Fe_{1-x}Ru_x)_2As_2$. Future studies will have to clarify this increase of the Fe magnetic moment for the Ru-substituted system.

Chapter 9

Summary

This work has dealt with a theoretical description of the electronic and magnetic properties of the $BaFe_2As_2$ 122-family of iron pnictide superconductors. Special focus was put on the antiferromagnetic, orthorhombic phase of the 122-compounds and its striking anisotropic properties. Therefore, the Munich SPR-KKR program package was applied with great success for the first time to the iron pnictides. Most of the properties crucial for the physics of iron pnictides could be well described within one framework, i.e. the treatment of magnetic properties in a fully relativistic way, the correct inclusion of disorder by means of the coherent potential approximation (CPA), calculations of angle-resolved photoemission spectroscopy (ARPES) data and of electrical transport properties including the in-plane anisotropic behavior. One can note, that the SPR-KKR method does indeed provide a useful and powerful tool in order to investigate the iron pnictide superconductors which will be also valuable for future studies.

In particular the anisotropic electronic structure and the magnetic properties of $BaFe_2As_2$ and $Ba(Fe_{1-x}Co_x)_2As_2$ were studied in great detail for a varying Co concentration. This includes also an investigation of the exchange coupling constants J_{ij} and of the temperature dependent magnetic behavior in terms of Monte-Carlo simulations. It was found that chemical disorder plays an important role and the in-plane anisotropy seen in the electronic structure stems mainly from the anisotropic magnetic order.[262]

Continuing the investigation of antiferromagnetic $BaFe_2As_2$ and $Ba(Fe_{1-x}Co_x)_2As_2$ also the ARPES spectra of detwinned crystals were calculated using the one-step model of photoemission. The results showed very good agreement with experiment and the anisotropy seen in ARPES could be fully reproduced. In addition, the importance of surface effects for the ARPES spectra of $Ba(Fe_{1-x}Co_x)_2As_2$ was stressed, which is a valuable finding for future studies. In particular, this information could be used to specify the surface termination to be As terminated, which was not identified without doubt by experiment so far.[273]

Having the opportunity to deal accurately with ARPES data of the iron pnictides, subsequently the ARPES spectra of nonmagnetic, tetragonal $(Ba_{1-x}K_x)Fe_2As_2$ were investigated within an cooperation with experimental groups at the Swiss Light Source of the Paul Scherrer Institute, Switzerland. This was the first time theoretical results could be presented which exhaustively explaining all salient features of the ARPES spectra in $(Ba_{1-x}K_x)Fe_2As_2$ by using a combination of local density approximation (LDA), plus dynamical mean field theory (DMFT), plus one step model ARPES calculations. Especially electron-electron correlations which are accounted for by the LDA+DMFT approach were found to have a significant influence on the Lifshitz transition which is crucial for the emergence of superconductivity in this compound. Furthermore, it was shown that there is an inevitable difference between the spectra seen in ARPES and the true band dispersion, e.g. derived from DMFT. This goes back to inherent effects of the ARPES process, i.e. surface effects, matrix element effects or final state effects. Thereby especially the three-dimensional momentum definition of the photoemission final states must be accounted for. This means in particular that the mass renormalization observed in all previous ARPES works on iron pnictides is actually not an entirely intrinsic property but has a significant extrinsic contribution due to the photoemission process itself.[274]

Concerning the in-plane anisotropic properties also the resistivity anisotropy of antiferromagnetic $Ba(Fe_{1-x}Co_x)_2As_2$, $(Ba_{1-x}K_x)Fe_2As_2$ and $Ba(Fe_{1-x}Ru_x)_2As_2$ was investigated. This topic was extensively studied during the last five years and the strong anisotropy of the resistivity between the orthorhombic a and b axes was commonly ascribed to spin fluctuations or extended impurity states in the order of 22 Å. Quite on the contrary, it was found that the resistivity anisotropy of all three compounds could be reproduced on the basis of the anisotropic electronic structure within first-principles theory. Thus, the important phenomenon of the resistivity anisotropy and its peculiar sign can be fully explained and reinterpreted in terms of an anisotropic magnetoresistance (AMR).[275]

Finally, the hyperfine fields of the $BaFe_2As_2$ 122-family were studied and the relation to the magnetic moment was clarified. Therefore, a wide range of different substitutions was investigated, covering electron doped $Ba(Fe_{1-x}Co_x)_2As_2$ and $Ba(Fe_{1-x}Ni_x)_2As_2$, hole doped $(Ba_{1-x}K_x)Fe_2As_2$ and also isovalently doped compounds $Ba(Fe_{1-x}Ru_x)_2As_2$ and $BaFe_2(As_{1-x}P_x)_2$. It was found that the hyperfine fields show a strong dependence on the respective dopant and its concentration x. In particular, it could be quantified that relativistic contributions to the hyperfine field play a much more crucial role for bulk Fe. This effect hinders a straightforward relation between the total hyperfine field and the average magnetic moment. Thus, the longstanding discrepancy in the reported magnitude of the magnetic moment of $BaFe_2As_2$ between neutron diffraction and ^{57}Fe Mössbauer spectroscopy could be resolved.[276]

Conclusion

In conclusion, based on the results obtained within this thesis, three main messages can be formulated which should be accounted for by all future theoretical studies of the iron pnictide superconductors.

1. Despite their layered crystal structure the members of the 122-family show a distinct three-dimensional electronic structure. Thus, the iron pnictides in general are clearly three-dimensional materials and this three-dimensional character of the electronic properties should be always accounted for. Furthermore, chemical disorder is important when considering the substituted compounds.

2. The dispersion of the ARPES spectra of iron pnictides significantly deviates from the electronic band dispersion which can be obtained from LDA or LDA+DMFT. Therefore, theoretical approaches which study the ARPES spectra of iron pnictides should be able to account for these inherent effects. This is in particular true if one is interested in the effective mass renormalization related to strong correlations.

3. The in-plane anisotropic behavior of the 122-compounds in their antiferromagnetic phase is mainly controlled by the anisotropic electronic structure. In particular the ferromagnetically ordered chains along the b axis and the antiferromagnetic coupling along the a axis is of most importance, whereas the orthorhombic lattice distortion has a negligible contribution. This applies not only to the anisotropy seen in ARPES but also to the in-plane resistivity anisotropy. Thus, the phenomenon of the resistivity anisotropy can be reinterpreted by means of an anisotropic magnetoresistance (AMR).

Appendix A

Computational details

A detailed investigation and benchmarking of all input parameters was always performed in order to obtain reliable results. The following will extensively record all chosen input details for the sake of reproducibility and validity. First, general information is given and then a separation is done into the self-consistent field (SCF) calculations, the ARPES calculations and the resistivity calculations. Details on the chosen structural input are given in Appendix B.

All calculations have been performed in the framework of density functional theory self-consistently and fully relativistically within the four component Dirac formalism, using the Munich SPR-KKR program package using version 7.2 or higher.[61] The chosen exchange-correlation potential was always based on the local density approximation (LDA) with the parameterization as given by Vosko, Wilk and Nusair.[277]

A.1 Self-consistent field calculations

All SCF calculations used a dense k-mesh of $20 \times 18 \times 20$ for the orthorhombic crystal, respectively a k-mesh of $20 \times 20 \times 20$ for tetragonal systems, corresponding to around 8000 k-points. For magnetic systems the magnetization direction was rotated in-plane along the a axis in agreement with experiment.[25] For a reliable determination of the Fermi level, Lloyd's formula was generally applied, unless indicated otherwise.

The first calculations shown in Chapter 4 used an angular momentum expansion of $\ell_{\max} = 2$ and a full-charge (FC) ansatz as spherical approximation. Although all aspherical parts of the charge density are fully accounted for by the FC approach, the aspherical parts of the potential are neglected. Improvements were done for the subsequent calculations, in particular in all following chapters a $\ell_{\max} = 4$ within the atomic sphere approximation (ASA) was used. It was found that these input parameters provided the best results within reasonable computational effort. It is possible, but often not necessary, to introduce an additional empty sphere in the Ba layer. The corresponding electronic structure and magnetic moments of $BaFe_2As_2$ are however almost identical for $\ell_{\max} = 4$, meaning $\mu(\mathrm{Fe}) = 0.73\ \mu_{\mathrm{B}}$ without empty spheres and $\mu(\mathrm{Fe}) = 0.79\ \mu_{\mathrm{B}}$ including an empty sphere. Going from the ASA to a full-charge or a full-potential scheme does typically increase the magnetic moments, in agreement with the literature.[16] In particular, additional empty spheres and higher angular momentum expansions seem necessary for full-potential approaches in order to reduce the problem of very sharp and asymmetric Voroni polyhedra for the As atom site which significantly increases the computational effort up to a point where the calculations are no longer feasible. Consequently, good results can be obtained using the ASA as long as the angular momentum expansion $\ell_{\max}$ is high enough.

The LDA+DMFT calculations presented in Chapter 6 were performed strictly nonmagnetic and without Lloyd's formula. The DMFT FLEX solver was generally applied and different values for the on-site Coulomb interaction U and the exchange interaction J of Fe were tested ($U = 2.0 – 5.0$ eV and $J = 0.7 – 0.9$ eV). Best agreement with experiment was found for $U = 3.0$ eV and $J = 0.9$ eV, which were used for the subsequent ARPES calculations.

A.2 ARPES calculations

The presented spectroscopical analysis is based on the fully relativistic one-step model of photoemission in its spin density matrix formulation.[278,279] The geometry of the setup was always chosen in line with experiment as far as possible, including a tilt of the sample around either the a or b axis. The incident light hits the sample typically under a constant polar angle $\theta_{\mathrm{light}} = -45°$ (p-polarized light) or $\theta_{\mathrm{light}} = 0°$ (s-polarized light) with an azimuthal angle ϕ_{light} of either 180° or 270°. The corresponding electrons were collected with an angle ϕ_{electron} of 0° or 90° and a varying angle $\theta_{\mathrm{electron}}$ between approximately $-40°$ and $40°$ at maximum. The imaginary part of the energy of the initial states was in the order of typically 0.015 – 0.05 eV and imaginary part of the energy of the final states was between 2.0 – 5.0 eV. The applied work function was always 5.0 eV. LDA+DMFT calculations were done using the input parameters presented in section A.1. The angular momentum cut-off was for every ARPES calculation $\ell_{\max} = 3$, including f-orbitals to account reasonably for excitation processes. If not indicated otherwise, always an As-terminated surface with an As-Fe-As-Ba stacking was chosen. Alternatively, a Ba-terminated surface was used for comparison.

A.3 Resistivity calculations

All calculations of the resistivity tensor applying the Kubo-Greenwood formalism used an angular momentum expansion of $\ell_{\text{max}} = 3$, including f-orbitals. Of most computational relevance is a sufficiently high number of k-points, thus convergence with k-points has to be carefully investigated. For the antiferromagnetic, orthorhombic crystals a k-mesh of $162 \times 150 \times 162$ was found to be sufficient, corresponding to around $4 \cdot 10^6$ k-points. Calculations were tested up to $6 \cdot 10^6$ k-points, showing no significant changes any more.

Appendix B

Structural details

The chosen lattice parameters are of great importance for theoretical work on the iron pnictides.[16,18] Within this work it was the goal to stay with crystallographic data from experiment concerning the lattice constants as well as concerning the free As position z in $BaFe_2As_2$. However, for large concentration regimes in the case of substituted compound it is reasonable to consider structural relaxation as well. Because there is typically no complete experimental dataset for the whole substitutional range a linear extrapolation based on available experimental data and Vegard's Law was applied, which is commonly used for alloys.[280] Thus, within this work the lattice constants and sometimes also the free As parameter z were linearly extrapolated based on experimental data and individually for different kinds of substitution. For the sake of completeness and the sake of reproducibility, all used parameter sets will be given in this appendix.

It should be noted, that in the early years after the discovery of the iron pnictides some unreliable structure optimizations were performed based on nonmagnetic general gradient approximation (GGA) calculations.[18] These optimizations reported significant deviations in the As position z. This, on the other hand, influenced the magnetic moments which are reproduced by DFT, leading this way to wrong results in the end. Only by including the correct magnetic state in the structure optimizations this error could be avoided, giving again reasonable results. For comparison: $z(\text{GGA-nonmagnetic}) = 0.3448$, $z(\text{GGA-magnetic}) = 0.3520$ and $z(\text{exp.}) = 0.3545$).[18] It should be stressed, that the extrapolation of z in this work is based on experimental data and is thus completely different and more reasonable than the much stronger deviating and unreliable data derived from nonmagnetic GGA based structure optimizations.

B.1 Undoped mother compound

The lattice parameters and the free As position z for undoped $BaFe_2As_2$ were taken directly from experimental data of Rotter *et al.*[22] without further adaption. The corresponding data for the tetragonal and orthorhombic phase including Wykoff positions are summarized in Tab. B.1.

Table B.1. Experimental, crystallographic data of the tetragonal phase and the low-temperature orthorhombic phase of $BaFe_2As_2$ according to Rotter *et al.*[22]

Tetragonal phase

Spacegroup	**Wykoff positions**			**Lattice parameters [Å]**
$I4/mmm$ (139)	Ba	$2a$	$(0\,0\,0)$	$a = 3.9625$
Free parameter	Fe	$4d$	$(\frac{1}{2}\,0\,\frac{1}{4})$	$b = a$
$z = 0.3545$	As	$4e$	$(0\,0\,z)$	$c = 13.0168$

Orthorhombic phase

Spacegroup	**Wykoff positions**			**Lattice parameters [Å]**
$Fmmm$ (69)	Ba	$2a$	$(0\,0\,0)$	$a = 5.6146$
Free parameter	Fe	$8f$	$(\frac{1}{4}\,\frac{1}{4}\,\frac{1}{4})$	$b = 5.5742$
$z = 0.3538$	As	$8i$	$(0\,0\,z)$	$c = 12.9453$

B.2 Co-122 compound

The experimentally observed lattice constants from Sefat *et al.*[27] for $BaFe_2As_2$ and $Ba(Fe_{0.9}Co_{0.1})_2As_2$ in their tetragonal phase were used and extrapolated linearly on this basis for the orthorhombic phase. The lattice constants a and b were not changed, because their deviation in experiment is reported small enough to be assumed as unchanged within experimental uncertainty.[27] The validity of such an extrapolation is further supported by other work.[224,241] The linear change of the As position was accounted for on the basis of single crystal x-ray diffraction data from Merz *et al.*[281,282]. All parameters are summarized in detail in Tab. B.2.

The same lattice parameters were applied for the Ni-122 compound. This is justified due to the strong similarity of both compounds and because for $Ba(Fe_{1-x}Ni_x)_2As_2$ only low dopant concentrations $x \leq 0.075$ were relevant.

Table B.2. Crystallographic data of the orthorhombic phase of $Ba(Fe_{1-x}Co_x)_2As_2$ used within this work, based on linear extrapolation of experimental data.[27,281,282]

Co-122: $Ba(Fe_{1-x}Co_x)_2As_2$

Dopant concentration	Lattice parameters [Å]			Free As parameter
x	a	b	c	z
0.000	5.6146	5.5742	12.9453	0.3538
0.025	5.6146	5.5742	12.9349	0.3536
0.050	5.6146	5.5742	12.9244	0.3534
0.075	5.6146	5.5742	12.9140	0.3531
0.100	5.6146	5.5742	12.9035	0.3529
0.125	5.6146	5.5742	12.8931	0.3527
0.150	5.6146	5.5742	12.8827	0.3525
0.175	5.6146	5.5742	12.8722	0.3522
0.200	5.6146	5.5742	12.8618	0.3520
0.213	5.6146	5.5742	12.8564	0.3519
0.225	5.6146	5.5742	12.8514	0.3518
0.250	5.6146	5.5742	12.8409	0.3516

B.3 K-122 compound

The experimentally observed lattice parameters a, b and c and the As position z from Rotter[283] for $BaFe_2As_2$ and $(Ba_{0.8}K_{0.2})Fe_2As_2$ in their orthorhombic phase were used and extrapolated linearly on this basis. All parameters are summarized in detail in Tab. B.3.

Table B.3. Crystallographic data of the orthorhombic phase of $(Ba_{1-x}K_x)Fe_2As_2$ used within this work, based on linear extrapolation of experimental data.[283]

K-122: $(Ba_{1-x}K_x)Fe_2As_2$

Dopant concentration	**Lattice parameters [Å]**			**Free As parameter**
x	a	b	c	z
0.00	5.6146	5.5742	12.9453	0.3538
0.05	5.6043	5.5673	12.9821	0.3538
0.10	5.5940	5.5603	13.0190	0.3538
0.15	5.5837	5.5534	13.0558	0.3537
0.20	5.5734	5.5464	13.0926	0.3537
0.25	5.5631	5.5395	13.1294	0.3537
0.30	5.5528	5.5325	13.1663	0.3537
0.35	5.5425	5.5256	13.2031	0.3536
0.40	5.5322	5.5186	13.2399	0.3536
0.45	5.5219	5.5117	13.2767	0.3536
0.50	5.5116	5.5047	13.3136	0.3536

B.4 Ru-122 compound

The experimentally observed linear extrapolation of the lattice parameters a and c from Thaler *et al.*[28] for $Ba(Fe_{1-x}Ru_x)_2As_2$ in its tetragonal phase was used and applied for the orthorhombic phase. An extrapolation of the free As position z was not applied due to missing experimental data. All parameters are summarized in detail in Tab. B.4.

Table B.4. Crystallographic data of the orthorhombic phase of $Ba(Fe_{1-x}Ru_x)_2As_2$ used within this work, based on linear extrapolation of experimental data.[283]

Ru-122: $Ba(Fe_{1-x}Ru_x)_2As_2$

Dopant concentration	Lattice parameters [Å]			Free As parameter
x	a	b	c	z
0.00	5.6146	5.5742	12.9453	0.3538
0.05	5.6244	5.5840	12.9162	0.3538
0.10	5.6343	5.5937	12.8870	0.3538
0.15	5.6441	5.6035	12.8579	0.3538
0.20	5.6539	5.6132	12.8288	0.3538
0.25	5.6637	5.6230	12.7997	0.3538
0.30	5.6736	5.6327	12.7705	0.3538
0.35	5.6834	5.6425	12.7414	0.3538
0.40	5.6932	5.6522	12.7123	0.3538
0.45	5.7030	5.6620	12.6832	0.3538
0.50	5.7129	5.6717	12.6540	0.3538

B.5 P-122 compound

The experimentally observed lattice parameters a and c and the As position z from Rotter[283] for $BaFe_2As_2$ and $BaFe_2(As_{0.53}P_{0.47})_2$ in their tetragonal phase were used and extrapolated linearly on this basis for the orthorhombic phase. All parameters are summarized in detail in Tab. B.5.

Table B.5. Crystallographic data of the orthorhombic phase of $BaFe_2(As_{1-x}P_x)_2$ used within this work, based on linear extrapolation of experimental data.[283]

P-122: $BaFe_2(As_{1-x}P_x)_2$

Dopant concentration	**Lattice parameters [Å]**			**Free As parameter**
x	a	b	c	z
0.00	5.6146	5.5742	12.9453	0.3538
0.05	5.6062	5.5659	12.9162	0.3538
0.10	5.5978	5.5575	12.8872	0.3539
0.15	5.5894	5.5492	12.8581	0.3539
0.20	5.5810	5.5409	12.8291	0.3539
0.25	5.5726	5.5325	12.8000	0.3540
0.30	5.5642	5.5242	12.7710	0.3540
0.35	5.5558	5.5158	12.7419	0.3540
0.40	5.5474	5.5075	12.7128	0.3541
0.45	5.5390	5.4992	12.6838	0.3541
0.50	5.5306	5.4908	12.6547	0.3541

Bibliography

[1] A. P. Drozdov, M. I. Eremets, I. A. Troyan, V. Ksenofontov, and S. I. Shylin, Nature **525**, 73 (2015).

[2] N. W. Ashcroft, Phys. Rev. Lett. **21**, 1748 (1968).

[3] D. Duan, Y. Liu, F. Tian, D. Li, X. Huang, Z. Zhao, H. Yu, B. Liu, W. Tian, and T. Cui, Sci. Rep. **4**, 6968 (2014).

[4] I. Errea, M. Calandra, C. J. Pickard, J. Nelson, R. J. Needs, Y. Li, H. Liu, Y. Zhang, Y. Ma, and F. Mauri, Phys. Rev. Lett. **114**, 157004 (2015).

[5] I. I. Mazin, Nature **525**, 40 (2015).

[6] H. K. Onnes, Comm. Leiden **120b** (1911).

[7] H. K. Onnes, Comm. Leiden **Suppl. Nr. 34** (1913).

[8] J. Bardeen, L. N. Cooper, and J. R. Schrieffer, Phys. Rev. **108**, 1175 (1957).

[9] J. G. Bednorz and K. A. Müller, Z. Physik B **64**, 189 (1986).

[10] Y. Kamihara, T. Watanabe, M. Hirano, and H. Hosono, J. Amer. Chem. Soc. **130**, 3296 (2008).

[11] H. Takahashi, K. Igawa, K. Arii, Y. Kamihara, M. Hirano, and H. Hosono, Nature **453**, 376 (2008).

[12] Y. Kamihara, H. Hiramastsu, M. Hirano, R. Kawamura, H. Yanagi, T. Kamiya, and H. Honsono, J. Amer. Chem. Soc. **128**, 10012 (2006).

[13] M. Tegel, D. Bichler, and D. Johrendt, Solid State Sci. **10**, 193 (2008).

[14] T. Watanabe, H. Yanagi, T. Kamiya, Y. Kamihara, H. Hiramastsu, and M. H. H. Honsono, Inorg. Chem. **46**, 7719 (2007).

[15] Z. A. Ren, W. Lu, J. Yang, W. Yi, X. L. Shen, Z. C. Li, G. C. Che, X. L. Dong, L. L. Sun, F. Zhou, and Z. X. Zhao, Chin. Phys. Lett. **25**, 2215 (2008).

[16] I. I. Mazin, M. D. Johannes, L. Boeri, K. Koepernik, and D. J. Singh, Phys. Rev. B **78**, 085104 (2008).

[17] Z. P. Yin, S. Lebègue, M. J. Han, B. P. Neal, S. Y. Savrasov, and W. E. Pickett, Phys. Rev. Lett. **101**, 047001 (2008).

[18] I. I. Mazin and M. D. Johannes, Nature Physics **5**, 141 (2009).

[19] I. I. Mazin, D. J. Singh, M. D. Johannes, and M. H. Du, Phys. Rev. Lett. **101**, 057003 (2008).

[20] R. M. Fernandes, D. K. Pratt, W. Tian, J. Zarestky, A. Kreyssig, S. Nandi, M. G. Kim, A. Thaler, N. Ni, P. C. Canfield, R. J. McQueeney, J. Schmalian, and A. I. Goldman, Phys. Rev. B **81**, 140501 (2010).

[21] D. J. Singh, Phys. Rev. B **78**, 094511 (2008).

[22] M. Rotter, M. Tegel, D. Johrendt, I. Schellenberg, W. Hermes, and R. Pöttgen, Phys. Rev. B **78**, 020503 (2008).

[23] M. Rotter, M. Tegel, and D. Johrendt, Phys. Rev. Lett. **101**, 107006 (2008).

[24] Q. Huang, Y. Qiu, W. Bao, M. A. Green, J. W. Lynn, Y. C. Gasparovic, T. Wu, G. Wu, and X. H. Chen, Phys. Rev. Lett. **101**, 257003 (2008).

[25] Y. Su, P. Link, A. Schneidewind, T. Wolf, P. Adelmann, Y. Xiao, M. Meven, R. Mittal, M. Rotter, D. Johrendt, T. Brueckel, and M. Loewenhaupt, Phys. Rev. B **79**, 064504 (2009).

[26] D. K. Pratt, M. G. Kim, A. Kreyssig, Y. B. Lee, G. S. Tucker, A. Thaler, W. Tian, J. L. Zarestky, S. L. Bud'ko, P. C. Canfield, B. N. Harmon, A. I. Goldman, and R. J. McQueeney, Phys. Rev. Lett. **106**, 257001 (2011).

[27] A. S. Sefat, R. Jin, M. A. McGuire, B. C. Sales, D. J. Singh, and D. Mandrus, Phys. Rev. Lett. **101**, 117004 (2008).

[28] A. Thaler, N. Ni, A. Kracher, J. Q. Yan, S. L. Bud'ko, and P. C. Canfield, Phys. Rev. B **82**, 014534 (2010).

[29] L. J. Li, Y. K. Luo, Q. B. Wang, H. Chen, Z. Ren, Q. Tao, Y. K. Li, X. Lin, M. He, Z. W. Zhu, G. H. Cao, and Z. A. Xu, New Journal of Physics **11**, 025008 (2009).

[30] S. Jiang, H. Xing, G. Xuan, C. Wang, Z. Ren, C. Feng, J. Dai, Z. Xu, and G. Cao, J. Phys.: Cond. Mat. **21**, 382203 (2009).

[31] J. Fink, S. Thirupathaiah, R. Ovsyannikov, H. A. Dürr, R. Follath, Y. Huang, S. de Jong, M. S. Golden, Y.-Z. Zhang, H. O. Jeschke, R. Valentí, C. Felser, S. Dastjani Farahani, M. Rotter, and D. Johrendt, Phys. Rev. B **79**, 155118 (2009).

[32] D. H. Lu, M. Yi, S.-K. Mo, A. S. Erickson, J. Analytis, J.-H. Chu, D. J. Singh, Z. Hussain, T. H. Geballe, I. R. Fisher, and Z.-X. Shen, Nature **455**, 81 (2008).

[33] V. B. Zabolotnyy, D. S. Inosov, D. V. Evtushinsky, A. Koitzsch, A. A. Kordyuk, G. L. Sun, J. T. Park, D. Haug, V. Hinkov, A. V. Boris, C. T. Lin, M. Knupfer, A. N. Yaresko, B. Büchner, A. Varykhalov, R. Follath, and S. V. Borisenko, Nature **457**, 569 (2009).

[34] M. Yi, D. H. Lu, J. G. Analytis, J.-H. Chu, S.-K. Mo, R.-H. He, M. Hashimoto, R. G. Moore, I. I. Mazin, D. J. Singh, Z. Hussain, I. R. Fisher, and Z.-X. Shen, Phys. Rev. B **80**, 174510 (2009).

[35] C. Liu, T. Kondo, R. M. Fernandes, A. D. Palczewski, E. D. Mun, N. Ni, A. N. Thaler, A. Bostwick, E. Rotenberg, J. Schmalian, S. L. Bud'ko, P. C. Canfield, and A. Kaminski, Nature Physics **6**, 419 (2010).

[36] M. Yi, D. Lu, J.-H. Chu, J. G. Analytis, A. P. Sorini, A. F. Kemper, B. Moritz, S.-K. Mo, R. G. Moore, M. Hashimoto, W.-S. Lee, Z. Hussain, T. P. Devereaux, I. R. Fisher, and Z.-X. Shen, Proc. Nat. Ac. Sci. US. **108**, 6878 (2011).

[37] R. S. Dhaka, S. E. Hahn, E. Razzoli, R. Jiang, M. Shi, B. N. Harmon, A. Thaler, S. L. Bud'ko, P. C. Canfield, and A. Kaminski, Phys. Rev. Lett. **110**, 067002 (2013).

[38] M. A. Tanatar, E. C. Blomberg, A. Kreyssig, M. G. Kim, N. Ni, A. Thaler, S. L. Bud'ko, P. C. Canfield, A. I. Goldman, I. I. Mazin, and R. Prozorov, Phys. Rev. B **81**, 184508 (2010).

[39] J.-H. Chu, J. G. Analytis, K. De Greve, P. L. McMahon, Z. Islam, Y. Yamamoto, and I. R. Fisher, Science **329**, 824 (2010).

[40] T.-M. Chuang, M. P. Allan, J. Lee, Y. Xie, N. Ni, S. L. Bud'ko, G. S. Boebinger, P. C. Canfield, and J. C. Davis, Science **327**, 181 (2010).

[41] J.-H. Chu, H.-H. Kuo, J. G. Analytis, and I. R. Fisher, Science **337**, 710 (2012).

[42] S. Ishida, M. Nakajima, T. Liang, K. Kihou, C. H. Lee, A. Iyo, H. Eisaki, T. Kakeshita, Y. Tomioka, T. Ito, and S. Uchida, Phys. Rev. Lett. **110**, 207001 (2013).

[43] E. C. Blomberg, M. A. Tanatar, R. M. Fernandes, I. I. Mazin, B. Shen, H.-H. Wen, M. D. Johannes, J. Schmalian, and R. Prozorov, Nature Communications **4**, 1914 (2013).

[44] H.-H. Kuo and I. R. Fisher, Phys. Rev. Lett. **112**, 227001 (2014).

[45] M. Rotter, M. Tegel, I. Schellenberg, F. M. Schappacher, R. Pöttgen, J. Deisenhofer, A. Günther, F. Schrettle, A. Loidl, and D. Johrendt, New Journal of Physics **11**, 025014 (2009).

[46] P. Bonville, F. Rullier-Albenque, D. Colson, and A. Forget, Europhys. Lett. **89**, 67008 (2010).

[47] I. Nowik, I. Felner, N. Ni, S. L. Bud'ko, and P. C. Canfield, J. Phys.: Cond. Mat. **22**, 355701 (2010).

[48] V. R. Reddy, A. Bharathi, A. Gupta, K. Sharma, S. Chandra, S. Sharma, K. Vinod, and C. S. Sundar, J. Phys.: Cond. Mat. **26**, 356002 (2014).

[49] T. Berlijn, C.-H. Lin, W. Garber, and W. Ku, Phys. Rev. Lett. **108**, 207003 (2012).

[50] T. Berlijn, P. J. Hirschfeld, and W. Ku, Phys. Rev. Lett. **109**, 147003 (2012).

[51] L. Wang, T. Berlijn, Y. Wang, C.-H. Lin, P. J. Hirschfeld, and W. Ku, Phys. Rev. Lett. **110**, 037001 (2013).

[52] S. N. Khan and D. D. Johnson, Phys. Rev. Lett. **112**, 156401 (2014).

[53] S. V. Borisenko, D. V. Evtushinsky, Z.-H. Liu, I. Morozov, R. Kappenberger, S. Wurmehl, B. Büchner, A. N. Yaresko, T. K. Kim, M. Hoesch, T. Wolf, and N. D. Zhigadlo, Nature Physics **12**, 311 (2016), Letter.

[54] Z. P. Yin, K. Haule, and G. Kotliar, Nature Physics **7**, 294 (2011).

[55] P. Werner, M. Casula, T. Miyake, F. Aryasetiawan, A. J. Millis, and S. Biermann, Nature Physics **8**, 331 (2012).

[56] J. Ferber, H. O. Jeschke, and R. Valentí, Phys. Rev. Lett. **109**, 236403 (2012).

[57] J. M. Tomczak, M. van Schilfgaarde, and G. Kotliar, Phys. Rev. Lett. **109**, 237010 (2012).

[58] N. Xu, P. Richard, A. van Roekeghem, P. Zhang, H. Miao, W.-L. Zhang, T. Qian, M. Ferrero, A. S. Sefat, S. Biermann, and H. Ding, **3**, 011006 (2013).

[59] Z. P. Yin, K. Haule, and G. Kotliar, Nature Physics **10**, 845 (2014).

[60] H. Ebert *et al.*, The Munich SPR-KKR Package, Version 7.2 http://olymp.cup.uni-muenchen.de/ak/ebert/SPRKKR.

[61] H. Ebert, D. Ködderitzsch, and J. Minár, Rep. Prog. Phys. **74**, 096501 (2011).

[62] L. de Broglie, Ann. Phys. **3**, 22 (1925).

[63] W. Heisenberg, Z. Physik **33**, 879 (1925).

[64] M. Born and P. Jordan, Z. Physik **34**, 858 (1925).

[65] E. Schrödinger, Ann. Phys. **79**, 361 (1926).

[66] P. A. M. Dirac, Proc. Roy. Soc. (London) A **117**, 778 (1928).

[67] P. A. M. Dirac, Proc. Roy. Soc. (London) A **126**, 801 (1930).

[68] P. A. M. Dirac, *Principles of Quantum Mechanics*, Oxford University Press, 4th edition, 1958.

[69] D. R. Hartree, Proc. Camb. Phil. Soc. **24**, 89 (1928).

[70] V. Fock, Z. Physik **61**, 126 (1930).

[71] C. Møller and M. S. Plesset, Phys. Rev. **46**, 618 (1934).

[72] A. Szabo and N. S. Ostlund, *Modern Quantum Chemistry - Introduction to Advanced Electronic Structure Theory*, Dover Publications, Inc., 1996.

[73] C. Ochsenfeld, J. Kussmann, and D. S. Lambrecht, Linear-scaling methods in quantum chemistry, in *Reviews in Computational Chemistry*, volume 23, page 1, VCH Publishers, New York, 2007.

[74] L. H. Thomas, Proc. Camb. Phil. Soc. **23**, 542 (1927).

[75] E. Fermi, Rend. Accad. Naz. Lincei **6**, 602 (1927).

[76] E. Fermi, Z. Physik **48**, 73 (1928).

[77] P. Hohenberg and W. Kohn, Phys. Rev. **136**, B864 (1964).

[78] O. K. Anderson, Phys. Rev. B **12**, 3060 (1975).

[79] D. J. Singh, *Planewaves, Pseudopotentials and the LAPW Method*, Kluwer Academic Publishers, Boston, 1994.

[80] J. Korringa, Physica **13**, 392 (1947).

[81] W. Kohn and N. Rostoker, Phys. Rev. **94**, 1111 (1954).

[82] J. L. Beeby, Proc. Roy. Soc. (London) A **302**, 113 (1967).

[83] J. S. Faulkner, J. Phys. C: Solid State Phys. **10**, 4661 (1977).

[84] J. S. Faulkner, Phys. Rev. B **19**, 6186 (1979).

[85] J. S. Faulkner and G. M. Stocks, Phys. Rev. B **21**, 3222 (1980).

[86] B. L. Gyorffy and G. M. Stocks, *Electronic States in Random Substitutional Alloys: the CPA and beyond*, volume 42, page 89, Plenum, New York, 1979.

[87] Y. Onodera and M. Okazaki, J. Phys. Soc. Japan **21**, 2400 (1966).

[88] P. Strange, H. Ebert, J. B. Staunton, and B. L. Gyorffy, J. Phys.: Cond. Mat. **1**, 2959 (1989).

[89] P. Weinberger, *Electron Scattering Theory for Ordered and Disordered Matter*, Oxford University Press, Oxford, 1990.

[90] H. Ebert, Fully relativistic band structure calculations for magnetic solids – formalism and application, in *Electronic Structure and Physical Properties of Solids*, edited by H. Dreyssé, volume 535 of *Lecture Notes in Physics*, page 191, Berlin, 2000, Springer.

[91] R. Zeller and P. H. Dederichs, Phys. Rev. Lett. **42**, 1713 (1979).

[92] I. Turek, V. Drchal, J. Kudrnovský, M. Šob, and P. Weinberger, *Electronic structure of disordered alloys, surfaces and interfaces*, Kluwer Academic Publ., Boston, 1997.

[93] P. Soven, Phys. Rev. **156**, 809 (1967).

[94] H. Ebert, *Introduction to Relativistic Quantum Mechanics*, Lecture Notes, LMU Munich, 2009.

[95] H. Ebert, *Relativistic Green function for general potentials*, Lecture Notes, LMU Munich, 2013.

[96] H. Ebert, *An introduction to the KKR-GF method*, Lecture Notes, LMU Munich, 2014.

[97] J. Minár, *Spin-orbit coupling influenced X-ray spectroscopies and resonant X-ray magneto-optical properties of transition metal systems*, PhD thesis, LMU Munich, 2003.

[98] S. Lowitzer, *Relativistic electronic transport theory - The spin Hall effect and related phenomena*, PhD thesis, LMU Munich, 2010.

[99] S. Bornemann, *Theoretical Investigations on the Magnetic Properties of Fe and Co Nanostructures on Noble Metal Surfaces*, PhD thesis, LMU Munich, 2011.

[100] E. N. Economou, *Green's Functions in Quantum Physics*, Springer-Verlag, New York, 1990.

[101] F. W. Byron and R. W. Fuller, *Mathematics of Classical and Quantum Physics*, Dover Publications, New York, 1992.

[102] A. Gonis, *Green functions for ordered and disordered systems*, North-Holland, Amsterdam, 1992.

[103] M. Abramowitz and I. A. Stegun, *Handbook of Mathematical Functions*, Dover Publications, New York, 1964.

[104] R. Feder, F. Rosicky, and B. Ackermann, Z. Physik B **52**, 31 (1983).

[105] H. Ebert and B. L. Gyorffy, J. Phys. F: Met. Phys. **18**, 451 (1988).

[106] B. L. Gyorffy and M. J. Stott, *Band Structure Spectroscopy of Metals and Alloys*, Academic Press, New York, 1973.

[107] A. Gonis and W. H. Butler, *Multiple Scattering in Solids*, Springer, New York, 2000.

[108] J. Korringa, J. Phys. Chem. Solids **7**, 252 (1958).

[109] J. L. Beeby, Phys. Rev. **135**, A130 (1964).

[110] R. Mills, L. J. Gray, and T. Kaplan, Phys. Rev. B **27**, 3252 (1983).

[111] D. A. Rowlands, J. B. Staunton, and B. L. Györffy, Phys. Rev. B **67**, 115109 (2003).

[112] D. Ködderitzsch, H. Ebert, D. A. Rowlands, and A. Ernst, New Journal of Physics **9**, 81 (2007).

[113] M. Battocletti and H. Ebert, Phys. Rev. B **64**, 094417 (2001).

[114] H. Akai, M. Akai, S. Blügel, R. Zeller, and P. H. Dederichs, J. Magn. Magn. Materials **45**, 291 (1984).

[115] M. E. Elzain, D. E. Ellis, and D. Guenzburger, Phys. Rev. B **34**, 1430 (1986).

[116] B. Lindgren and J. Sjostrom, J. Phys. F: Met. Phys. **18**, 1563 (1988).

[117] H. Ebert, H. Winter, D. D. Johnson, and F. J. Pinski, Hyperfine Interactions **51**, 925 (1989).

[118] G. Y. Guo and H. Ebert, Phys. Rev. B **53**, 2492 (1996).

[119] E. Pavarini, E. Koch, D. Vollhardt, and A. Lichtenstein (Eds.), *The LDA+DMFT approach to strongly correlated materials*, volume 1, Forschungszentrum Jülich GmbH, 2011.

[120] J. Minár, J. Phys.: Cond. Mat. **23**, 253201 (2011).

[121] W. Metzner and D. Vollhardt, Phys. Rev. Lett. **62**, 324 (1989).

[122] A. Georges, G. Kotliar, W. Krauth, and M. J. Rozenberg, Rev. Mod. Phys. **68**, 13 (1996).

[123] M. D. Johannes and I. I. Mazin, Phys. Rev. B **79**, 220510 (2009).

[124] A. Sanna, F. Bernardini, G. Profeta, S. Sharma, J. K. Dewhurst, A. Lucarelli, L. Degiorgi, E. K. U. Gross, and S. Massidda, Phys. Rev. B **83**, 054502 (2011).

[125] H. Hertz, Ann. Phys. **257**, 988 (1887).

[126] A. Einstein, Ann. Phys. **322**, 132 (1905).

[127] A. Damascelli, Z. Hussain, and Z. Shen, Rev. Mod. Phys. **75**, 473 (2003).

[128] J. Braun, Rep. Prog. Phys. **59**, 1267 (1996).

[129] J. Braun and M. Donath, J. Phys.: Cond. Mat. **16**, S2539 (2004).

[130] J. Braun and M. Donath, Europhys. Lett. **59**, 592 (2002).

[131] G. Borstel, Appl. Physics A **38**, 193 (1985).

[132] W. Nolting, Z. Physik B **80**, 73 (1990).

[133] J. B. Pendry, Surf. Sci. **57**, 679 (1976).

[134] J. B. Pendry, *Low energy electron diffraction*, Academic Press, London, 1974.

[135] J. F. L. Hopkinson, J. B. Pendry, and D. J. Titterington, Comp. Phys. Commun. **19**, 69 (1980).

[136] J. B. Pendry, Phys. Rev. Lett. **45**, 1356 (1980).

[137] R. Feder and H. J. Meister, Z. Physik **209**, 309 (1969).

[138] M. Grass, J. Braun, G. Borstel, R. Schneider, H. Durr, T. Fauster, and V. Dose, J. Phys.: Cond. Mat. **5**, 599 (1993).

[139] G. Malmström and J. Rundgren, Comp. Phys. Commun. **19**, 263 (1980).

[140] P. M. Echenique and J. B. Pendry, J. Phys. C: Solid State Phys. **11**, 2065 (1978).

[141] E. G. McRae, Rev. Mod. Phys. **51**, 541 (1979).

[142] J. Banhart, *Transporteigenschafter komplexer metallischer Systeme*, Habilitation, Bremen University, 1997.

[143] H. Nakano, Prog. Theo. Phys. **15**, 77 (1956).

[144] H. Mori, **11**, 1029 (1956).

[145] R. Kubo, J. Phys. Soc. Japan **12**, 570 (1957).

[146] M. S. Green, J. Chem. Phys. **20**, 1281 (1952).

[147] A. Bastin, C. Lewiner, O. Betbeder-matibet, and P. Nozieres, J. Phys. Chem. Solids **32**, 1811 (1971).

[148] P. Středa, J. Phys. C: Solid State Phys. **15**, L717 (1982).

[149] A. Crépieux and P. Bruno, Phys. Rev. B **64**, 094434 (2001).

[150] D. A. Greenwood, Proc. Phys. Soc. **71**, 585 (1958).

[151] D. C. Johnston, Adv. Phys. **59**, 803 (2010).

[152] H.-H. Wen and S. Li, Annu. Rev. Condens. Matter Phys. **2**, 121 (2011).

[153] I. I. Mazin, Nature **464**, 183 (2010).

[154] S. Kasahara, H. J. Shi, K. Hashimoto, S. Tonegawa, Y. Mizukami, T. Shibauchi, K. Sugimoto, T. Fukuda, T. Terashima, A. H. Nevidomskyy, and Y. Matsuda, Nature **486**, 382 (2012).

[155] M. N. Gastiasoro, I. Paul, Y. Wang, P. J. Hirschfeld, and B. M. Andersen, Phys. Rev. Lett. **113**, 127001 (2014).

[156] W. J. Moore and L. Pauling, J. Amer. Chem. Soc. **63**, 1392 (1941).

[157] W. Nieuwenkamp and J. M. Bijvoet, Z. Kristallogr. **171**, 23 (1985).

[158] Z. Ban and M. Sikirica, Acta Crystallogr.F **18**, 594 (1965).

[159] V. Johnson and W. Jeitschko, J. Solid State Chem. **11**, 161 (1974).

[160] F. C. Hsu, J. Y. Luo, K. W. Yeh, T. K. Chen, T. W. Huang, P. M. Wu, Y. C. Lee, Y. L. Huang, Y. Y. Chu, D. C. Yan, and M. K. Wu, Proc. Nat. Ac. Sci. US. **105**, 14262 (2008).

[161] C. W. Chu, F. Chen, M. Gooch, A. M. Guloy, B. Lorenz, B. Lv, K. Sasmal, Z. J. Tang, J. H. Tapp, and Y. Y. Xue, Physica C **469**, 326 (2009).

[162] J. Zhao, Q. Huang, C. de la Cruz, S. Li, J. W. Lynn, Y. Chen, M. A. Green, G. F. Chen, G. Li, Z. L. J. L. Luo, N. L. Wang, and P. Dai, Nature Materials **7**, 953 (2008).

[163] K. Miyazawa, K. Kihou, P. M. Shirage, C. Lee, H. Kito, H. Eisaki, and A. Iyo, J. Phys. Soc. Japan **78**, 34712 (2009).

[164] X. H. Chen, T. Wu, G. Wu, R. H. Lui, H. Chen, and D. F. Fang, Nature **453**, 376 (2008).

[165] G. F. Chen, Z. Li, D. Wu, G. Li, W. Z. Hu, J. Dong, P. Zheng, J. L. Luo, and N. L. Wang, Phys. Rev. Lett. **100**, 247002 (2008).

[166] J. Yang, Z. C. Li, W. Lu, W. Yi, X. L. Shen, Z. A. Ren, G. C. Che, X. L. Dong, L. L. Sun, F. Zhou, and Z. X. Zhou, Supercond. Sci. Technol. **21**, 82001 (2008).

[167] Z. A. Ren, J. Yang, W. Lu, W. Yi, X. L. Shen, Z. C. Li, G. C. Che, X. L. Dong, L. L. Sung, F. Zhou, and Z. X. Zhao, Europhys. Lett. **82**, 57002 (2008).

[168] A. D. Christianson, E. A. Goremychkin, R. Osborn, S. Rosenkranz, M. D. Lumsden, C. D. Malliakas, I. Todorov, H. Claus, D. Y. Chung, M. G. Kanatzidis, R. I. Bewley, and T. Guidi, Nature **456**, 930 (2008).

[169] K. Sasmal, L. Bing, B. Lorenz, A. M. Guloy, F. Chen, Y. Xue, and C. Chu, Phys. Rev. Lett. **101**, 107007 (2008).

[170] X. Zhu, F. Han, G. Mu, P. Cheng, B. Shen, B. Zeng, and H. Wen, Phys. Rev. B **79**, 220512 (2009).

[171] A. Pal, A. Vajpayee, R. S. Meena, H. Kishan, and V. P. S. Awana, J. Supercond. Nov. Magn. **22**, 619 (2009).

[172] M. Tegel, F. Hummel, S. Lackner, I. Schellenberg, R. Pöttgen, and D. Johrendt, Z. Anorg. Allg. Chem. **635**, 2242 (2009).

[173] C. Löhnert, T. Stürzer, M. Tegel, R. Frankovsky, G. Friederichs, and D. Johrendt, Angew. Chem. Int. Ed. **50**, 9195 (2011).

[174] N. Ni, J. M. Allred, B. C. Benny, C. Chan, and R. J. Cava, Proc. Nat. Ac. Sci. US. **108**, E1019 (2011).

[175] S. Kakiya, K. Kudo, Y. Yoshihiro, K. Oku, E. Sawa, T. Yamamoto, T. Nozaka, and M. Nohara, J. Phys. Soc. Japan **80**, 93704 (2011).

[176] T. Stürzer, G. Derondeau, and D. Johrendt, Phys. Rev. B **86**, 060516 (2012).

[177] T. Stürzer, G. Derondeau, E.-M. Bertschler, and D. Johrendt, Solid State Commun. **201**, 36 (2015).

[178] U. Pachmayr, F. Nitsche, H. Luetkens, S. Kamusella, F. Brückner, R. Sarkar, H.-H. Klauss, and D. Johrendt, Angew. Chem. Int. Ed. **54**, 293 (2015).

[179] Z. A. Ren, G. C. Che, X. L. Dong, J. Yang, W. Lu, W. Yi, X. L. Shen, Z. C. Li, L. L. Sun, F. Zhou, and Z. X. Zhao, Europhys. Lett. **83**, 17002 (2008).

[180] H. Kito, H. Eisaki, and A. Iyo, J. Phys. Soc. Japan **77**, 63707 (2008).

[181] C. Wang, Y. K. Li, Z. W. Zhu, S. Jiang, X. Lin, Y. K. Luo, S. Chi, L. J. Li, Z. Ren, M. He, H. Chen, Y. T. Wang, Q. Tao, G. H. Cao, and Z. A. Xu, Phys. Rev. B **79**, 054521 (2009).

[182] H. Shishido, A. F. Bangura, A. I. Coldea, S. Tonegawa, K. Hashimoto, S. Kasahara, P. M. C. Rourke, H. Ikeda, T. Terashima, R. Settai, Y. Ōnuki, D. Vignolles, C. Proust, B. Vignolle, A. McCollam, Y. Matsuda, T. Shibauchi, and A. Carrington, Phys. Rev. Lett. **104**, 057008 (2010).

[183] S. Sharma, A. Bharathi, S. Chandra, V. R. Reddy, S. Paulraj, A. T. Satya, V. S. Sastry, A. Gupta, and C. S. Sundar, Phys. Rev. B **81**, 174512 (2010).

[184] C. Lester, J.-H. Chu, J. G. Analytis, S. C. Capelli, A. S. Erickson, C. L. Condron, M. F. Toney, I. R. Fisher, and S. M. Hayden, Phys. Rev. B **79**, 144523 (2009).

[185] C. Hess, A. Kondrat, A. Narduzzo, J. E. Hamann-Borrero, R. Klingeler, J. Werner, G. Behr, and B. Büchner, Europhys. Lett. **87**, 17005 (2009).

[186] M. G. Kim, R. M. Fernandes, A. Kreyssig, J. W. Kim, A. Thaler, S. L. Bud'ko, P. C. Canfield, R. J. McQueeney, J. Schmalian, and A. I. Goldman, Phys. Rev. B **83**, 134522 (2011).

[187] M. D. Lumsden and A. D. Christianson, J. Phys.: Cond. Mat. **22**, 203203 (2010).

[188] J. T. Park, D. S. Inosov, C. Niedermayer, G. L. Sun, D. Haug, N. B. Christensen, R. Dinnebier, A. V. Boris, A. J. Drew, L. Schulz, T. Shapoval, U. Wolff, V. Neu, X. Yang, C. T. Lin, B. Keimer, and V. Hinkov, Phys. Rev. Lett. **102**, 117006 (2009).

[189] E. Wiesenmayer, H. Luetkens, G. Pascua, R. Khasanov, A. Amato, H. Potts, B. Banusch, H.-H. Klauss, and D. Johrendt, Phys. Rev. Lett. **107**, 237001 (2011).

[190] D. Mandrus, A. S. Sefat, M. A. McGuire, and B. C. Sales, Chem. Mater. **22**, 715 (2010).

[191] M. A. Tanatar, A. Kreyssig, S. Nandi, N. Ni, S. L. Bud'ko, P. C. Canfield, A. I. Goldman, and R. Prozorov, Phys. Rev. B **79**, 180508 (2009).

[192] H.-H. Kuo, J.-H. Chu, S. C. Riggs, L. Yu, P. L. McMahon, K. De Greve, Y. Yamamoto, J. G. Analytis, and I. R. Fisher, Phys. Rev. B **84**, 054540 (2011).

[193] Y. Kim, H. Oh, C. Kim, D. Song, W. Jung, B. Kim, H. J. Choi, C. Kim, B. Lee, S. Khim, H. Kim, K. Kim, J. Hong, and Y. Kwon, Phys. Rev. B **83**, 064509 (2011).

[194] J. C. Davis and P. J. Hirschfeld, Nature Physics **10**, 184 (2014), News and Views.

[195] M. P. Allan, T.-M. Chuang, F. Massee, Y. Xie, N. Ni, S. L. Bud'ko, G. S. Boebinger, Q. Wang, D. S. Dessau, P. C. Canfield, M. S. Golden, and J. C. Davis, Nature Physics **9**, 220 (2013).

[196] E. P. Rosenthal, E. F. Andrade, C. J. Arguello, R. M. Fernandes, L. Y. Xing, X. C. Wang, C. Q. Jin, A. J. Millis, and A. N. Pasupathy, Nature Physics **10**, 225 (2014).

[197] A. W. Overhauser and A. Arrott, Phys. Rev. Lett. **3**, 414 (1959).

[198] P. Monceau, Adv. Phys. **61**, 325 (2012).

[199] E. C. Stoner, Proc. Roy. Soc. (London) A **165**, 372 (1938).

[200] A. W. Overhauser, Phys. Rev. **128**, 1437 (1962).

[201] S. Mankovsky, G. H. Fecher, and H. Ebert, Phys. Rev. B **83**, 144401 (2011).

[202] A. A. Aczel, E. Baggio-Saitovitch, S. L. Bud'ko, P. C. Canfield, J. P. Carlo, G. F. Chen, P. Dai, T. Goko, W. Z. Hu, G. M. Luke, J. L. Luo, N. Ni, D. R. Sanchez-Candela, F. F. Tafti, N. L. Wang, T. J. Williams, W. Yu, and Y. J. Uemura, Phys. Rev. B **78**, 214503 (2008).

[203] T. Goko, A. A. Aczel, E. Baggio-Saitovitch, S. L. Bud'ko, P. C. Canfield, J. P. Carlo, G. F. Chen, P. Dai, A. C. Hamann, W. Z. Hu, H. Kageyama, G. M. Luke, J. L. Luo, B. Nachumi, N. Ni, D. Reznik, D. R. Sanchez-Candela, A. T. Savici, K. J. Sikes, N. L. Wang, C. R. Wiebe, T. J. Williams, T. Yamamoto, W. Yu, and Y. J. Uemura, Phys. Rev. B **80**, 024508 (2009).

[204] N. Ni, S. L. Bud'ko, A. Kreyssig, S. Nandi, G. E. Rustan, A. I. Goldman, S. Gupta, J. D. Corbett, A. Kracher, and P. C. Canfield, Phys. Rev. B **78**, 014507 (2008).

[205] Z. Bukowski, S. Weyeneth, R. Puzniak, P. Moll, S. Katrych, N. D. Zhigadlo, J. Karpinski, H. Keller, and B. Batlogg, Phys. Rev. B **79**, 104521 (2009).

[206] F. Ronning, T. Klimczuk, E. D. Bauer, H. Volz, and J. D. Thompson, J. Phys.: Cond. Mat. **20**, 322201 (2008).

[207] C. Krellner, N. Caroca-Canales, A. Jesche, H. Rosner, A. Ormeci, and C. Geibel, Phys. Rev. B **78**, 100504 (2008).

[208] A. Leithe-Jasper, W. Schnelle, C. Geibel, and H. Rosner, Phys. Rev. Lett. **101**, 207004 (2008).

[209] A. I. Goldman, D. N. Argyriou, B. Ouladdiaf, T. Chatterji, A. Kreyssig, S. Nandi, N. Ni, S. L. Bud'ko, P. C. Canfield, and R. J. McQueeney, Phys. Rev. B **78**, 100506 (2008).

[210] J. Zhao, W. Ratcliff, J. W. Lynn, G. F. Chen, J. L. Luo, N. L. Wang, J. Hu, and P. Dai, Phys. Rev. B **78**, 140504 (2008).

[211] M. S. Torikachvili, S. L. Bud'ko, N. Ni, and P. C. Canfield, Phys. Rev. Lett. **101**, 057006 (2008).

[212] K. Prokes, A. Kreyssig, B. Ouladdiaf, D. K. Pratt, N. Ni, S. L. Bud'ko, P. C. Canfield, R. J. McQueeney, D. N. Argyriou, and A. I. Goldman, Phys. Rev. B **81**, 180506 (2010).

[213] S. R. Saha, N. P. Butch, T. Drye, J. Magill, S. Ziemak, K. Kirshenbaum, P. Y. Zavalij, J. W. Lynn, and J. Paglione, Phys. Rev. B **85**, 024525 (2012).

[214] M. Rotter, M. Pangerl, M. Tegel, and D. Johrendt, Angew. Chem. Int. Ed. **47**, 7949 (2008).

[215] D. V. Evtushinsky, D. S. Inosov, V. B. Zabolotnyy, A. Koitzsch, M. Knupfer, B. Büchner, M. S. Viazovska, G. L. Sun, V. Hinkov, A. V. Boris, C. T. Lin, B. Keimer, A. Varykhalov, A. A. Kordyuk, and S. V. Borisenko, Phys. Rev. B **79**, 054517 (2009).

[216] D. V. Evtushinsky, D. S. Inosov, V. B. Zabolotnyy, M. S. Viazovska, R. Khasanov, A. Amato, H.-H. Klauss, H. Luetkens, C. Niedermayer, G. L. Sun, V. Hinkov, C. T. Lin, A. Varykhalov, A. Koitzsch, M. Knupfer, B. Büchner, A. A. Kordyuk, and S. V. Borisenko, New Journal of Physics **11**, 055069 (2009).

[217] D. V. Evtushinsky, V. B. Zabolotnyy, T. K. Kim, A. A. Kordyuk, A. N. Yaresko, J. Maletz, S. Aswartham, S. Wurmehl, A. V. Boris, D. L. Sun, C. T. Lin, B. Shen, H. H. Wen, A. Varykhalov, R. Follath, B. Büchner, and S. V. Borisenko, Phys. Rev. B **89**, 064514 (2014).

[218] D. V. Evtushinsky, V. B. Zabolotnyy, L. Harnagea, A. N. Yaresko, S. Thirupathaiah, A. A. Kordyuk, J. Maletz, S. Aswartham, S. Wurmehl, E. Rienks, R. Follath, B. Büchner, and S. V. Borisenko, Phys. Rev. B **87**, 094501 (2013).

[219] S. V. Borisenko, V. B. Zabolotnyy, D. V. Evtushinsky, T. K. Kim, I. V. Morozov, A. N. Yaresko, A. A. Kordyuk, G. Behr, A. Vasiliev, R. Follath, and B. Büchner, Phys. Rev. Lett. **105**, 067002 (2010).

[220] S. Thirupathaiah, D. V. Evtushinsky, J. Maletz, V. B. Zabolotnyy, A. A. Kordyuk, T. K. Kim, S. Wurmehl, M. Roslova, I. Morozov, B. Büchner, and S. V. Borisenko, Phys. Rev. B **86**, 214508 (2012).

[221] J. Maletz, V. B. Zabolotnyy, D. V. Evtushinsky, A. N. Yaresko, A. A. Kordyuk, Z. Shermadini, H. Luetkens, K. Sedlak, R. Khasanov, A. Amato, A. Krzton-Maziopa, K. Conder, E. Pomjakushina, H.-H. Klauss, E. D. L. Rienks, B. Büchner, and S. V. Borisenko, Phys. Rev. B **88**, 134501 (2013).

[222] S. Ishida, M. Nakajima, T. Liang, K. Kihou, C.-H. Lee, A. Iyo, H. Eisaki, T. Kakeshita, Y. Tomioka, T. Ito, and S. Uchida, J. Amer. Chem. Soc. **135**, 3158 (2013).

[223] L. Fang, H. Luo, P. Cheng, Z. Wang, Y. Jia, G. Mu, B. Shen, I. I. Mazin, L. Shan, C. Ren, and H.-H. Wen, Phys. Rev. B **80**, 140508 (2009).

[224] N. Ni, M. E. Tillman, J.-Q. Yan, A. Kracher, S. T. Hannahs, S. L. Bud'ko, and P. C. Canfield, Phys. Rev. B **78**, 214515 (2008).

[225] J.-H. Chu, J. G. Analytis, C. Kucharczyk, and I. R. Fisher, Phys. Rev. B **79**, 014506 (2009).

[226] J.-H. Chu, J. G. Analytis, D. Press, K. De Greve, T. D. Ladd, Y. Yamamoto, and I. R. Fisher, Phys. Rev. B **81**, 214502 (2010).

[227] M. Nakajima, S. Ishida, T. Tanaka, K. Kihou, Y. Tomioka, T. Saito, C. H. Lee, H. Fukazawa, Y. Kohori, T. Kakeshita, A. Iyo, T. Ito, H. Eisaki, and S. Uchida, Sci. Rep. **4**, 5873 (2014).

[228] P. C. Canfield, S. L. Bud'ko, N. Ni, J. Q. Yan, and A. Kracher, Phys. Rev. B **80**, 060501 (2009).

[229] N. Ni, A. Thaler, A. Kracher, J. Q. Yan, S. L. Bud'ko, and P. C. Canfield, Phys. Rev. B **80**, 024511 (2009).

[230] N. Ni, A. Thaler, J. Q. Yan, A. Kracher, E. Colombier, S. L. Bud'ko, P. C. Canfield, and S. T. Hannahs, Phys. Rev. B **82**, 024519 (2010).

[231] A. N. Thaler, *Structural and magnetic properties and superconductivity in Ba(*$Fe_{1-x}TM_x)_2As_2$*(TM=Ru, Mn, Cr/Co, Mn/Co) single crystals*, PhD thesis, Iowa Stata University, 2012.

[232] P. F. S. Rosa, C. Adriano, T. M. Garitezi, M. M. Piva, K. Mydeen, T. Grant, Z. Fisk, M. Nicklas, R. R. Urbano, R. M. Fernandes, and P. G. Pagliuso1, Sci. Rep. **4**, 6252 (2014).

[233] M. G. Kim, A. Kreyssig, A. Thaler, D. K. Pratt, W. Tian, J. L. Zarestky, M. A. Green, S. L. Bud'ko, P. C. Canfield, R. J. McQueeney, and A. I. Goldman, Phys. Rev. B **82**, 220503 (2010).

[234] G. S. Tucker, D. K. Pratt, M. G. Kim, S. Ran, A. Thaler, G. E. Granroth, K. Marty, W. Tian, J. L. Zarestky, M. D. Lumsden, S. L. Bud'ko, P. C. Canfield, A. Kreyssig, A. I. Goldman, and R. J. McQueeney, Phys. Rev. B **86**, 020503 (2012).

[235] R. S. Dhaka, C. Liu, R. M. Fernandes, R. Jiang, C. P. Strehlow, T. Kondo, A. Thaler, J. Schmalian, S. L. Bud'ko, P. C. Canfield, and A. Kaminski, Phys. Rev. Lett. **107**, 267002 (2011).

[236] G. Derondeau, *Comprehensive Study of the Electronic and Magnetic Properties for the Tetragonal and Orthorhombic Phase of* $Ba(Fe_{1-x}Co_x)_2As_2$, Master's thesis, LMU Munich, 2013.

[237] H. Wadati, I. Elfimov, and G. A. Sawatzky, Phys. Rev. Lett. **105**, 157004 (2010).

[238] E. M. Bittar, C. Adriano, T. M. Garitezi, P. F. S. Rosa, L. Mendon ça Ferreira, F. Garcia, G. d. M. Azevedo, P. G. Pagliuso, and E. Granado, Phys. Rev. Lett. **107**, 267402 (2011).

[239] M. Merz, F. Eilers, T. Wolf, P. Nagel, H. v. Löhneysen, and S. Schuppler, Phys. Rev. B **86**, 104503 (2012).

[240] S. N. Khan, A. Alam, and D. D. Johnson, Phys. Rev. B **89**, 205121 (2014).

[241] D. Kasinathan, A. Ormeci, K. Koch, U. Burkhardt, W. Schnelle, A. Leithe-Jasper, and H. Rosner, New Journal of Physics **11**, 025023 (2009).

[242] A. N. Yaresko, G.-Q. Liu, V. N. Antonov, and O. K. Andersen, Phys. Rev. B **79**, 144421 (2009).

[243] E. Aktürk and S. Ciraci, Phys. Rev. B **79**, 184523 (2009).

[244] T. Kondo, R. M. Fernandes, R. Khasanov, C. Liu, A. D. Palczewski, N. Ni, M. Shi, A. Bostwick, E. Rotenberg, J. Schmalian, S. L. Bud'ko, P. C. Canfield, and A. Kaminski, Phys. Rev. B **81**, 060507 (2010).

[245] M. Fuglsang Jensen, V. Brouet, E. Papalazarou, A. Nicolaou, A. Taleb-Ibrahimi, P. Le Fèvre, F. Bertran, A. Forget, and D. Colson, Phys. Rev. B **84**, 014509 (2011).

[246] I. R. Fisher, L. Degiorgi, and Z. X. Shen, Rep. Prog. Phys. **74**, 124506 (2011).

[247] F. Massee, S. de Jong, Y. Huang, J. Kaas, E. van Heumen, J. B. Goedkoop, and M. S. Golden, Phys. Rev. B **80**, 140507 (2009).

[248] V. B. Nascimento, A. Li, D. R. Jayasundara, Y. Xuan, J. O'Neal, S. Pan, T. Y. Chien, B. Hu, X. B. He, G. Li, A. S. Sefat, M. A. McGuire, B. C. Sales, D. Mandrus, M. H. Pan, J. Zhang, R. Jin, and E. W. Plummer, Phys. Rev. Lett. **103**, 076104 (2009).

[249] G. Profeta, C. Franchini, K. A. I. L. W. Gamalath, and A. Continenza, Phys. Rev. B **82**, 195407 (2010).

[250] J. E. Hoffman, Rep. Prog. Phys. **74**, 124513 (2011).

[251] F. Bisti, V. A. Rogalev, M. Shi, T. Schmitt, J. Ma, H. Ding, and V. N. Strocov, personal communication, 2015.

[252] D. V. Evtushinsky, A. A. Kordyuk, V. B. Zabolotnyy, D. S. Inosov, T. K. Kim, B. Büchner, H. Luo, Z. Wang, H.-H. Wen, G. Sun, C. Lin, and S. V. Borisenko, J. Phys. Soc. Japan **80**, 023710 (2011).

[253] K. Nakayama, T. Sato, P. Richard, Y.-M. Xu, T. Kawahara, K. Umezawa, T. Qian, M. Neupane, G. F. Chen, H. Ding, and T. Takahashi, Phys. Rev. B **83**, 020501 (2011).

[254] N. Xu, P. Richard, X. Shi, A. van Roekeghem, T. Qian, E. Razzoli, E. Rienks, G.-F. Chen, E. Ieki, K. Nakayama, T. Sato, T. Takahashi, M. Shi, and H. Ding, Phys. Rev. B **88**, 220508 (2013).

[255] Y.-Z. Zhang, H. Lee, I. Opahle, H. O. Jeschke, and R. Valentí, J. Phys. Chem. Solids **72**, 324 (2011).

[256] V. Brouet, P.-H. Lin, Y. Texier, J. Bobroff, A. Taleb-Ibrahimi, P. Le Fèvre, F. Bertran, M. Casula, P. Werner, S. Biermann, F. Rullier-Albenque, A. Forget, and D. Colson, Phys. Rev. Lett. **110**, 167002 (2013).

[257] V. Brouet, D. LeBoeuf, P.-H. Lin, J. Mansart, A. Taleb-Ibrahimi, P. Le Fèvre, F. Bertran, A. Forget, and D. Colson, Phys. Rev. B **93**, 085137 (2016).

[258] I. M. Lifshitz, Sov. Phys. J.E.T.P. **11**, 1130 (1960).

[259] S. Backes, D. Guterding, H. O. Jeschke, and R. Valentí, New Journal of Physics **16**, 083025 (2014).

[260] L. Moreschini, P.-H. Lin, C.-H. Lin, W. Ku, D. Innocenti, Y. J. Chang, A. L. Walter, K. S. Kim, V. Brouet, K.-W. Yeh, M.-K. Wu, E. Rotenberg, A. Bostwick, and M. Grioni, Phys. Rev. Lett. **112**, 087602 (2014).

[261] M. Wang, C. Zhang, X. Lu, G. Tan, H. Luo, Y. Song, M. Wang, X. Zhang, E. A. Goremychkin, T. G. Perring, T. A. Maier, Z. Yin, K. Haule, G. Kotliar, and P. Dai, Nature Communications **4**, 2874 (2013).

[262] G. Derondeau, S. Polesya, S. Mankovsky, H. Ebert, and J. Minár, Phys. Rev. B **90**, 184509 (2014).

[263] L. Liu, T. Mikami, S. Ishida, K. Koshiishi, K. Okazaki, T. Yoshida, H. Suzuki, M. Horio, L. C. C. Ambolode, J. Xu, H. Kumigashira, K. Ono, M. Nakajima, K. Kihou, C. H. Lee, A. Iyo, H. Eisaki, T. Kakeshita, S. Uchida, and A. Fujimori, Phys. Rev. B **92**, 094503 (2015).

[264] B. Valenzuela, E. Bascones, and M. J. Calderón, Phys. Rev. Lett. **105**, 207202 (2010).

[265] R. M. Fernandes, E. Abrahams, and J. Schmalian, Phys. Rev. Lett. **107**, 217002 (2011).

[266] M. N. Gastiasoro, P. J. Hirschfeld, and B. M. Andersen, Phys. Rev. B **89**, 100502 (2014).

[267] Y. Wang, M. N. Gastiasoro, B. M. Andersen, M. Tomić, H. O. Jeschke, R. Valentí, I. Paul, and P. J. Hirschfeld, Phys. Rev. Lett. **114**, 097003 (2015).

[268] K. Sugimoto, P. Prelovšek, E. Kaneshita, and T. Tohyama, Phys. Rev. B **90**, 125157 (2014).

[269] M. Breitkreiz, P. M. R. Brydon, and C. Timm, Phys. Rev. B **90**, 121104 (2014).

[270] M. Breitkreiz, P. M. R. Brydon, and C. Timm, Phys. Rev. B **89**, 245106 (2014).

[271] S. Dubiel, J. Alloys Comp. **488**, 18 (2009).

[272] H. Pang, Y. Fang, and F. Li, Hyperfine Interactions **199**, 387 (2011).

[273] G. Derondeau, J. Braun, H. Ebert, and J. Minár, Phys. Rev. B **93**, 144513 (2016).

[274] G. Derondeau, F. Bisti, J. Braun, V. A. Rogalev, M. Kobayashi, M. Shi, T. Schmitt, J. Ma, H. Ding, H. Ebert, V. N. Strocov, and J. Minár, arXiv:1606.08977v2, 2016.

[275] G. Derondeau, J. Minár, S. Wimmer, and H. Ebert, arXiv:1608.08077, 2016.

[276] G. Derondeau, J. Minár, and H. Ebert, Phys. Rev. B **94**, 214508 (2016).

[277] S. H. Vosko, L. Wilk, and M. Nusair, Can. J. Phys. **58**, 1200 (1980).

[278] J. Minár, J. Braun, and H. Ebert, J. Electron. Spectrosc. Relat. Phenom. **189**, 129 (2013).

[279] J. Braun, K. Miyamoto, A. Kimura, T. Okuda, M. Donath, H. Ebert, and J. Minár, New Journal of Physics **16**, 015005 (2014).

[280] L. Vegard, Z. Physik **5**, 17 (1921).

[281] M. Merz, P. Schweiss, P. Nagel, T. Wolf, H. v. Loehneysen, and S. Schuppler, arXiv:1306.4222, 2013.

[282] M. Merz, P. Schweiss, P. Nagel, M.-J. Huang, R. Eder, T. Wolf, H. von Löhneysen, and S. Schuppler, J. Phys. Soc. Japan **85**, 044707 (2016).

[283] M. Rotter, *High-Temperature Superconductivity in Doped* $BaFe_2As_2$, PhD thesis, LMU München, 2010.

Curriculum Vitae

Gerald Derondeau

Lebenslauf

Ausbildung

10 / 2011 – 11 / 2013	**Master of Science M.Sc.**, *Chemie*, Ludwig-Maximilians-Universität München. Thema der Masterarbeit: Comprehensive Study of the Electronic and Magnetic Properties for the Tetragonal and Orthorhombic Phase of $Ba(Fe_{1\text{-}x}Co_x)_2As_2$
10 / 2008 – 09 / 2011	**Bachelor of Science B.Sc.**, *Chemie und Biochemie*, Ludwig-Maximilians-Universität München. Thema der Bachelorarbeit: Design and Fabrication of TiO_2/SiO_2 Photonic Crystals with Various Architectures for Sensing Applications
06 / 2008	**Abitur**, Thomas-Mann-Gymnasium, München.

Berufspraxis

01 / 2014 – 09 / 2016	**Wissenschaftlicher Mitarbeiter**, Ludwig-Maximilians-Universität München, Department Chemie, Lehrstuhl Physikalische Chemie. Promotion in Physikalischer Chemie in der Gruppe von Prof. Dr. Ebert

Auszeichnungen

12 / 2014	**Römerpreis der Dr. Klaus Römer Stiftung**, *Kategorie Masterarbeit*.

Auslandserfahrung

07 / 2015 – 08 / 2015	**Gastwissenschaftler an der Universität Chiba, Japan**, *Gruppe von Prof. Dr. Krüger der Universität Chiba*, Chiba, Japan.

List of Publications

1. *Role of different negatively charged layers in* $Ca_{10}(FeAs)_{10}(Pt_4As_8)$ *and superconductivity at 30 K in electron-doped* $(Ca_{0.8}La_{0.2})_{10}(FeAs)_{10}(Pt_3As_8)$

   T. Stürzer, **G. Derondeau** and D. Johrendt
   Phys. Rev. B **86**, 060516(R) (2012).

2. *A step towards the electrophotonic nose: integrating 1D photonic crystals with organic light-emitting diodes and photodetectors*

   A. T. Exner, I. Pavlichenko, D. Baierl, M. Schmidt, **G. Derondeau**, B. V. Lotsch, P. Lugli and G. Scarpa
   Laser & Photon. Rev. **8**, 726 (2014).

3. *Theoretical investigation of the electronic and magnetic properties of the orthorhombic phase of* $Ba(Fe_{1-x}Co_x)_2As_2$

   G. Derondeau, S. Polesya, S. Mankovsky, H. Ebert and J. Minár
   Phys. Rev. B **90**, 184509 (2014).

4. *Superconductivity by rare earth doping in the 1038-type compounds* $(Ca_{1-x}RE_x)_{10}(FeAs)_{10}(Pt_3As_8)$*; with RE = Y, La–Nd, Sm–Lu*

   T. Stürzer, **G. Derondeau**, E.-M. Bertschler and D. Johrendt
   Solid State Commun. **201**, 36 (2015).

5. *Theoretical study on the anisotropic electronic structure of antiferromagnetic* $BaFe_2As_2$ *and Co-doped* $Ba(Fe_{1-x}Co_x)_2As_2$ *as seen by angle-resolved photoemission*

   G. Derondeau, J. Braun, H. Ebert and J. Minár
   Phys. Rev. B **93**, 144513 (2016).

6. *Fermi surface and effective masses in photoemission response of the* $(Ba_{1-x}K_x)Fe_2As_2$ *superconductor*

   G. Derondeau, F. Bisti, J. Braun, V. A. Rogalev, M. Kobayashi, M. Shi, T. Schmitt, J. Ma, H. Ding, H. Ebert, V. N. Strocov and J. Minár
   arXiv:1606.08977v2 (2016), submitted to Scientific Reports

7. *In-plane anisotropic magnetoresistance in antiferromagnetic* $Ba(Fe_{1-x}Co_x)_2As_2$, $(Ba_{1-x}K_x)Fe_2As_2$ *and* $Ba(Fe_{1-x}Ru_x)_2As_2$

   G. Derondeau, J. Minár, S. Wimmer and H. Ebert
   arXiv:1608.08077 (2016), submitted to Physical Review Letters

8. *Hyperfine fields in the* $BaFe_2As_2$ *family and their relation to the magnetic moment*

   G. Derondeau, J. Minár and H. Ebert
   Phys. Rev. B **94**, 214508 (2016).

Conference Contributions

Talks

- Spring Meeting DPG 2016, TT 79.9, Regensburg, Germany, 10.03.2016.
- Workshop DFG Research Unit FOR 1346, Würzburg, Germany, 24.02.2016.
- 3rd MSNano Workshop, Chiba, Japan, 28.07.2015.
- University of Chiba, Department Nanoscience, Chiba, Japan, 17.07.2015.
- Spring Meeting DPG 2015, TT 110.9, Berlin, Germany, 20.03.2015.
- Workshop DFG Research Unit FOR 1346, Würzburg, Germany, 11.02.2015.
- Spring Meeting DPG 2014, TT 68.3, Dresden, Germany, 02.04.2014.
- Max Planck Institute for Solid State Research, Group of Prof. Dr. Keimer, Stuttgart, Germany, 28.01.2014.

Poster

- Psi-k (Ψ_k) Conference 2015, Donostia/San-Sebastian, Spain, 06.09.–10.09.2015
- International Workshop on Itinerant Magnetism and Superconductivity (IMS 2014), Dresden, Germany 23.06.–25.06.2014
- Autumn School on Correlated Electrons: Emergent Phenomena in Correlated Matter, Jülich, Germany, 23.09.–27.09.2013
- Computation meets Experiment - KKR Greens functions for calculations of spectroscopic, transport and magnetic properties, Warwick, England, 08.07.–15.07.2013